

ISTC 2196P

**Final
Project Technical Report
of ISTC 2196p**

MHD Flow Control

(From June 1, 2002 to May 31, 2006)

**Valentin A. Bityurin
(Project Manager)**

Institute of High Temperatures RAS

September 2006

This work was supported financially by European Office of Aerospace Research and Development (EOARD) and performed under the contract to the International Science and Technology Center (ISTC), Moscow.

20071029033

REPORT DOCUMENTATION PAGE				Form Approved OMB No. 0704-0188	
<p>Public reporting burden for this collection of information is estimated to average 1 hour per response, including the time for reviewing instructions, searching existing data sources, gathering and maintaining the data needed, and completing and reviewing the collection of information. Send comments regarding this burden estimate or any other aspect of this collection of information, including suggestions for reducing the burden, to Department of Defense, Washington Headquarters Services, Directorate for Information Operations and Reports (0704-0188), 1215 Jefferson Davis Highway, Suite 1204, Arlington, VA 22202-4302. Respondents should be aware that notwithstanding any other provision of law, no person shall be subject to any penalty for failing to comply with a collection of information if it does not display a currently valid OMB control number.</p> <p>PLEASE DO NOT RETURN YOUR FORM TO THE ABOVE ADDRESS.</p>					
1. REPORT DATE (DD-MM-YYYY) 12-10-2006		2. REPORT TYPE Final Report		3. DATES COVERED (From - To) 01-Jun-02 - 19-Mar-07	
4. TITLE AND SUBTITLE MHD Flow Control			5a. CONTRACT NUMBER ISTC Registration No: 2196p		
			5b. GRANT NUMBER		
			5c. PROGRAM ELEMENT NUMBER		
6. AUTHOR(S) Dr. Valentin Bityurin			5d. PROJECT NUMBER		
			5d. TASK NUMBER		
			5e. WORK UNIT NUMBER		
7. PERFORMING ORGANIZATION NAME(S) AND ADDRESS(ES) Institute of High Temperatures RAS Izhorskaya str., 13/19 Moscow 127412 Russia			8. PERFORMING ORGANIZATION REPORT NUMBER N/A		
9. SPONSORING/MONITORING AGENCY NAME(S) AND ADDRESS(ES) EOARD PSC 821 BOX 14 FPO AE 09421-0014			10. SPONSOR/MONITOR'S ACRONYM(S)		
			11. SPONSOR/MONITOR'S REPORT NUMBER(S) ISTC 01-7003		
12. DISTRIBUTION/AVAILABILITY STATEMENT Approved for public release; distribution is unlimited.					
13. SUPPLEMENTARY NOTES					
14. ABSTRACT <p>This report results from a contract tasking Institute of High Temperatures RAS as follows: Task 1: Renewed scientific interest has arisen throughout the world as to the potential application of Magneto Hydrodynamics (MHD) processes for advancement of flight. Among the areas of interest is the utilization of MHD as a means for enhancing the speed and range of scramjets through a concept known as MHD energy by-pass. Currently, scramjet operation is limited to free stream flight Mach numbers around 10. This limitation arises from the excessive temperature that develops at high Mach conditions as a result of the slowing down of the propulsion drafted hypersonic air stream within the propulsion system inlet. The extra benefit of this proposed Project is the experimental facility to be used for experimental studies of MHD effects in hypervelocity flows that is an MHD assisted wind tunnel. Therefore, operation of this facility will provide valuable information on MHD interaction taking place in MHD accelerator. All experimental results can be and will be used to validate existing computer codes for such processes.</p> <p>Task 2: One of the main problems of stable combustion in high-speed flow is an effective mixing of gaseous fuel and oxidant providing full combustion during the resident time in combustor chamber. Generally speaking in-flow mixing consists of two main mechanisms: kinematics mixing (convection) and molecular diffusion. The latter is a final stage of mixing needed to provide extended combustible mixture. Kinematics mixing is more effective in vortex flows; the higher vortices the better kinematics mixing which means the larger fuel/oxidant interface surface. The second mixing mechanisms, diffusion, forms a reacting volume estimated as the interface surface times diffusion length.</p>					
15. SUBJECT TERMS EOARD, Physics, Fluid Mechanics					
16. SECURITY CLASSIFICATION OF:			17. LIMITATION OF ABSTRACT UL	18. NUMBER OF PAGES 234	19a. NAME OF RESPONSIBLE PERSON SURYA SURAMPUDI
a. REPORT UNCLAS	b. ABSTRACT UNCLAS	c. THIS PAGE UNCLAS			19b. TELEPHONE NUMBER (Include area code) +44 (0)20 7514 4299

ISTC 2196P

**Final
Project Activities Report
of ISTC 2196p**

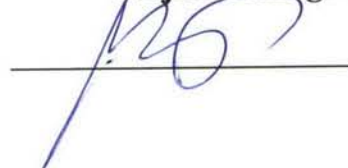
MHD Flow Control.

(From June 1, 2002 to May 31, 2006)

Vyacheslav M. Batenin
Director of IVTAN



Valentin A. Bityurin
Project Manager



Institute of High Temperatures RAS

September 2006

This work was supported financially by European Office of Aerospace Research and Development (EOARD) and performed under the contract to the International Science and Technology Center (ISTC), Moscow.

AQ F08-01-00324

ISTC 2196P

**Final
Project Technical Report
of ISTC 2196p**

MHD Flow Control.

(From June 1, 2002 to May 31, 2006)

Valentin A. Bityurin
(Project Manager)

Institute of High Temperatures RAS*

September 2006

This work was supported financially by European Office of Aerospace Research and Development (EOARD) and performed under the contract to the International Science and Technology Center (ISTC), Moscow.

ISTC 2196P

**Final
Project Summary Report
of ISTC 2196p**

MHD Flow Control.

(From June 1, 2002 to May 31, 2006)

Valentin A. Bityurin
(Project Manager)

Institute of High Temperatures RAS*

September 2006

This work was supported financially by European Office of Aerospace Research and Development (EOARD) and performed under the contract to the International Science and Technology Center (ISTC), Moscow.

The goal of the project is the fundamental study in the field of magneto plasma aerodynamics, and in particular, MHD control of external and internal flows. The MHD control of the external hypersonic flow over the simplest bodies such as circular cylinder and wedge is analyzed experimentally and numerically to estimate the peak heat flux reduction due to MHD interaction in up-stream area.

The MHD control of internal flows is considered as an effective way to intensify the processes of the convective-diffusive mixing in high-speed gas-plasma flows. The new concept of the reacting volume formation formulated and validated with numerical simulations for such processes earlier is to be studied experimentally.

Key words: magneto-hydrodynamics (MHD), hypersonic flow, heat flux, diffusive-convective mixing, ignition, high-speed co-flow streams

* Izhorskzya Street, 13/19, Moscow, 125412, Russia
Tel.: +7 (495) 484-28 44, Fax : +7 (495) 483-22 85
E-mail: bityurin@ihed.ras.ru

The work is performed by the following institutions and partners:

1. Participating Institutions:

1.1 Leading Institution

Institute of High Temperatures of Russian Academy of Sciences
Izhorskaya 13/19, Moscow, 125412, Russian Federation
Tel.: +7-(495) 484-28 44, Fax.: +7-(495) 483-22 85

E-mail: bityurin@ihed.ras.ru

2. Partners

European Office of Aerospace Research and Development (EOARD).
223-231 Old Marylebone Road
London, UK
Phone: +44-171-514-4299; Fax: +44-171-514-4960
E-mail: surya.surampudy@london.af.mil

3. Foreign Collaborators:

Not Applicable

The main results of the work are to be discussed at Seminars and International Conferences with participating of representatives of Russian and foreign institutions and research organizations.

List of Participants

List of Participants

1	Bityurin Valentin Anatol'evich	IHIM	1	Project Manager
2	Bocharov Aleksey Nikolaevich	IHYK	1	SubTask (1-1), Task (2) Manager
3	Krasilnikov Arthur Vladimirovich	JUJV	1	SubTask (1.2) Manager
4	Alferov Vadim Ivanovich	HTDL	1	Senior researcher
5	Baranov Dmitrii Sergeevich	IOKD	1	Senior Researcher
6	Bocharova Elena Anatol'evna	IHYM	3	Publication
7	Boushmin Aleksey Stepanovich	JFFB	1	Data analysis
8	Bychkov Sergei Sergeevich	HQYB	2	Flow diagnostics
9	Chinnov Valery Fedorovich	JYAM	2	Flow diagnostics
10	Filimonova Elena Aleksandrovna	KITF	2	Plasma-Chemical kinetics
11	Gouskov Oleg Vyacheslavovich	HSBZ	2	Numerical simulation Experimental models development
12	Grushin Vyacheslav Acimovich	JFFG	2	development
13	Gudelev Victor Alexandrovich	AVZN	1	Lead Expert
14	Karabadjack Georgi Fevzievich	JDNR	1	Senior Researcher
15	Klement'eva Irina Boridovna	KCRO	2	Experimental data treatment
16	Knotko Valery Borisovich	AUCI	1	HFP WT Operation
17	Kolpakov Andrei Vladimirovich	IOKE	1	Radiation proceses
18	Kopchenov Valeriy Igorevich	HSAY	1	Numerical simulation
19	Kuznetsov Aleksey Semenovich.	IIHC	2	Instrumentation
20	Moralev Ivan Aleksandrovich	KMJK	3	Flow diagnostics
21	Plastinin Yuri Aleksandrovich	JDNS	1	Senior Researcher
22	Podmasov Anatoly Victorovich	JFFC	1	MHDWT operation
23	Rudakova Al'berta Petrovna	JFFD	3	Data analysis
24	Semenova Tat'yna Mikhailovna	IHYN	3	Documentation
25	Sukhov Valeriy Nikolaevich	IHIN	2	Experimental model development
26	Talvirsky Alexander Dmitrievich	HQYC	2	Flow diagnostics
27	Vatazhin Alexander Benetsianovich	JFFA	1	Numerical simulation
28	Vlasov Vyacheslav Ivanovich	IORQ	1	Lead Expert
29	Zalogin Georgi Nikolaevich	AVZW	1	Senior Researcher
30	Savelkin Konstantin Victorovich	IHCT	4	Diagnostics
31	Yarantsev Dmitrii Alekseevich	IXKA	4	Diagnostics
32	Alekseev Ivan Yur'evich	JFGS	4	Data Treatment
33	Margolin Sergey Leonidovich		4	Data Treatment

CONTENT

I. INTRODUCTION.....8

II. NUMERICAL SIMULATION APPROACH.....18

III.1. TASK 1. MHD FLOW CONTROL.....36

 III.1.1. HYPERSONIC MHD FLOW CONTROL.....36

 II.2. SUBSONIC MHD FLOW CONTROL.....103

IV. MHD CONTROL OF INTERNAL FLOW.....168

V. GENERAL CONCLUSION.....231

1. INTRODUCTION

The project is characterized as fundamental and multidisciplinary study. The project efforts are devoted to provide the new fundamental knowledge in fields of physical gas dynamics of chemically reacting flows and applied magnetogasdynamics.

The project is motivated by the renewed scientific interest that has arisen throughout the world as to the potential application of MagnetoHydroDynamics (MHD) processes for advancement of flight.

Both, external and internal flows are experimentally and analytically considered as a subject of MHD interaction effects.

In the EXTERNAL MHD FLOW Control (Task 1) the new experimental and theoretical information on MHD interaction characteristics near bodies of the simplest but still basic configurations: circular cylinder; single and multi-angle wedges; plates under variable angle-of-attack; axi-symmetric body of evolution, - in hyper-, super-, and subsonic airflow will be obtained. Such data are primarily necessary in any analysis and design of a hypersonic vehicle using Advanced Flow/Flight Control (AFFC) methods.

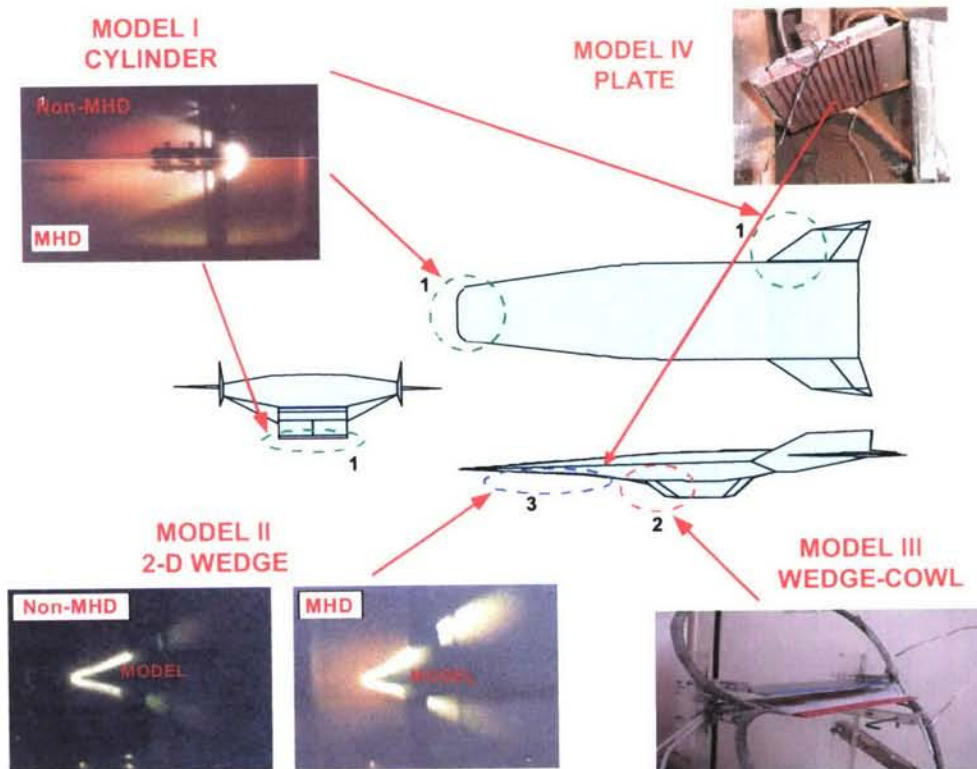


Figure 1. Experimental Model reference map

In the INTERNAL MHD FLOW Control (Task 2) the newly proposed MHD flow control and MHD enhancement of in-flow fuel/oxidizer mixing is concentrated on the experimental and analytical studies of the mixing, ignition and combustion control in non-premixed fuel/oxidizer co-flow streams

The sophisticated 2D CFD code being developed and improved over preceding period of the MHD FC study is widely used to planning of experiment, predict, and treat experimental data. The code family, *PlasmaAero* based on full Navier-Stokes

equations, MHD approximation of Maxwell equations, and plasma-chemical kinetics equations is an important powerful tool of the study within the proposed project.

The experimental data set are to be the reference data for the validation of various numerical codes used for simulation of MHD interaction near bodies in high speed flows.

The experimental program of this project is based on the unique experiments conducted at two sub-full scale facilities: hypervelocity MHD driven WT of blow-down operation rented at TsAGI (hypersonic flow tests) and subsonic HFP driven WT of continuous operation at TsNIIMash (sub- and transonic flow tests) both of MW level of flow power. These experiments are supported by wide range numerical simulations with PlasmAero family computer code. The results of this study is mostly available in publications [1-29] and reports on EOARD/ISTC projects 1809 and 2196.

Task 1: MHD Control of External Flows

Among the areas of interest is the utilization of MHD interaction as a tool for enhancing the speed and range of scramjets operation through a concept known as MHD energy by-pass, and/or through another configuration of MHD related elements (magnet, electrodes, ionizers,...) [1].

MHD interaction enhancement is considered as that can: (1) improve the scramjet in-take operation at off-design flight conditions; (2) reduce the heat flux at upstream edges of hypersonic vehicles; (3) control the boundary layer flows; (4) enhance the fuel/oxidizer mixing rate in co-flow streams; (5) provide on-board electrical power generation at MWs levels. There are several well-defined basic model configurations that are very suitable for MHD flow control basic research [2]. The



Figure 2. Plate-type model at the nozzle outlet of HFP WT facility.

candidates are (1) a 2-D Wedge Model with Steady State and Embedded Surface Electrodes; and (2) an Axi-Symmetric Model (Circular Cylinder) with included 'on-board' magnetic field generation tools. The first model proposed for the basic MHD-flow control research several years ago, specifically for this facility, considered now as a main experimental polygon. The main feature of Candidate-1 model is the combination of many different mechanisms of flow control that can be carefully checked in experiments and with analysis. The Candidate-2 advantage is probably the simplest and as expected most effective way to demonstrate the effectiveness of high-speed flow manipulation including bow shock, leading edge heat transfer, overall drag

and other fundamental characteristics optimizations. The recent study has involved two further developed models: (3) a wedge-with-cowl, and (4) plate with embedded electrodes under an angle-of-attack. The schematic diagram of the experimental study mapping is presented in Fig.1. This represents the experimental activity performed at MHD Driven hypervelocity WT. The recently involved second experimental bed – subsonic HFP Driven WT is used to study the MHD interaction phenomena with a plate-type model similar to the shown in Fig.1 Model IV and presented in Fig.2.

A new MHD role for aerospace applications was formulated at fiftieth [1] when the re-entry problem became real and critically important. Several proposals have been developed to reduce heat flux strength at critical point by means of magnetic field created by an on-board system. At the same time two new areas were formed where the MHD effects are the primary importance – MHD electrical power generation as a direct heat energy conversion into electricity and thermonuclear reactors with magnetic sustain of active matter –hot high temperature plasma.

A number of successful demonstration of MHD interaction stimulated research and development a numerous applications and particularly for space. One of the practically developed branches is the development of so called MHD low thrust accelerators for long term interplanetary journey. Another example of the successful development of a large-scale MHD system is pulse MHD generator in power output range from 1MWe till 100MWe for special applications in defense systems.

Since 50th the considerable attention has been paid to the flows around blunt body in the presence of external magnetic field. At high magnetic Reynolds number the fluid deforms the magnetic field, rather than passes through it. As a result liquid free cavities are produced near the body, which prevents to appearing of large heat flux into the body surface [2]. The application problems of author's interest are those in which magnetic Reynolds number values are of order of unit or even much less. In this case the feasibility of MHD flow control relies on other principles and should be investigated in more details. The incompressible MHD flows around bodies including cylindrical that were vastly studied in 60th (see, for example, [3]). Many exact and approximate analytical methods were developed for solving problems on the MHD flow over bodies of different shape. The bibliography of earlier studies on the finite conductivity MHD flows can be found in [4]. In one of the first work on the supersonic MHD flow around a body [5] it was shown that increasing MHD interaction factor leads to increasing of the bow-shock stand-off distance. Many fundamental features of MHD flows have been revealed in works of Bush [6,7] and Bleviss [8]. From recent studies on MHD flows around bodies note the works [9-13]. In papers [9-12] the Hall effect was neglected. In [10] the effects of chemistry on the MHD flow around a blunt body were evaluated. In [13] the two-dimensional analysis of the Scramjet inlet has been carried out.

Later a number of papers are published at AIAA Aerospace Science meetings (USA), Weakly Ionized Gas Workshop (AF,USA) , Moscow Workshop on Magneto-Aerodynamics for Aerospace Applications (RAS/EOARD) and at many others forums.

In hypersonic low-pressure air flows ($M > 10$) the electrical conductivity behind the bow-shock may become sufficient for the strong MHD interaction to appear in the presence of magnetic field of order of one Tesla.

The primary conditions for the implementation of any on-board MHD technology are the first - to provide a sufficient level of electrical conductivity of airflow and, the second – to make proper design of the magnetic system, which is known to be the weight critical component. In this respect, the physical background of flow parameters modification and the magnetic system assessments are to be

considered together. The magnet size and weight must be gauged against the gain that can be obtained in terms of flow optimization. Some general relationships are obtained in [10] that should be useful for the development of a systematic approach to this problem.

The main goal of this study is to extend the knowledge on fundamental aspects of MHD flow control being prospective for potential aerospace applications. Two topics of the MHD flow control are to be considered:

- Task 1 – MHD control of external flows; and
- Task 2 – MHD control of internal flows.

Under **Task 1** the MHD interaction effects in hypersonic and subsonic flow over the simplest aerodynamics bodies are to be studied by physical and numerical experiments. The conditions of the real hypersonic flights in the Earth atmosphere have to be simulated. These conditions are:

- ✓ Hypersonic airflow;
- ✓ On-board magnetic field system.

The requirement of the simplest body introduced in the approach development is dictated by the high complexity of the studied phenomena in general cases. To simplify the post-test analysis the simplest model geometries are considered. Several configurations satisfying the aforementioned conditions are chosen:

- (1) – a circular cylinder in cross-flow;
- (2) – a wedge
- (3) a wedge with a cowl;
- (4) a flat plate under AoA.

For each configuration the flow field is basically 2D that significantly reduces the complexity of the post-test numerical simulation for experimental data treatment. The second simulated real flight condition – the magnetic field is to be generated by an on-board system is satisfied for the circular cylinder case with the axial electrical current of needed magnitude. The same type of magnetic system is used for the wedge models as well. However, for the plate model the magnetic field symmetry doesn't coincide with the model-in-flow symmetry that results in significantly 3D nature of electrical and gas dynamical fields.

The physical experiments on hypersonic flows for the conditions of interest are still problematic and only few ones are in principle available. For this reason for a long time the experiments on MHD interaction in hypersonic airflow performed in this project was unique, and only very recently an Italian team at Bologna university has started the series of experiments with rather similar models configuration in hypersonic Ar flow (not air!)

In this study the rented Hypervelocity Wind Tunnel Facility with MHD Accelerator is used. One of the main arguments of such a choice was the fact that the MHD interaction is already utilized in the facility itself, and the MHD interaction experiment looks like to be very natural.

Starting from the second year of the project work the second – subsonic experimental was also rented. The facility –High Frequency Plasmotron driven Wind Tunnel can provide the simulation of real flight flow conditions behind the bow shock in hypersonic flight at altitudes of 40-60 km.

Under **Task 2** the MHD interaction effects in supersonic flows of Mach around 2 typical of flow train of scramjet operation are to be studied. The main idea is to stimulate the mixing and ignition in co-flow streams of gaseous fuel and air. The proposed mechanisms of the processes enhancement are the additional vortex generation by the MHD body force and heat release due to Joule dissipation. The configuration needed for these mechanisms is the constricted current passing across the external magnetic field. Such an experimental study could be provided on laboratory scale facility. However, 2D nature of the processes is even more problematic as compared with the Task 1 case.

MHD control of external flow

In this project at the first stage the hypersonic flows around a circular cylinder and over a wedge are investigated. These are probably the simplest objects by their design and from the viewpoint of studying the specific MHD effects. It is of practical interest since it is used as the diagnostic tool in some hypersonic MHD facilities like MHD WT of TSAGI [14-15]. Furthermore, the flow over these simplest objects is interesting from the scientific point of view since it is characterized by a large set of similarity parameters and by interaction of many physical effects.

This study is a continuation of our preceding work [8-9, 15-17], in which the significant background of the present stage has been developed. The strong MHD effects were predicted for the conditions similar to experimental conditions of the planned experiments.

Numerical simulation of the hypersonic flow over the circular cylinder in the presence of external magnetic field has been carried out. The azimuthal magnetic field is created by the electrical current flowing in the direction of cylinder axis. The study has been performed for the conditions close to that realized in the hypersonic MHD Wind Tunnel facilities: the free-stream Mach number is in a range of 12-15; the static pressure is about 40Pa, the static temperature is 550 - 700K, the characteristic magnetic induction magnitude is about 1 Tesla. As consequence of such conditions, the high temperature behind the bow shock takes place (up to 20,000K). This may lead to the high values of electrical conductivity and, in turn, to appearance of feasibility of MHD flow control.

At that stage several numerical models were developed and implemented.

The first model was intended to investigate the MHD flow in vicinity of the stagnation point of the cylinder in more details. The electrodynamics part of the whole problem was simplified by the assumption of the constant conductivity, no Hall effect and reduced the MHD interaction area to the up-stream region in the vicinity of the stagnation line.

In the second model the MHD-interaction is considered in the entire domain upstream and downstream the magnetic field generating cylinder, the anisotropic electrical conductivity is taken into account, and ionization equilibrium is assumed. Effects of radiation transfer are also taken into account.

The third model implements rather sophisticated treatment of the real gas flow including finite rate chemical kinetics. The wide range of magnitude of MHD interaction factor was considered and the flow fields were calculated. The important integral characteristics were obtained, namely the bow shock stand off distance, total pressure force, friction, magnetic force and total head flux to the cylinder surface. It was found that MHD interaction could lead to reducing the heat flux onto the surface as much as one order of magnitude under the free-stream conditions mentioned above.

The specific flow features were revealed such that the presence of cold gas circulation zone near the critical point and the existence of the widely spread region with MHD interaction downstream the blunt body. The dominating role of the Hall effect was outlined that results in dramatic reduction of MHD interaction and, in particular, in the fact of practically no dependence of MHD interaction parameter upon magnetic field magnitude under considered conditions is revealed.

It has been concluded that real gas MHD flow pattern can dramatically differ from ones based on simplified assumptions on an electrical conductivity, Hall parameter, and effective electrodynamics boundary conditions are primary important.

MHD control of internal flow

One of the main problems of stable combustion in high-speed flow is an effective mixing of gaseous fuel and oxidant providing full combustion during the resident time in combustor chamber. Generally speaking in-flow mixing consists of two main mechanisms: kinematics mixing (convection) and molecular diffusion. The latter is a final stage of mixing needed to provide extended combustible mixture. Kinematics mixing is more effective in vortex flows; the higher vorticity the better kinematics mixing which means the larger fuel/oxidant interface surface. The second mixing mechanisms – diffusion forms a *reacting volume* estimated as the interface surface times *diffusion length*. The only place where the combustion can occur is the *reacting volume*. Both *interface surface* and *diffusion length* are increasing functions of time. Having these two functions explicitly one can calculate a *reacting volume* formation and, with chemical kinetics scheme known, the combustion process can be described in detail. Such an approach has been developed in IVTAN for simulation of high-speed flow of chemically reacting mixture for plasma chemistry applications and simulation of combustion in compressor-type chemical reactors basing on Diesel engine.

Because very short residence time is typical of ram/scram jet operation conditions the measures providing a significant increasing rate of *reacting volume* are very actual.

The proposed Advanced Mixing approach is to increase the reacting volume growth by

- (1) Pulse electrical discharge; and
- (2) MHD interaction - $\mathbf{J} \times \mathbf{B}$ body force.

The preliminary information about such a mixing process was collected in IVTAN while an MHD generator flow with current-carrying non-uniformities was studied. At that time the main question was how to decrease the time of the mixing process intensified by vorticity generation. Now the amplification of mixing by MHD and Pulse Plasma affects should be studied in turn and recommended.

Very sophisticated physical and mathematical models are needed to treat these phenomena at acceptable accuracy. From the other hand, not all input data required for the closed formal description are available, and for this reason the experimental validation is absolutely necessary.

One of the main problems of stable combustion in high-speed flow is an effective mixing of gaseous fuel and oxidant providing full combustion during the resident time in combustor chamber. Generally speaking in-flow mixing consists of two main mechanisms: kinematics mixing (convection) and molecular diffusion. The latter is a final stage of mixing needed to provide extended combustible mixture. Kinematics mixing is more effective in vortex flows; the higher vorticity the better kinematics mixing which means the larger fuel/oxidant interface surface. The second

mixing mechanisms – diffusion forms a reacting volume estimated as the interface surface times diffusion length. Both interface surface and diffusion length are increasing functions of time. The theoretical background has been developed in IVTAN and by others authors (see, for example, [12-14]). Having these two functions explicitly, one can calculate a reacting volume formation and, with chemical kinetics scheme known, the combustion process can be described in detailed. Such an approach has been developed in IVTAN for simulation of high-speed flow of chemically reacting mixture for plasma chemistry applications and simulation of combustion in compressor-type chemical reactors based on Diesel engine. The proposed Advanced Mixing approach is to increase the reacting volume growth by (1) pulse electrical discharge and (2) by MHD interaction - $\mathbf{J} \times \mathbf{B}$ body force. It was found recently both experimentally and theoretically that under certain conditions typical of so-called Plasma Aerodynamics experiments the filamentary structure of high frequency discharge (streamer discharge) results sometimes in high-speed jet formation [15]. Such a jet can transfer a significant mass of fluid from one point to another rather distant location. Thus, providing a controllable filamentary discharge across a primary fuel/oxidant interface one can intensify the initial mixing of fuel/oxidant composition. The second component of Advanced Mixing is vortex generation by a highly non-potential $\mathbf{J} \times \mathbf{B}$ body force. This force is defined by current density component \mathbf{J} perpendicular to the external applied magnetic field \mathbf{B} . The experimental and numerical simulations conducted in the first two years activity under the Project have revealed many new aspects of the physical and chemical processes [16-18]. Some of them are: the discharge structure in a cross high speed is strongly affected by external magnetic field apparently provoking an instability of the electrical current path; a pulse discharge mode results in a strong non-equilibrium of plasma inside of the discharge channel especially at the initial stage of the breakdown; the initial shock wave created at the breakdown plays an important role in a discharge formation and mixing development; the chemical kinetics schemes seem to be modified significantly to meet the



Figure 3. The visualization (bottom) and simulation of the temperature field (upper) of the counter flow fuel injection with electrical discharge ignition.

experiment conditions; the process is a significantly 3D time dependent and hardly could be described numerically within a standard approach; the simplified models are urgently needed to provide an adequate quantitatively and qualitatively interpretation of the observed results. One of the results of the comparison of the visualization and numerical simulation is presented in Fig.3. The low time and spatial resolution makes hardly possible a quantitative analysis. Only qualitative correlation could be assumed.

The new more sophisticated models have been developed [19-20]. Basing on the previous stages experimental data analysis and parametric studies with improved

physical and numerical models a new configuration of the experiments is developed. The main flow is organized as fully axisymmetric one, the external magnetic created by two coaxial Helmholtz coils is also axisymmetric, the only essentially 3D factor is a radial electrical discharge providing an azimuthal motion due to interaction with magnetic field. The experiment is now in progress and the first results will be presented in the annual 2004 report on the 2196 Project. The more advanced diagnostics is used: the fast digital camera of higher spatial and time resolution in compare with the previously used camera,

The general goal of the Task 2 of the Project is the same, and the efforts are concentrated on the detailed and accurate experiment and multi-level numerical simulation development in order to provide the resolution of the process in different scale: diffusion length, micro kinematics mixing, vortex generation by a single discharge channel, MHD generated vortexes interaction with macro scale non-uniformity of the flows, and chemical kinetics development for significantly non-uniform mixture in electric field. The recent results are published in papers [21-29].

References.

1. V.A.Bityurin, V.A.Zeigarnik, A.L.Kuranov, On a Perspective of MHD Technology in Aerospace Applications, AIAA-Paper 96-2355, New Orleans, 1996
2. V.A.Bityurin, A.N.Bocharov, J.Lineberry, MHD Aerospace Applications, Invited Lecture, Intern Conf, on MHD Electrical Power Generation and High Temp. Technologies, Beijing, PDC, October 12-15, 1999.
3. J.T.Lineberry, V.A.Bityurin, A.N.Bocharov, D.S.Baranov, A.B.Vatazhin, V.I.Kopchenov, O.B.Gousskov, V.I.Alferov, A.S.Boushmin, Cylinder with Current in Hypersonic Flow, In: The 3rd Workshop on Magento-Plasma-Aerodynamics in Aerospace Applications, Moscow, April 24-26, 2001, pp15-25
4. V.A.Bityurin, D.S.Baranov, et al Experimental Study of MHD Interaction in a Hypersonic Flow with Cylindrical Body, , In: The 4th Workshop on Magento-Plasma-Aerodynamics in Aerospace Applications, Moscow, April 9-11, 2002, pp144-151
5. J. Lineberry, V.A.Bityurin, A.N.Bocharov, Analytical Study of MHD Flow Interaction Around a Right Circular Cylinder in Transverse Hypersonic Flow // 14th International Conference on MHD Power Generation and High Temperature Technologies, AIAA-2002-2112, Maui, Hawaii, May 20-23 2002.
6. V.A.Bityurin, D.S.Baranov, A.N.Bocharov, J. Lineberry, MHD Interaction at a Cylinder in Hypersonic Flow, In: The 5th Workshop on Magento-Plasma-Aerodynamics in Aerospace Applications, Moscow, April 7-9, pp 109-125
7. V.A.Bityurin, A.N.Bocharov, J. Lineberry, C.Suchomel, Studies on MHD Interaction in Hypervelocity Ionized Air Flow over Aero-Surface, 34th Plasmadynamics and Lasers Conference, June 23-26, 2003, AIAA Paper 2003-4303, Orlando, FL
8. V.A.Bityurin, Prospective of MHD Interaction in Hypersonic and Propulsion Technologies, In: von Karman Series :Lectures, Introduction of Magneto-Fluid Dynamics for AeroSpace Applications, von Karman Institute, Brussels, October 27-30, 2003
9. V.A.Bityurin , Russian Efforts in MHD AeroSpace Applications, In: von Karman Series :Lectures, Introduction of Magneto-Fluid Dynamics for AeroSpace Applications, von Karman Institute, Brussels, October 27-30, 2003

10. V.A.Bityurin, D.S.Baranov, A.N.Bocharov, and J.T.Lineberry, Experimental and Theoretical Study of MHD Interaction at a Wedge in Hypersonic Flows, 3 - 6 January 2004, Reno, NV
11. V.A.Bityurin, A.N.Bocharov, J. Lineberry, Results of Experiments on MHD Hypersonic Flow Control, AIAA Paper 2004-2263, 35th Plasmadynamics and Lasers Conference, 28 June- 1 July 2004, Portland, Oregon
12. V.A.Bityurin, V.G.Potebnya, A.L.Tseskis, On Evolution of A Current-Carrying Plasma Clot in Media with A Random Velocity Field, // Letter to JTP), 1996, V.22, №2, pp.80-83
13. V.A.Bityurin, V.G.Potebnya, A.L.Tseskis, On Energy Transfer in Gas-Plasma Flows with Current-Carrying Clusters, Magnetohydrodynamics, 1997, V.33, №3, pp.297-305
14. J.M.Ottino, The kinematics of mixing: stretching, chaos, and transport, Cambridge University Press, 1997. 364 pp
15. V.A.Bityurin, A.I.Klimov, S.B.Leonov, V.G.Potebnya. On interaction of Longitudinal Pulse Discharge with Bow Shock // In Prospectives of MHD and Plasma Technologies in aerospace Applications, Moscow, IVTAN, March 24-25, 1999, pp 114-119
16. V.A.Bityurin, A.N.Bocharov, Advanced MHD Mixing of Reacting Streams, 39th AIAA Aerospace Sciences Meeting & Exhibit, 8-11 January 2001/Reno, NV, AIAA Paper 2001-0793
17. A.N.Bocharov, S.B.Leonov, D.S.Baranov, I.B.Klement'eva, V.A.Bityurin. On MHD Enhanced Mixing and Combustion in Co-Flow Streams // The 4rd Workshop on Magneto- and Plasma- Aerodynamics for Aerospace Application, IVTAN, Moscow, 9-11 April, 2002
18. A.N. Bocharov, V.A. Bityurin, I.B. Klement'eva, S.B.Leonov, Experimental and Theoretical Study of MHD Assisted Mixing and Ignition in Co- Flow Streams // 14th International Conference on MHD Power Generation and High Temperature Technologies, Maui, Hawaii, May 20-23 2002.
19. A.N. Bocharov, V.A. Bityurin, I.B. Klement'eva, S.B.Leonov, A Study of MHD Assisted Mixing and Combustion // 41st AIAA Aerospace Sciences Meeting and Exhibit, Reno, Nevada, 6-9 Jan 2003.
20. A. N. Bocharov, V.A. Bityurin, E.A.Filimonova, A.I.Klimov, Numerical Study of Mixing and Combustion in Non-Premixed Flow, AIAA Paper -2004-1017, 3-6 January 2004, Reno, NV
21. I.Klement'eva, A.Bocharov, V.Bityurin, A.Klimov. Study of MHD Assisted Mixing and Combustion in Counter-Flow Streams // The 15th International Conference on MHD Energy Conversion and the 6th International Workshop on MagnetoPlasma Aerodynamics, IVTAN, Moscow, 24-27 May, 2005, p.365
22. A.N.Bocharov, V.A.Bityurin, J.Lineberry. Study of MHD Interaction in Hypersonic Flows // The 15th International Conference on MHD Energy Conversion and the 6th International Workshop on MagnetoPlasma Aerodynamics, IVTAN, Moscow, 24-27 May, 2005, p.399
23. V.A.Bityurin, A.N.Bocharov. MHD Flow Control in Hypersonic Flight // The 15th International Conference on MHD Energy Conversion and the 6th International Workshop on MagnetoPlasma Aerodynamics, IVTAN, Moscow, 24-27 May, 2005, p.429
24. V.A. Bityurin, A.N. Bocharov, D.S.Baranov, A.V. Krasilnikov, V.B.Knotko, Yu.A. Plastinin. Experimental Study of Flow Parameters and MHD Generator Models at High Frequency Plasmatron // The 15th International Conference on

- MHD Energy Conversion and the 6th International Workshop on MagnetoPlasma Aerodynamics, IVTAN, Moscow, 24-27 May, 2005, p.444
25. V.A. Bityurin, A.N. Bocharov and E.A. Filimonova // Numerical investigation of NO effect on the ignition of hydrogen and hydrocarbons in non-premixed layers of cold fuel and hot air. In Proc. of The 17 Inter. Symp on Plasma Chemistry, Aug. 7-12, 2005, Toronto, Canada.
 26. V. Bityurin, A. Bocharov, O. Baranov, and S. Bychkov, A Krasilnikov and V. Knotko, and J. Lineberry, Study of MHD Flow Control and On-board Electrical Power Generation // AIAA-2006-1008, 44th AIAA Aerospace Sciences Meeting and Exhibit, Reno, Nevada, Jan. 9-12, 2006
 27. V. Bityurin, A. Bocharov, and E. Filimonova, Effects of Nitrogen Oxide on Ignition of Non-Premixed System // AIAA-2006-1218, 44th AIAA Aerospace Sciences Meeting and Exhibit, Reno, Nevada, Jan. 9-12, 2006
 28. V. Bityurin, A. Bocharov, I. Klement'eva, and A Klimov, Experimental and Numerical Study of MHD Assisted MixinQ and Combustion // AIAA-2006-1009, 44th AIAA Aerospace Sciences Meeting and Exhibit, Reno, Nevada, Jan. 9-12, 2006
 29. A. Krasilnikov, G. Makarevich, A. Mikhailov, V. Bityurin, A. Bocharov, and V. Grushin, Electrophysical Parameters Study of MHD Generator Operating on Supersonic Hydrogen Combustion Products in Air Flow // AIAA-2006-1374, 44th AIAA Aerospace Sciences Meeting and Exhibit, Reno, Nevada, Jan. 9-12, 2006

II. NUMERICAL SIMULATION APPROACH

The physical background for both tasks considered in the present work is basically the same. For this reason the approaches used in numerical simulation of external flows and internal flows are similar with small difference related to different scales typical of the external and internal flow environment.

In the present work the following physical effects are of primary interest:

a) Molecular viscosity and heat conductivity. The turbulence effects are hoped to be resolved directly rather than via some turbulence model. Most of turbulence models are capable of describing the mean flow only if the flow is stationary or the flow field varies slowly. We shall consider the earlier stages of mixing process, when undeveloped turbulence may exist. At this stage we consider originally undisturbed flow; therefore the only mechanism of mixing seems to be the molecular transport.

b) Multi-component diffusion. Traditional approach to the diffusion of particles in multi-component mixtures will be applied in this work. It is assumed that the diffusive flux of any species is proportional to the local gradient of its concentration (Fick's law). The baro-diffusion and thermo-diffusion fluxes can be neglected in the flows under consideration. The energy fluxes consist of heat-conductance fluxes and the fluxes due to mass diffusion.

c) Magneto-hydrodynamics and plasma. Three main MHD flow models are considered within the Project. In the first two flow models MHD interaction is considered in hypersonic flows. In turn, two types of hypersonic flows are considered. First flow type appropriate to the flow in the experimental facility. Second type corresponds to the re-entry conditions. These flow models are developed within Task I of the Project. For these models several plasma models were developed. First model is referred to as one-fluid seeded plasma model. For the second flow model both the equilibrium-air model and chemical kinetics model were developed. Third model is developed to describe interaction of plasma discharges in the flow in the presence of magnetic field. This model is developed within Task II of the Project. The air-wise plasma formation can be created either in fuel or oxidizer and sustained due to external electric source or external ionizer. The arc current interacts with the transversal magnetic field so that the arc moves toward the fuel-oxidizer interface and enhances stirring of components. For the goals of the work the quasi-steady approach to MHD-interaction is certainly applicable: the characteristic speeds of the processes under consideration are much smaller compared to speed of light. In addition, the induced magnetic field due to electric currents can be neglected, so the current flow under constant external magnetic field can be considered.

d) Finite-rate chemistry. For the reacting flow computations we shall apply a general, finite-rate chemistry approach, based on the solution of chemical kinetics equations to obtain the species rates of production at each spatial point. Any chemical reaction is assumed to be subject to the acting-mass law and reaction rate constant are assumed to be of Arrhenius type. The chemical kinetics numerical model has been extended during the work to handle with plasma specific reactions. Namely, every reaction may have several branches specified by ceiling temperatures or, for example,

electric field. Plasma-specific reactions can be processed, which use electron temperature or electric field as governing parameters rather than temperature.

Within the Project several chemical kinetics mechanisms have been developed, which are summarized below:

- 1) hydrogen/air combustion model, which includes 9 species/42 reactions;
- 2) gasoline/air brutto-kinetics model;
- 3) high-temperature air kinetics model for re-entry conditions, which includes 11 species/98 reactions;
- 4) re-entry air kinetics, taking into account vibrational excitation, vibrational-translational relaxation and dependence of rate constants upon the vibrational energy of diatomic molecules;
- 5) equilibrium-air thermodynamics model, in which composition and air properties are calculated as functions of pressure and temperature;
- 6) non-equilibrium air plasma discharge kinetics model, in which electric field determines the reaction rates;

The first two flow models are realized within the Computational Model I. It simulates the flow on the base of Navier-Stokes equations for the fluid. These are coupled with the solution of electrodynamics equations in the presence of external magnetic field. The electric transport properties are estimated from the appropriate plasma models mentioned above.

Third flow model is realized within the Computational Model II. In addition to the Navier-Stokes equations for the whole fluid, the transport of species constituting the fluid is considered in frames of the multi-component diffusion approach. These computations are usually accompanied with the finite-rate chemistry computations. The electrodynamic part of the model is basically same as in the Computational Model I. However, the electric properties of the fluid are estimated from the sophisticated models taking into account local composition and transport properties of individual species.

Both flow models were realized as fortran-language based codes (currently, most of code runs in parallel environment) and described in details below.

1. COMPUTATIONAL MODEL I

The flows under consideration can be described by the coupled system of two-dimensional equations reflecting the conservation of mass, momentum and total energy for the whole mixture (Navier-Stokes equations), conservation of mass of different species with taking in to account the chemical conversions. The system is enclosed equations of state, by estimation of transport coefficients, and by relationships describing the electromagnetic interaction. Below, the general mathematical model is given as it is implemented in the code.

Governing equations.

Two-dimensional equations specifying the conservation of mass, momentum and total energy for a whole fluid in the presence of electric and magnetic fields can be written as

$$\frac{\partial \mathbf{U}}{\partial t} + \frac{\partial \mathbf{F}}{\partial x} + \frac{\partial \mathbf{G}}{\partial y} + \frac{\partial \mathbf{F}_v}{\partial x} + \frac{\partial \mathbf{G}_v}{\partial y} = \mathbf{S} , \quad (1.1)$$

\mathbf{U} is the conservative-variable vector,

$$\mathbf{U} = \begin{pmatrix} \rho \\ \rho v_x \\ \rho v_y \\ \rho E \end{pmatrix} \quad (1.2)$$

where ρ is the fluid density, v_x and v_y are the velocity components, E is the total specific energy, P thermodynamic pressure defined later.

The inviscid flux-vectors are given as

$$\mathbf{F} = \begin{pmatrix} \rho v_x \\ \rho v_x^2 + P \\ \rho v_x v_y \\ v_x \rho E + v_x P \end{pmatrix}, \quad \mathbf{G} = \begin{pmatrix} \rho v_y \\ \rho v_x v_y \\ \rho v_y^2 + P \\ v_y \rho E + v_y P \end{pmatrix} \quad (1.3)$$

Viscous fluxes, \mathbf{F}_v and \mathbf{G}_v are specified as follows

$$\mathbf{F}_v = \begin{pmatrix} 0 \\ \tau_{xx} \\ \tau_{xy} \\ e_x \end{pmatrix}, \quad \mathbf{G}_v = \begin{pmatrix} 0 \\ \tau_{xy} \\ \tau_{yy} \\ e_y \end{pmatrix} \quad (1.4)$$

The components of viscous stress tensor:

$$\begin{aligned} \tau_{xx} &= -2\mu \frac{\partial v_x}{\partial x} - \frac{2}{3}\mu \nabla v, \\ \tau_{xy} &= \tau_{yx} = \mu \left(\frac{\partial v_x}{\partial y} + \frac{\partial v_y}{\partial x} \right), \\ \tau_{yy} &= 2\mu \frac{\partial v_y}{\partial y} - \frac{2}{3}\mu \nabla v \end{aligned} \quad (1.5)$$

where μ is the molecular viscosity, $\nabla v = \frac{\partial v_x}{\partial x} + \frac{\partial v_y}{\partial y}$. The Stokes' hypothesis on the second viscosity has been taken into account in (1.5).

Note, that current version of the Computational Model I is capable of describing the flows in both Cartesian and axi-symmetric geometries. The governing

equations for axi-symmetric problems are properly modified.

Energy fluxes are specified as:

$$\begin{aligned} e_x &= -\lambda \frac{\partial T}{\partial x} + (v_x \tau_{xx} + v_y \tau_{xy}) \\ e_y &= -\lambda \frac{\partial T}{\partial y} + (v_x \tau_{xy} + v_y \tau_{yy}) \end{aligned} \quad (1.6)$$

Here, λ is the heat conductivity coefficient and T is the temperature.

Viscosity and heat conductivity coefficients can be estimated from different models. The most usable model in the code is curve-fitting, in which the coefficients are taken as tabulated approximations of temperature and pressure.

Thermodynamic properties of fluid.

To close the Navier-Stokes equations two equations of state are required, thermodynamic equation of state and caloric equation of state. Thermodynamic equation of state relates density, pressure and temperature:

$$P = \rho R \cdot T \quad (1.7)$$

where P is the pressure, T is the temperature, R is the gas constant, $R=R^0/W$.

Caloric equation of state gives the relation of pressure and energy:

$$e = h - P/\rho \quad (1.8)$$

where e is the specific internal energy and h is the specific enthalpy. Total energy is defined as

$$E = e + \frac{1}{2}(v_x^2 + v_y^2) \quad (1.9)$$

The most usable thermodynamic model is the perfect gas one, in which total energy and pressure are related as

$$(\gamma - 1)e = P / \rho \quad (1.10)$$

Here, γ is the ratio of specific heats.

Also implemented in the code is the model of equilibrium air, in which specific enthalpy, molecular weight, specific heats, ratio of specific heats and other properties are computed from the algebraic equilibrium-air model. All functions are treated as those of pressure and temperature, therefore in general non-linear problem is solved at each spatial point to find pressure and temperature from transport equations and equations of state.

The source-term vector \mathbf{S} is given as

$$\mathbf{S} = \begin{pmatrix} 0 \\ S_x \\ S_y \\ S_e \end{pmatrix} \quad (1.11)$$

Here, S_x and S_y represent the components of electro-magnetic force, S_e represents the energy rate of change due to Joule heating and radiation. These terms are detailed in the sub-section "Electrodynamics Model" below.

Electrodynamics Model.

In general, the electrodynamics of steady-state poorly-ionized gas discharge can be described by the steady equation of electric charge conservation together with Ohm's law:

$$\begin{aligned} \text{div } \mathbf{j} &= 0 \\ \mathbf{j} + \frac{\beta}{B} [\mathbf{j} \times \mathbf{B}] &= \sigma (\mathbf{E} + [\mathbf{v} \times \mathbf{B}]) \\ \mathbf{E} &= -\nabla \phi \end{aligned} \quad (1.12)$$

where \mathbf{j} is the electric current density, \mathbf{E} is the electric field strength, σ is the electric conductivity, \mathbf{B} is the magnetic field induction, β is the Hall parameter, and ϕ is the electric potential.

The components of electro-magnetic force are defined as

$$S_{x,y} = [\mathbf{J} \times \mathbf{B}]_{x,y} \quad (1.13)$$

Energy rate of change is

$$S_e = (\mathbf{J} \cdot \mathbf{E}) - Q_{rad} \quad (1.14)$$

where approximated for radiative power Q_{rad} is taken of the form:

$$Q_{rad} = \varepsilon \cdot \sigma_{SB} \cdot T^4, \quad (1.15)$$

where ε is the effective absorption coefficient, and σ_{SB} is Stefan-Boltzman constant.

The set of equations (1.12) can be reduced to one two-dimensional (three-dimensional in general) equation for electric potential.

Initial and boundary conditions.

The set of transport equations (1.1) has to be enclosed by specifying initial and boundary conditions. Usually, the free-stream flow conditions are set as initial guess and inlet conditions. At solid walls, the no-slip conditions are specified, and either wall temperature or adiabatic conditions are applied. At outlet boundaries the extrapolation from the interior is normally applied.

For the equation for potential (1.12) the following set of boundary conditions is implemented to the code: a) the potential value can be set; b) electric field can be specified; c) current density can be specified; d) linear combination of potential and current density can be set.

One important option has been recently added to the electrodynamic part of the code. Namely, a common solution to the general boundary value problem (of type of (1.12)) can be found. This option is know-how of IVT RAN, developed in 1970th for MHD generator computations. This option can be and it is quite useful and effective in solving problems with complicated boundary conditions (non-local, periodic, functional); in solving problems with the large and complicated external electric circuits; in optimizing some integral values like total power or total force.

2. COMPUTATIONAL MODEL II

The flows under consideration can be described by the coupled system of two-dimensional equations reflecting the conservation of mass, momentum and total energy for the whole mixture (Navier-Stokes equations), conservation of mass of different species with taking into account the chemical conversions. The system is enclosed equations of state, by definition of transport coefficients, by definitions of chemical rates of productions for every species and by relationships describing the electromagnetic interaction. Below, the general mathematical model is given as it is implemented in the code.

Governing equations.

Two-dimensional and species transport for a chemically reacting gas of N species in the presence of electric and magnetic fields are given by

$$\frac{\partial \mathbf{U}}{\partial t} + \frac{\partial \mathbf{F}}{\partial x} + \frac{\partial \mathbf{G}}{\partial y} + \frac{\partial \mathbf{F}_v}{\partial x} + \frac{\partial \mathbf{G}_v}{\partial y} = \mathbf{S} , \quad (2.1)$$

\mathbf{U} is the conservative-variable vector,

$$\mathbf{U} = \begin{pmatrix} \rho \\ \rho v_x \\ \rho v_y \\ \rho E \\ \rho Y_1 \\ \vdots \\ \rho Y_N \end{pmatrix} \quad (2.2)$$

where ρ is the fluid density, v_x and v_y are the velocity components, E is the total specific energy, and $\{Y_i, i=1, N\}$ are the species mass-fractions, $Y_i = \rho_i / \rho$, $\sum_{i=1}^N Y_i \equiv 1$, P is thermodynamic pressure defined later.

The inviscid flux-vectors are given as

$$\mathbf{F} = \begin{pmatrix} \rho v_x \\ \rho v_x^2 + P \\ \rho v_x v_y \\ v_x \rho E + v_x P \\ \rho v_x Y_1 \\ \vdots \\ \rho v_x Y_N \end{pmatrix}, \quad \mathbf{G} = \begin{pmatrix} \rho v_y \\ \rho v_x v_y \\ \rho v_y^2 + P \\ v_y \rho E + v_y P \\ \rho v_y Y_1 \\ \vdots \\ \rho v_y Y_N \end{pmatrix} \quad (2.3)$$

Viscous fluxes, \mathbf{F}_v and \mathbf{G}_v are specified as follows

$$\mathbf{F}_v = \begin{pmatrix} 0 \\ \tau_{xx} \\ \tau_{xy} \\ e_x \\ J_{x1} \\ \vdots \\ J_{xN} \end{pmatrix}, \quad \mathbf{G}_v = \begin{pmatrix} 0 \\ \tau_{xy} \\ \tau_{yy} \\ e_y \\ J_{y1} \\ \vdots \\ J_{yN} \end{pmatrix} \quad (2.4)$$

The components of viscous stress tensor:

$$\begin{aligned} \tau_{xx} &= -2\mu \frac{\partial v_x}{\partial x} - \frac{2}{3}\mu \nabla v, \\ \tau_{xy} &= \tau_{yx} = \mu \left(\frac{\partial v_x}{\partial y} + \frac{\partial v_y}{\partial x} \right), \\ \tau_{yy} &= 2\mu \frac{\partial v_y}{\partial y} - \frac{2}{3}\mu \nabla v \end{aligned} \quad (2.5)$$

where μ is the molecular viscosity, $\nabla v = \frac{\partial v_x}{\partial x} + \frac{\partial v_y}{\partial y}$. The Stokes' hypothesis on the second viscosity has been taken into account in (2.5).

Energy fluxes are specified as:

$$\begin{aligned} e_x &= -\lambda \frac{\partial T}{\partial x} + (v_x \tau_{xx} + v_y \tau_{xy}) + \sum_{i=1}^N h_i J_{xi} \\ e_y &= -\lambda \frac{\partial T}{\partial y} + (v_x \tau_{xy} + v_y \tau_{yy}) + \sum_{i=1}^N h_i J_{yi} \end{aligned} \quad (2.6)$$

Here, λ is the heat conductivity coefficients and T is the temperature. The last terms in (2.6) represent the enthalpy fluxes due to multi-component diffusion.

Diffusive fluxes are defined according to Fick's law:

$$\begin{aligned} J_{xi} &= -\rho D_{im} \frac{\partial Y_i}{\partial x}, \quad i=1, N \\ J_{yi} &= -\rho D_{im} \frac{\partial Y_i}{\partial y}, \quad i=1, N \end{aligned} \quad (2.7)$$

Transport coefficients D_{im} , μ , λ .

$$D_{im} = (1 - X_i) \left/ \sum_{j \neq i}^N X_j / D_{ij} \right., \quad (2.8)$$

$X_i = W \cdot Y_i / W_i$ is the mole fraction of i -th species, W_i is the molecular weight of i -th species and $W = 1 / \sum_{i=1}^N Y_i / W_i$ is the molecular weight of mixture. The binary diffusions coefficients, D_{ij} , are defined as follows:

$$D_{ij} = 2.68 \cdot 10^{-7} \frac{T^{3/2} \sqrt{(W_i + W_j) / (2W_i W_j)}}{P \cdot \sigma_{ij}^2 \cdot \Omega_{ij}^{(1.1)}(T_{ij}^*)} \left[\frac{m^2}{s} \right] \quad (2.9)$$

Here, $\sigma_{ij} = \frac{1}{2}(\sigma_i + \sigma_j)$ represent the characteristic collision diameter, $T_{ij}^* = kT / \epsilon_{ij}$ (k is Boltzman's constant) is the characteristic temperature, $\epsilon_{ij} = \sqrt{\epsilon_i \cdot \epsilon_j}$ is the parameter of function describing the inter-molecular interaction.

Collision integral $\Omega_{ij}^{(1.1)}(T_{ij}^*)$ is approximated as $\Omega_{ij}^{(1.1)} = 1.074 \cdot (T_{ij}^*)^{-0.1604}$.

Viscous coefficient, μ , is calculated as

$$\mu = \sum_{i=1}^N \mu_i \left(1 + \sum_{j \neq i} G_{ij} \cdot \frac{X_j}{X_i} \right)^{-1} \quad (2.10)$$

where i -th species viscous coefficient is defined as

$$\mu_i = 2.6693 \cdot 10^{-6} \frac{T^{3/2} \sqrt{W_i \cdot T}}{\sigma_i^2 \cdot \Omega_i^{(2.2)}(T_i^*)} \left[\frac{mg}{m \cdot s} \right] \quad (2.11)$$

Collision integral $\Omega_i^{(2.2)}(T_i^*)$ is approximated as $\Omega_i^{(2.2)} = 1.157 \cdot (T^*)^{-0.1472}$, and function G_{ij} are defined as

$$G_{ij} = \frac{\left[1 + (\mu_i/\mu_j)^{1/2} (W_i/W_j)^{1/4}\right]^2}{2^{3/2} [1 + W_i/W_j]^{1/2}}$$

The heat conductance coefficient is defined as follows:

$$\lambda = \sum_{i=1}^N \lambda'_i \left(1 + 1.065 \sum_{j \neq i} G'_{ij} \cdot \frac{X_j}{X_i}\right)^{-1} \quad (2.12)$$

where $\lambda'_i = \lambda_i (0.115 + 0.354 \cdot c_{pi}/R_i)$

Functions G'_{ij} are given as

$$G'_{ij} = \frac{\left[1 + (\lambda_i/\lambda_j)^{1/2} (W_i/W_j)^{1/4}\right]^2}{2^{3/2} [1 + W_i/W_j]^{1/2}} \quad (2.13)$$

i -th species heat conductivity

$$\lambda_i = \frac{5}{2} \mu_i c_{vi}, \quad c_{vi} = \frac{3}{2} \cdot \frac{R^0}{W_i}$$

R^0 is the universal gas constant, R_i is the gas constant of i -th species, $R_i = R^0/W_i$, c_{vi} and c_{pi} are species heats at constant volume and constant pressure, respectively.

It should be noted that several models for transport properties are currently implemented. The advanced non-equilibrium air model is applied in calculating the re-entry, combusting or plasma flows. This model employs the calculation of pair-to-pair collision cross-sections and forms reduced collision integrals $\Omega_i^{(1.1)}$, $\Omega_i^{(2.2)}$ in the way that transport coefficients (including electric conductivity and Hall parameter) correspond to the higher-order approximation within the Chapman-Enskog approach. The model was found to be appropriate for the flows with the electrically charged particles.

Thermodynamic properties of mixture.

Equation of state

$$P = \rho R \cdot T \quad (2.14)$$

where P is the pressure, T is the temperature, R is the gas constant, $R = R^0/W$.

Caloric equation of state relates pressure with energy:

$$e = h - P/\rho \quad (2.15)$$

where e is the specific internal energy and h is the specific enthalpy. Total energy is defined as

$$E = e + \frac{1}{2}(v_x^2 + v_y^2) \quad (2.16)$$

and

$$h = \sum_{i=1}^N Y_i h_i(T) \quad (2.17)$$

i -th species enthalpy, $h_i(T)$, is expressed as

$$h_i(T) = h_{i,f} + \int_{T_{ref}}^T c_{pi}(T) dT \quad (2.18)$$

where $h_{i,f}$ is the formation enthalpy of i -th component.

The source-term vector \mathbf{S} is given as

$$\mathbf{S} = \begin{pmatrix} 0 \\ S_x \\ S_y \\ S_e \\ \dot{w}_1 \\ \vdots \\ \dot{w}_N \end{pmatrix} \quad (2.19)$$

Here, S_x and S_y represent the components of electro-magnetic force, S_e represents the energy rate of change due to Joule heating and radiation. These terms are detailed in the sub-section "Electrodynamics Model" below. The terms $\{\dot{w}_i\}$, $i=1,N$ represent the rates of production of species due to chemical reactions. They are described in "Finite-rate Chemistry Model".

Electrodynamics Model.

In general, the electrodynamics of steady-state poorly-ionized gas discharge can be described by the steady equation of electric charge conservation together with Ohm's law:

$$\text{div } \mathbf{j} = 0$$

$$\mathbf{j} + \frac{\beta}{B} [\mathbf{j} \times \mathbf{B}] = \sigma (\mathbf{E} + [\mathbf{v} \times \mathbf{B}]) \quad (2.20)$$

$$\mathbf{E} = -\nabla \phi$$

where \mathbf{j} is the electric current density, \mathbf{E} is the electric field strength, σ is the electric conductivity, \mathbf{B} is the magnetic field induction, β is the Hall parameter, and ϕ is the electric potential.

The components of electro-magnetic force are defined as

$$S_{x,y} = [\mathbf{J} \times \mathbf{B}]_{x,y} \quad (2.21)$$

Energy rate of change is

$$S_e = (\mathbf{J} \cdot \mathbf{E}) - Q_{rad} \quad (2.22)$$

where approximation for radiative power Q_{rad} can taken in the form:

$$Q_{rad} = \varepsilon \cdot \sigma_{SB} \cdot T^4, \quad (2.23)$$

where ε is the effective absorption coefficient, and σ_{SB} is Stefan-Boltzman constant.

The set of equations (2.20) can be reduced to one two-dimensional (three-dimensional in general) equation for electric potential.

The crucial point in investigating the MHD interaction is the estimation of conductivity and electron mobility. It is seen from (2.20) that the smaller conductivity and/or higher mobility, the lower is the electromagnetic force $[\mathbf{j} \times \mathbf{B}]$ and, hence, the effect of MHD interaction on the flow characteristics. The electrical conductivity and electron mobility coefficients are defined as follows:

$$\sigma = \frac{e^2 n_e \tau_e}{m_e}, \quad \tau_e^{-1} = \sum_K \tau_{eK}^{-1}. \quad (2.24)$$

Here, n_e is the electron number density and τ_e^{-1} is the characteristic collision frequency of electron with neutrals and ions. Both are estimated in the usual way, i.e.

$$\tau_{en}^{-1} = n_n v_e Q_{en}, \quad \tau_{ei}^{-1} = n_e v_e Q_{ei} \quad (2.25)$$

where n_n is the concentration of neutral particles, v_e is the average electron velocity, and Q 's are the impact cross-sections. Q_{en} is electron-neutral collision cross-section, which is calculated for each electron-neutral pair from the data for reduced collision-integrals described above. Electron-ion cross-section can be estimated from formula

$$Q_{ei} = \frac{4\pi}{9} \frac{e^4 \Lambda}{(kT_e)^2}, \quad \Lambda = \ln \left[\frac{3}{2\sqrt{\pi}} \frac{(kT_e)^{3/2}}{e^3 n_e^{1/2}} \right], \quad v_e = \sqrt{\frac{3kT_e}{m_e}}. \quad (2.26)$$

Electron number density is determined from the finite-rate chemistry calculations coupled with the Navier-Stokes equations. For some problems, the equilibrium electron number density is calculated from the Saha' formula.

$$\frac{n_e^2}{N} = AT^{3/2} \exp(-I/T), \quad A=2.414 \cdot 10^{15} \text{ cm}^{-3} \text{ K}^{-3/2}, \quad I=10^5 \text{ K}. \quad (2.27)$$

$$\text{Finally, } \mu_e = \frac{e\tau_e}{m_e} = \frac{\sigma}{en_e}.$$

Finite-Rate Chemistry Model

The chemical kinetics model is applied to determine the species rates of production $\{\dot{w}_i\}_x$ due to chemical conversions, or reactions.

Any chemical reaction can be represented symbolically as:



where $v'_{l,r}$ and $v''_{l,r}$ are the stoichiometric coefficients of reagents and products, respectively.

The i -th species rate of production is then defined in accordance with the acting-mass law:

$$\dot{w}_i = W_i \sum_{r=1}^{N_r} [v''_{i,r} - v'_{i,r}] \cdot \left(k_{fr} \prod_{l=1}^N c_l^{v'_{l,r}} - k_{br} \prod_{l=1}^N c_l^{v''_{l,r}} \right) \quad (2.29)$$

Here, $c_e = \rho \cdot Y_i / W_i$ are the molar concentrations. k_{fr} and k_{br} are r th reaction rate constants, forward and backward, respectively. The Arrhenius form is assumed for both k_{fr} and k_{br} :

$$k_{fr} = a \cdot T^b \cdot \exp(-E_a/T) \quad (2.30)$$

where a, b and E_a are reaction parameters. These can be evaluated theoretically or from experimental data. For the hydrogen-air mixture these data are tabulated as well as that for many other reactions.

During the work on the Project the chemical kinetics numerical model has been extended to handle with plasma specific reactions. Namely, every reaction may have

several branches specified by ceiling temperatures or, for example, electric field. Plasma-specific reactions can be processed, which use electron temperature or electric field as governing parameters rather than temperature.

Initial and boundary conditions.

The set of transport equations (2.1) has to be enclosed by specifying initial and boundary conditions. Usually, the free-stream flow conditions are set as initial guess and inlet conditions. At solid walls, the no-slip conditions are specified, and either wall temperature or adiabatic conditions are applied. At outlet boundaries the extrapolation from the interior is normally applied.

For the chemical species the following boundary conditions can be specified. The value of concentration of the given species can be given (catalytic and super-catalytic conditions) at the boundary. Normal-derivative or normal-flux can also be specified.

For the equation for potential (2.20) the following set of boundary conditions is implemented to the code: a) the potential value can be set; b) electric field can be specified; c) current density can be specified; d) linear combination of potential and current density can be set.

One important option has been recently added to the electrodynamic part of the code. Namely, a common solution to the general boundary value problem (of type of (2.20)) can be found. This option is know-how of IVT RAN, developed in 1970th for MHD generator computations. This option can be and it is quite useful and effective in solving problems with complicated boundary conditions (non-local, periodic, functional); in solving problems with the large and complicated external electric circuits; in optimizing some integral values like total power or total force.

3. NUMERICAL ALGORITHM

In order to obtain all flow fields in any point of the domain under consideration, the entire computational domain is divided onto small domains called cells. Within each computational cell, the flow variables may be assumed to be constant (first – order accurate solution) or, for example, to be linear (second – order accurate solution). Other cell-distributions are possible, but are extremely expensive from the viewpoint of computational time. Only constant and linear variable distributions are implemented in the codes

The set of equations (1.1 or 2.1) is discretized in space and time starting from conservation laws written in integral form (weak formulation):

$$\frac{\partial}{\partial t} \int_{\omega} \mathbf{U} d\omega + \int_{\partial\omega} \mathbf{F} dS_{\omega} = \int_{\partial\omega} \mathbf{F}_v dS_{\omega} + \int \mathbf{S} d\omega \quad (3.1)$$

This integral form (3.1) is valid for any computational cell with the volume ω enclosed by the surface S_{ω} (in two-dimensional case ω is the surface and S_{ω} is the curve surrounding the cell). For both constant and linear variable distribution-in-cell, the transient term in (3.1) can be approximated as follows:

$$\frac{\partial}{\partial t} \int_{\omega} U d\omega \cong \omega \cdot \frac{\Delta U}{\Delta t}, \quad (3.2)$$

where $\Delta U = U(t+\Delta t) - U(t)$ represents 1-st order approximation of time-derivate. The surface fluxes are integrated as follows. For example,

$$\int_{S_{\omega}} \mathbf{F} dS_{\omega} = \int F dS_{\omega}^x + \int G dS_{\omega}^y = \int (Fn_x + Gn_y) dS_{\omega} = \langle F \cdot n_x + G \cdot n_y \rangle \Delta S_{\omega} \quad (3.3)$$

Here, ΔS_{ω} is the surface area value, n_x and n_y are the components of unit normal-vector directed outward the cell considered. The average-flux value depends on the grid partition and on the variable distribution-in-cell. We shall consider the quadrilateral cells, so that any internal computational cell has four neighbors. The relation ships (3.3) are then rewritten as follows:

$$\int \mathbf{F} dS_{\omega} = \sum_{j \in \omega} \int F dS_j \cong \sum_j F_j \Delta S_j \quad (3.4)$$

where F_j stands for the face-averaged flux and S_j stands for the face area. The face implies the line-segment, part of the whole cell-surface, straddling two adjusting cells. Four faces enclose each computational cell. For 1st- and 2nd order accurate solutions, the one-integration-point is sufficient, i.e. the surface flux can be evaluated at the mid-point of the face:

$$\int F_j dS_j \cong \mathbf{F}(\mathbf{U}_m) \Delta S_j = [F(\mathbf{U}_m)n_x + G(\mathbf{U}_m)n_y] \Delta S_j \quad (3.5)$$

The flux components, F and G , were presented in the previous Section. The dissipative fluxes, F_v and G_v , are handled with analogously.

$$\int \mathbf{S} d\omega \cong \omega \cdot \mathbf{S}(\mathbf{U}_{\omega}).$$

Hereafter, all the flow variables are implied as the cell-volume-averaged,

$$\int U d\omega = \omega \cdot \mathbf{U}_{\omega}, \text{ or simply, } \omega \cdot \mathbf{U}.$$

Collecting surface-flux integrations and giving variable distribution-in-cell leads to a system of algebraic non-linear equations for each cell state-vector \mathbf{U} :

$$\omega \frac{\Delta \mathbf{U}}{\Delta t} + \mathbf{R} = 0 \quad (3.6)$$

where residual-vector \mathbf{R} is the approximation of surface-flux quadratures plus source term:

$$\mathbf{R} = \sum_{j \in \omega} \left[F_j^\Sigma(\mathbf{U}_{mj})n_{xj} + G_j^\Sigma(\mathbf{U}_{mj})n_{yj} \right] \Delta S_j + [\mathbf{S} d\omega \quad (3.7)$$

This system (3.6) is integrated in time using explicit low-memory Runge-Kutta method:

$$\begin{aligned} \mathbf{U}_0 &= \mathbf{U}^n \\ \mathbf{U}_i &= \mathbf{U}_0 - \alpha_i \frac{\Delta t}{\omega} \mathbf{R}(\mathbf{U}_{i-1}), \quad i=1, I \\ \mathbf{U}^{n+1} &= \mathbf{U}_I \end{aligned} \quad (3.8)$$

where \mathbf{U}^n is the solution on time-level t^n and \mathbf{U}^{n+1} is the solution on time-level

$$t^{n+1} = t^n + \Delta t$$

The time-step, Δt , is selected as minimum of convective and diffusive time-scales for all the mesh control-volumes. While source-terms for momentum and energy equations are computed explicitly, calculation of chemical species production rates is carried out implicitly employing special chemical-kinetics solver.

$$\dot{w}_i = \left. \frac{d(\rho Y_i)}{dt} \right|_{chem} = \frac{1}{\Delta t} \int_{t^n}^{t^n + \Delta t} \dot{w}_i dt \quad (3.9)$$

Integration in time is performed by the program KINEL developed in IVTAN Low-Temperature Plasma Division for solution of systems of ordinary differential equations of high stiffness inherent to problems with chemical and thermal non-equilibrium. On every time-step, Δt , system (3.9) is integrated based on "chemical" time-steps and implicit treatment of production-rates. The chemical time-steps are evaluated within KINEL on the base of eigen-values of chemical source-term Jacobian matrix. Low-cost LU-decomposition of Jacobian is applied on each chemical time-step to solve the system.

Implicit treatment of chemical source-term allows one to avoid strong restrictions to the gas-dynamic time-steps imposed by finite-rate chemistry.

The integration of inviscid and viscous flux-vector over the control-volume surface is performed as follows. One-integration-point on the each surface-element (cell-interface straddling two neighboring cells) is suitable to obtain both 1-st order solution (piece-wise constant variable distribution within the cell) and 2-nd order solution (piece-wise linear variable distribution) in space. The inviscid flux at the integration-point is found from exact solution of Riemann problem (Godunov' method) or from approximate solution to the Riemann problem (Roe method, Advective Upwind Splitting Method are currently implemented and are intensively used), i.e.

$$\mathbf{F}_{ip} = \mathbf{F}(\mathbf{U}_{ip}), \text{ and } \mathbf{U}_{ip} = \text{Rie}(\mathbf{U}_L, \mathbf{U}_R) \quad (3.10)$$

$\text{Rie}(\mathbf{U}_L, \mathbf{U}_R)$ implies solution of Riemann problem between two states \mathbf{U}_L and \mathbf{U}_R , left and right state-vectors on both sides of the inter-face. For two adjacent cells, P and E ,

$$\begin{aligned} \mathbf{U}_L &= \mathbf{U}_P + \psi_P(\nabla \mathbf{U}_P, \Delta \mathbf{r}_{Pm}) \\ \mathbf{U}_R &= \mathbf{U}_E - \psi_E(\nabla \mathbf{U}_E, \Delta \mathbf{r}_{Em}) \end{aligned} \quad (3.11)$$

$\nabla \mathbf{U}_{P,E}$ are the cell-centered gradients and $\Delta \mathbf{r}_{EM}$ is the vector directed from cell-center $P(E)$ to mid-point of the interface M . The gradient in each cell, $\nabla \mathbf{U}_P$, is calculated by the least-square method as minimum of functional

$$\begin{aligned} \Phi_P &= \sum_{J \in \omega_P} [\Delta U_{Pj} - (\nabla \mathbf{U}_P \cdot \Delta \mathbf{r}_{Pj})]^2, \\ \Delta U_{Pj} &= U_j - U_P, \end{aligned} \quad (3.12)$$

Here J stands for any cell from the stencil associated with cell P . Usually, five-point stencil of the nearest neighbors (including P) is considered. The limiter-functions ψ_P 's are taken to satisfy the monotonical distributions near the strong flow discontinuities. In the smooth-flow regions, the second-order accurate spatial distributions are recovered. In one-dimensional problem, this method becomes equivalent to the well-known Van Leer MUSCL method.

Viscous fluxes at cell interface may be constructed in two ways. In first way, the face-gradient is taken to be the algebraic average of two cell-gradients described just above with adding up the projection of normal-derivative to prevent the non-physical oscillations. In second way, the gradient at interface is calculated by application of Gauss' theorem to auxiliary cell

$$\omega_a(\nabla \mathbf{U}_M) = \int_{\partial \omega_a} (\mathbf{U} \cdot \mathbf{n}_a) dS_a \quad (3.13)$$

Auxiliary cell represents the quadrilateral vortices of which are two cell-centers (P and E) and start-point and end-point of the interface segment itself. Both approaches were found to be equally appropriate.

The equation (2.20) for electric potential is discretized in the similar approach. The difference from the conservation equations is that transient term is equal to zero as well as the convective fluxes are zero. At the same time, in approximating electric current transport through the cell faces so called cross-derivative due to Hall effect are appeared. They are also approximated using standard central-difference approach. In general, the nine-point algebraic equation should be solved for every cell. The whole equation-matrix is in this case nine-diagonal sparse matrix. To solve the set of algebraic equations approximating equation for potential several techniques are applied from which Multi-Grid together with LU-decomposition is usually the most effective

method. Also Line- and Point Gauss-Seidel methods are implemented in Multi-Grid concept. For some problems direct method (it may be referred as Block TDMA) turns out to be effective.

III. TASK 1. MHD FLOW CONTROL.

III.1. HYPERSONIC AIRFLOW

1. PARAMETRIC STUDY OF MHD EFFECTS IN FLOW AROUND CYLINDER

Problem formulation

Consider a flow over the circular cylinder of radius of r in which the electric current flows along the cylinder axis (Fig.4). This current produces the circular or azimuthal

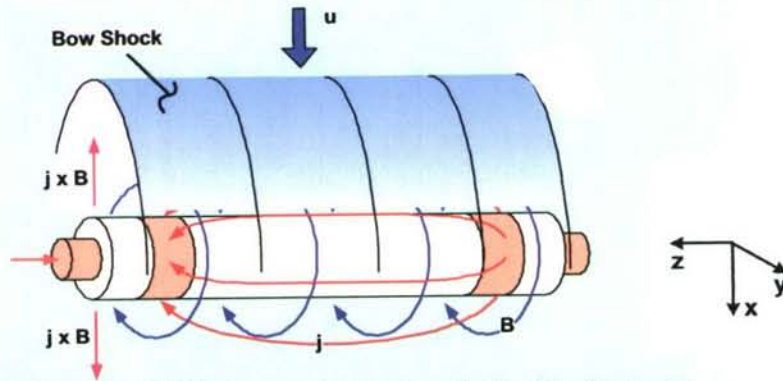


Figure 4. Schematic of MHD flow over the circular cylinder with axial electric current

magnetic field which amplitude can be characterized by the value of magnetic induction on the cylinder surface. Designate the density of the flow as ρ_∞ , pressure as P_∞ , velocity as v_∞ and the magnetic induction on the cylinder surface as B^* . Outside the cylinder the external electric field $E=(0,0,E_z)$ can be applied. It is assumed that z -directed electric current is provided by the electrodes located at $z=\pm L$ planes (see Fig.4). The surface of cylinder is considered as electrical insulator. The flow over cylinder in the azimuthal magnetic field can be described by the Navier-Stokes equations in which the electro-magnetic force $\mathbf{f}=[\mathbf{j}\times\mathbf{B}]$ appears in the momentum equations and the source $\mathbf{j}\cdot\mathbf{E}$ appears in the energy equation. Air is assumed to be a working gas. The radiation from the high temperature region is described by the model of optically thin media. The absorption coefficient is taken to be constant, for simplicity. At the cylinder surface the constant temperature, T_w , is specified.

Electrodynamic part of the whole equation system includes the Maxwell equations enclosed by the generalized Ohm's law in which anisotropy of electric conductivity is accounted for. The conductivity σ and electron mobility factor $\mu_e=e\tau_e/m_e$ (e is the electron charge, m_e is the mass of electron, τ_e is the average free-path time of electron) are assumed to be functions of electron number density and thermodynamic parameters.

Under assumptions made above the MHD flow is described by the following set of the governing parameters:

$$\rho_\infty, p_\infty, \nu_\infty, r, c_p, \mu_e, \lambda, \gamma, T_w, q_R, T, B^*, E_z, \alpha \quad (1)$$

In (1) c_p is the heat capacity at constant pressure, γ is the ratio of heat capacities, q_R is the characteristic radiation power, or the value of divergence of radiative heat flux, $\mu_e = \omega_e \tau_e / B$, $\omega_e \tau_e$ is the Hall parameter.

According to the theory of similarity and dimensionality (see, for example [18]), any dimensionless flow characteristics is the function of the set of the following parameters

$$\Gamma = \{M, Re, \gamma, Pr, \bar{T}_w, \bar{q}_R, S, K, \beta, Re_m\}, \quad (2)$$

Here M is the Mach number, Re is the Reynolds number, Pr is the Prandtl number, \bar{T}_w is the temperature factor, the ratio of surface temperature and the free-stream stagnation temperature. \bar{q}_R is the characteristic radiation power. S and K are MHD interaction factor and electric load coefficient, respectively. β is the Hall parameter, Re_m is the magnetic Reynolds number. These magnitudes are defined as follows:

$$M^2 = \frac{u_\infty^2 \rho_\infty}{\gamma p_\infty}, \quad Re = \frac{\rho_\infty u_\infty r}{\mu_g}, \quad Pr = \frac{c_p \mu_g}{\lambda}, \quad S = \frac{\sigma B_*^2 r}{\rho_\infty u_\infty},$$

$$K = \frac{E_z}{u_\infty B_*}, \quad \beta_e = \frac{e \tau_e B_*}{m}, \quad Re_m = u_\infty r \sigma \mu_0 \quad (3)$$

(μ_0 is the magnetic permeability of vacuum, μ_g stands for dynamic viscosity of the gas). Variety of flow regimes is determined by first six gasdynamics parameters and by four electrodynamic ones.

It is notable that under hypersonic flight conditions the non-equilibrium and finite rate kinetics effects play an important role. Thus, for the full characterization of the hypersonic flow over a body the Damkoeler number $Da = \tau_{ch} u_\infty / L$ is to be introduced into the expression (2). Moreover, taking into account the low pressure at high altitude and the rather limited size of the bodies considered the Knudsen number $Kn = l_f / L$ is to be added into the right hand part of the symbolic expression (2).

The flow characteristics of primary interest are: the bow shock stand-off distance $\Delta/r = A_1(\Gamma)$; surface heat flux density $q_w = St(\Gamma, \theta) \cdot \rho_\infty u_\infty c_p (T_\infty - T_w)$, where St is Stanton number and θ is the angle coordinate along the surface; the total force \mathbf{F} acting on cylinder. The total force \mathbf{F} is calculated as

$$F_i = \int_{\Sigma} P_{ik} n_k d\Sigma - \int_V [\mathbf{j} \times \mathbf{B}]_i dV, \quad i=1,2,3 \quad (4)$$

$$\mathbf{n} = (n_1, n_2, n_3)$$

Here, V is the volume occupied by the fluid only, Σ is the surface of cylinder, $\mathbf{n} = (n_1, n_2, n_3)$ is the outward unit normal to the surface, P_{ik} is the hydrodynamic stress tensor.

The flow conditions of interest are such that $Re_m \leq 0.1$ (see below). Therefore induced magnetic field can be neglected and electrodynamics equations can be cast as

$$\begin{aligned} \text{div } \mathbf{j} &= 0 \\ \mathbf{j} + \mu_e [\mathbf{j} \times \mathbf{B}] &= \sigma \mathbf{E}^* \\ \mathbf{E}^* &= \mathbf{E} + [\mathbf{v} \times \mathbf{B}] \\ \mathbf{E} &= -\nabla \phi, \mu_e = e\tau_e/m_e = \beta_e/B \end{aligned} \quad (5)$$

Where \mathbf{j} is the electric current density, \mathbf{B} is the magnetic induction vector, \mathbf{E} is the electric field strength, \mathbf{v} is the fluid velocity vector, and ϕ is the electric potential. The set of equations (5) readily reduces to one elliptic equation for electric potential.

The crucial point in investigating the MHD interaction under conditions discussed above is the question of conductivity and electron mobility distribution. It is seen from (5) that the smaller conductivity and/or higher mobility, the lower is the electromagnetic force $[\mathbf{j} \times \mathbf{B}]$ and, hence, the effect of MHD interaction on the flow characteristics. Following [19] the electrical conductivity and electron mobility coefficients are defined as flows:

$$\sigma = \frac{e^2 n_e \tau_e}{m_e}, \quad \tau_e^{-1} = \sum_K \tau_{eK}^{-1}. \quad (6)$$

Here, n_e is the electron number density and τ_e^{-1} is the characteristic collision frequency of electron with neutrals and ions. Both are estimated in the usual way, i.e.

$$\tau_{en}^{-1} = n_n v_e Q_{en}, \quad \tau_{ei}^{-1} = n_e v_e Q_{ei}$$

where n_n is the concentration of neutral particles, $\langle v \rangle$ is the average electron velocity, and $\langle Q \rangle$ is the impact cross-sections. $\langle Q_{en} \rangle$, electron-neutral collision cross-section, is taken as constant, $Q_{en} \sim 10^{-15} \text{ cm}^2$.

$$Q_{ei} = \frac{4\pi}{9} \frac{e^4 \Lambda}{(kT_e)^2}, \quad \text{where } \Lambda = \ln \left[\frac{3}{2\sqrt{\pi}} \frac{(kT_e)^{3/2}}{e^3 n_e^{1/2}} \right], \quad v_e = \sqrt{\frac{3kT_e}{m_e}}.$$

Electron number density is determined from the finite-rate chemistry calculations coupled with the Navier-Stokes equations. For the purposes of the paper the equilibrium electron number density is calculated from the Saha' formula [18].

$$\frac{n_e^2}{N} = AT^{3/2} \exp(-I/T), \quad (7)$$

$$A = 2.414 \cdot 10^{15} \text{ cm}^{-3} \text{ K}^{-3/2}, \quad I = 10^5 \text{ K}.$$

Finally,

$$\mu_e = \frac{e\tau_e}{m_e} = \frac{\sigma}{en_e}.$$

The Hall effect results in appearance of the x - and y -components of electric current. They in turn generate the force along the cylinder axis and can violate the two-dimensional flow field. However, the calculations showed that total force $[\mathbf{j} \times \mathbf{B}]_z$ is several orders of magnitude less than x - and y -components of electromagnetic force. Therefore the MHD flow field is considered to be two-dimensional. The complete model used to describe all the MHD flow characteristics includes the Navier-Stokes equations, the chemical species transport equations and electrodynamics model described above. The electromagnetic force term appears in momentum equations and Joule dissipation term appears in the total energy equation.

The air chemical kinetics model used to calculate production rates due to chemical reactions occurring usually behind the bow shock is a well-known 11 species – 98 elementary reactions model. Details can be found in [20].

The transport coefficients, molecular viscosity, heat conductivity and ordinary diffusion coefficients (Fick's law is assumed for species diffusion fluxes) are calculated with the model, which takes into account the neutral-neutral, neutral-electron, ion-electron charge-transfer collisions [21]. The thermodynamic properties of species, formation enthalpy, heat capacity at constant pressure are, in general, considered as functions of temperature.

In first two problems declared in introduction the simplified gas models are used. In particular, the perfect gas thermodynamics is implied, and Sutherland-like approximations are used for viscosity and heat conductivity.

The MHD flow is considered in the domain including both regions upstream and downstream of cylinder. The symmetry is assumed to hold on the $y=0$ line (Fig.1). The "short-circuit" operation mode is mainly studied, i.e. $E_z=0$ everywhere. The radiation power is estimated from formula $Q_R = \kappa \cdot \sigma_{SB} T^4$, where $\kappa = 10^{-3} \text{ cm}^{-1}$, and σ_{SB} is the Stefan-Boltzman constant. For absorption coefficient, approximate estimations were made from the data presented in [22].

In the current paper the MHD flow over a circular cylinder is numerically studied for the conditions of MHD WT facility [14]

$$\begin{aligned} M &= 12 \div 15, p_\infty = 30 \div 40 \text{ Pa}, \\ T_\infty &= 500 \div 700 \text{ K}, \\ T_w &= 1200 \div 2500 \text{ K}, \\ B_\bullet &= 0 \div 2 \text{ Tesla.} \end{aligned}$$

Problem 1. Analysis of MHD flow near the critical point of cylinder (No Hall Effect, Constant Conductivity)

The reduced model is used in this study to analyze the MHD flow features near the critical point. The detailed description of the results was presented in our preceding papers [16-18]. The conductivity is set to constant value in the subsonic region behind the shock. The Hall effect is neglected. The following dimensionless parameters characterize the flow:

$$\begin{aligned} M=3\div 12, Re=10^2\div 10^3, \gamma=1.4 \text{ and } 1.2, \\ Pr=0.72, S=0\div 20, \kappa=0, \beta=0, Re_m=0, \overline{Q}_r=0 \end{aligned} \quad (8)$$

The temperature factor $\bar{T}_w = T_w/T_\infty^0$ is determined from $\gamma, M, T_w=1200K, E_z=0$.

The results presented in those papers indicate dramatic decrease in the heat fluxes on the cylinder surface and hydrodynamic part of total drag for large MHD interaction factors. At the same time the total cylinder drag increases essentially. This study has confirmed our earlier results obtained with the simpler numerical models [9]. More details can be found in [23-25].

Problem 2. Equilibrium MHD flow over cylinder with the Hall effect

The possibility of formulation of Problem 2 is based on the estimation of the electrical currents in the solution plane. As they generate a force in the axial direction, the two-dimensional formulation can be violated. However, as it will be shown, below the integrated violating force is as low as five orders of magnitude in comparison with x - and y -components of electromagnetic force. The local values of axial force component are at least 20 times less than two other components. Therefore, the two-dimensional MHD flow character is assumed to hold.

The electrodynamics part of the entire equation set is described by the equations from (5) to (7). Equilibrium electron number density is assumed to take place in the entire domain. Equations (5) are reduced to one equation of elliptic type for electric potential. The boundary conditions suitable for the flow in the MHD WT Facility are proposed to be as follows. The cylinder surface is considered as an insulator. On symmetry lines, $y=0$, zero normal derivative of potential is set. On the rest of boundary the $\varphi=0$ condition is specified. The short circuit operation mode is considered, $E_z=0$. Cylinder radius $r = 6\text{mm}$ was taken, $T_w=2400K$.

Computational details

The problem (5)-(7) is solved on the exactly same grid as the Navier-Stokes equations. The control-volume conservative formulation is used to discretize the equation for potential expressing the conservation of electric charge. One integration-point was used to calculate the current through any cell-face, while 7-point Gauss quadrature was applied to calculate the at-face average resistance between two cell-centers. The obtained sparse nine-diagonal linear equation set was solved with Additive Correction Multigrid method of Hutchinson and Raithby [26]. Four Grid-Level Flexible-Cycle approach was utilized. Modified Incomplete Choleski method of Gustaffson [27] was used as smoother on any grid-level. One-dimensional Additive Correction procedure was applied to accelerate convergence. From 21 to 25 fine-grid iterations was normally needed to reduce the residual in six orders of magnitude.

Results of Calculations

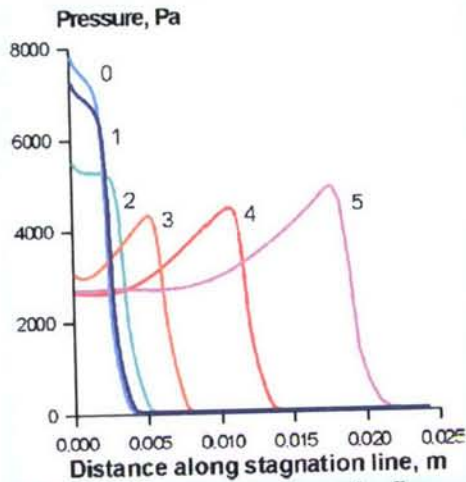


Figure 5. Pressure along stagnation line

$B=0$; 1- $B=0.2$; 2- $B=0.4$; 3- $B=0.6$; 4- $B=0.8$; 5- $B=1.0$

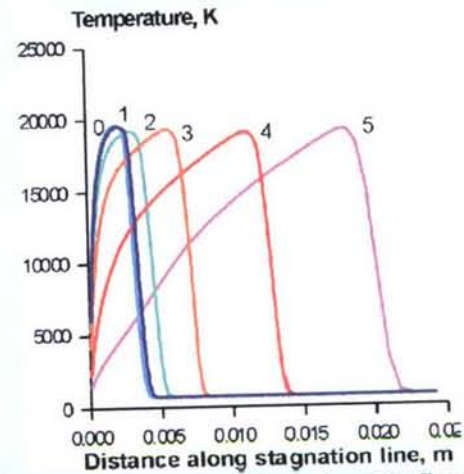
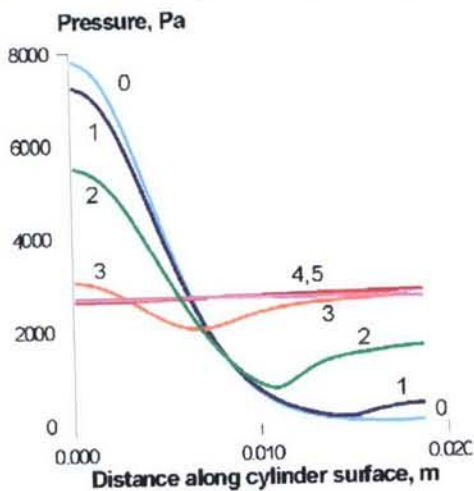
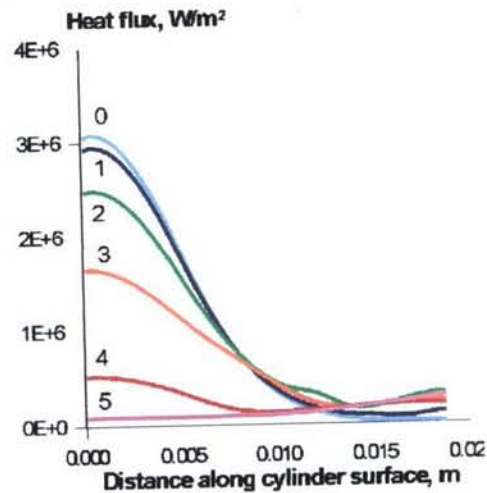


Figure 6. Temperature along stagnation line.

The influence of MHD interaction on the bow shock stand-off distance is demonstrated by Fig.5. The pressure distribution along the stagnation line is shown in Fig.5 for several magnetic fields values, $B^*=0 \div 1$ Tesla. Increasing the magnetic field increases the stand-off distance while the pressure drops on the cylinder surface. The temperature distribution along stagnation line vs magnetic field is shown in Fig.6. It is well seen that the temperature gradient decreases significantly in the region between the shock and cylinder surface, as magnetic field rises. As consequence, the conductive heat flux into surface drops when the magnetic field amplitude increases.

Pressure and heat flux density on the cylinder surface vs magnetic field amplitude are shown in Fig.7 and Fig.8, respectively. Unlike the non-MHD flow, when both

Figure 7. Distribution of pressure along cylinder surface. 0- $B=0$; 1- $B=0.2$; 2- $B=0.4$; 3- $B=0.6$; 4- $B=0.8$; 5- $B=1.0$.Figure 8. Distribution of heat flux along cylinder surface. 0- $B=0$; 1- $B=0.2$; 2- $B=0.4$; 3- $B=0.6$; 4- $B=0.8$; 5- $B=1.0$.

pressure and heat flux have well- distinguished maximum at critical point, their distributions along the surface become more uniform in MHD-flow. Level out of pressure is also demonstrated by Fig.7, where the pressure field is shown for non-MHD case $B^*=0$, and for $B^*=1$ Tesla case. In the second case there is a large zone of nearly constant pressure both downstream and upstream the cylinder. The strongest interaction takes place in the region just behind the shock, where the velocity vector is still perpendicular to the magnetic field lines. Action of electromagnetic force is similar to the flow over a larger size body. In this case the cylinder itself appears in the region of wake of such effective body, where the lower and uniform pressure takes place flow.

The components of total force (4) acting on the cylinder are plotted in Fig.9. Also total conductive heat flux and total axial current are presented. Similar to the no Hall effect flow discussed in the previous section the hydrodynamic part of the total force dramatically decreases compared to the non-MHD flow. The same is valid relative to the total heat flux into cylinder.

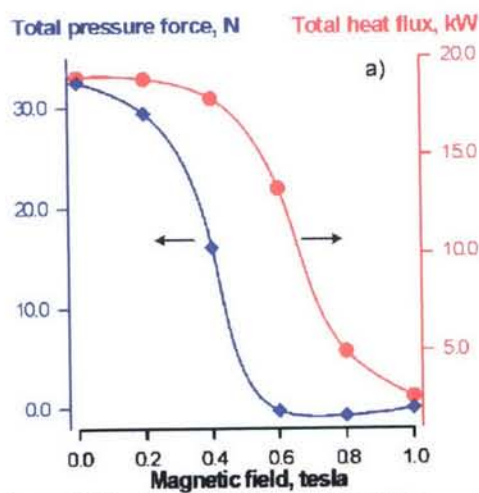


Figure 9. Total pressure force and heat flux

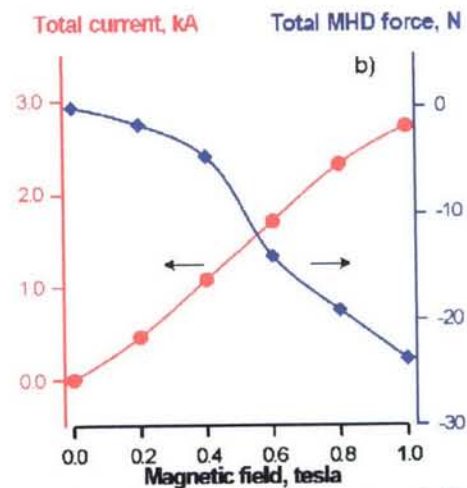


Figure 10. Total axial current and electromagnetic force

The changes in the flow structure are seen from Fig.11-Fig.13. The temperature fields are shown in Fig.8 for non-MHD case and for the MHD flow with $B^*=1$ Tesla. The highest temperature zone locates just behind the shock, whereas in the rest of the domain rather moderate temperature is observed. The distribution of the axial current, J_z , is shown in Fig.12. It is seen that there is a small region between the shock and cylinder surface where the current is negative. This current mainly provides the interaction and effects on the position and shape of the bow shock. In the larger part of the entire domain it is positive and electromagnetic force acts in opposite direction, toward the body. However, the amplitude of the opposite force is much smaller than those acting in the front region.

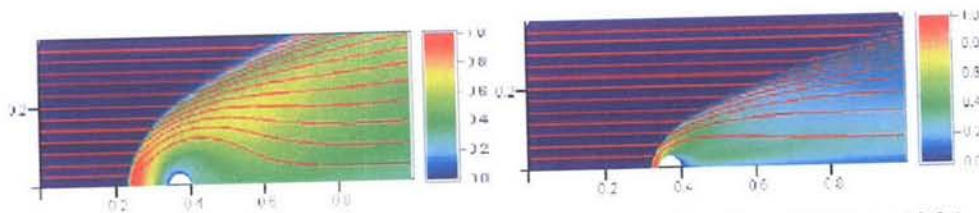


Figure 11. Temperature and flow stream lines for MHD flow (left) and non-MHD flow (right).

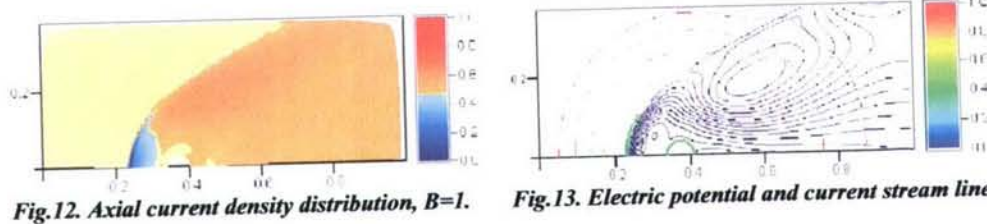


Fig.12. Axial current density distribution, $B=1$.

Fig.13. Electric potential and current stream lines

The electric current flow in the solution plane is presented in Fig.13 by the current stream lines. The main interaction zone is also well detected by the "negative" current vortex. In the larger part of the domain the current vortex of opposite sign exists. It should be noted that the amplitude of the "plane" current is essentially smaller than the amplitude of axial one. Therefore, the electromagnetic force it generates in axial direction is much smaller than that created by the axial current component. This allows one to neglect with the three-dimensional flow pattern and to consider the two-dimensional MHD flow. Also note that in the problem considered the Hall effect appeared to be small, which is a consequence of equilibrium conductivity assumption. In the main interaction zone the electron mobility β/B is of order of unit due to high temperature and, hence, sufficiently high electron number density. The Hall parameter, β , appears to be less than unit since the magnetic field amplitude drops with increasing of distance as $B \cdot r/L$. The Hall parameter is large in the cold near surface region, but this is compensated by the zero-current boundary condition specified on the cylinder surface. From this follows that under the considered conditions the Hall effect can be neglected and the model becomes suitable for analyzing the MHD flow over the cylinder.

Problems 3. Non-Equilibrium Finite Rate Kinetics Chemistry MHD Flow

In first attempts to simulate the MHD flow over a test cylinder under conditions of the MHD Wind Tunnel Facility [14,15] the great differences in the compared characteristics have been revealed. Calculations significantly over predicted the shock stand-off distance, which was attributed to the high interaction observed in simulations. The latter was recognized due to equilibrium ionization approach applied in the previous Section. The equilibrium ionization approach gives very high values of ionization degree at temperatures of interest; therefore the conductivity is high while the electron mobility is low. The electromagnetic force appeared to be too large, which determined much larger bow-shock stand-off distance compared to the estimated from experiment.

From the other hand it was known that the oncoming flow is not in chemical equilibrium [14]. Both these circumstances led us to necessity to consider the

chemically non-equilibrium flows in order to treat the experimental conditions observed in the MHD facility.

The 11 species air chemical kinetics model has been implemented into the Navier-Stokes / MHD code. The set of chemical reactions and the reactions rate constant coefficients were taken from the work [20]. The seed (Na or K) ionization-recombination reactions were added to the reaction set to treat the possible presence of the seed atoms or ions in the flow. The transport coefficients necessary to calculate the viscous, heat and diffusion fluxes were calculated with the model published in [19] suitable for non-equilibrium and ionized air compositions.

Numerical predictions were made for the following conditions:

$$P_{\infty}=33\text{Pa}, T_{\infty}=550\text{K}, v_{\infty}=7500\text{m/s},$$

radius of cylinder $r=0.008\text{m}$, magnetic field grew from 0 to 2 Tesla for 1ms. The composition of oncoming flow was assumed to correspond to those obtained at the MHD accelerator exit ($T=4500\text{K}$) and is frozen while expanding in the secondary nozzle. Mass fraction of seed (Na) was assumed to equal to 2%. We also assumed that the seed is fully ionized since Na ionization degree was determined at $T=4500\text{K}$ and is frozen while expanding in the nozzle. At the same time electron temperature was assumed to follow the vibrational temperature, $T_v=4500\text{K}$, rather than translational one, $T=550\text{K}$.

In Fig.14 the profiles of temperature along the cylinder stagnation line are presented. Lower curve corresponds to the non-MHD case and upper curve

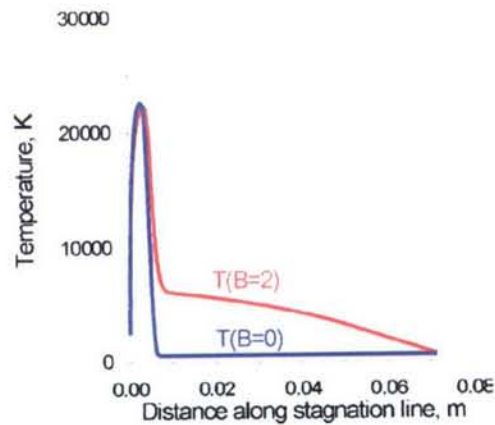


Figure 14. Temperature profiles for $B=0$ (bottom) and $B=2\text{Tesla}$ (upper) cases.

corresponds to the MHD-interaction case at the magnetic field $B^*=2$ Tesla. It is seen that differences are negligible. The only new feature appeared with the MHD is gas heating upstream the cylinder. The distributions of electrical characteristics presented in Fig.15 show that the situation is absolutely opposite to that observed in the previous Section. The electromagnetic force is directed toward the surface. The large values of Hall parameter determine the large Hall current while “working” current, J_z , is nearly β_e times less. Effective conductivity $\sigma_{eff} = \frac{\sigma}{1 + \beta_e^2}$, which should be used in

estimating the MHD interaction factor (see Discussion), appeared to be small for the remarkable MHD effect to take place.

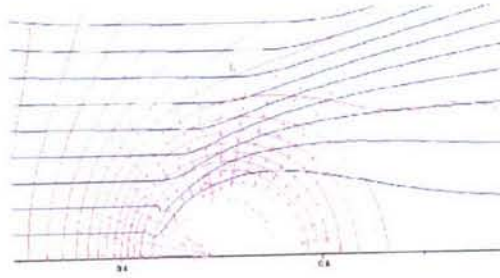


Figure 15. Electric potential contours(red), current stream lines(blue) and body force vectors.

From the numerical predictions described in this Section two preliminary conclusions can be made. First, our general understanding of the processes taking place in MHD Wind Tunnel Facility is correct. Effects related to the non-equilibrium chemistry are important. Second, in weakly ionized gas the Hall effect determines the MHD interaction features. The detailed analysis of the final rate chemistry will be presented later.

MHD interaction

Under the thermodynamic/plasmadynamic condition of the hypervelocity flow that is typical to the MHD WT facility experiments with the cylindrical model, the principal MHD interaction effect is attributable to the Lorentz body force, $\mathbf{j} \times \mathbf{B}$, that acts on the flow. The second MHD interaction effect, redistribution of the enthalpy in the flow field due to the MHD related electrical energy source/sink, $\mathbf{j} \cdot \mathbf{E}$, is no thought to be significant because the internal short-circuiting in the experimental configuration results in a strong reduction of the electrical field strength, \mathbf{E} .

The nature of this short-circuit phenomena can be understood from the earlier reported detailed results of our two-dimensional simulations. The Faraday component of the electromotive force $\mathbf{u} \times \mathbf{B}$ is directed along the cylinder axis. The sign of the electromotive force is opposite for the upstream and downstream regions of the cylinder. This results in low (to negligible) value of the average electromotive force when integrated over the whole interaction region.

The corresponding component of the electric field is defined by the net Faraday current, I_F , and the averaged electromotive force, which is negligible small in comparison with scaling value uB (u is a characteristic value of the flow velocity). The Hall component of electric field is also very small in comparison with scaling value $\omega \tau uB$ ($\omega \tau$ is the Hall parameter) due to effective shorting of azimuthal non-uniformities of the Faraday current density. For these reasons, the energy redistribution factor will be omitted from the consideration of the MHD interaction effects in the following exercise.

The Lorentz body force is the cross-product of current density vector, \mathbf{j} , and magnetic induction vector, \mathbf{B} , i.e., $\mathbf{j} \times \mathbf{B}$. The B-field intensity is defined by the magnet configuration and its current. Under the geometric model configuration of our experiments, the magnetic field is azimuthal and its intensity falls off as one moves radially from the cylinder surface, i.e.,

$$\mathbf{B} = \mathbf{e}_\theta B_0 \frac{r_0}{r}, \quad (9)$$

where $B_0 = \frac{\mu_0 I}{2\pi r_0}$, \mathbf{e}_θ is unit azimuthal vector and I is magnetic system current.

The current density generated in the plasma is defined in accordance with the generalized Ohm's law,

$$\mathbf{j} + \mu_e \mathbf{j} \times \mathbf{B} = \sigma(\mathbf{E} + \mathbf{u} \times \mathbf{B}), \quad (10)$$

where μ_e stands for electron mobility.

Taking into account the premise that the electric field is essentially shorted (see above), Ohm's law can be reduced to the simplified form,

$$\mathbf{j} + \mu_e \mathbf{j} \times \mathbf{B} = \sigma \cdot \mathbf{u} \times \mathbf{B}. \quad (11)$$

Resolving Equation (11) with respect to the current density vector components yields

$$\begin{aligned} j_r &= \frac{\sigma \mu_e u_r B^2}{1 + \mu_e^2 B^2}, \\ j_\theta &= \sigma E_\theta, \\ j_z &= \frac{\sigma u_r B}{1 + \mu_e^2 B^2}. \end{aligned} \quad (12)$$

In the preceding relations, the axial velocity u_z is assumed to be zero, the azimuthal component of electric field E_θ is accounted for to drive the azimuthal current that is needed to satisfy current conservation.

Based on these definitions of the current density components, the components of the Lorentz body force are:

$$\begin{aligned} f_r &= -j_z B = -\frac{\sigma u_r B^2}{1 + \mu_e^2 B^2}, \\ f_\theta &= 0, \\ f_z &= j_r B = \frac{\sigma \mu_e u_r B^3}{1 + \mu_e^2 B^2}. \end{aligned} \quad (13)$$

It is notable that the axial body force component that appears due to the Hall effect only is $\omega_e \tau_e = \mu_e B$ times larger than the radial 'Faraday' component. This fact implicates that the situation is significantly three-dimensional, which creates additional difficulties in the interpretation of the experimental data. Nevertheless, in further analysis herein, we approach this with the traditional two-dimensional approximation for illustration. The three-dimensional nature of these phenomena is reserved to be analyzed later.

The MHD interaction parameter is conventionally defined as a ratio of a characteristic body force value times a characteristics length to the dynamic pressure of incoming flow, i.e.,

$$S_u = \frac{f \cdot L}{\rho u^2}. \quad (14)$$

The characteristic length, L , is essentially the length of the region over which interaction exists and on the order of magnitude of the dimensions of the body of revolution. By substituting f_r as f and assuming $u_r = u$ one can obtain,

$$S_u = \frac{\sigma B^2 L}{\rho u (1 + \mu_e^2 B^2)}. \quad (15)$$

For the purposes of this analysis, it is informative to integrate the body force over the upstream interaction area defined as a unit angle sector centered at the model axis. The motivation for such an approach is that a significant non-uniformity (decay) in magnetic field is present and correspondingly, non-uniformity in Hall parameter exists. This integration yields,

$$S_b = \frac{1}{\rho u^2 L} \int_{r_0}^L \frac{\sigma u B_0^2 r_0^2 / r^2 \cdot r \cdot dr}{1 + \mu_e^2 B_0^2 r_0^2 / r^2} = \frac{1}{2} \frac{\sigma B_0^2 r_0}{\rho u \zeta} \ln \frac{\zeta^2 + \mu_e^2 B_0^2}{1 + \mu_e^2 B_0^2}. \quad (16)$$

where $\zeta = L/r_0$.

The derived expression shows that the levels of the governing electrophysical properties, i.e., conductivity and Hall parameter (or the electron mobility), are of primary importance for introducing the MHD interaction effects.

A simplified representation of the electrical conductivity is given by,

$$\sigma = n_e e \mu_e, \text{ where } \mu_e = \frac{e \tau_e}{m_e}. \quad (17)$$

where, e , is the electron charge, n_e , the electron number density, m_e , the electron mass, τ_e is the free path time of electron, and σ and μ_e are conductivity and electron mobility, respectively. The Hall parameter is defined according to,

$$\omega_e \tau_e = \mu_e B \quad (18)$$

where B is the absolute value of magnetic induction.

In the case typical our considered conditions (compare the simulation results of the preceding section) the situation of a very high value of the Hall parameter needs to be analyzed separately.

If $(\mu_e B_0)^2 \gg 1$, then the argument of the logarithm in Equation 8 can be written as,

$$\ln \left(1 + \frac{\zeta^2}{\mu_e^2 B_0^2} \right) = \ln(1 + \chi), \text{ where } \chi = \frac{\zeta^2}{\mu_e^2 B_0^2}. \text{ If } (\mu_e B_0)^2 \gg 1.$$

Then expression (16) becomes,

$$S_{br} \cong \frac{1}{2} \frac{\sigma B_0^2 r_0}{\rho_\infty u_\infty \zeta} \frac{\zeta^2}{\mu_e^2 B_0^2} = \frac{1}{2} \frac{\sigma_0 \zeta}{\rho_\infty u_\infty \mu_e^2}$$

Introducing the electron free part length

$$l_e = v_e \tau_e \quad (19)$$

and using (18), the following expression for the limiting interaction parameter, S_{br} , is obtained

$$S_{br} = \frac{1}{2} \frac{n_e e r_0 \zeta}{\rho_\infty u_\infty \mu_e^2} \approx \frac{n_e}{n_a} \frac{m_e}{m_a} \frac{L}{l_e} \frac{v_e}{u_\infty} \quad (20)$$

or,

$$S_{br} \approx \frac{\alpha \zeta}{Kn_e} \frac{v_e}{u_\infty} \quad (21)$$

where α is the ionization degree, ζ stands for the electron to molecular mass ratio, and Kn_e is the electron Knudsen number.

This final expression is revealing that the MHD interaction parameter for very large Hall parameter value is essentially independent of the magnetic induction.

To apply this result to the conditions of the recent experiments on the MHD WT facility, two characteristic flow regions should be viewed independently. The first region is the flow located between the bow shock and the cylinder. The second one is located upstream the bow shock extending a distance equal to the cylinder length. (This length is dictated by the '1/r' variation in magnetic induction.) Outside of this area the magnetic induction decreases much faster with distance from the cylinder axis.

Consideration of these two regions separately is motivated by the dramatic difference of flow/plasma properties upstream and downstream of the bow shock. It is noted that for the experimental conditions the MHD interaction upstream of the bow shock is not zero because a 'frozen' electron number density can exist due to the short duration process of the expansion in the secondary nozzle and strong coupling of the vibrational T_v and electron T_e temperatures. Another 'geometrical' reason is that a significantly larger characteristic length is involved for the upstream interaction than in the short region located between the bow shock and the cylinder.

In our parametric analysis two plasma related parameters are varied: the ionization degree α and the electron temperature T_e . Moreover, considerable uncertainty exists to these values in the experiments.

In Fig. 16 the integral MHD interaction parameter S_b and asymptotic (i.e., high Hall parameter) MHD interaction parameter S_{br} as functions of electron temperature are plotted for three value of ionization degree: $\alpha=0.1$ (optimistic), $\alpha=.01$ (realistic), and $\alpha=.001$ (pessimistic). The 'realistic' tag is based on the anticipated level of ionization corresponding to full seed ionization. The downstream flow parameters are as follows:

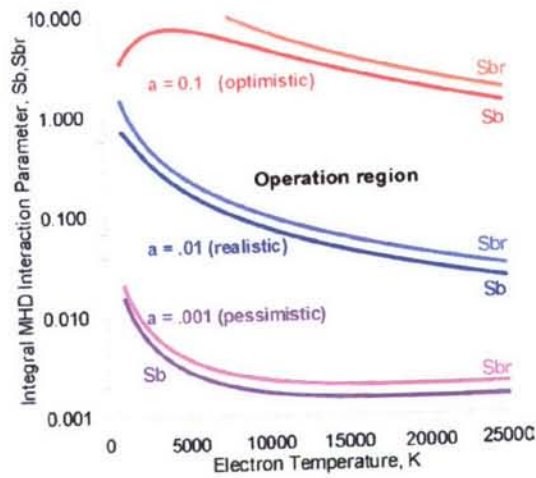


Figure 16. The Downstream Integral MHD Interaction Parameter as a Function of Electron Temperature.

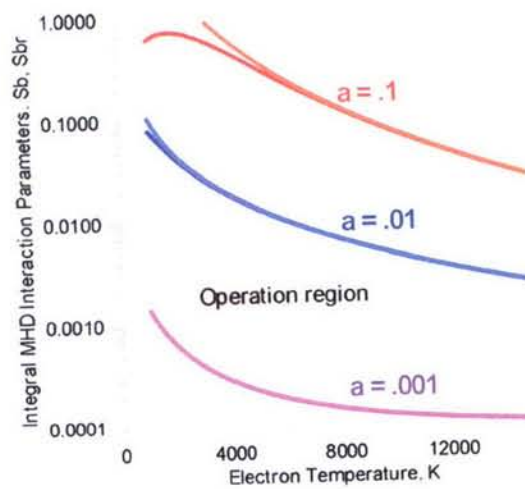


Figure 17. The Integral MHD Interaction Parameter for Upstream Region.

temperature, $T_s = 10,000\text{K}$,
 pressure, $p_s = 7\,000\text{ Pa}$,
 seed percentage $\alpha = 1\%$,
 $B_0 = 2\text{T}$,
 $r_0 = .01\text{ m}$.

The characteristic interaction length is set for this region as $L = r_0$. The electron mobility μ_e is calculated as a function of electron temperature and gas composition with the same procedure that is used in our 2-D simulations presented in the previous Section.

Plots for the upstream region are presented in Fig.17. The flow parameters are specified as follows:

temperature $T_s = 550\text{K}$,
 pressure $p_s = 33\text{ Pa}$,
 seed percentage $\alpha = 1\%$,
 $B_0 = 2\text{T}$,
 $r_0 = .01\text{ m}$.

The characteristic MHD interaction length is set for this region as $L = 15r_0$.

The plots presented in Fig. 16 and 17 demonstrate the importance of ionization degree of the plasma. The higher ionization degree, the higher the level of MHD interaction.

This result implies that seeding in the experiments could be higher than 1%. That is, higher MHD interaction is more readily achievable with higher seed percentages at electron temperatures not lower than approximately 5,000K.

It is interesting to note that increasing of electron temperature results in a significant decrease of the MHD interaction. This fact, as borne out in this analysis, is a consequence of increased electron mobility and higher Hall parameter values. Similar reasoning can be used to explain the rapid decay of the MHD interaction with decreasing ionization degree. The increase in electron mobility means increase of Hall parameter as related to the lack of the dominating role of electron-ion collisions in comparison to electron-neutral particle collisions.

This observation may be extremely important for real flight conditions when an external ionization means are required. The needed power consumption can be enormously high to provide effective MHD interaction.

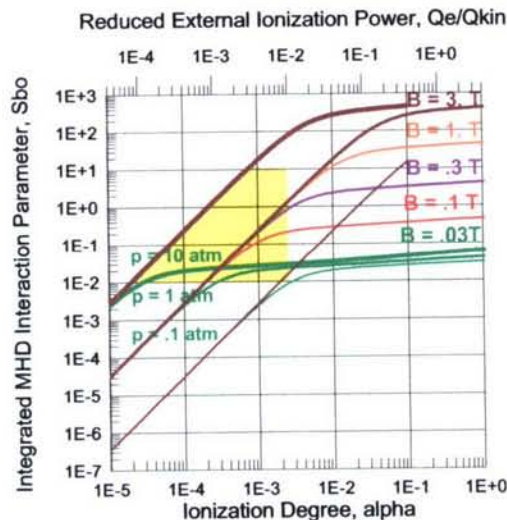


Fig. 18. MHD Interaction Parameter Evaluation for Flow over a Cylinder.

With regard to the recent experiments, an important conclusion was derived from this analysis. The total MHD interaction effect in MHD tunnel experiments with the cylinder model is indicated to be a combination of upstream and downstream interaction effects. The contribution of upstream region is surprisingly not negligible in comparison to the downstream region effect. It is smaller but still rather remarkable.

In order to extend this analysis for hypersonic flight conditions that are assumed as follows: dynamic pressure varies in range of 0.1-10 atm, magnetic induction varies between 0.3 and 3 Teslas; characteristics length is 1m; partially ionized air is considered as a working fluid; the free stream velocity is 5 000m/sec. The main input parameter is the ionization degree that is assumed to be provided with some external mechanism such as electron beam ionization proposed for free flight conditions elsewhere (see, for example, [28,29]). For rough evaluation of energy cost to produce ionization of desirable level the energy cost of one electron production of 30eV [30] is used in this analysis. The summarizing map is presented in Fig.18.

Three families represent three dynamics pressure values: 0.1, 1.0, and 10 atm. Fifth different magnetic induction values are used for the $p_{din}=1.atm$ to demonstrate the magnetic field strength effect. The left side linear in respect to ionization degree part of the graphs corresponds to the Hall effect dominating mode when no influence of magnetic field is observed. The saturated right hand part of the curves corresponds to Coulomb collision dominating and low Hall effect resulting in recovery of $S \sim B^2$ rule. The filled area is a rough estimation for operation region based on assumption that (1) the ionization cost would not exceed 1% of the total kinetic energy of oncoming flow, (2) the characteristic (maximal) magnetic induction is not higher than 3 T, and the required MHD interaction parameter is not less than .01. For these conditions the available operation region is rather limited and practically fully located in the Hall effect dominating region. This conclusion reveals the real difficulties in the practical implementation of MHD flow control technique at least for simple configuration such as considered here circular cylinder with axial current inducing magnetic field.

It should be noted, however, that upstream interaction area doesn't represent whole MHD interaction process. The downstream, and in particularly, wake interaction seems to be very important because of its larger extension in comparison with rather limited interaction region located between body and bow shock. This is especially important for a real flight condition when the oncoming airflow would hardly be electrically conductive while the wake flow heated up by shocks and additionally by Joule dissipation can be conductive even in far field.

Another interesting comment resulting from the above analysis relates to the simulation models used for studies of the MHD interaction in hypersonic airflows. In many recent papers (see, for example, [10-12, 31-33]) the strong attention is paid to the self-induced magnetic field – the case of high magnetic Reynolds number. Magnetic Reynolds number defined as $Re_m = \sigma \mu_0 U L$ can be physically treated as a ratio of the magnetic field induced by the current in the interaction region to the externally applied magnetic field, indeed

$$Re_m = B_{ind}/B_0 \sim \mu_0 j L / B_0 \sim \mu_0 \sigma U B_0 L / B_0 = \mu_0 \sigma U L,$$

and for the experimental conditions of the MHD WT facility where the experimental study of the cylinder problem is being carried out, one can find

$$Re_{m,exp} \sim 10^{-6} \times 2 \times 10^3 \times 7 \times 10^3 \times 1 > 1.$$

For the flight conditions used in the preceding analysis the similar estimation yields

$$Re_{m,fl} \sim 10^{-6} \times 5 \times 10^2 \times 5 \times 10^3 \times 1 = 2.5.$$

Correspondingly, for both cases the accurate description of induced magnetic field would be needed. However, due to dramatic reduction of effective conductivity by Hall

effect the actual induced magnetic field is scaled with the value of two-three order of magnitude less. Thus, the induction equation is not necessary to include into the MHD equation set. This allows us to use much simpler formulation of boundary conditions (in terms of measurable physical values such as current density rather the combination of magnetic field component derivations) and more mobile numerical algorithms.

Gasdynamics and electrodynamics fields

As it was mentioned above one of the most surprising results obtained in the experiments both physical and numerical was very low effect of MHD interaction on bow shock location and its shape. The analysis of numerical solution reveals many interesting details.

The configuration considered in this study can be treated as a Hall type MHD generator under nearly short circuit conditions. One of the general features of this configuration is that the Hall component of the electric field is directed opposite to the flow velocity. Considering for simplicity the short circuit condition for the 'Faraday' field component ($E_z=0$) that is the practically important case of well conductive cylinder (metallic) material. (It was already mentioned above that the axial component of electric field is practically very close to zero due to reversing sign of the induced e.m.f. $\mathbf{u} \times \mathbf{B}$ in upstream and downstream areas even in a case of insulator made cylinder). The main component of body force interested for this analysis is radial directed (in the cylinder center reference frame)

$$f_r = (\mathbf{j} \times \mathbf{B})_r = -j_z B_\theta \quad (22)$$

For the assumed conditions one can derive from the Ohm's law

$$j_z = \sigma u_r B_\theta - \omega_e \tau_e j_r = (n_e e u_r - j_r) \omega_e \tau_e, \quad (23)$$

where $j_{conv} = n_e e u_r$ can be called as a *convective current*. The radial current for the case $E_r=0$ (the local short circuit condition) is

$$j_r(E_r=0) = \sigma \omega_e \tau_e u_r B_\theta / (1 + \omega_e \tau_e^2) \sim j_{conv} \quad (24)$$

when $\omega_e \tau_e \gg 1$.

The radial current can be also presented in the form

$$j_r = j_{conv} (1 - E_r / E_r^*), \quad (25)$$

where

$$E_r^* = -\omega_e \tau_e u_r B_\theta \quad (26)$$

resulting in

$$j_z \sim \omega_e \tau_e j_{conv} E_r / E_r^* \quad (27)$$

Thus, the radial body force is defined as

$$f_r = -j_z B_\theta \sim -j_{conv} B_\theta \omega_e \tau_e E_r / E_r^* = -j_{conv} B_\theta^2 \mu_e k_H \quad (28)$$

that reveals the governing role of the 'a local Hall load factor' $k_H = E_r / E_r^*$.

It is useful here to introduce the power extraction/release associated with Hall component of electrical field

$$q_r = j_r E_r \sim -j_{conv} u_r B_\theta \omega_e \tau_e (1 - k_H) k_H. \quad (29)$$

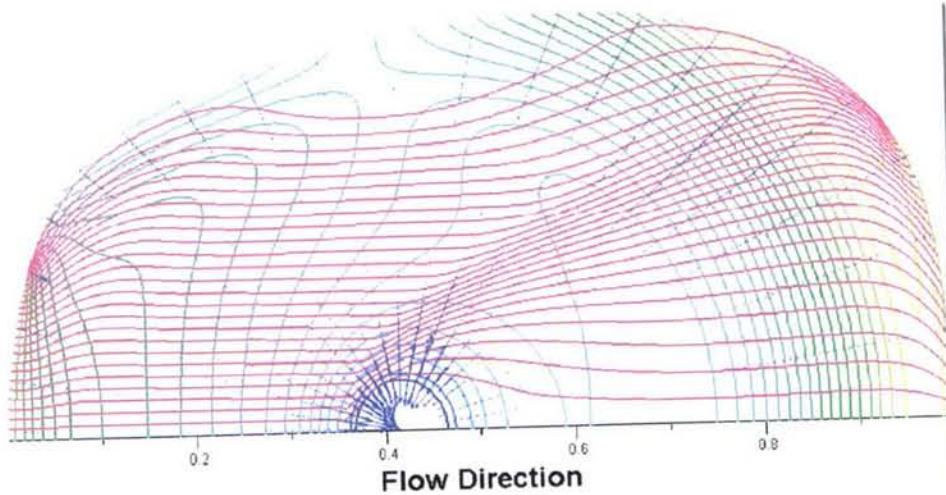


Fig.19. Electrical potential, current stream lines and body force vectors for insulator cylinder and global shorting conditions.

The sign of the right hand expression is defined only by the Hall load factor k_H , because of $(j_{conv} u_r B_\theta)$ is always non-negative being proportional to $(u_r B_\theta)^2$. The power generation mode (power extraction) corresponds to condition $0 < k_H < 1$; the conditions $k_H < 0$ and $k_H > 1$ define the power release mode.

The difference of these two cases becomes clear from comparison of body force direction. The sign of the scalar product $(f_r u_r) \sim -j_{conv} u_r B_\theta^2 \mu_e k_H$ is defined by the sign of k_H . Thus, when the Hall load factor is negative $k_H < 0$ then both $q_r > 0$ and $(f_r u_r) > 0$ that corresponds to the *MHD acceleration mode* (body force acts along the flow velocity). When, in turn, the Hall load factor k_H is greater than one ($k_H > 1$) then $q_r > 0$ (power release mode) and $(f_r u_r) < 0$ (body force acts against the flow velocity). That corresponds to the *MHD break mode*.

Typically of the operation conditions of the circular cylinder in a transverse hypersonic flow the MHD interaction reveals all of three modes simultaneously. To demonstrate this let us consider in more detail an example of electrodynamics parameters distribution for the case similar to the case presented in Fig.15. In Fig.19 the electrical potential, the current streamlines and the body force vectors are presented for whole calculating domain. The peculiarities of this case are related to the specified electrodynamics boundary conditions. They are as follows: the cylinder surface is of insulator material made that defines zero normal component of the current density: $j_n = j_r = 0$. To simulate the conditions of the experimental MHD WT facility [14], where free jet flow can be electrically contacted with the test section walls, zero potential boundary conditions are specified at the inlet and outlet portion of the calculating domain (these portions of the border are clearly recognized by the border crossing electrical current streamline). The free of contact with the test section walls side border of the free jet is simulated by zero current density condition. Finally, the symmetry conditions are applied to lower boundary of the calculating domain.

The important features of the solutions are as follows.

- The electrical current streamlines coincide generally with flow direction.
- The electrical potential is significantly non-monotonic along the flow direction approaching the minimum level at the cylinder locations.
- The equi-potential lines are similar to the cylinder surface in the vicinity of the cylinder.
- The body force vectors are mostly directed to the cylinder surface especially at the upstream portion of the near cylinder flowfield.

The dominating direction of the electrical streamlines is defined by the closed circuit condition of the 'effective Hall MHD generator'. Generally speaking the induced total voltage of such a generator is positive in respect to flow direction through generation region and, correspondingly, the induced total current is also positive (i.e. the electrical current goes in downstream direction). This feature causes the number 2: the non-monotonic character of the potential distribution with a rather deep minimum is defined by the fact that the downstream portion of the 'Hall generator' is significantly more powerful than the upstream one. So, the downstream generator works against the upstream as a load that resulting in reverse electrical field sign there. And the latter is a key issue to understand why the body force vectors are in opposite direction to be expected one.

In terms of expressions (28) and (29) the local Hall load factor k_H becomes negative in the upstream region that resulting in the MHD accelerating mode: both power and momentum are released in the flow field.

2. EXPERIMENTS WITH CIRCULAR CYLINDER IN CROSS-FLOW

The experimental study discussed in this paper is performed hypervelocity wind tunnel facility with MHD acceleration (MHD WT) of the airflow. The facility has been described in many details elsewhere [14,15]. The facility was recently modified in order to meet the new experimental conditions requirements. The new configuration and the operation modes of the facility used in this experimental are described in [15]. In the present configuration the MHD WT facility consists of the following main



Fig. 20. General view of the MHD WT facility

components: the arc preheater, the seed injection system, the primary supersonic nozzle; the MHD accelerator equipped with the 2.4 Tesla electromagnet and with the Faraday segmented type of MHD channel of the rectangular cross-section linearly increased from the inlet to the exit; the power supply system providing the independent power feed of each electrode pair; the secondary nozzle accelerating the airflow till Mach number from 8 to 15; the test section of approximately $.5 \times .5 \times .5 \text{ m}^3$; the supersonic diffuser and the vacuum chamber. The general view of the MHD WT facility test section part is presented in Fig.20.



Before MHD acceleration



During MHD acceleration

Fig. 21. A model in the test section before and during the MHD acceleration

In the present configuration air flow at the pressure of 3 atm preheated in the archeater up to 3500K, the airflow is seeded with ~1% NaK and accelerated in the MHD channel that provides parameters of the flow in the test section as following: the airflow cross-section at the secondary nozzle is $.11 \times .11 \text{ m}^2$, the static pressure is 33Pa, the static temperature is about 600K, the density is about 2.10^{-4} kg/m^3 , the velocity is

about 7000m/sec ($M \sim 15$), that corresponds approximately to hypersonic flight at the altitudes between 60 – 80 km. One of the airflow characteristics of most important for the experimental study is the gas composition that differs significantly from the atmospheric air being more (non-equilibrium) excited and dissociated during the intensive energy impute in the MHD channel.

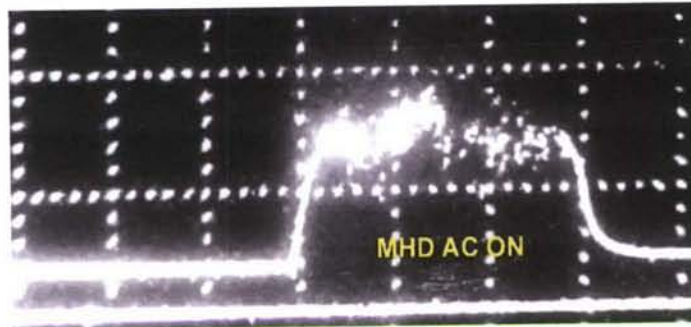


Fig. 22. The Pitot' tube response to the MHD acceleration

The working cycle of the facility provides approximately 0.5 sec period of the MHD accelerated flow in the test section. The operation mode is confirmed by the static pressure probes along the flow train and the Pitot' tube in the test section. The typical view of a model and airflow in the test section is presented in the Fig.21.

The Pitot' tube response to the MHD acceleration is shown in Fig.22.

Model Definition

Because the main goal of this program is fundamental study of MHD interaction in hypersonic flows under on-board conditions the model definition aims to find the configuration as simplest as possible but keeping of the main features of the phenomenon. The compromise solution found is a circular cylinder in a cross flow. The externally applied magnetic field for such a case could be created by the axial current passing through cylinder. The azimuthal magnetic field with intensity dropping down in inverse proportion to the distance from the cylinder axis simulates one of the

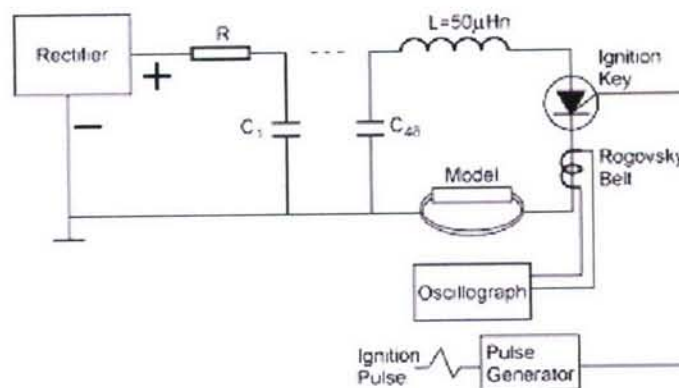


Fig. 23. The electrical scheme of GOS-1000 power supplier.

most important features of on-board systems that are the magnetic field non-uniformity. The bow shock at the cylinder results in the high temperature region downstream of it and, under certain conditions, in air ionization. The higher ionization degree the higher electrical conductivity. The latter is the primarily important value for the MHD interaction intensity. The preliminary analysis carried out at the beginning of this program has shown that under thermodynamics equilibrium condition the bow shock in the Mach 15 perfect gas flow has created the ionization high enough to provide the electrical conductivity at the level of several hundreds mhO/m. The size of the model is defined from the other hand by the flow size of the facility and by the condition of limited blockage of the flow by the model. From this the cylinder diameter is limited by the value of 30mm for the facility. The intensity of the MHD interaction is scaled by the MHD interaction parameter that is $S_u = \sigma B^2 d / \rho u$ where σ stands for electrical conductivity, B - for magnetic induction, r (the cylinder radius) - for the characteristics length, and ρu - for the mass flux density. For $S_u=1$ the estimation of the magnetic field required is

$$B \sim (\rho u / \sigma)^{1/2} \sim (2.10^{-4} \times 7.10^3 / 10^{-2} \times 10^3)^{1/2} \approx 4 \sim 1 \text{ T.}$$

The axial current required to induce such a field at the cylinder surface is estimated as

$$I_m = 2\pi r B / \mu \sim 10^{-2} \times 1 \times 10^7 / 2 = 5.10^4 \text{ Amps.}$$



Fig. 24. The general view of the power supplier

Taking into account non-ideal conditions at real experiments the magnetic system current requirements are estimated as several tens of kAmps. The Joule dissipation for this current is too high for steady state operation with no cooling. For this reason the pulse operation mode of magnetic system was chosen. The standard pulse power supplier GOS-1000 is used with approximate pulse duration of 2 msec. In Fig.23 and Fig.24 the schematic diagram and the general view of the power supplier are presented.

The working part of the cylindrical model exposed into the flow is made of either electrically conductive or non-conductive material. For the first option the copper is used, the second option is realized with glass or quartz. The cylinder diameter was varied from 16mm till 32 mm. The most recent configuration is of 16mm in diameter. While the non-conductive material was used for the model two belt-wise

electrodes were mounted at the cylinder ends distant from each other in 10 cm, which is approximate size of the flow in the test section.

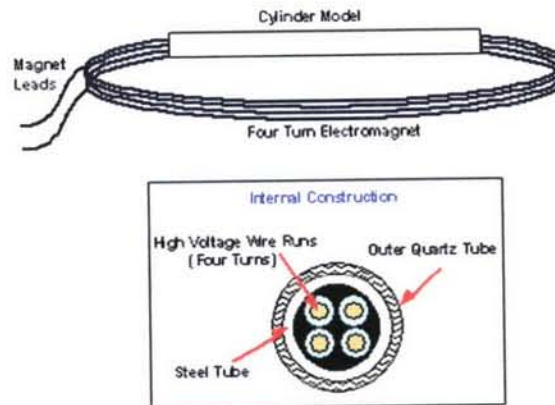


Fig. 25. The model concept structure

The principle design of the model is illustrated in Fig.25.

Two main configuration of the model are used. The first one corresponds to the schematic diagram presented in Fig.25, and the second one resulting from the modification made after the first series of experiments with the original configuration. The modification was motivated by the observed deformation and displacement of the model during the magnetic field pulse due to unbalanced electromagnetic forces between different parts of the electromagnet turns. The modification solves such a problem with change of the external electromagnet turns configuration made now symmetrical in respect to the cylinder part, that provides practically full balance of the forces acting on the cylinder part from the different turns. The one of the particular realizations of the modified model is exemplified in Fig.26.

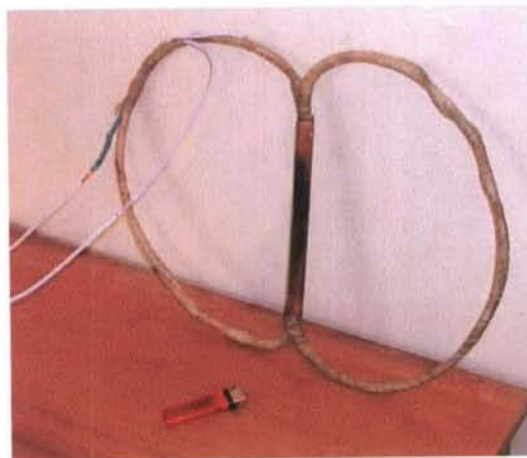


Fig26. The modified Double-Oval model configuration



Fig. 27. The double oval model installed in the test section. The cylinder is made of quartz; two belt electrodes are also shown.

Three different orientations are used in the experiments: horizontal, vertical and sloped with proximately 40° to the flow direction. Two first are basically equivalent, and the reason is to provide different visualization direction: along the cylinder axis for horizontal orientation and across the cylinder for the vertical one. The sloped orientation involves the significantly 3D interaction caused by the axial component of the flow velocity with azimuthal magnetic field. An example of the model location in the test section is shown in Fig.27.

Typically, in the case of double oval configuration 8 turns of electromagnet were used.

Measurements

The main types of diagnostics available in the test section at the model unto now in these experiments are different visualization, electrical potential and currents,

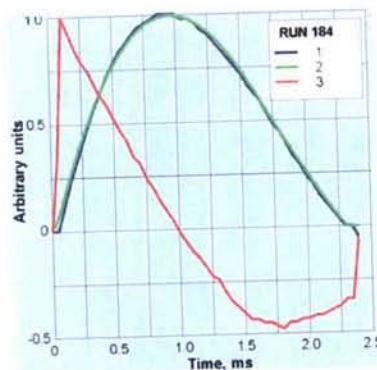


Fig28. The correlation of Rogovsky's belt and magnetic flux signals. 1 –Rogovsky' belt, 2 – integrated magnetic flux, 3 – magnetic flux signal

spectroscopy. Besides of these the standard measurements of the pressure along the flow train and the Pitot' tube near the model are also applied. The problems of the diagnostics extension connect to the very heavy physical conditions in the test section during the MHD interaction period. First of all, the pulse magnetic field creates a rather

strong electromagnetic noise practically avoiding any electronics devices inside the test section. The short duration of the interaction period makes also problematic to measure directly one the main MHD effects studied in this program – the heat flux reduction (or changing) at the leading edge of the model. The fine flow field structure and fast time variation of it require the very high space and time resolution of non-intrusive optical techniques, including spectroscopy and fast speed visualization. The typical metric scale of the flow structure in this experiment is millimeters and the variation time is less than 100 msec. The front edge highly sophisticated diagnostics equipment is not available now within this program. Thus, the approach used here is the accumulation of maximum available information even not satisfying the requirements formulated above and the development of the numerical simulation strongly related to the given experimental conditions in order to extract the physical information from the correlation of the numerical and physical models.

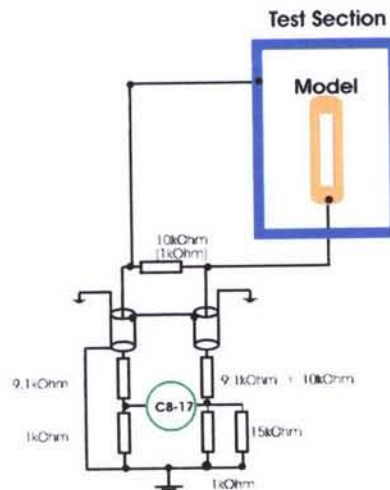


Fig. 29. e scheme of the model potential measurement.

The characteristics of the magnetic field in the test section are defined by the current measurement with the Rogovsky' belt installed at the magnetic system leads outside of the test section. In order to be sure that the current measured in such a way represents correctly the magnetic induction inside the test section in several first runs the measurement of the magnetic flux variation was used. This parameter was measured at two locations with the frames installed at the secondary nozzle wall as schematically indicated in Fig.27. Typical correlation of the magnetic system current measured by Rogovsky' belt and the integrated signal from the magnetic flux probe is presented in Fig.29. The time behavior of these two parameters is practically identical that validates the magnetic field estimation based on the Rogovsky' belt measurements. This conclusion has been checked for both the conductive and non-conductive material of the cylinder.

In the previous analysis [9,14-16,36] the critically important role of the Hall effect was indicated. The experimental evidence of the Hall effect can be demonstrated in the rather simple and available measurements of the model potential induced during the MHD interaction period. The scheme of the model potential measurement is presented in Fig.29. By varying of the resistance between the model and the practically grounded test section the leakage current can be also estimated. This current is

collected by the model surface in a case of the electrically conductive material is used

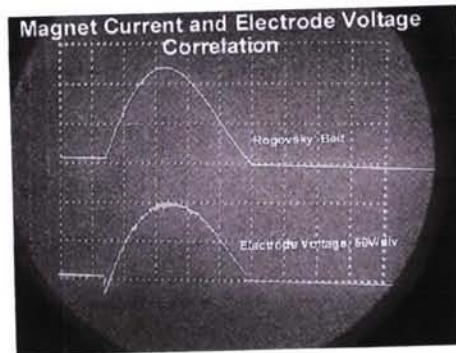


Figure 30. Rogovsky' belt signal and model potential correlation.

for the cylinder. The typical voltage between the electrically conductive model and the test section is about 40 Volts that is in good correlation with the numerical simulation. The voltage evolution is well correlated with the magnetic field intensity. The typical example of such a correlation is presented in Fig.30.

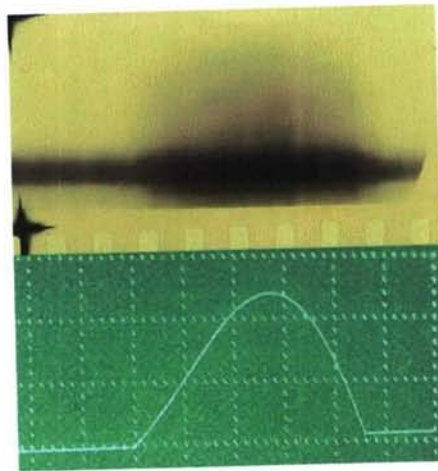


Figure 31. The streak photography record. The time from left to right 0.4msec/div, flow direction from top to bottom scaled as 1:1

In a case of the non-conductive cylinder the most informative measurement is the Faraday voltage induced between two belt electrodes of the cylinder. This parameter is also well correlated with magnetic field that is illustrated in Fig.30.

One of the main efforts of experimental program was devoted to the fast visualization of the interaction zone behind the bow shock.

Three different techniques were used:

1. Streak photography with a photo-electronic multiplier
2. Fast camera visualization with analogous camera KC-2 providing visualization on the conventional photo film with the seed 5000f/s or 10000 f/s;
3. Fast digital camera visualization

As a rule only one technique of the fast visualization is used during particular run. The visualization of the MHD effect on the bow shock stand-off distance is provided with the streak photography technique. The luminosity from the narrow region of the flow

along the up-stream stagnation line is recorded with the high time resolution that characterizes the MHD interaction in the $x-t$ diagram. The streak photography is applied both for vertical and horizontal orientations. With the streak photography one of the most important features of the facility has been revealed – a rather strong interaction upstream of bow shock. This effect is discussed above. The example of correlation of the streak record and the Rogovsky' belt signal is presented in Fig.31.

The whole flow field visualization is applied to estimate the MHD interaction

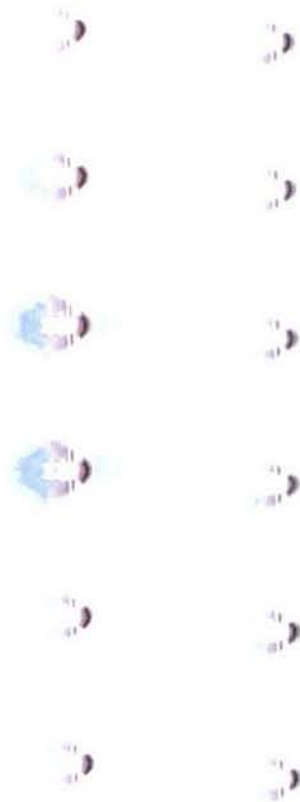


Fig.32. Fragmen of the film obtained with horizontal orientation. The flow is from the right to the left. The brighter frames of the left column correspond to the magnetic field pulse interval.



Fig.34. Imaging of the flow around cylinder with and without MHD interaction as recorded with Pulnix digital camera. The flow direction is from the right to the left.

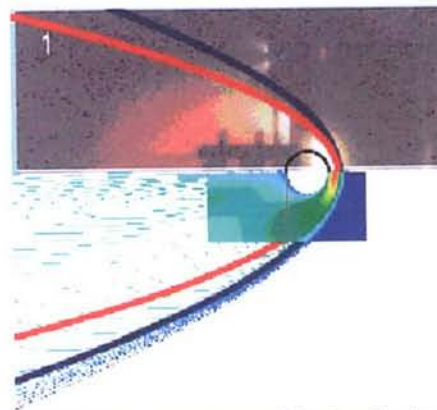


Fig.33. The comparison of the visualization of the flow during MHD interaction (upper) with 2D calculated temperature distribution and Billig' correlation (1 - $M=15$ and 2 - $M=10$).

effects on the structure of the flow field. . The model orientation is chosen for each particular run depending on the task. Three different orientations were typically used: vertical, horizontal and slanted. For two first orientations the flow direction is perpendicular to the cylinder axis. The difference is only the visualization direction – for the vertical orientation the optical axis crosses the bow shock area from the side view of the cylinder; for the horizontal orientation the imaging of

the interaction area summarizes the luminosity along the whole length of the cylinder. The sloped orientation corresponds to $\sim 40^\circ$ angle of attack of the cylinder axis. The visualization conditions are similar to those of the vertical orientation case.

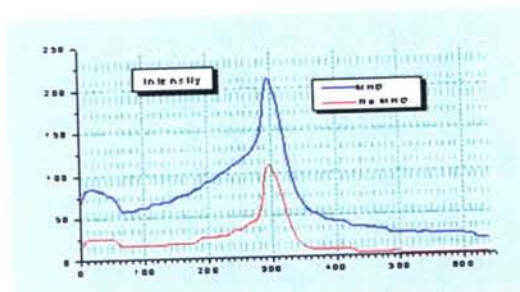


Fig.35. Intensity distribution along the flow direction for non-MHD (lower) and MHD (upper) cases. The maximum intensity is located up-stream of the leading edge of the cylinder. The leading and tailoring edges locations can be recognized from well visible curve broken.

In Fig.32 the horizontal visualization is exemplified. The visualization was carried out with the speed camera KC-3 utilizing a Kodak colour film of 400 sensitivity units at 5000f/sec speed. The exposure time is several microseconds. The single shot of the camera provides approximately 100 frames arranged in two columns. Unfortunately the optical conditions are different for each column and for this reason cannot be combined in a single consequence of the images. This also results in the limiting number of frames directly related to the magnetic pulse interval – typically, three-four frames from each column can be attributed to the interaction process. The film was developed in the standard way with the following digitising by a scanner with 600ppi resolution. Due to the configuration limitation the film imaging is approximately 1/22 scaled to the original model size. In Fig.33 the correlation of the visualization and calculation is shown. The fast digital camera Pulnix was also used for flow visualization with vertical orientation of the model. This camera has a rather low speed (~ 250 f/s) but can be synchronized very precise that provides at least one frame in desirable moment. In Fig.34 the comparison of the flow luminosity with and without magnetic field is presented. The flow is from the right to the left. The cylinder edges are clearly seen. The digitised intensity distribution along the flow direction is plotted in Fig.35.

Simulation and Analysis

As it was mentioned above the experimental data analysis is performed with a wide utilization of the numerical simulation. The numerical model used in this analysis is based on the full 2D time-dependent Navier-Stocks equations coupled with 2D electrodynamics equation in the low magnetic Reynolds number approximation and, optionally, with the finite rate chemical kinetics for standard reduced air kinetics scheme including up to 11 species and 80 chemical reactions. The effects of the NaK seed are described

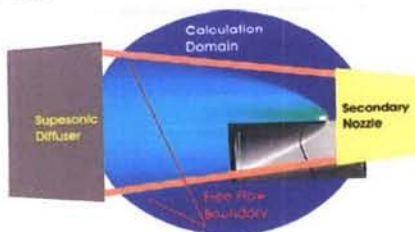


Fig. 36. The calculation domain used in the recent simulations.

in several different models revealing not important deference. The detailed description of the model can be found in our previous publications. The recent modification is a remarkable extension of the calculation domain. It was motivated by preceding analysis shown us the potential importance, of first – the MHD interaction in down stream area (wake interaction) and, second, by the intention to check the effect of electrodynamics boundary conditions. The newly constructed calculation domain covers now practically whole flow area inside of the test section. The grid consists of 120×181 -mesh points with the finest resolution used for close-up region of the cylinder surface. Inspite the symmetrical nature of the phenomena in the frame of the applied approximation the whole area was considered to suppress randomly appeared numerical instabilities at the symmetry line while it was used as a boundary. The structure of the calculation domain is schematically presented in Fig.36 along with indication of the main hardware elements of the facility potentially affecting the flow field in the test section. In the lower right part of the picture the fragment of the flow visualization (b&w background) is introduced to specify the free flow configuration in the experiments.

The extended calculation domain reveals a significant advantage in specifying the outlet boundary conditions. Indeed during the MHD interaction a rather large region of subsonic flow could form. Typically used supersonic conditions are no longer valid when subsonic sub-region reaches the outlet border.

All numerical results discussed in this paper are obtained with the simplified version of the model not including the chemical finite rate kinetic. Such a simplification influences, of course, in some cases on the quantitative results, but still provides the qualitative physically correct description of the processes with significantly lower computational resources.

Wake effects

The Fig.33 shows from the other hand that the downstream effects are much more resolvable. The angle of the downstream part of the bow shock is clearly changed



Fig. 37. The experimental arrangement for wake interaction study.



Fig.38. The visualization (b&w) and computation (colored) comparison of the wake area flow field under MHD-off and MHD-on conditions.

during MHD interaction, and the luminosity distribution in the close wake area is changed remarkably too. In order to prove this conclusion the special configuration of the model support was developed recently to free wake area for visualization (see Fig.37, where the flow direction is from the right to the left).

The comparison of MHD-off and MHD-on cases both for the experiment and simulation are presented in Fig.38.

The experiment confirms the strong temperature elevation in the near cylinder wake, which was predicted numerically. At the same time it is clearly seen that simulation gives the wider bow shock shape in the upstream portion. Note, that simulation predicts also the weak but still resolvable bow shock stand-off distance increasing. The satisfactory correlation of the experimental and calculated the modification of the shock shape of its downstream part confirms implicitly the adequate inlet boundary conditions used in this simulation. Let us consider the inlet boundary conditions effects in more details.

Inlet boundary conditions effects

One of the most important features of the MHD WT facility used in this experimental study is the MHD accelerator that provides the elevation of stagnation pressure of the airflow after the arc heater. Namely MHD accelerator defines the unique characteristics of this WT for hypervelocity steady-state experiments. From the other hand airflow in the test section after fast expansion in the secondary nozzle seems to be very non-equilibrium, the vibrational temperature and dissociation degree of two-atomic molecules, first of all - oxygen, both correspond more likely to the temperature at the MHD accelerator exit rather than to the in-test section temperature. This results in the higher than equilibrium electron temperature and, consequently, in high ionization degree of NaK seed used to provide acceptable electrical conductivity in the MHD channel. Thus, the oncoming airflow in the test section is well electrically conductive. Consequently, the MHD interaction can take place anywhere while the local magnetic induction is high enough. The fact of the intensive MHD interaction is experimentally confirmed by the streak photography (see Fig.29) clearly demonstrated the strong increase of the flow luminosity from the flow far upstream of the cylinder leading edge with no visible displacement of the bow shock. This effect was detailed investigated and described in our earlier publications [14-16]. It was recognized recently, however, that the upstream interaction reveals another important mechanism of losses – the overall shorting of the Hall field. Such a shorting occurs in MHD devices with poor insulation of the flow train from the ground.

Bow Shock

The correlation of the bow shock shape and location as from the flow visualization results, numerical simulation and the Billig' formula is presented in Fig.33. The curve 1 of Billig' correlation formula corresponds to Mach 15, and the curve 2 – to Mach 10. The space resolution of the flow visualization (the brightest frame from the series of Fig.32) is not good enough that probable leads to uncertainties in the localization of the experimental bow shock: the upstream part corresponds more likely to the lower Mach number but the downstream part is closer to the high Mach number case. One could also conclude that the perfect gas model used in this simulation is not fully adequate to the physical situation. It was also confirmed in our calculation including the finite rate kinetics. The important result is also that it is hardly possible to derive the bow shock displacement and/or deformation caused by MHD interaction near the stagnation point from flow visualization in this experiment. It should be noted also that the Billig's correlation is hardly valid for $M > 10$ flows.

Hall Field shorting

The Hall component of electric field is originated from the tensor nature of the electrical conductivity of plasma in the presence of magnetic field. The generalized Ohm's law with neglecting of the typically small so-called ion slip effect is as

$$\mathbf{j} + \beta[\mathbf{j}\mathbf{B}] = \sigma(\mathbf{E} + [\mathbf{u}\mathbf{B}]), \quad (1)$$

where σ and β stand for scalar electrical conductivity and Hall parameter, correspondingly. The Hall parameter $\beta = \omega_e \tau_e$ with ω_e is the cyclotron frequency and τ_e is the free path time of electron. The simplified relation between these important values is

$$\sigma = n_e e \mu_e = n_e e \beta / B, \text{ with } B = |\mathbf{B}|. \quad (2)$$

It is convenient for this analysis to define the local frame reference $\{\mathbf{e}_1, \mathbf{e}_2, \mathbf{e}_3\}$ in respect to the magnetic induction vector \mathbf{B} as $(\mathbf{B}\mathbf{e}_1) = B$, $(\mathbf{B}\mathbf{e}_2) = (\mathbf{B}\mathbf{e}_3) = 0$. Furthermore, let us decompose the flow velocity vector as

$$\mathbf{u} = \mathbf{u}_\perp + \mathbf{u}_\parallel, \quad \text{where } (\mathbf{e}_1 \mathbf{u}_\perp) = 0.$$

By choice of \mathbf{e}_2 and \mathbf{e}_3 to provide $(\mathbf{e}_3 \mathbf{u}_\perp) = 0$, the generalized Ohm's law can be rewritten in the form

$$\begin{aligned} j_1 &= \sigma E_1, \\ j_2 &= \sigma E_2 - \beta j_3, \\ j_3 &= \sigma (E_3 - uB) + \beta j_2. \end{aligned} \quad (3)$$

In resolved form this gives

$$\begin{aligned} j_B &= \sigma E_B, \\ j_H &= \sigma E_H - \beta j_F, \\ j_F &= \sigma / (1 + \beta^2) (E_F - uB + \beta E_H), \end{aligned} \quad (4)$$

where the new indexes B, H , and F denote now B field direction, Hall field directions, and Faraday field directions, correspondingly, and $u = |\mathbf{u}_\perp|$. With no Hall component of current density ($j_H = 0$) the Hall field is defined by Faraday component of current density

$$E_H^{ideal} = \beta j_F / \sigma. \quad (5)$$

It can be easily found that the Hall field is always opposite to flow direction (in the plane normal to the B -field vector) and naturally scaled with the 'ideal' value $E_H^{sc} = -\beta uB$, which can be attributed to the value of E_H^{ideal} at the Faraday short circuit condition ($E_F = 0$). Substituting the ideal Hall field (5) into (4.3) one can obtain

$$j_F^{ideal} = \sigma (E_F - uB), \quad (6)$$

that reveals no Hall effect appearance. From the other hand the case of total Hall field shorting reads

$$j_F^{shorted} = \sigma / (1 + \beta^2) (E_F - uB), \quad (6)$$

which is $(1 + \beta^2)$ -times less as compared with ideal value. For $\beta \gg 1$ typical of the conditions considered here the reduction of the primary importance value – Faraday component current density can be dramatically high. This is why the main rule for any MHD based application is to keep the Hall field value as close as possible to its ideal level. The general way to provide such conditions is to prevent the Hall current leakage.

At the facility used in this experimental studies the upstream and downstream hardware components of the flow train seem to be grounded. At least no Hall voltage was measured between the MHD accelerator entrance and the test section. At the same time it was definitely confirmed a rather high insulation between the model (when made of copper) and the test section wall. Thus, the model environment can be grounded only through the oncoming flow while the working media in the secondary nozzle and behind the model location near the diffuser is electrically conducting. In order to check this assumption the series of calculation of the MHD interaction was undertaken. The variable parameters of this series are the ionization degree of the oncoming flow and the inlet boundary conditions. The electrodynamics boundary conditions at the outlet of the calculation domain specify for all cases the grounded electrical potential value: $\varphi_{out} = 0$.

The stagnation line potential distributions for several cases are presented in Fig.39. In cases 1 and 2 the inlet boundary conditions are $j_n = 0$, and potential grounded conditions $\varphi_{in} = 0$ for cases 3 through 5. The experimental values of the cylinder potential are localized in the dashed area in the Fig.37. These results demonstrate clearly, first, the importance of the inlet boundary conditions as it follows from comparison of curves 1 and 3 as well as curves 2 and 4. For each pair the oncoming flow conductivity is the same. Note that the ionization degree value equal to .01 corresponds to full ionization of seed, and it is most likely maximal available ionization degree under conditions considered here. The second conclusion can be derived from the comparison of calculation and experimental results is that the only non-equilibrium conductivity ahead of the bow shock is not enough to explain the

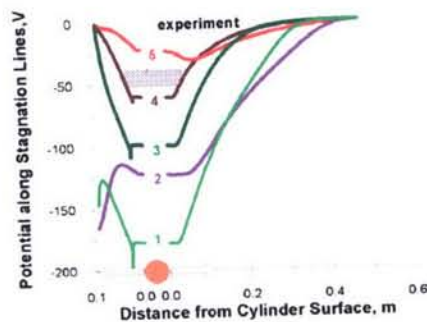


Fig.39. The stagnation line electrical potential distribution for different ionization degrees in oncoming flow.

1 - 10^{-4} ; 2 - 10^{-2} ; 3 - 10^{-4} ; 4 - $5 \cdot 10^{-3}$; 5 - 10^{-2} .

experimental values of the cylinder potential. The satisfactory agreement can be reached if the inlet grounded condition is implemented.

Thus, it can be concluded that the inlet and outlet flow in the test section are effectively grounded, and, secondly, the conductivity of the oncoming flow is non-equilibrium corresponding to ionization degree 70 to 80 percent of seed. The latter agrees with the electron concentration measured by the microwave adsorption technique at the earlier stages of the MHD WT facility utilization for hypervelocity

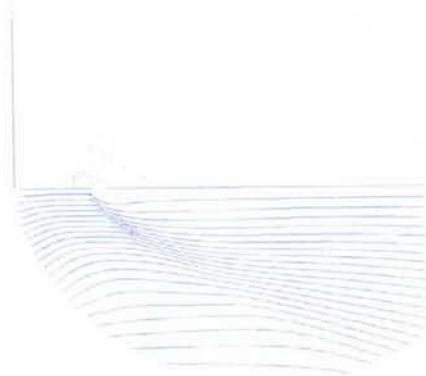


Fig.40. The electrical current stream lines are as for non-shorted (red, upper half) and shorted (blue, bottom half) conditions.

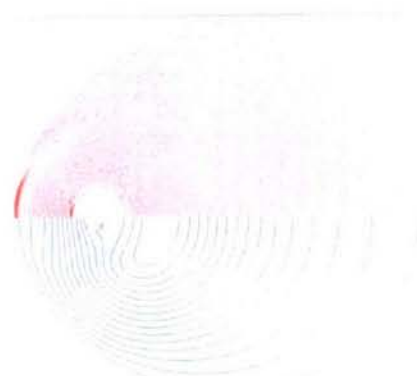


Fig.41. The equipotential lines are as for non-shorted (red, upper half) and shorted (blue, bottom half) conditions.

experiments [37].

To illustrate the difference between shorted and non-shorted conditions the current streamlines are shown in Fig.40. The upper half corresponds to non-shorted conditions (case 1 from Fig.39), and the bottom half – to shorted ones (case 5 from Fig.39). The line intervals are the same for both cases. The equipotential lines structures for the same conditions are presented in Fig.41.

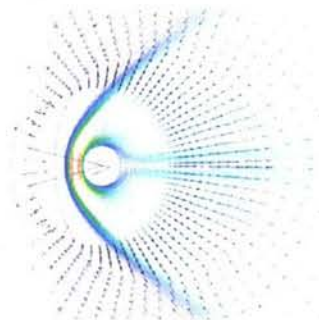


Fig.42. The planar component of the body force vector distribution in close-up cylinder area. The length of the vectors represents relative value of the physical quantity.

The non-shorted conditions cases demonstrate several features important for understanding of the phenomena studied. The current loops are localized behind the bow shock only. The intensity of the circulating current density is relatively low. (Note the current concentration at the upper boundary is caused by switching of boundary condition type from Neumann' ($j_n = 0$) to Dirichlet' ($\varphi = 0$) and have no physical sense for the experimental considered here.) Three main current loops are clearly

recognized: first localized in upstream of cylinder, the second - in near wake region, and the third located at the outlet part of the calculation domain and can be attributed to the particular boundary structure used in this simulation. In the opposite shorted conditions case the current streamlines pattern is totally different. The electrical current goes practically along the flow field streamlines that agrees well with the analysis of the preceding section.

As for potential distributions for two cases the clearly visible effect is that the totally shorted area is formed in close vicinity of the cylinder even for the non-shorter conditions case in spite the net Hall current is canceled by boundary conditions applied for this case. Thus, the Hall field shorting phenomenon reveals rather local nature. It will be discussed later in more detailed.

The current streamline pattern effectively visualizes the bow shock locations for both considered cases. As it can be seen from the Fig.38, for example, the predicted bow shock location for non-shorter case is shifted upstream for about two cylinder diameters as compared with still very little shock displacement for the shorter conditions case. It could be attributed to the different body force intensity (MHD interaction intensity, which is the main subject of this study) ahead of the cylinder leading edge. To check this hypothesis let us consider the body force vector distribution at the close-up region of the cylinder shown in Fig.42 for the shorter conditions case. Surprisingly, the body force vector is directed *downstream* but not upstream as it could be expected in upstream area of the cylinder from rough estimations. Furthermore, the intensity of the body force is negligible small as compared with the value typical of whole interaction area. The qualitatively similar situation occurs for the non-shorter conditions case. Thus, it would be hardly possible to motivate the difference in the bow shock locations by the different MHD interaction in upstream zone.

It is now the time to analyze the electrodynamics and gasdynamics fields' interaction in more detailed.

Gasdynamics and electrodynamics fields

The particular task for this section is to understand the main electrodynamics features found from experimental and calculation data comparison. The summary of the above comparison could be as following:

- The electrical current streamlines coincide generally with flow direction.
- The electrical potential is significantly non-monotonic along the flow direction approaching the minimum level at the cylinder locations.
- The equi-potential lines are similar to the cylinder surface in the vicinity of the cylinder.
- The body force vectors are mostly directed to the cylinder surface especially at the upstream portion of the near cylinder flowfield.

Basing on the analysis started above one can conclude that the configuration considered in this study can be treated as a Hall type MHD generator under nearly short circuit conditions. One of the general features of this configuration is that the Hall component of the electric field is directed opposite to the flow velocity. Considering for simplicity the short circuit condition for the 'Faraday' field component ($E_F = E_z = 0$) that is the practically important case of well conductive cylinder (metallic) material. (It was already mentioned above that the axial component of electric field is

practically very close to zero due to reversing sign of the induced e.m.f. $\mathbf{u} \times \mathbf{B}$ in upstream and downstream areas even in a case of insulator made cylinder). The main component of body force interested for this analysis is radial directed (in the cylinder center reference frame)

$$f_r = (\mathbf{j} \times \mathbf{B})_r = -j_z B_\theta \quad (7)$$

For the assumed conditions one can derive from the Ohm's law

$$j_z = \sigma u_r B_\theta - \omega_e \tau_e j_r = (n_e e u_r - j_r) \omega_e \tau_e, \quad (8)$$

where $j_{conv} = n_e e u_r$ can be called as a *convective current*. The radial current for the case $E_r = 0$ (the local short circuit condition) is

$$j_r(E_r = 0) = \sigma \omega_e \tau_e u_r B_\theta / (1 + \omega_e \tau_e^2) \sim j_{conv} \quad (9)$$

when $\omega_e \tau_e \gg 1$.

The radial current can be also presented in the form

$$j_r = j_{conv} (1 - E_r / E_r^*), \quad (10)$$

where

$$E_r^* = -\omega_e \tau_e u_r B_\theta \quad (11)$$

resulting in

$$j_z \sim \omega_e \tau_e j_{conv} E_r / E_r^*. \quad (12)$$

Thus, the radial body force is defined as

$$f_r = -j_z B_\theta \sim -j_{conv} B_\theta \omega_e \tau_e E_r / E_r^* \\ = -j_{conv} B_\theta^2 \mu_e k_H \quad (13)$$

that reveals the governing role of the 'a local Hall load factor' $k_H = E_r / E_r^*$.

It is useful here to introduce the power extraction/release associated with Hall component of electrical field

$$q_r = j_r E_r \sim -j_{conv} u_r B_\theta \omega_e \tau_e (1 - k_H) k_H. \quad (14)$$

The sign of the right hand expression is defined only by the Hall load factor k_H , because of $(j_{conv} u_r B_\theta)$ is always non-negative being proportional to $(u_r B_\theta)^2$. The power generation mode (power extraction) corresponds to condition $0 < k_H < 1$; the conditions $k_H < 0$ and $k_H > 1$ define the power release mode.

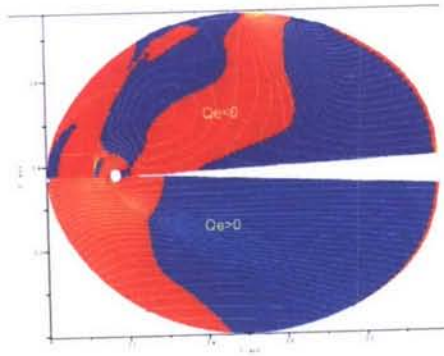


Fig.43. The electrical power released (red) and extracted (blue) from the flow for two cases: the upper – non-shortcd conditions, the bottom – shortcd conditions.

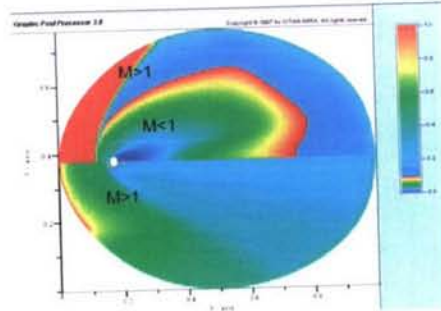


Fig.44. Comparison of the Mach number distribution in two cases. The upper half represents the non-shortcd conditions case, the bottom half – the shortcd conditions case.

The difference of these two cases becomes clear from comparison of body force direction. The sign of the scalar product $(f, u_r) \sim -j_{conv} u_r B_\theta^2 \mu_e k_H$ is defined by the sign of k_H . Thus, when the Hall load factor is negative $k_H < 0$ then both $q_r > 0$ and $(f, u_r) > 0$ that corresponds to the MHD acceleration mode (body force acts along the flow velocity). When, in turn, the Hall load factor k_H is greater than one ($k_H > 1$) then $q_r > 0$ (power release mode) and $(f, u_r) < 0$ (body force acts against the flow velocity).

That corresponds to the MHD brake mode.

Typically of the operation conditions of the circular cylinder in a transverse hypersonic flow the MHD interaction reveals all of three modes simultaneously. The dominating direction of the electrical streamlines is defined by the closed circuit condition of the 'effective Hall MHD generator'. Generally speaking the induced total voltage of such a generator is positive in respect to flow direction through generation region and, correspondingly, the induced total current is also positive (i.e. the electrical current goes in downstream direction). This feature leads to the non-monotonic character of the potential distribution with a rather deep minimum (see Fig.39) that is defined by the fact that the downstream portion of the 'Hall generator' is significantly more powerful than the upstream one. So, the downstream generator works against the upstream as a load that resulting in reverse electrical field sign there. And the latter is a key issue to understand why the body force vectors are in opposite direction to be expected one.

In terms of expressions (13) and (14) the local Hall load factor k_H becomes negative in the upstream region that resulting in the MHD accelerating mode: both power and momentum are released in the flowfield. In the upper vicinity of the cylinder where the body force is also mostly directed to the cylinder surface the MHD generation mode takes place because the radial component of flow velocity has changed its sign. The power is extracted from the flow and the flow decelerated by the body force.

The distribution of the power released/extracted from the flow for two cases (shorted and non-shortcd conditions) is presented in Fig.43.

In the shortcd conditions case the only downstream area works as an MHD generator extracting the power from the flow. This power is released in upstream area in two modes: MHD brake (mostly in wake area behind the cylinder) and MHD

accelerator in ahead of the cylinder. In the case of non-shortcd Hall field (the upper half of the distribution in Fig.43) the strong MHD generating zone is formed along the bow shock. These distributions agree well with the estimations given above in this subsection.

The structures of the flow field and electrodynamics field are strongly interconnected; therefore the flow field for two different cases considered here are to be different as well. This obvious suggestion is proved by Mach number distributions for corresponding conditions presented in Fig.44.

For clarity the subsonic area is leveled separately. Besides of general difference of flow fields of two cases related to the strong difference of the bow shock locations, an important feature of the non-shortcd case is that the extended subsonic zone is formed around the cylinder especially in the wake area. The reason of the formation of such a subsonic zone in the wake can be found in the MHD break mode occurring here. Indeed, the MHD body force is directed counter flow, the high temperature defines a low density, and the flow velocity is originally low due to the friction at the cylinder surface, all of these results in the relatively high MHD interaction parameter for wake region. Thus, it is the most likely that the wake interaction resulting in the significant extension of low velocity region is responsible for the bow shock upstream displacement. The bow shock location along with its shape corresponds for given oncoming flow parameters to an effective body of modified shape. In the shortcd conditions case this effect is much weaker pronounced because of the strong reduction of overall interaction. As it was indicated above (see Fig.38 and corresponding comments) the relatively high wake interaction was observed even in the experiment under conditions close to the totally shortcd Hall voltage.

Peak Heat Flux Reduction

The practical aspect important for potential applications of this study is to limit the peak heat flux at the leading edge of the body in hypersonic flows. Many optimistic predictions based on various numerical simulations of the MHD interaction at a blunt body in hypersonic flows have published recently [30-35]. The prediction of the heat

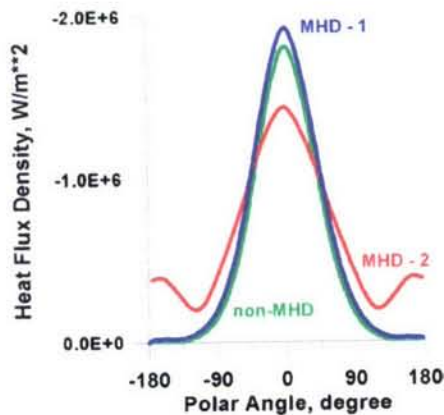


Fig.46. Heat Flux Density vs polar angle for three cases: non-MHD stands for reference case of a conventional flow; MHD-1 presents the result for the shortcd conditions case; and MHD-2 – for the non-shortcd conditions case.

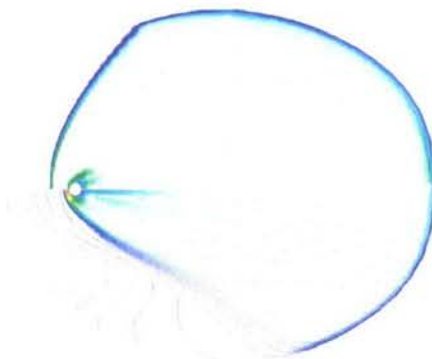


Fig.45. Temperature distributions for the conditions of Fig.28.

flux reduction by an order of magnitude was made in papers directly related to the experiment discussed here. From results of all cited above papers it be concluded definitely that under given flow conditions there is strong correlation between the peak heat flux density at the stagnation point and the bow shock stand-off distance. It is also in full agreement with the rules of classical hypersonic aerodynamics. After this short prelude looking at the flow field calculated for two cases often referred here (exampled in temperature distribution in Fig.45) one could expect a rather significant effect for the non-shortd conditions case and probably poor result for the shortd conditions case. The prove of such suggestion is given in Fig.46, where the distributions of the normal-to-wall heat flux density are plotted. The shortd conditions case with poor MHD interaction and a negligible bow shock displacement reveals as expected a rather low effect in the heat flux distribution. Even more, some increasing occurs near the stagnation point that could be attributed to the heat addition with the Joule heating taking place along the stagnation line. In turn, a significant (but not dramatic as it was in optimistic predictions) heat flux density reduction is found for the non-shortd conditions case. Some penalty of this 'positive' effect is the increasing of the heat flux density at downstream cylinder surface. And the total effect would be probably equalized. Nevertheless, the primary goal to reduce the peak heat fluxes seems to be available.

A notable comment on this result is that the downstream (wake) interaction provides the desirable effect at upstream part of the cylinder.

Conclusions

1. An MHD hypersonic flow at the dynamics pressure of tenths atmosphere over the circular cylinder with the azimuthal magnetic field was studied with three different numerical models.
2. The 2-D Navier-Stokes/MHD coupled perfect gas based models both neglecting and including Hall effect demonstrate dramatic influence of MHD interaction on hypervelocity flow around cylinder:
 - The significant shock front displacement and dispersion;
 - The significant relaxation of pressure distribution around cylinder;
 - The significant reduction in temperature around cylinder;
 - The dramatic reduction in heat flux.
 - On the other hand a significant total drag penalty accompanies interaction due to $j \times B$ body force.
 - The potential practical application to hypersonic flights is predicted for such a configuration.
3. The real gas based model including finite rate chemical kinetics of (seeded) air has changed the evaluation of the originally considered approach:
 - The natural ionization degree is rather low resulting in the dominating role of the Hall effect that reduces the effective MHD interaction by orders of magnitude;
 - The actual MHD interaction parameter reveals no dependence of magnetic field magnitude since the Hall parameter square becomes much higher of 1;

- Under low-pressure conditions the characteristic size of the MHD interaction area is to be 1m or larger and the required ionization degree is to be higher than 1%. The latter seems to be very problematic for real flight conditions even with external ionization because of energy consumption;
- To block the negative influence of the Hall effect on the MHD interaction effectiveness new revolutionary conceptual configurations of MHD on-board systems are required.

3. EXPERIMENTS WITH A WEDGE

Model II Design and Fabrication

The Model II is a wedge with a magnetic system providing the magnetic field around the model in such a way that there is an angle between mainstream velocity and magnetic induction vector. The similar approach is used to create appropriate magnetic field in the experiments. The basic idea is illustrated in Fig.47. In this particular case the wedge is made of copper sheet shaped as a wedge with $\sim 10^\circ$ half angle at the edge.

The preliminary tests with this model have shown some disadvantages related to the rather strong deformation of the surface shape caused by internal strength during magnetic field pulse. For this reason several modifications of the model were designed and fabricated.



Figure 47. The wedge model with magnetic system

The ceramic model is made of the high temperature ceramics bricks as it can be seen from Fig.48.

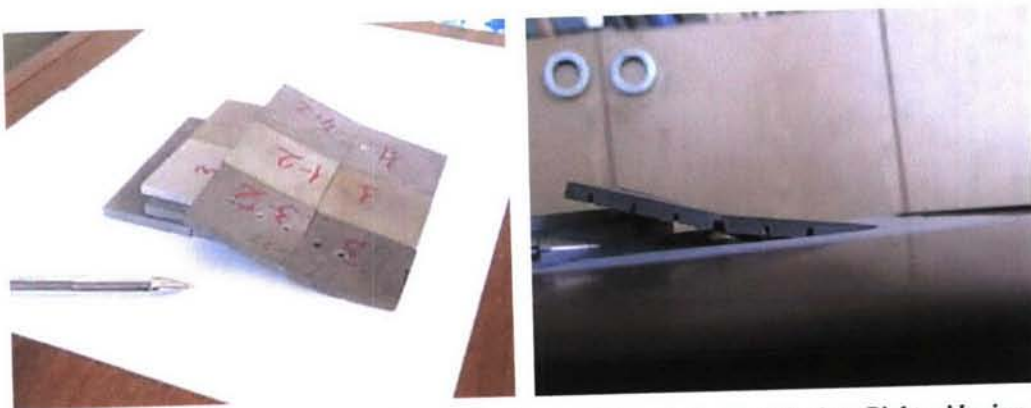


Figure 48. The ceramics wedge model during the assemblage. Left - Topside view; Right -side view.

The ceramics model is designed as a double-angle model with two steps by $\sim 10^\circ$. The grooves well visible at the side view photo are designed for the magnetiystem electrical leads locations.

The third modification tested is a model to simulate the hypersonic intake configuration. The corresponding photo is presented in Fig. 49.



Figure 49. The third modification of the wedge model on the holder before testing.

The test results are illustrated in Fig. 50. The filtered luminosity is roughly corresponding to the temperature field. The left picture represents the case with no magnetic field, the right picture represents the case of maximal magnetic field.

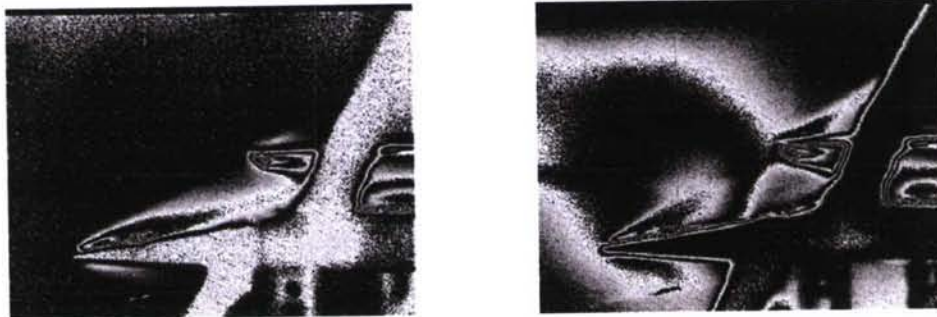


Figure 50. Experimental observation of the MHD interaction effects with a Cowl-Wedge model.

MHD Interaction over a wedge

The first impressions on the MHD flow over the wedge can be obtained from Fig. 51. These figures map the pressure fields for the two electrical conductivity models and for two distinct values of magnetic field intensity.

The first conductivity model assumes that gas is ionized everywhere with relative electron concentration as high as 0.01. The second model assumes that seeding atoms can be ionized only at high temperatures behind the oblique shock. As a measure of magnetic field intensity, the value of magnetic induction at the outer surface of magnetic system conductors is used.

The top pictures in Figure 51 correspond to a magnetic induction value of 1 Tesla and the bottom pictures correspond to 2 Tesla. (It should be mentioned that magnetic field in the domain is inversely proportional to the distance from the magnetic system. Therefore, the domain-averaged magnetic induction value is approximately one order of magnitude less than characteristic one.) The left row of

pictures correspond to the first conductivity model while the right rows correspond to the second one. The black-colored lines on the pictures show the location of shock for undisturbed flow field (no MHD).

The main feature of these distributions is that MHD interaction takes place for both conductivity models. The oblique shock deviates from the wedge surface which is considered as the most prominent effect of MHD interaction on the flow. It is seen from Figure 51 that shock deviation increases with increasing the magnetic field level.

Experimental photographs with evidence of the presence /effects of MHD interaction on the flow over the wedge can be seen in Figure 52. The left photos represent the flow visualization made by 2000 fps camera. The right images of the same flow were obtained with spectral filtering. A filter with the wavelength 779 nm and the width 15 nm was used. The top photos correspond to the non-MHD case and bottom pictures correspond to the MHD-On case. The influence of MHD interaction can be detected both by increasing the luminosity and by increasing the angle of deviation of oblique shock from the wedge surface. The right bottom image shows that there is a disturbance of intensity in the region upstream the body leading edge. This is caused by the presence of MHD interaction in the oncoming flow specific for the first conductivity model.

The qualitative agreement of the experimental and computational flow fields can be seen by comparing photographs to calculations in Figure 52. The temperature field is shown corresponding to the calculations made with the two conductivity models and with characteristic magnetic induction value 2 Tesla.

The effect of conductivity model on the flow field is well seen. In general, stronger MHD interaction takes place in the case of second model. This displays in a

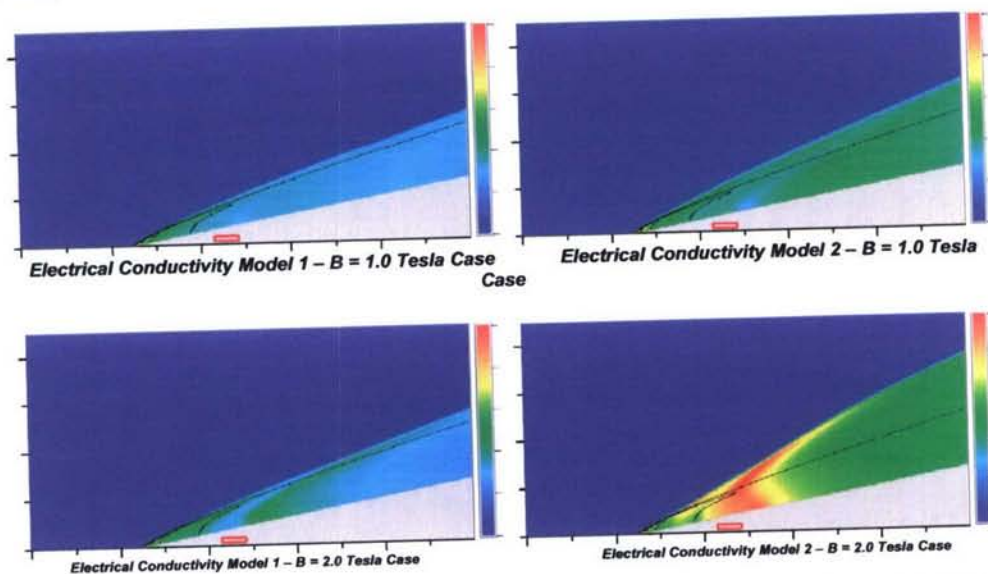


Figure 51. Representative Numerical Simulations of Ionized Air Flow Over a Wedge Surface With Varying Level of MHD Interaction

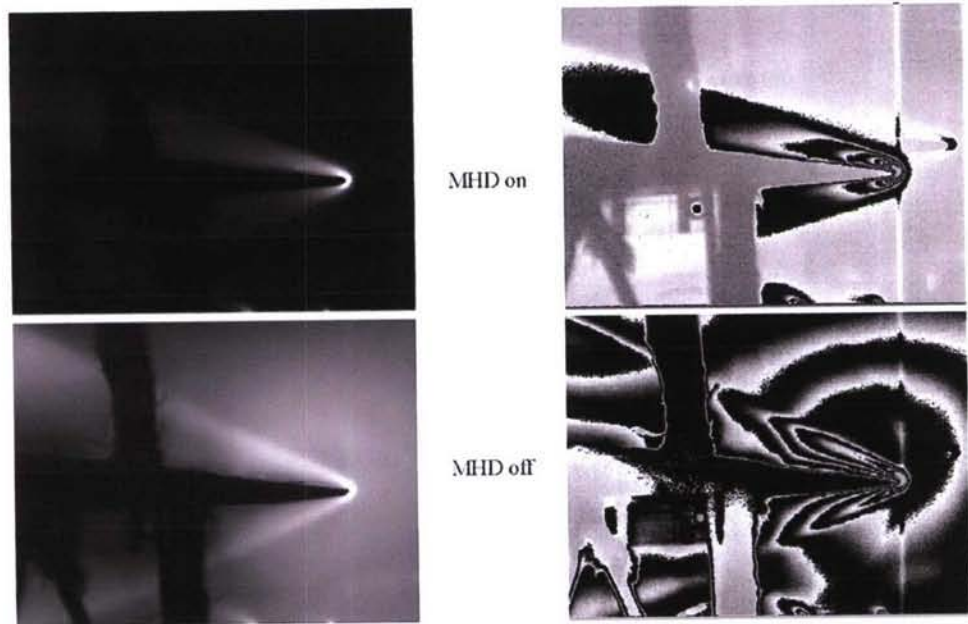
higher level of pressure and a larger deviation of shock from the wedge surface. The reasons for these distinctions were recognized in References 5-8 where experimental and theoretical study of flow around a circular cylinder was reported.

Negligible MHD effect was detected in the experiments and in the computations using the first conductivity model, whereas, visible MHD interaction

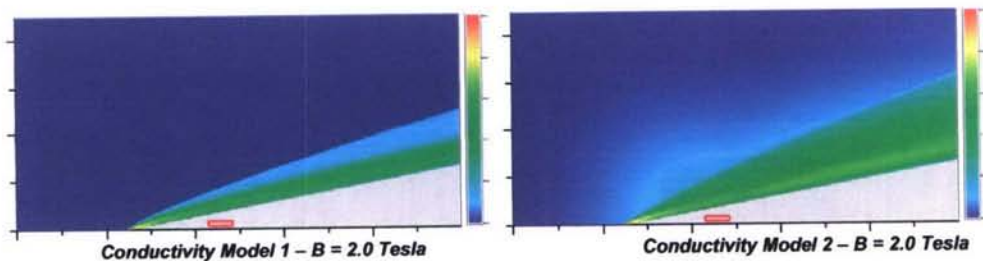
took place in computations with the second model. In addition, remarkable interaction in the wake was detected both experimentally and numerically.

It was determined in the previous work with the cylinder geometry, that the Hall effect is the primary influence on the flow structure. In the case of the first conductivity model, the fluid is conductive in the entire domain and since all the test cell elements are grounded, near zero electric field in the direction of main flow exists (i.e., short-circuit conditions). This results in a large current leakage in the flow direction (Hall current) and the force-generating Faraday current (perpendicular to the flow plane) is small. Whereas, the case of the second conductivity model, the situation is closer to open-circuit conditions, i.e. non-zero electric field along with the small Hall current. As a consequence, non-zero Faraday current prevails. It was also noted that there are several MHD operation modes within the flow field. For the shorted Hall electric field (experimental conditions), the region just upstream the cylinder is the MHD-acceleration zone, i.e., the electromagnetic force acts toward the body surface. At the same time the large region behind the cylinder was the

MHD power generation zone. The energy from MHD generation zone is transferred to the MHD acceleration and flow braking zones. The latter zone is located



Experimental Photographs of Wedge Model Test (Right Side Photo Images – Left Side Spectral Enhanced Images)



Representative Numerical Simulations of Temperature Field

Figure 52. Hypersonic Flow Over a Single Wedge – Experimental and Numerical Results

between the nozzle and the bow shock.

All these effects as derived from analysis of the cylinder studies also take place in the flow over the wedge. Figure 53 shows the distribution of flow directed component of electromagnetic force $[\mathbf{J} \times \mathbf{B}]_x$ (upper picture) and the distribution of energy source-term $(\mathbf{J} \cdot \mathbf{E})$. (On all pictures the blue color corresponds to negative values of the force and power rate, yellow-red color corresponds to positive values, and green denotes close-to-zero values.) These distributions were obtained for the characteristic magnetic field value 2 Tesla with the upper pair being for the first conductivity model (or Hall field shorted condition) and the lower pair being for the

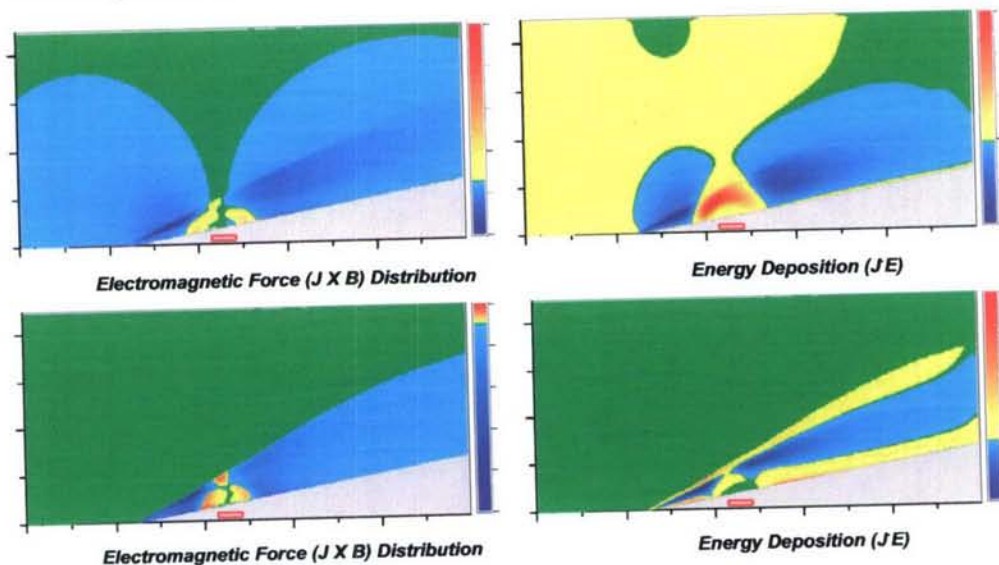


Figure 53. Numerical Simulations of MHD Interacting Flow Over a Wedge

second conductivity model (open-circuit Hall field).

Most of the oncoming flow experiences an the MHD brake force since energy is released and the flow decelerates. Two regions left and right of magnetic system operate as the MHD generator: energy is extracted and flow decelerates. The region just above the magnetic system operates as the MHD accelerator both power and force are positive. This structure is almost the same as was observed in the circular cylinder studies of previous works. In the wedge case both generation zones are placed near the surface. Unlike the cylinder, MHD-induced flow deformations occur in the region of flow to be modified. As a result noticeable changes in the flow field take place even in non-ideal, short-circuit case.

Two MHD generation zones left and right of the magnetic system are present in both cases calculated, as well as, the MHD acceleration zone between them. However, the intensities of interaction in the cases differ essentially as can be seen from reference values shown in Figures. The differences in MHD interaction intensity for two conductivity (or circuit) models lead to differences in flow structure.

For example, Figure 54 plots the flow streamlines and electromagnetic force field vectors for the 2.0 Tesla, second conductivity model (Hall field open-circuit) case. MHD-induced flow separation followed by a large vortex is observed. Whereas, no visible flow separation was revealed for the short-circuit conditions.

Now, let's consider several integral characteristics of the MHD flow. Table 1 presents three dimensionless quantities as functions of magnetic field obtained for the first conductivity model (short-circuit conditions). Here, B_0 denotes the characteristic

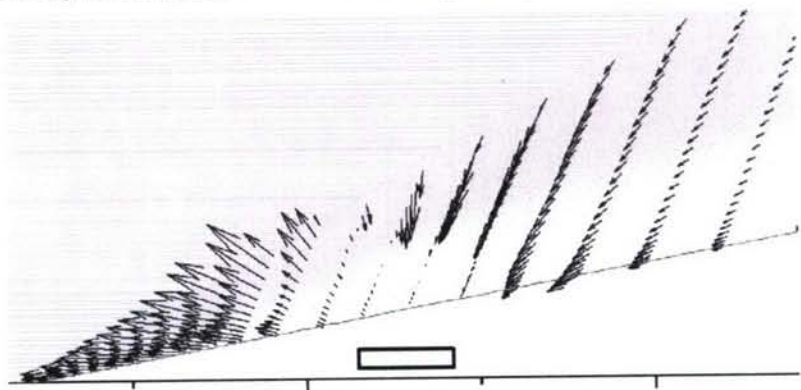


Figure 54. Numerical Simulations of MHD Interacting Flow Over a Wedge – Flow Streamlines and MHD Force Vectors

magnetic induction value at the surface of each conductor of magnetic system. $B_1 = \int B d\Omega / \int d\Omega$ is the volume-averaged magnetic induction value, S_1 is the MHD interaction factor specified for the locally open-circuit conditions (Hall current density equals to zero), S_3 is the MHD interaction factor calculated for the locally short-circuit conditions, (Hall field equals to zero), and S_2 corresponds to the MHD interaction factor based upon computed field of electromagnetic force.

Table 1. MHD interaction factor for the first conductivity model

B_0 , Tesla	B_1 , Tesla	S_1	S_2	S_3	I_z , Amps	I_x , Amps
0.25	0.017	0.0036	0.0017	0.0002	8	30
0.50	0.034	0.015	0.0057	0.0009	16	81
1.00	0.068	0.061	0.0205	0.0030	36	225
1.50	0.103	0.184	0.0434	0.0053	65	472
2.00	0.137	0.379	0.0670	0.0077	94	785
2.50	0.171	0.661	0.0880	0.0102	118	1112
3.00	0.206	1.033	0.1066	0.0128	137	1428

These quantities are defined as follows.

$$S_1 = F_1/F_0, S_2 = F_2/F_0, S_3 = F_3/F_0,$$

where forces F_1, F_2, F_3 and F_0 are calculated as

$$\begin{aligned} F_1 &= \int \sigma |\mathbf{V}| \cdot B^2 d\Omega, \\ F_3 &= \int \sigma (1 + \alpha^2) |\mathbf{V}| \cdot B^2 d\Omega, \\ F_2 &= \int |\mathbf{f}| d\Omega. \end{aligned} \tag{19}$$

$F_0 = Y*(P + \rho \cdot V^2)$ is the force (per unit depth) of total pressure in free-stream flow, and Y is the height of the computational domain. The parameter, S_1 , is analogous to commonly used evaluation of the MHD interaction factor, $S_0 = \sigma \cdot B^2 \cdot L \cdot \rho \cdot V$, obtained for no Hall effect flow.

Table 2 represents the same quantities calculated for the second conductivity model (open-circuit conditions). Also presented in Tables are the values of total Faraday current designated as I_z and total Hall current designated as I_x .

Table 2. MHD interaction factor for the second conductivity model

B_0 , Tesla	B_1 , Tesla	S_1	S_2	S_3	I_z , Amps	I_x , Amps
0.50	0.034	0.009	0.0044	$7 \cdot 10^{-5}$	18	0
1.00	0.068	0.043	0.0181	0.0003	49	0
1.50	0.103	0.112	0.0459	0.0012	111	0
2.00	0.137	0.216	0.1040	0.0033	264	0
2.50	0.171	0.379	0.1880	0.0045	463	0

The MHD interaction factors are plotted in Figure 54 as functions of magnetic field. Figure 54a corresponds to Table 1; Figure 54b corresponds to the Table 2. It should be noted that the MHD interaction factors evaluated at real flow properties are rather low, only at the highest value of the characteristic magnetic field 3 Tesla (which corresponds to the domain-averaged field of 0.2 Tesla) the MHD interaction factor S_1 is or order of unit for the first conductivity model. Nevertheless, the MHD interaction impacts on the flow structure. MHD interaction factor S_1 has larger values for the first model because of the larger conductive region. At the same time, real MHD interaction factor, S_2 , evaluated for the second model rises faster as the magnetic field increases and exceeds nearly two times that quantity for the first model at highest magnetic fields.

According to the analysis made in References 6, 7, and 8, the absence of total Hall current may restore the MHD interaction characterized to the ideal factor S_0 which is realized in non-magnetized fluid. In the case of second conductivity model, the total

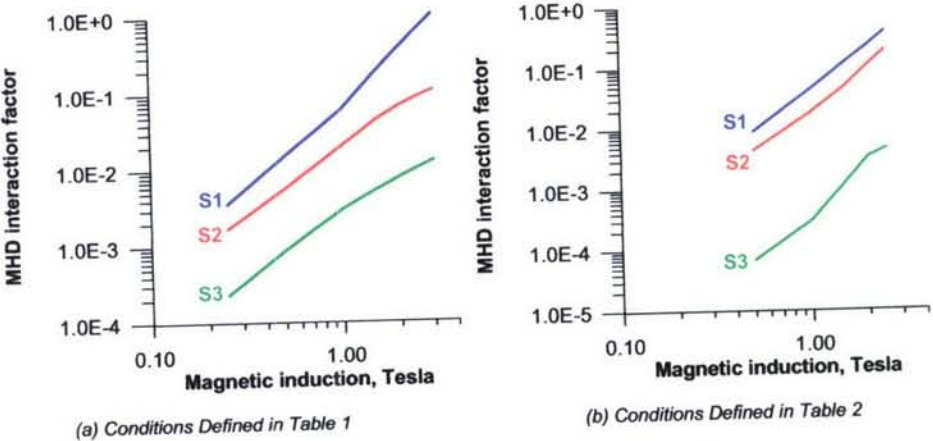


Figure 55. Variations in Characteristic MHD Interaction Parameters

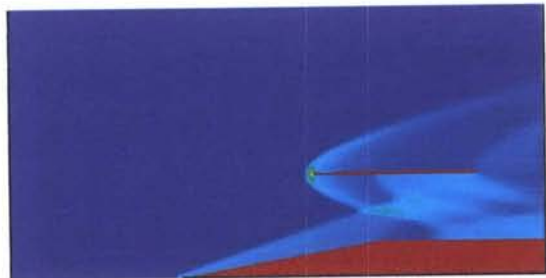
Hall current is close to zero because of the closed loop character of the current pattern. This circumstance reduces the nominal MHD interaction by a factor of two at higher characteristic values of magnetic field, but, not by an order of magnitude as seen in the

case of the first model. From one viewpoint, this is due to applied boundary conditions (zero electric potential). From another, these boundary conditions simulate the grounded conditions of bottom ends of the testbed. In the case of short-circuit conditions, a large Hall current (consequence of small amplitude of Hall electric field) results in a situation, when the integral interaction is characterized by the factor S_3 in

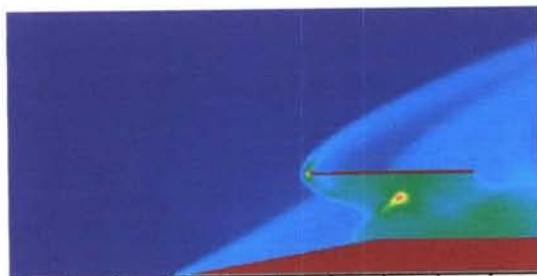
more extent than S_1 , i.e., the intensity of MHD interaction is significantly affected by a factor of $1/(1 + \beta_e^2)$.

This study revealed two important features of hypersonic MHD flow. First, even under not the best conditions realized in experimental facility the MHD interaction can significantly impact the flow structure, such that desirable flow properties can be achieved. This has been demonstrated both by experiments and numerical analyses. The unanticipated results obtained in the experimental study of flow around the cylinder was due to the fact that short-circuit conditions specific for the MHD WT facility which resulted little interaction in the region near the cylinder stagnation point which was considered as the region of primary interest. At the same time, significant MHD interaction was detected in the region far downstream the cylinder.

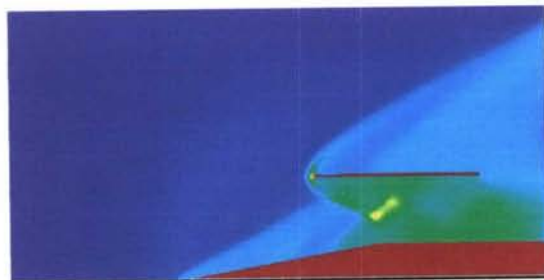
As far as the flow over a wedge is concerned the structure of electric fields is qualitatively



(a) Pressure Distribution with No Magnetic Field



(b) Pressure Distribution - Magnetic Field = 1.75 T



(c) Pressure Distribution - Magnetic Field = 2.5 T

Figure 56. Numerical Simulations for Wedge-Cowl Model - Variable Magnetic Field Intensity

same as in the case of the cylinder. However, the small interaction region located just above the magnetic system which is similar to the region just in front of the cylinder is in general surrounded by two regions where strong MHD interaction is observed. These strong interaction regions, similar to the downstream regions for the cylinder case, provide a positive effect on the flow structure over a wedge. Namely a significant change in the oblique shock angle as confirmed by both the experimental studies and computations.

Second, much stronger MHD interaction has been observed in the numerical simulations for the open-circuit conditions, i.e. for conditions close to those of real flight. In spite of the large values of Hall parameter inherent to the low-density flows, the configuration of electric fields is such that the undesirable Hall currents have a bounded influence on the MHD interaction intensity. This gives an opportunity for the

MHD flow control under real flight conditions and some predictions will be discussed later.

MHD interaction over a wedge with a cowl

Numerical and experimental study of MHD interaction over a single wedge of the previous sub-section showed that essential changes in the flow structure can be made even under the flow conditions of the real test section. Encouraging results from those studies motivated consideration of simulating the inlet of a hypersonic vehicle. In this effort, the same wedge with built-in magnetic system was used with the cowl plate positioned over the wedge.

Figure 56 demonstrates the pressure distributions obtained in the numerical simulations of the wedge-cowl configuration. Figure 56a shows the pressure field obtained without MHD interaction. The oncoming flow conditions correspond to test Run 138. The flow in the gap between the wedge and cowl represents an intersection of several oblique shocks due to geometry and viscous-inviscid interaction. Figure 56b represents the pressure field calculated for a characteristic magnetic induction value of 1.75 Tesla. As seen, the original oblique shock from the leading edge comes nearly to the cowl-lip. The pressure level in the gap is larger than in the MHD-off flow and a second shock appears near the mid-cross section of the gap. MHD interaction also results in a remarkable change in the geometry of the bow shock originating from the cowl-lip.

Further increase of magnetic field amplitude made small changes in the flow field structure, see Figure 56c. The second, MHD-induced oblique shock moved to the left from its 1.75 Tesla position and the angle of the cowl bow shock increased. This is in accordance with analysis made in Reference 7, where it was shown that at higher magnetic field values and under Hall field shorting conditions, the MHD interaction factor becomes independent on the magnetic field.

4. HYPERVELOCITY MHD WT EXPERIMENTS WITH A SURFACE MHD GENERATOR MODEL

Model Definition

To study MHD interaction in high-speed seeded air at Hypervelocity MHD Wind Tunnel Facility (HV MHD WT) the compact MHD generator the model of the same design as used at HFP WT was fabricated. The insignificant modifications were introduced into the model configuration in order to fit the test section requirements. This model shown in Fig.57 through Fig.60 comprises 13 pairs of stripped electrodes located at one of surface of the thick plate.

This surface is coated with the layer of thermal-protective ceramics. Within the



Fig.57. The model assembled.



Fig.59. The magnetic system coil.

plate body the oval-shaped magnetic system is mounted. The magnetic system represents the coil with 20 turns of copper wire of 2 mm diameter (Fig.58). Such a compact model has advantaged in that it can be positioned into the core of flow, and no flow halt takes place as was with the earlier models. These compact MHD generator

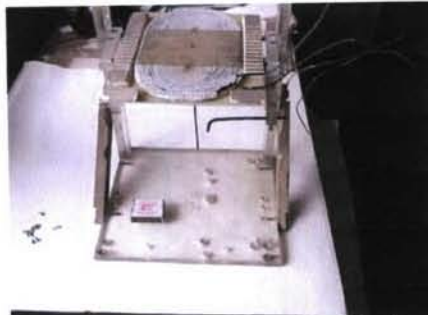


Fig.58. The model on the holder during assemblage.

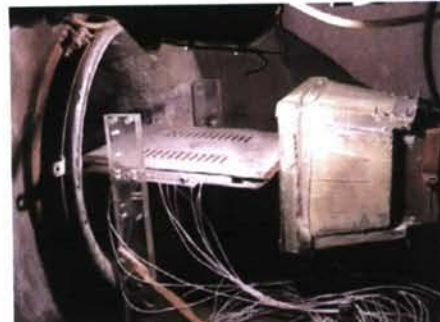


Fig.60. The model in the test section

models were used in both HV MHD WT Facility and in HFP WT Facility.

Six runs have been carried out at HV MHD WT Facility in which standard flow in test section has been performed. The MHD generator model described above was positioned in the core of the flow at angle-of-attack 2 grads just at the secondary nozzle exit (Fig.60). The maximum current in the magnetic coil was 8 kAmps that corresponds to the maximal magnetic field near the model surface about 2 Tesla.

Measurements

The electric characteristics were measured with 4-Channel digital oscillograph ACK-3107. This device is capable of measuring the input signals of frequency up to 100 MHz.

The schematic diagram of the measurements is shown in Fig.61.

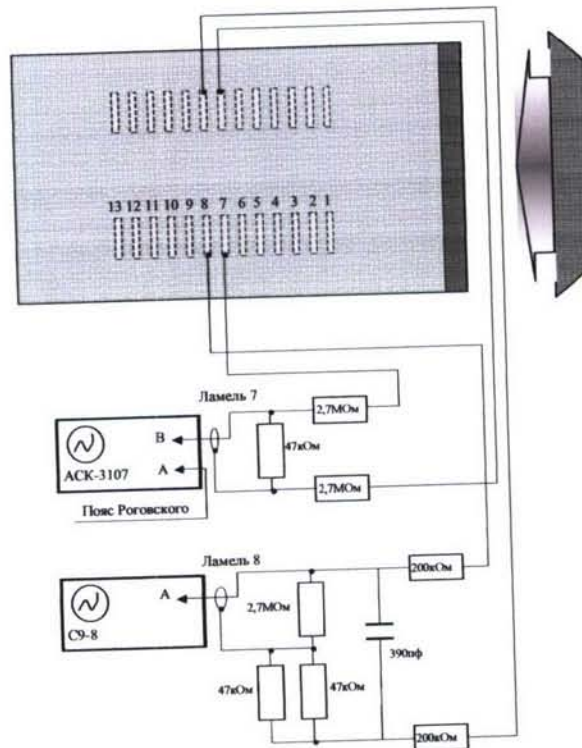


Fig.61. The schematic diagram of the electrical measurements.

Photography was made with the digital camera Image Citius C100.

The Faraday voltage has been measured between electrodes of first and seventh electrode pair. This voltage ranged in between 200 – 360 Volts in different runs and was found to correlate well with the current feeding the magnetic system. Fig.62 through Fig.64 represent the voltage and Rogovsky belt signal obtained in one of the runs as function of time.

The MHD interaction process has been recorded with the 2000 fps camera with applying the optical filter designed for atomic oxygen 777.2 nm spectral line. Typically five frames appeared to capture the MHD interaction time period.

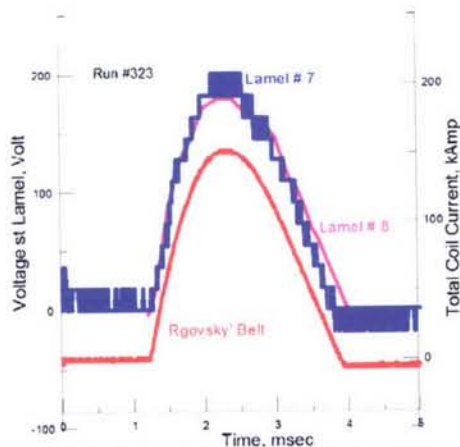


Fig.62. Potential variation in Run 323.

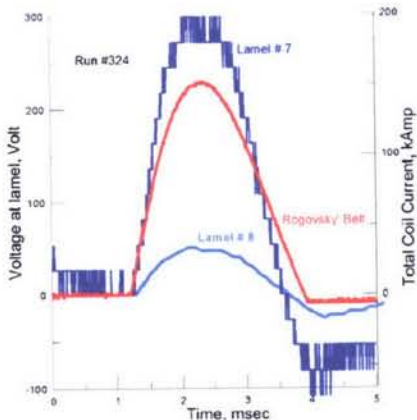


Fig.63. Potential variation in Run 324.

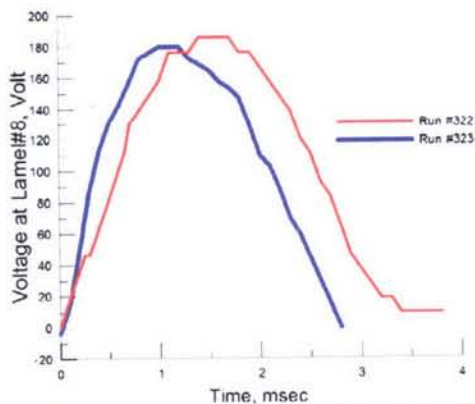


Fig.64. Comparison of the potential variations in Runs 322 and 323.

The comparison of the potential variation in two runs 322 and 323 could help in principle to evaluate the effective resistance of the near electrodes area. The potential curve recorded in Run 322 is shifted due to a capacitor introduced into measurement scheme. The interpretation of this effect is now in progress.

Visualization of the flow is presented in Fig.65. In the pictures the flow comes on the plate from right to left. The flow angle-of-attack is ~ 2.0 grad. Visualization reveals some new

features of MHD interaction in comparison with those found in the previous studies of

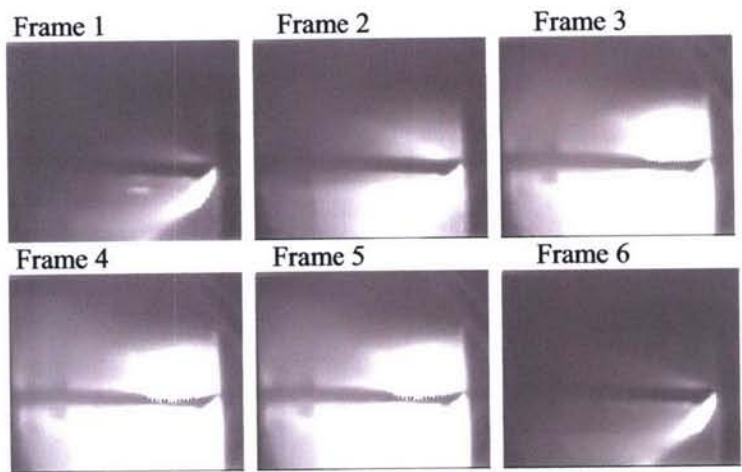
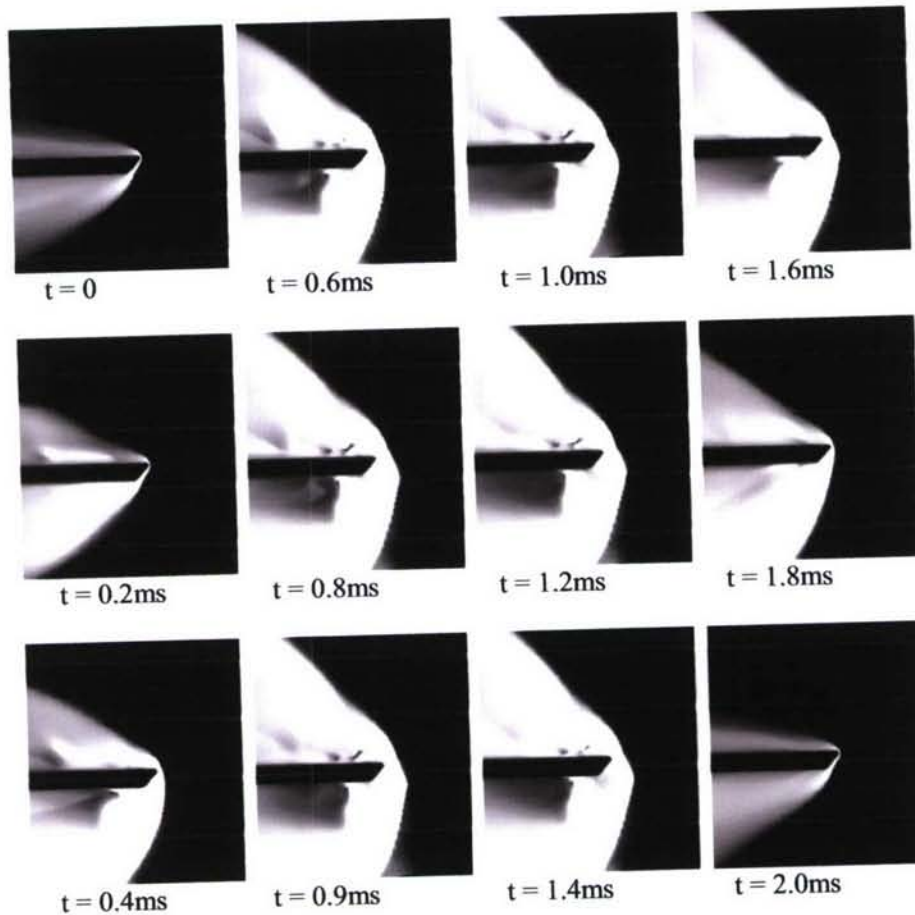


Fig.65. Visualization of flow around a thick plate; 2 ms magnetic field pulse; $B_{max} \sim 2$ T.

MHD flow over the wedges. Namely, more intensive interaction takes place below the opposite (bottom) side of the plate. This is probably due to skewed leading edge of the plate. The fact of MHD interaction around the plate, rather than other phenomena, detected with higher luminosity has been checked through the numerical simulations.



*Fig.66. Numerical simulation of flow around a thick plate.
2ms sinusoidal magnetic field pulse; $B_{max} = 2T$.*

Numerical Simulation

Numerical simulations of MHD flow around the plate have been carried out with the computational model proved to be adequate to simulate flow in HV MHD WT Facility. It is based on solution to Navier-Stokes equations for hypersonic flows coupled with solution to equations for quasi-steady electrodynamics field. There two key features taken into account in solving the electrodynamics equations, namely, the electric conductivity model and Hall effect. It was taken in simulations that electron concentration appears in high temperature region behind the bow shock at the leading edge of the plate, with maximum value of 1%. The electric conductivity and Hall parameter are then estimated with known electron-neutral and charged-particles collisions. The magnetic system used in computations exactly simulates the real one. 2 ms current pulse has generated sinusoidal magnetic field with maximum value of magnetic induction at the upper plate surface as large as 2 Tesla. The following gas dynamics parameters were specified as initial and inlet boundary conditions.

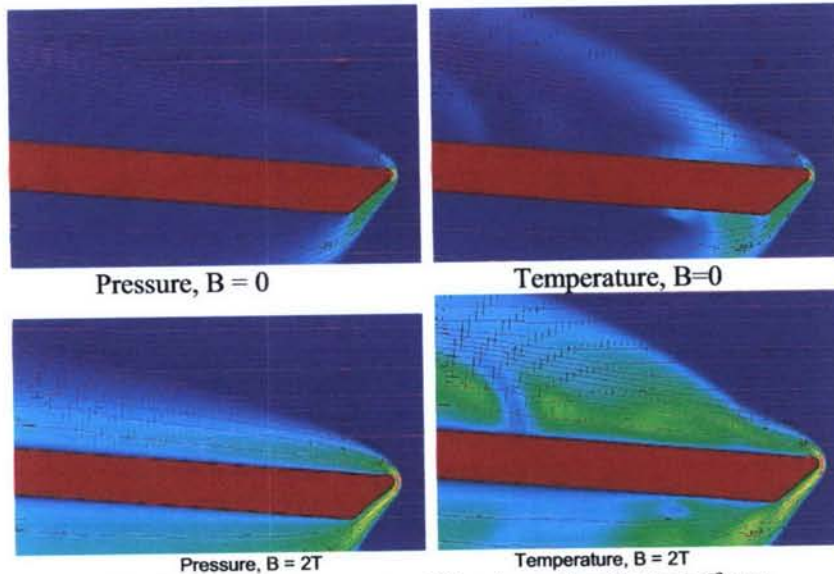


Fig.67. Pressure, temperature and flow stream lines for $AoA=5^\circ$ case

Fig.66 demonstrates the time-dependent evolution of MHD flow during the magnetic field pulse. In the pictures, the temperature field is shown. It is seen that in

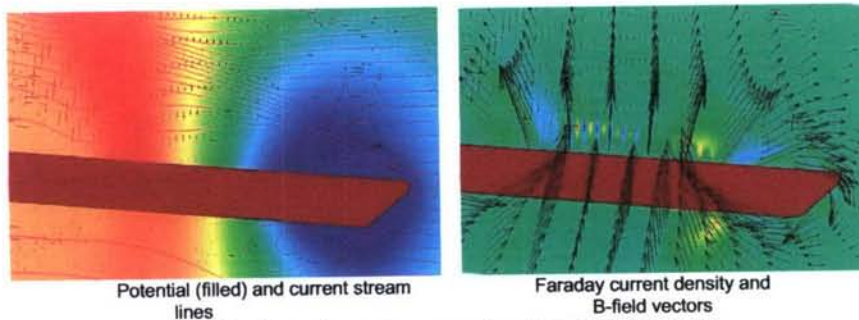


Fig.68. Electrodynamics parameters for the case $B = 2T$.

general evolution of temperature field agrees with experimental frames, i.e. high luminosity correlates with the temperature rise in the regions of interaction. In turn, dramatic changes in the temperature field are due to MHD interaction below and over the plate.

Gasdynamics and electrodynamic parameter distribution in the center plane in flow direction are presented in Fig.67 and Fig 68. for the case of $AoA = 5^\circ$.

The electrodynamic parameter distributions in the central cross flow plane are presented in Fig.69. The only small details are changed due to the dramatic loading conditions.

The most disappointed experimental fact at this stage is that there is no current measured even in the case of short circuit conditions. The preliminary explanation is that the contact resistance (at the flow-electrode interface) is too high and the induced voltage at the level of 300V is not enough to breakthrough this resistance.

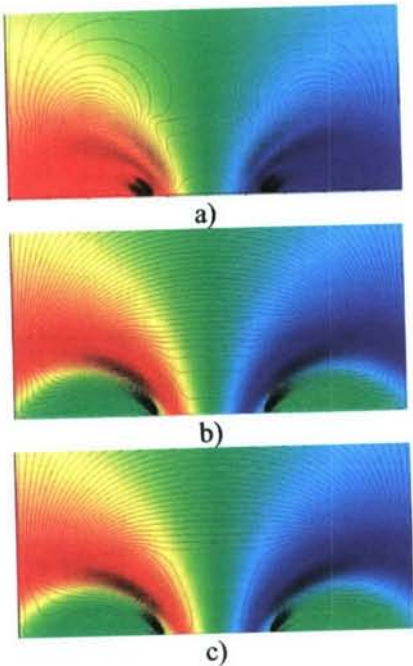


Fig.69. Potential and current streamlines in the cross flow plane.
a) Faraday open circuit, Hall short circuit;
b) Faraday short circuit, Hall open circuit;
c) Faraday short circuit, Hall short circuit.

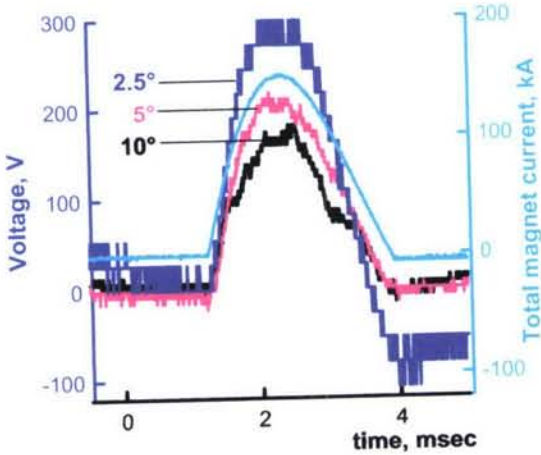


Fig.71. Faraday voltage at 7th electrode pair for three values of AoA (2.5°, 5°, and 10°)

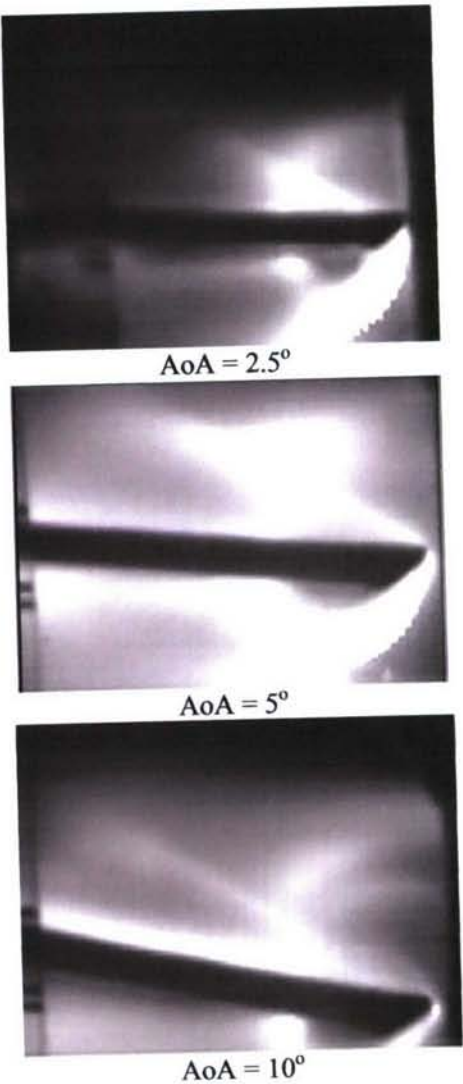


Fig.70. Visualization of the flow field for different Angle-of-attack at approximately maximal magnetic field strength.

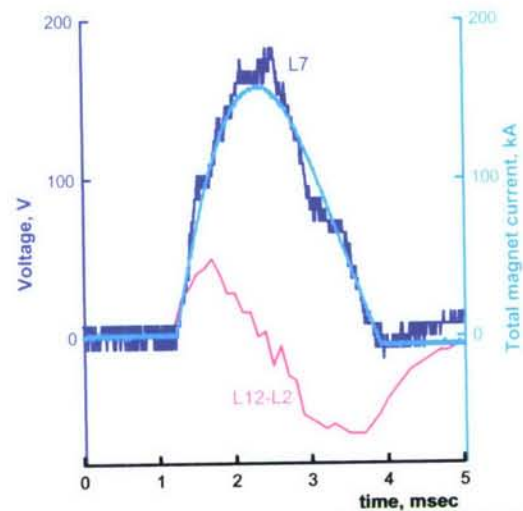


Fig.72. Faraday (blue curve) and Hall (pink curve) during the magnetic field pulse (light blue curve).

The measured Hall (longitudinal) voltage between 12th and 2nd electrode pairs is plotted in Figs.71,72. The behavior of the Hall voltage is not understandable and needs probably more deep 3D analysis.

Power Extraction Experiment with Pin Electrodes at HV MHD WT

The pin electrodes were installed at the HV Model 6 at the first electrode pair. The pin is a copper made cylinder of ~2 mm in diameter and ~20 mm length. The pin was screwed into the lamel normal to the working model surface as it is shown in Fig.73 through Fig.75. Two successful runs were performed with this configuration. The angle-of-attack was the same for both runs and equal to 10°.

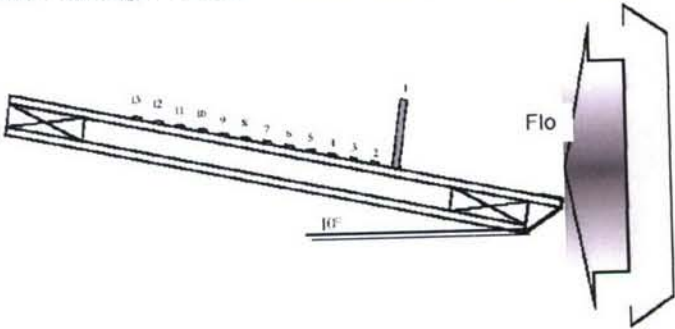


Figure 73. Positioning of the Model #6 with pin electrodes at Lamel 1 in the test section.

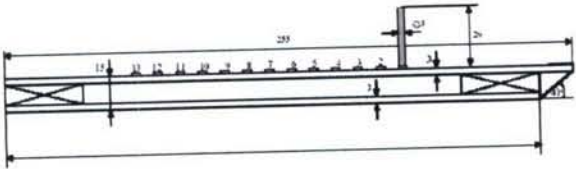


Figure 74. Side view of Model #6 with pin electrode at Lamel 1

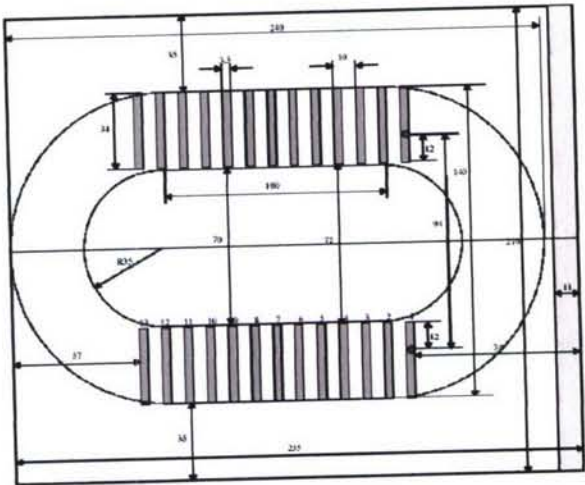


Figure 75. Model #6 with pin electrode at Lamel 1. Upper side view.

All operational parameters of the runs were also the same except the load resistance of the first electrode pair. In the first run of the series the load resistance was 1kOhm, and in the second run this value was 100 Ohms. Some parameters of the measurement scheme were also changed (see for details Fig.76 and Fig.78, correspondingly).

Besides of the electrical parameters measurements the now standard visualization with fast digital camera Citius was used.

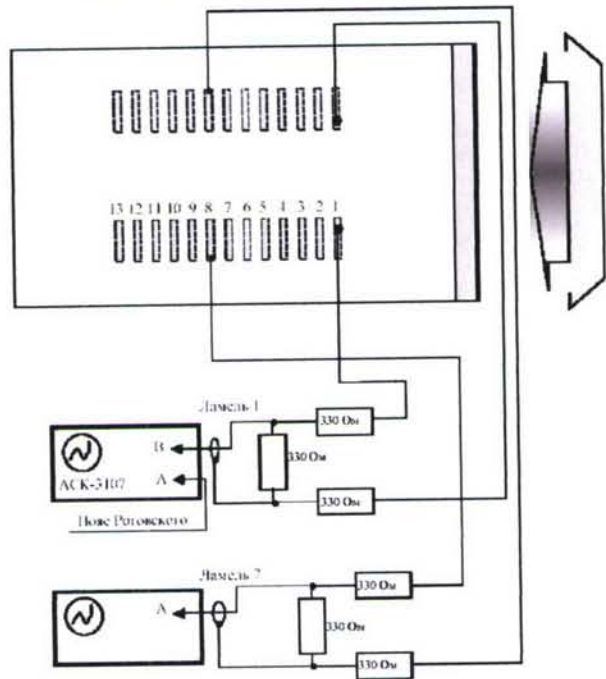


Figure 76. Schematic diagram of the potential measurement at Model #6 in run #331.

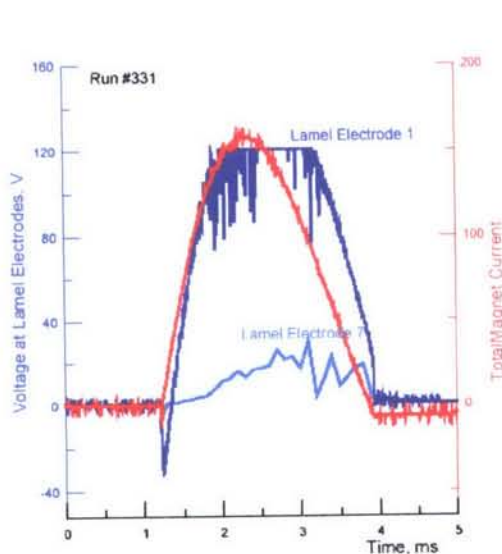


Figure 77. Schematic diagram of the potential measurement at Model #6 in run #331.

– only ~20 Volts at its maximal value. It should be noted that the voltages jump at the

moment of magnetic field is practically the same as it was found in the HFP experiments described above. (The magnet power supply systems are basically the same!) However, due to the high velocity in the HV MHD experiments $\mathbf{u} \times \mathbf{B}$ contribution into the total e.m.f. acting in the flow is much greater than $\partial B/\partial t$ part.

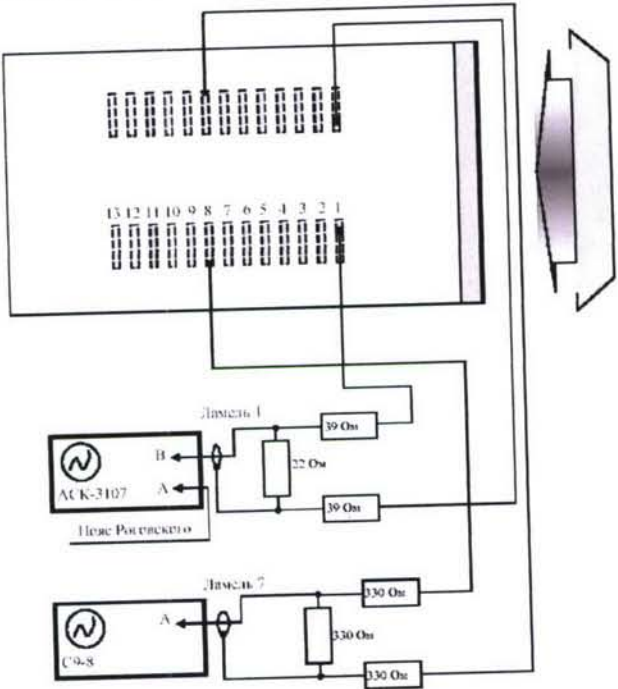


Figure 78. Schematic diagram of the potential measurement at Model #6 in run #332.

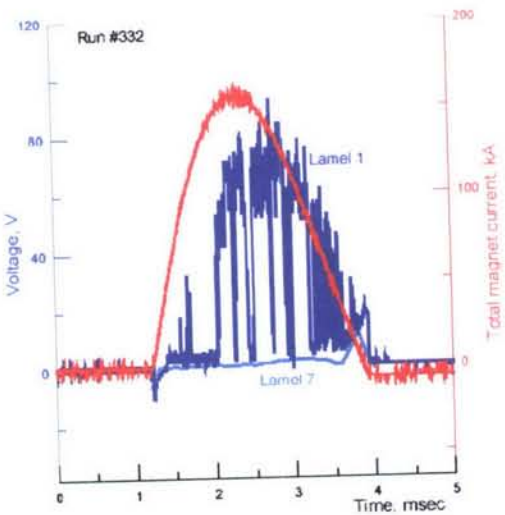


Figure 79. Rogovsky's belt signal (red), and voltage at the first pin (blue) and the seventh flush mounted electrode pairs in run#332. Load resistance 100 Ohm.

The second run of the series was conducted with ten times lower load resistance. The results are plotted in Fig.79. Unfortunately in this run the seed injection system worked unstable and several no current intervals are found on the voltage curve. Nevertheless, the result is now the record of the power extraction experiment in hypersonic flows. The maximal power reached exceeds 60Watts per electrode pair. (The level of 10 Watts/electrode was firstly demonstrated by our team more than three years ago

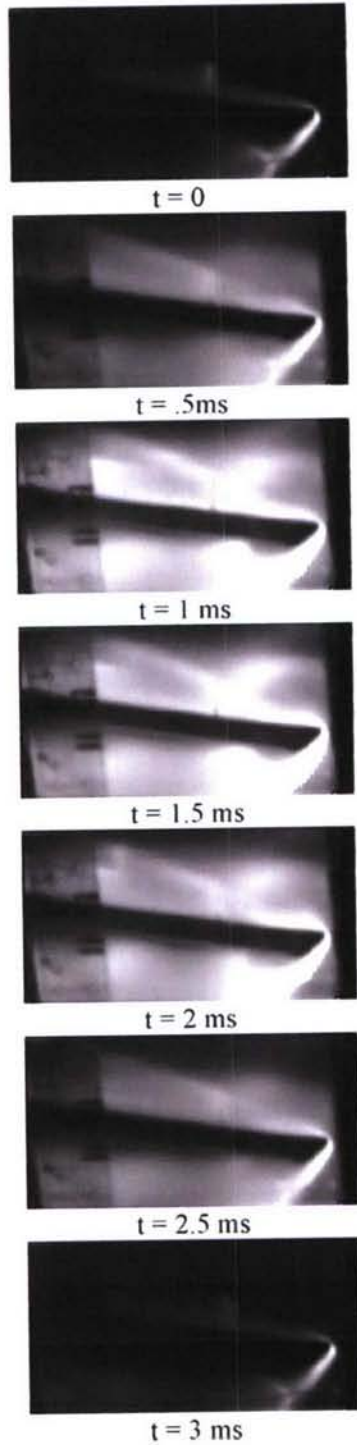


Fig. 80a. Flow visualization of the run 331 (Load resistance 1kOhm). Magnetic filed pulse covers time interval 0.5 ms – 2.5 ms

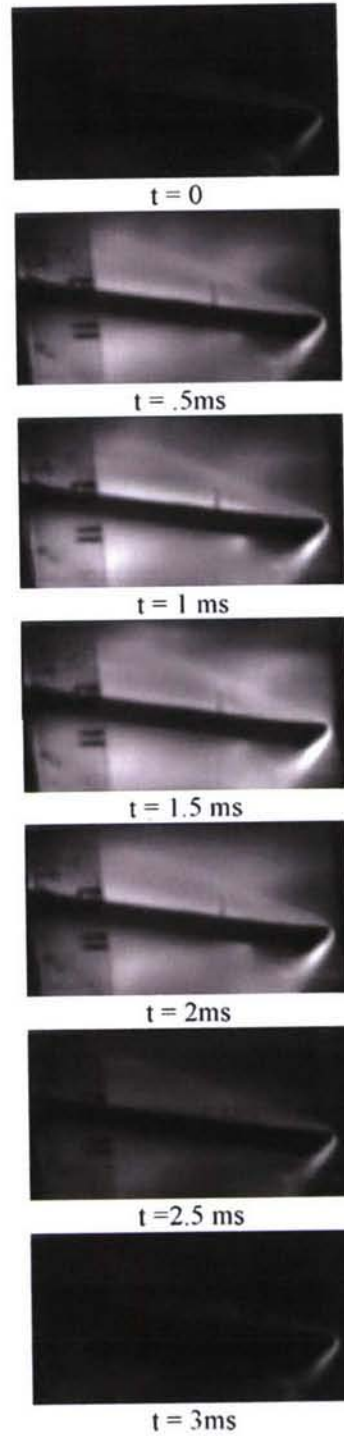


Fig. 80b. Flow visualization of the run 332 (Load resistance 100 Ohm). Magnetic filed pulse covers time interval 0.5 ms – 2.5 ms

with a very simple single-used model. In the previous run the level of the 30 Watts/electrode was reached.)

The linear extrapolation based on these two runs gives the maximal power extraction for the experimental conditions as high as 70 Watts/electrode that is only slightly higher than the result of the second run. It means in particular that the effective flow resistance in respect to single electrode pair loaded is about 200 Ohms. It corresponds to rather very low of effective conductivity of $\sim 5 \text{ mho/m}$, that could be attributed to the strong reduction by Hall effect (Hall parameter is not less than 10 at least).

The flow visualization of these runs is presented in Fig.80a and Fig.80b (note that the different brightness between two runs is mostly due to different exposure time rather than due to the physical conditions).

The most recent result on the power extraction with pin electrodes is the level of power extraction $\sim 100 \text{ W/electrode}$ that allows us to evaluate the total power extraction reached $\sim 1 \text{ kW}$ – a psychologically very important value of a ‘macroscopic’ amount for our small-scale experiment. The record of voltage measured at the load resistance of 100 Ohms is presented in Fig.81. (Note that voltage axis marked with 1/5 value corresponding to voltage divider used in the experiment.) The improvement utilized in this experiment has allowed the ‘screening’ effects of upstream pin electrodes on the downstream ones.

Magnet Current and Voltage at Electrode Pair 1

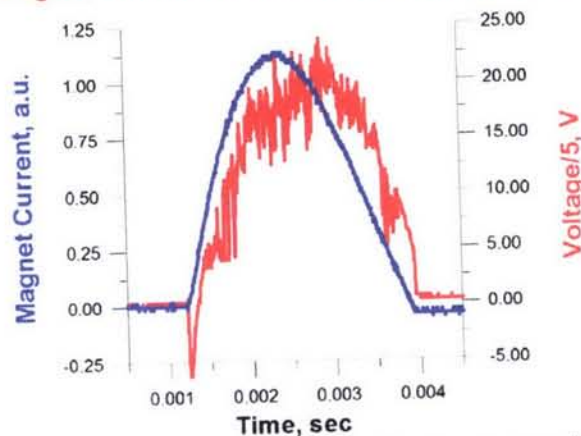


Figure 81. Rogovsky' belt and electrode voltage traces as in the most recent experiment at HV MHD facility.

5. NUMERICAL SIMULATION OF MHD FLOW UNDER RE-ENTRY CONDITIONS

The successful experiments performed with the surface MHD generator models have stimulated to extend the field of the potential applications of MHD interaction. In particular, the analysis work has extended to consider MHD interaction for flight scale hypersonic bodies. Emphasis has been in study of a blunt nose body and is made on two aspects: the effect of MHD interaction on the bow shock position and the decrease or redistribution of the heat flux on the surface of the body. It is assumed that the magnetic field is created by the coil producing dipole-like magnetic field near the

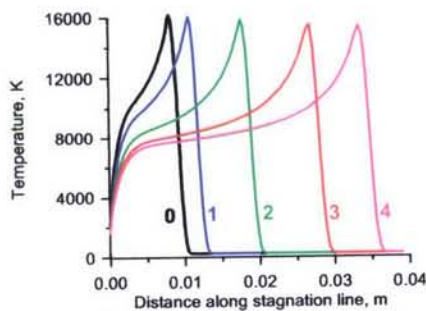


Fig. 82. Distribution of temperature along the stagnation line.

0 – $B=0$, 1 – $B=0.35T$, 2 – $B=0.625T$, 3 – $B=0.9T$, 4 – $B=1.1T$.

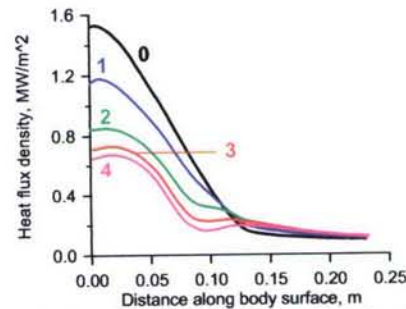


Fig. 83. Distribution of the heat flux density on the body surface.

0 – $B=0$, 1 – $B=0.35T$, 2 – $B=0.625T$, 3 – $B=0.9T$, 4 – $B=1.1T$

critical point of the body. The latter is assumed to consist of spherical part and conical one. The following flow conditions were considered. Radius of spherical part was taken as 10 cm, and 15 deg half-angle of cone was considered. Free-stream static pressure was taken as 11Pa; velocity is 7500 m/s; Mach number is 24. The constant

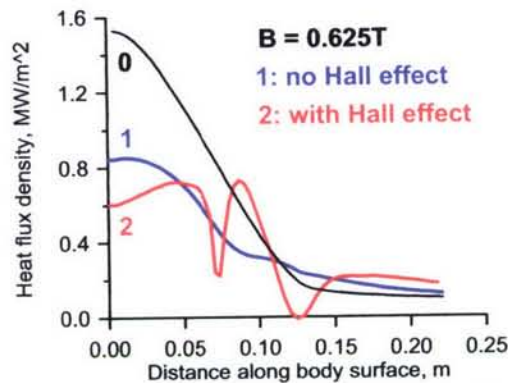


Fig. 84. Comparison of heat flux distributions for three flow cases.

0 – $B=0$; 1 – no Hall effect, $B = 0.625$ Tesla; 2 – with Hall effect, $B = 0.625$ Tesla.

temperature 1500K was specified at the body surface. The two-dimensional non-equilibrium thermo-chemical flow model coupled with quasi-steady electrodynamics was used to predict the MHD flow around the body.

As the first step, calculations in which Hall effect is neglected are considered. Such a formulation may have sense, since the total Hall current is expected to be small for the geometry considered here. As follows from our previous works¹⁶ the intensity of MHD interaction under small total Hall current may be close to that when Hall effect is neglected, even if the Hall parameter is much more than unit. Some results for the case of no Hall effect flow are shown in Fig.73 and Fig.74. The value of magnetic induction at the critical point of the body is pointed out in figures. These plots demonstrate that magnetic field strongly effects on the position of the bow shock and can significantly reduce the heat load on the body surface. The influence of Hall effect is demonstrated by Fig.75. From the first it is seen that the distribution of the heat flux density over the surface becomes essentially non-uniform for the case with Hall effect. This is a consequence of the flow structure demonstrated in Fig.76. It is clearly seen that non-uniformity of magnetic field created by realistic magnetic has serious impact

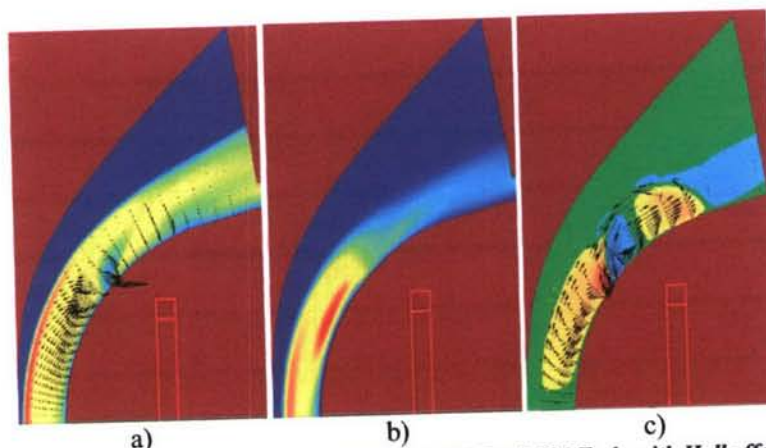


Fig. 85. MHD flow for reference magnetic field $B = 0.625$ Tesla with Hall effect.

- a) Temperature (filled) and electromagnetic force (vectors);
- b) Electron mole fraction;
- c) Faraday current (filled) and Hall current (vectors).

on the flow. More attractive (uniform) flow pattern can be achieved if one considers magnetic dipole positioned at the sphere centre. In this case, however, the current feeding the coil-type magnet should be of order of 20 MA. In the considered case the current in the range of 50 - 200 KA was required to generate the magnetic field of order of 0.3 - 1 Tesla within the shock layer. Making use of suitable magnetic materials can solve the problem of large magnetic system currents while providing the appropriate level of magnetic induction in the interaction region. The conclusion is that under some flight conditions MHD interaction arising from natural ionization of air behind the bow shock can be effective means for both flow control and on-board power generation.

The analysis of the large amount of experimental and simulations results on MHD flow control has clearly shown that the potential of MHD interaction in hypersonic flights, and, in particular, in re-entry flights is much wider than just the local flow field modification. MHD interaction being significantly distributed

practically over whole area where the magnetic field is presented even at low level intensity can efficiently influence on the integrated forces and moments applied to the vehicle. This could be used as a strong mechanism of flight control, providing additional tool of the trajectory optimization, maneuvering, stability control etc. MHD interaction flight control tool has advanced with very fast of response time typical of electrodynamics rather than mechanical device. The MHD interaction phenomena are rather complicated and realized in various form. In our papers 15,16 we discussed at first a so-called «MHD parachute effect» characterized by an extended subsonic flow region formed

behind the body (the cylinder was considered there). It was found that integral drag has increase several time for this reason in compare with classical gasdynamic drag. Because the cylinder is far from any practical application it was decided to check this result for more «practical» configuration shaped as an airfoil with magnet dipole inside. The flow conditions typical of the experimental facility are tried and several of angle-of-attack are considered. The drag and lift forces are found as functions of magnetic field intensity. The expectation was even exceeded. In Fig.78 the flow field is presented for reference case (no MHD) and regular MHD interaction case with

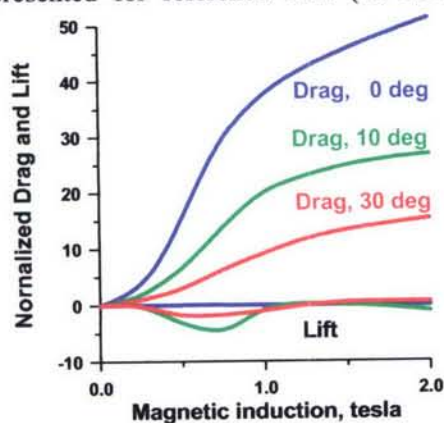


Fig. 87. Integral characteristics of MHD parachute effects

of-attack. The gasdynamic drag is not shown, as it is less than unit. MHD cases are

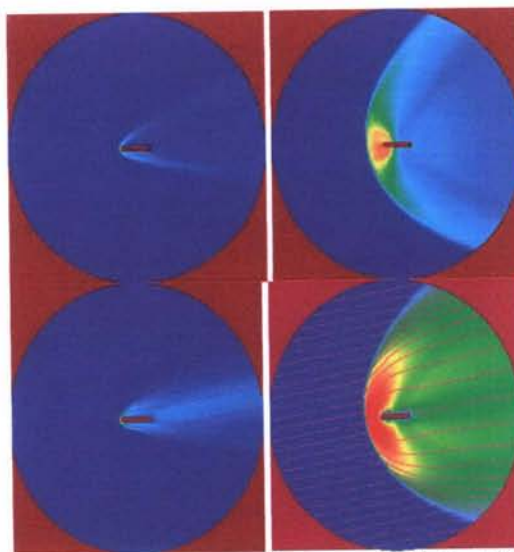


Fig. 86. Pressure (top) and temperature (bottom) fields for MHD-OFF case (left columns) and MHD-ON case (right columns).

$B = 2\text{ Tesla}$, Angle-of-Attack = 10 deg .

magnetic induction 2.0 Tesla and seed mole fraction 0.01. The magnetic system is a dipole type located at centres of upstream-and downstream-blunted edges shaped as a circular half cylinder. The case of 10 deg of angle-of-attack is shown. It is interesting to see that MHD interaction reveals a trend to «recover» the symmetry of the flow field. Absolute values of forces acting on the airfoil from plasma weakly depend on angle-of-attack. Normalized drag and lift are plotted in Fig.78 as function of magnetic field strength for several angle-of-attack values. Both drag and lift are normalized to dynamic pressure times the middle cross-section of airfoil corresponding to zero angle-

characterized by the drag one-two order of magnitude higher as compared to classical gasdynamic one. It is clearly seen that lift modification is relatively weak with configuration considered here. The negative lift values can be attributed to the secondary effect of the static pressure redistribution over the body surface due to MHD interaction in the bulk. It should be also mentioned here that the peak heat flux density near upstream stagnation point has usually decreased. However, the heat flux density integrated over the whole surface is slightly higher and changes irregularly with magnetic field strength. This effect needs probably more accurate analysis as well. The results of this Section have been used for evaluation of the potential effects of MHD interaction on the reentry trajectory [38-41]. It was found that 'MHD parachute effect' could provide the reduction of total and peak dynamic and heat loads by orders of magnitude.

Conclusions

Two variants of the modified plate model have been designed, fabricated and successfully tested at both experimental facilities: HFP WT and HV MHD WT. New high-speed visualization technique applied has provided to resolve the strong MHD interaction at both facilities. Numerical simulation has confirmed qualitatively the disturbed flow structure in a case of hypersonic tests. Numerical simulation of the MHD interaction at subsonic facilities is now in progress. The On-Board MHD electrical power generation has been proved experimentally and with numerical simulation.

Hypersonic flow around a blunt body under real flight conditions is characterized by low density, low electron concentration (of order of 10^{-3}), and high Hall parameter (10 to 100). However, the advantage compared to the MHD flow in the ground test facilities is low total Hall current. Numerical predictions to the MHD impact on the flow near the critical point of a blunt body showed that significant decrease of the heat flux onto the surface body could be obtained. The region of intensive MHD interaction is restricted by the magnetic system size. In this region the radial component of the electromagnetic force predominate, which decelerates flow. This results in formation of the re-circulation zone near the critical point such that a high temperature zone pushes away from the surface toward the outer boundary of the shock layer. The size of re-circulation zone, as well as the heat flux decrease, directly depends on the magnetic induction amplitude. At the same time, position of the bow-shock does not change as dramatically as the heat flux does. A common pattern of MHD interaction behind the bow shock looks like no Hall effect is available. This is because a total Hall current is small and Hall effect is essentially blocked out. For the considered flight conditions and electrical closing almost 50% of possible MHD potential available without Hall effect is recovered.

The MHD parachute effect has been confirmed with more sophisticated simulation and is proposed for detailed experimental and numerical study. The strategy of the practical implementation still has to be formulated on the base of critical analysis of existing approaches and missions. The first estimations of MHD parachute effect on the re-entry missions are very promising. Other related applications are also visible in this context.

References of Sections 4 and 5.

1. Kulikovski A.G., "On the Flow of Conducting Fluid Over the Magnetized Bodies", Doklady of USSR Academy of Sciences, 1957, v.17, No.2 (in Russian).
2. Zinober A.B., "Magnetohydrodynamic Flow Around Bodies", Riga, Zinatne, 1970, 291p. (in Russian).
3. Kulikovski A.G., Lyubimov G.A., "Magnetohydrodynamics", M: Fismatgiz, 1962, 246p. (in Russian).
4. Resler E.L., Sears W.R., "The Prospects for Magnetohydrodynamics", JAS, 1958, v.25, No.4, pp.235-245.
5. Bush W.B. "Magnetohydrodynamics – Hypersonic Flow Past a Blunt Body", Journal of the Aero/Space Sciences, v.25, Nov., 1958, pp.685-690.
6. Bush W.B. "Compressible Flat-Plate Boundary Layer Flow with an Applied Magnetic Field", Journal of the Aero/Space Sciences, v.26, Jan., 1960, pp.49-58.
7. Bleviss Z.O. "Magnetohydrodynamics of Hypersonic Quette Flow", Journal of the Aero/Space Sciences, v.25, Oct. 1958, pp.601-615.
8. Bityurin V.A., Potebnja V.G., Alferov V.I. "On MHD Control of Hypersonic Flows. Planning of Experimental Studies of MHD Effects on Bow Shock" In 34th SEAM, 1997, June 18-20, USA, Mississippi, p.4.4.1.
9. Lineberry J.T., Rosa R.J., Bityurin V.A., Bocharov A.N., Potebnja V.G. "Prospects of MHD Flow Control for Hypersonics", 35th Intersociety Energy Conversion Engineering Conference, AIAA 2000-3057, 24-28 July 2000, Las Vegas, NV.
10. Hoffmann K.A., Damevin H.-M., Dietiker J.-F. "Numerical Simulation of Hypersonic MHD Flow", AIAA Paper 2000-2259, June, 2000.
11. Poggie J., Gaitonde, "Magnetic Control of Hypersonic Blunt Body Flow", AIAA Paper 2000-0452, Jan, 2000.
12. Deb P., Agarwal R. "Numerical Simulation of Compressible Viscous MHD Flow with a Bi-Temperature, Model for Reducing Supersonic Drag of Blunt Bodies and Scramjet Inlets", AIAA Paper 2000-2419, June, 2000.
13. Alferov V.I. "Current Status and Potentialities of Wind Tunnels with MHD Acceleration", High Temperature, 2000, v.38, No.2, pp.300-313.
14. Bityurin V.A., Baranov D.S., Bocharov A.N., Margolin L.Ya., Bychkov S.S., Talvirsky A.D., Alferov V.I., Boushmin A.S., Podmasov A.V. Experimental Studies of MHD Interaction at Circular Cylinder in Hypersonic Airflow, In: Proc. of 4th Moscow Workshop on Magneto-Plasma Aerodynamics in Aerospace Applications, IVTAN, Moscow, 9-11 April, 2002.
15. J.T.Lineberry V.A.Bityurin, A.N.Bocharov, D.S.Baranov A.B.Vatazhin, V.I.Kopchenov, O.B.Goukov V.I.Alferov, A.S.Boushmin, "Cylinder with Current in Hypersonic Flow", In: 3rd Workshop on Magneto-Plasma Aerodynamics in Aerospace Applications, April 24-26, 2001, pp 15-25.
16. Bityurin V.A., Bocharov A.N., Baranov D.S., Vatazhin A.B., Kopchenov V.I., Goukov O.B. Alferov V.I., Boushmin A.S., Lineberry J.T., "Theoretical and Experimental Study of an MHD Interaction Effects at Circular Cylinder in a Transversal Hypersonic Flow", In: 40th AIAA Aerospace Sciences Meeting & Exhibit, January 14-17, 2002, AIAA Paper 2002-0491, Reno, NV.
17. Sedov L.I., "Similarity and Dimensionality Methods in Mechanics", 10th Edition, M: Nauka, 1987, 432p. (in Russian).
18. Sutton G.W. and Sherman A. "Engineering Magnetohydrodynamics", McGraw-Hill, 1965.

19. Andriatis A.V., Zhlukto S.A., Sokolova I.A. "Transport Coefficients for Chemical Nonequilibrium Components of Air Mixtures", *J. Mathematical Modeling*, 1992, v.4, No.1, pp.44-64 (in Russian).
20. Evans J.S., Schexnayder C.J., Huber P.W. "Computation of Ionization in Re-Entry Flowfields", *AIAA Journal*, 1970, No.6, pp.1082-1089.
21. Avilova I.V., Biberman L.M., Vorob'ev V.S., et.al., "Optical Properties of Hot Air", edited by Biberman L.M., M.:Nauka, 1970, Chapter 10.
22. Vatazhin A.B., Gouskov O.V., Kopchenov V.I., "Peculiarities of Deceleration of Two-Dimensional Hypersonic Flow of Conductive Gas in Channel in MHD Generation Operation Mode", *Proc. Of Steklov Mathematical Institute*, M.:MAIK Nauka, 1998, v.223, pp.153-162 (in Russian).
23. Vatazhin A.B., Gouskov O.V., Kopchenov V.I., "Assessment of Possibility to Use the MHD Control for Hypersonic Flow Deceleration", *AIAA Paper 99-4972*, 1999.
24. Vatazhin A.B., Gouskov O.V., Kopchenov V.I., "Assessment of Possibility to Use the MHD Control in Scramjet", *AIAA Paper 99-4971*, 1999.
25. Hutchinson B.R. and Raithby G.D. "A Multigrid Method on the Additive Correction Strategy", *Numerical Heat Transfer J.*, 1986, v.9, p.511-537.
26. Gustafsson I. "On Modified Incomplete Factorization Methods", *Lecture Notes in Mathematics, Proceedings, Bielefeld*, 1980, p.968.
27. Brichkin D.I., Kuranov A.L., Sheikin E.G. "The Potentialities of MHD Control for Improving Scramjet Performance", *AIAA Paper 99-4669*.
28. Macheret S.O., Miles R.B., Shneider M.N., "Modeling of Air Plasma Generation by Electron Beams and High Voltage Pulses", *AIAA 2000-2569*.
29. Macheret S.O. Private Communication, 2002
30. Damevin H.-M., Hoffman K.A. "Numerical Simulations of Hypersonic Magnetogasdynamic Flows over Blunt Bodies". In: 40th AIAA Aerospace Sciences Meeting & Exhibit, January 14-17, 2002, AIAA Paper 2002-0201, Reno, NV
31. Damevin H.-M., Hoffman K.A. Computation of Hypersonic, "Chemically Reacting Magnetogasdynamic Flows over a Cylinder" In: 40th AIAA Aerospace Sciences Meeting & Exhibit, January 14-17, 2002, AIAA Paper 2002-0648, Reno, NV
32. MacCormack R.W. "Three Dimensional Magneto-Fluid Dynamics Algorithm Development", In: 40th AIAA Aerospace Sciences Meeting & Exhibit, January 14-17, 2002, AIAA Paper 2002-0197.
33. Dietiker J.-F. and Hoffmann K.A., "Computations of Turbulent Magnetohydrodynamic Flows", In: *Proc. of 14th Intern. Conf. On MHD Electrical Power Generation and High Temp. Technologies*, Maui, Hawaii, May 20-2, 2002, pp. 123-135.
34. Gaitonde D., Poggie J., "Preliminary Analysis of 3-D Scramjet Flowpath with MGD Control", In: *Proc. of 14th Intern. Conf. On MHD Electrical Power Generation and High Temp. Technologies*, Maui, Hawaii, May 20-2, 2002, pp. 79-96.
35. Soloviev V.R., Krivtsov V.M., Konchakov A.M., Malmuth N.D., "Modeling of the MHD Effects in 2-D planar Flow over a Wedge", In: *Proc. of 14th Intern. Conf. On MHD Electrical Power Generation and High Temp. Technologies*, Maui, Hawaii, May 20-2, 2002, pp. 97-112.
36. Lineberry J.T., Bituryn V.A., Bocharov A.N., "MHD Flow Control Studies. Analytical Study of MHD Flow Interaction Around a Right Circular Cylinder in Transverse Hypersonic Flow", In: *Proc. of 14th Intern. Conf. On MHD Electrical*

- Power Generation and High Temp. Technologies, Maui, Hawaii, May 20-2, 2002, pp. 135-149.
37. Alferov V.I., Private Communications, 2002
 38. V.A.Bityurin, A.N. Bocharov, MHD Flow Control in Hypersonic Flight, In: 15th International Conference on MHD Energy Conversion, Vol.2, p 429-433, Moscow, May 24-27, 2005
 39. V. A. Bityurin, A.N. Bocharov, J.Lineberry, Study of MHD interaction in Re-Entry Flow, In: 4th International Symposium Atmospheric Reentry Vehicles & Systems, 21-23 March 2005, Arcachon-France
 40. V. Bityurin and A. Bocharov, J. Lineberry, MHD Flow Control in Hypersonic Flight, AIAA-2005-3225, AIAA/CIRA 13th International Space Planes and Hypersonics Systems and Technologies Conference, Capua, Italy, May 16-20, 2005
 41. V. A. Bityurin, A.N. Bocharov, D.S.Baranov, S.S.Bychkov, A.V.Podmazov, J.Lineberry, Effects of MHD Interaction in ReEntry Flights, In: 1th International ARA Days July 3-5, 2006, Arcachon, France

III.2. SUBSONIC MHD FLOW CONTROL

1. INTRODUCTION

The motivation to utilize the subsonic facility in studying of MHD interaction effects includes several reasons. They are as following:

- to have an extended base for experimental data analysis and more reliable the code validation process;
- to compare the influence of the working media composition and gasdynamics parameters on the MHD interaction (note that working media at the HF WT is the pure air);
- to use the extended diagnostics available at the facility;
- to use a long duration operation mode instead of pulse mode that is only possible at HV MHD WT.

The approach used in this study was based on the idea to use the similar model configuration and, in particular, the similar magnetic system. Practically all intention were successfully realized in the discussed experimental series.

2. FACILITY

The principal scheme of High Frequency Plasmotron is given in Fig.88, and basic specifications in the Table 1. The high-frequency generator and high-frequency

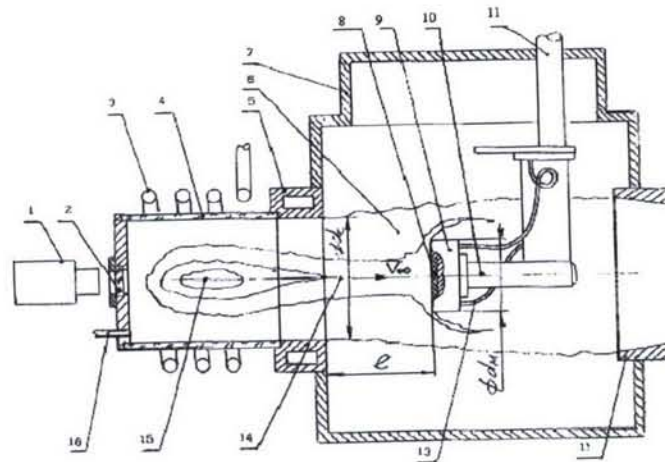


Figure 88. Schematic of High Frequency Plasmotron.

1- pirometer, 2- optical window, 3- inductor, 4- discharge chamber, 5- nozzle, 6- peripheral gas flow, 7- working chamber, 8- sample, 9- sample holder, 10- holder, 11- input-output mechanism, 12- diffuser, 13- water cooling system, 14- plasma stream, 15- discharge zone, 16- gas supplier.

induction plasmotron are the general units of the facility. The heating of gas and plasma formation occurs inside the discharge chamber 4, placed into inductor 3. The high-frequency electric voltage is carried from the generator to the inductor. As a result of it there is the alternative electromagnetic field 440 kHz in frequency inside the discharge chamber. This field initiates and supports the discharge in gas located in the chamber. The working gas moves through gas former 16, passes through the discharge zone 15, it is heated up there and then flows into the working chamber 7. The tested

samples 8 are placed in special holder 9, which is inserted into the gas stream 14 by the input-output unit 10, 11. At the calibration stage the measuring probes and models are established on the input-output unit. As the discharge chamber is used either quartz tube, or cooled chamber made from copper water-cooled sections, placed in a quartz tube. For the model temperature measurement the optical devices 1 are installed at an optical window 2 in an end face of the discharge chamber.

Table 1 Performance of the facility

Voltage, kV	10
Rated power of HF-generator, N, kW	1000
Working gas	air, nitrogen, argon, carbon
Dimensions of test chamber, m	0.8 x 0.8 x 0.8
Frequency of electromagnetic field,	440
Duration of non-stop work, s	up to 6000

The facility operates either in subsonic, and in a supersonic modes. The gas flow parameters, reached in these modes, are shown in Table 2.

Table 2

Parameter	Subsonic	Supersonic
Mach number, M	0.3	2.5
Gas temperature in the test chamber, T, K	3000 - 10000	5000 - 10000
Gas flow rate, G, g/s	1.5 - 30	5 - 20
Stagnation pressure on the model, p, bar	0.005 - 0.2	0.03 - 0.15
Flow velocity, V, m/s	400-600	2000 - 3000
Diameter of a gas stream, mm	200	50

3. NUMERICAL SIMULATION OF NONEQUILIBRIUM FLOW IN DISCHARGE CHAMBER OF HF-PLASMATRON

Statement of the problem

Detailed diagnostics of plasma jet flow is required for any type of studies in HF-plasmatron. Gas flow in the discharge chamber and jet of the HF-plasmatron is accompanied with numerous real gas processes (such as dissociation, ionization, chemical reactions, excitation of internal modes, energy translation between the particles of different kinds), which are nonequilibrium ones at low pressure. Therefore correct determination of plasma jet parameters issuing from the discharge chamber (its velocity, temperature, atom and electron concentrations, etc) is possible only in combination of experimental and numerical approaches.

Studies of high temperature plasma flow have been made for the conditions of

the HF-plasmatron facility [1] (discharge chamber length $L = 0,85$ m, radius $R = 0,09$ m, generator frequency $\omega = 440$ kHz)

The equation system for subsonic plasma flow within the discharge chamber of inductively coupled RF-plasmatron in an axisymmetric coordinate system can be written in the following form [2]:

Continuity equation for the mixture as a whole

$$\frac{\partial \rho u}{\partial x} + \frac{1}{r} \frac{\partial}{\partial r} (\rho v r) = 0,$$

momentum equations

$$\begin{aligned} \frac{\partial \rho u^2}{\partial x} + \frac{1}{r} \frac{\partial}{\partial r} (\rho u v r) &= -\frac{\partial p}{\partial x} + 2 \frac{\partial}{\partial x} \left(\mu \frac{\partial u}{\partial x} \right) + \frac{1}{r} \frac{\partial}{\partial r} \left(r \mu \left(\frac{\partial u}{\partial r} + \frac{\partial v}{\partial x} \right) \right) + F_x, \\ \frac{\partial \rho u v}{\partial x} + \frac{1}{r} \frac{\partial}{\partial r} (\rho v^2 r) &= -\frac{\partial p}{\partial r} + \frac{2}{r} \frac{\partial}{\partial r} \left(r \mu \frac{\partial v}{\partial r} \right) + \frac{\partial}{\partial x} \left(\mu \left(\frac{\partial u}{\partial r} + \frac{\partial v}{\partial x} \right) \right) + F_r - 2 \mu \frac{v}{r^2} + \rho \frac{w^2}{r}, \\ \frac{\partial \rho u w}{\partial x} + \frac{1}{r} \frac{\partial}{\partial r} (\rho v w r) &= \frac{\partial}{\partial x} \left(\mu \frac{\partial w}{\partial x} \right) + \frac{1}{r} \frac{\partial}{\partial r} \left(r \mu \frac{\partial w}{\partial r} \right) - \rho \frac{v w}{r} - \frac{w}{r^2} \frac{\partial \mu r}{\partial r}, \end{aligned} \quad (1)$$

total energy conservation

$$\frac{\partial \rho u h}{\partial x} + \frac{1}{r} \frac{\partial}{\partial r} (\rho v h r) = -\frac{\partial q_x}{\partial x} - \frac{1}{r} \frac{\partial (r q_r)}{\partial r} + Q_J - Q_{rad},$$

where (x, r) – axial and radial coordinates; (u, v, w) – axial, radial and azimuthal velocity vector components; μ, ρ, h, p – viscosity, density, enthalpy, gas pressure; \mathbf{F} – Lorentz force; Q_J, Q_{rad} – Joule heat and irradiation energy loss; \mathbf{q} – net heat flux of the gas mixture:

$$\mathbf{q} = -(\lambda_t + \lambda_{rot} + \lambda_{vib} + \lambda_e) \nabla T + \sum_i h_i \mathbf{J}_i.$$

Viscous dissipation in the energy equation as well as terms with the velocity divergence in the stress tensor of motion equations are neglected because of low Mach number of the flow. The chemical species conservation equations are

$$\frac{\partial \rho u c_i}{\partial x} + \frac{1}{r} \frac{\partial}{\partial r} (\rho v c_i r) = -\frac{\partial J_{xi}}{\partial x} - \frac{1}{r} \frac{\partial (r J_{ri})}{\partial r} + \omega_i.$$

where c_i and \mathbf{J}_i – mass concentrations and diffusion fluxes. The transport coefficients (μ, λ, D_{ij}) and plasma conductivity σ are evaluated with the relations [3]. Modified Fick's law is used to model plasma components diffusion (with account for ambipolar diffusion) that provides the sum of concentration equality to unity.

An approach allowing relevant determination of the EM field at the whole space (including the space with-out the discharge chamber) is used for numerical simulation of inductor field and plasma current simultaneous effect [4]. Assume that EM field depends on time by the law $\sim \exp(-i\omega t)$ where ω – current frequency of the

RF-plasmatron inductor. Then the complex amplitudes of electric and magnetic fields can be employed

$$\begin{aligned}\mathbf{E} &= (\mathbf{E}_1 + i\mathbf{E}_2) \exp(-i\omega t) \\ \mathbf{B} &= (\mathbf{B}_1 + i\mathbf{B}_2) \exp(-i\omega t)\end{aligned}$$

Suppose that the simplest formulation of the Ohm's law is valid

$$\mathbf{j} = \sigma \mathbf{E},$$

where \mathbf{j} – current density. In this case only the azimuthal component of the electric field E_ϕ is not equal to zero as well as axial and radial components of the magnetic field \mathbf{B} . Neglecting the displacement current the following equation for the complex amplitude E_ϕ can be derived from the Maxwell's equations:

$$\frac{\partial^2 E_\phi}{\partial x^2} + \frac{\partial}{\partial r} \left(\frac{1}{r} \frac{\partial(rE_\phi)}{\partial r} \right) + 4\pi\sigma i \frac{\omega}{c^2} E_\phi = 0$$

From the linear superposition the electric field E_ϕ can be expanded as a sum of known field of alternative current in the inductor E_0 and field induced by the plasma currents e ,

$$E_\phi = E_0 + e.$$

In axisymmetric case the EM field of actual inductor is replaced by the fields of the N_c circle rings of radius a with the current I_0 of frequency ω [6]:

$$\begin{aligned}E_{0\phi}(x, r) &= \frac{4i\omega}{c^2} I_0 \sqrt{\frac{a}{r}} \sum_{l=1}^{N_c} \left(\left(1 - \frac{k_l^2}{2}\right) K(k_l) - E(k_l) \right), \\ k_l^2 &= \frac{4ar}{(a+r)^2 + (x-x_l)^2},\end{aligned}$$

where x_l – l th ring abscissa, $K(k)$ и $E(k)$ – full elliptic integrals of first and second kind. Returning to real and imagine parts

$$e = e_1 + ie_2, \quad E_0 = iE_2,$$

from equation for complex amplitude two real equations for e_1 and e_2 can be derived

$$\begin{aligned}\frac{\partial^2 e_1}{\partial x^2} + \frac{\partial}{\partial r} \left(\frac{1}{r} \frac{\partial(re_1)}{\partial r} \right) - \frac{4\pi\omega}{c^2} e_2 &= \frac{4\pi\omega}{c^2} E_2, \\ \frac{\partial^2 e_2}{\partial x^2} + \frac{\partial}{\partial r} \left(\frac{1}{r} \frac{\partial(re_2)}{\partial r} \right) + \frac{4\pi\omega}{c^2} e_1 &= 0.\end{aligned}\tag{2}$$

In distinction to usual formulation of the boundary problem [5] the equations (2) in the present method can be solved within an arbitrary domain, which could not coincide with the solution domain of the hydrodynamic problem (1). In this case it is

convenient to align the outer boundary with the wall of metallic case surrounding the discharge chamber. Then the following boundary conditions are imposed on that boundary:

$$\begin{aligned} e_1 &= e_2 + E_0 = 0, \\ e_1 &= e_2 = 0. \end{aligned}$$

and at the symmetry axis

Such an approach allows accounting for effect of outer metallic parts of the plasmatron facility on the field inside the discharge chamber. Relationship for the ohmic heating can be obtained by time-averaging of instant dissipation rate of the EM field:

$$Q_J = \langle \mathbf{j} \cdot \mathbf{E} \rangle = \frac{1}{2} \sigma (e_1^2 + (e_2 + E_2)^2).$$

If the value of power delivered to the plasma $Q_{pl} = 2\pi \int_0^R Q_J(x, r) r dr dx$ is assumed to

be given then the inductor current I_0 should be corrected to meet this condition. Similarly, the value of magnetic force in the motion equations can be obtained by time-

averaging the Lorentz's force $\mathbf{F} = \frac{1}{c} \mathbf{j} \times \mathbf{B}$:

$$F_x = \frac{\sigma}{2\omega} \left(e_1 \frac{\partial(r(e_2 + E_0))}{\partial r} - \frac{e_2 + E_0}{r} \frac{\partial r e_1}{\partial r} \right),$$

$$F_r = \frac{\sigma}{2\omega} \left(e_1 \frac{\partial(e_2 + E_0)}{\partial x} - (e_2 + E_0) \frac{\partial e_1}{\partial x} \right)$$

Fig.89 illustrates the presented approach to solution of the Maxwell's equations. The electric field E_φ (V/cm) in the discharge chamber and outer metallic

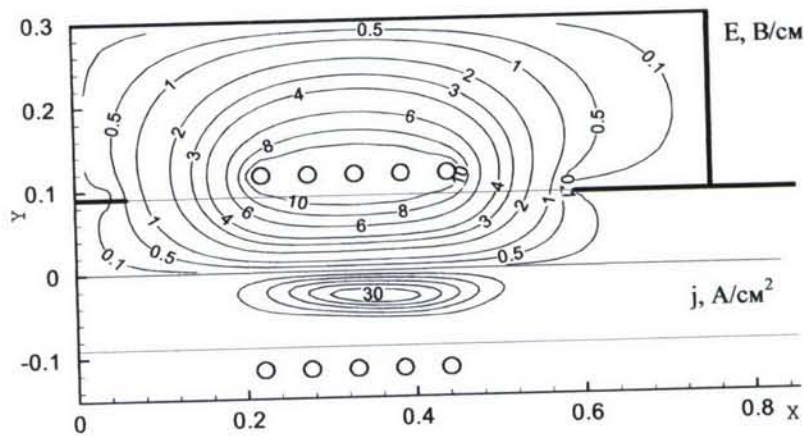


Fig.89. Electric field and plasma current density.

case (upper part of the figure) and plasma current density (j , A/cm²) are presented in the figure.

Navier–Stokes and Maxwell equations are approximated by the finite volume method on the rectangular collocated grid with the use of hybrid finite-difference scheme. The difference equations are solved successively by the linear Gauss–Seidel iterations with overrelaxation and Maxwell equations – coupled by the block-matrix tridiagonal algorithm.

Results

Using presented method the numerical simulation of the high temperature plasma flow in RF-plasmatron discharge chamber was carried out (mass flow rate $G = 7\text{ g/c}$, pressure $P = 50\text{ mbar}$ and power of anode supply $N = 100$ and 200 kW). These regimes were chosen for further investigation of the MHD-interaction. Strictly speaking the value of power delivered to the plasma Q_{pl} is not known exactly. For evaluation of the efficiency of the experimental facility additional calculations were conducted. Heat fluxes on the cooper calorimeter in plasma jet were obtained for several power values N . The value of Q_{pl} was adjusted to coincide of the numerical and experimental values of heat flux and dynamic pressure [7].

The obtained efficiency is about 60%.

Investigations of the MHD flow in plasmatron work chamber were carried out using plane nozzle. In frame of two-dimensional axisymmetric approach the plane nozzle was substituted by conic-cylindrical nozzle with the same exit area. In Fig.89 electric field and electric current density distribution are shown for the case $N=100\text{ kW}$. In Figs 90a,c the flow field, temperature field and electron number density distribution are presented for power of anode $N = 100\text{ kW}$. At the plasma jet axis the flow velocity is equal to $U_{jet} = 220\text{ m/s}$, temperature $T_{jet} = 5700\text{ K}$ and electron density $n_e = 1.8 \cdot 10^{13}\text{ cm}^{-3}$.

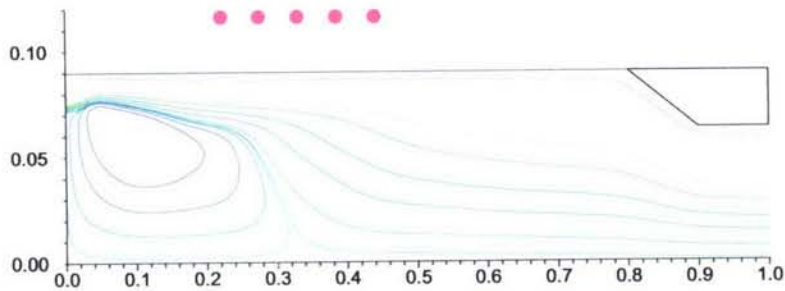


Fig.90a. Flow field for $N = 100\text{ kW}$.

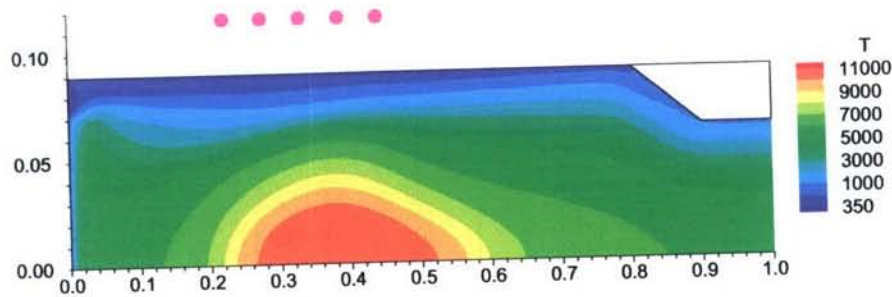


Fig.90b. Temperature field.

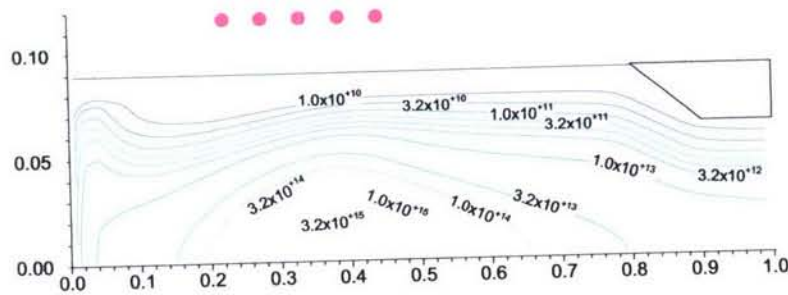


Fig.90c. Electron number density (cm^{-3}).

For comparison in Figs. 91a,b the temperature field and electron number density distribution are presented for power of anode $N = 200 \text{ kW}$. At the plasma jet axis the flow velocity is equal to $U_{jet} = 315 \text{ m/s}$, temperature $T_{jet} = 6350 \text{ K}$ and electron density $n_e = 4.3 \cdot 10^{13} \text{ cm}^{-3}$.

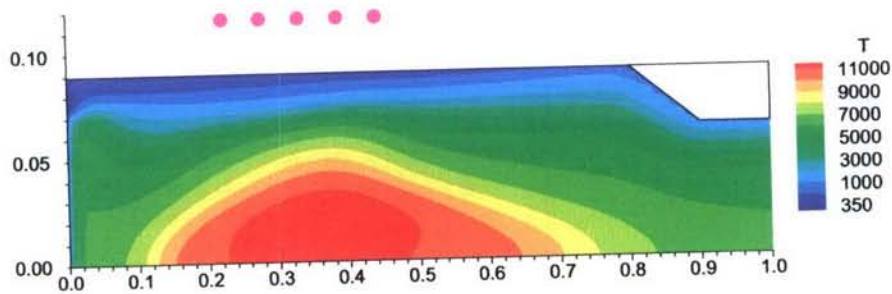


Fig.91a. Temperature field for $N = 200 \text{ kW}$.

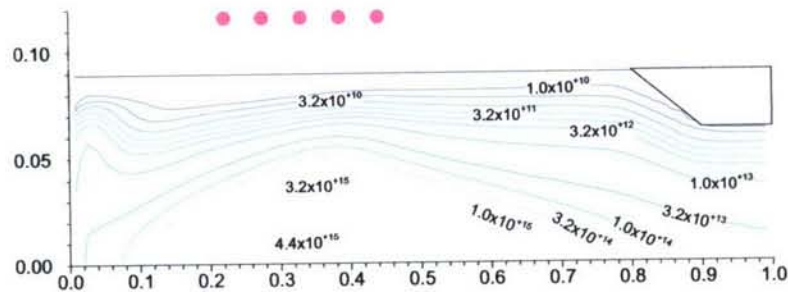


Fig.91b. Electron number density (cm^{-3}).

The distributions of the flow parameters at the exit cross-section are presented in Figs. 92a-d.

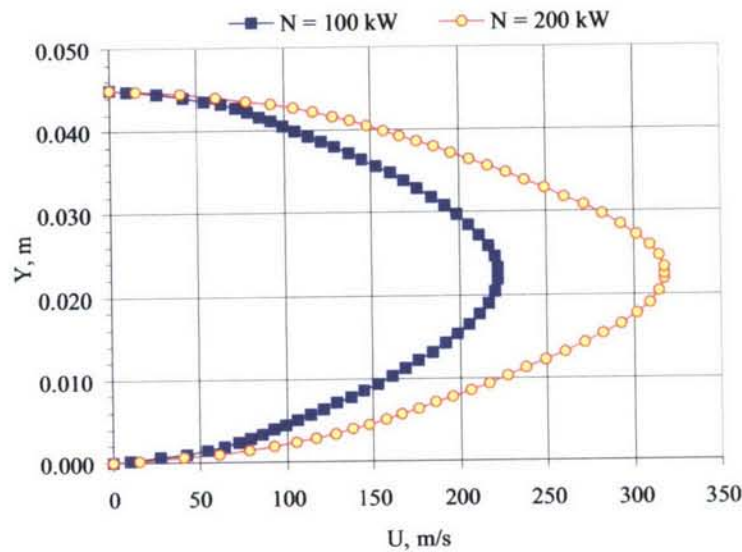


Fig.92a. Axial velocity (m/s) distributions.

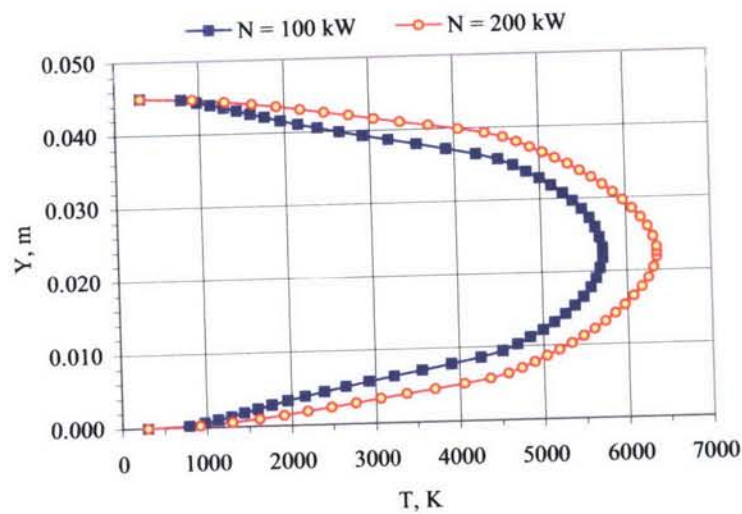


Fig.92b. Temperatures (K).

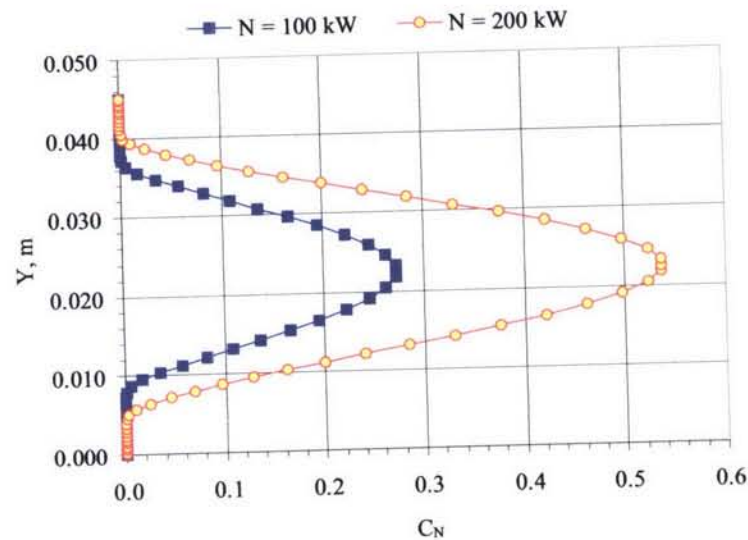


Fig.92c. Nitrogen atoms mass concentrations.

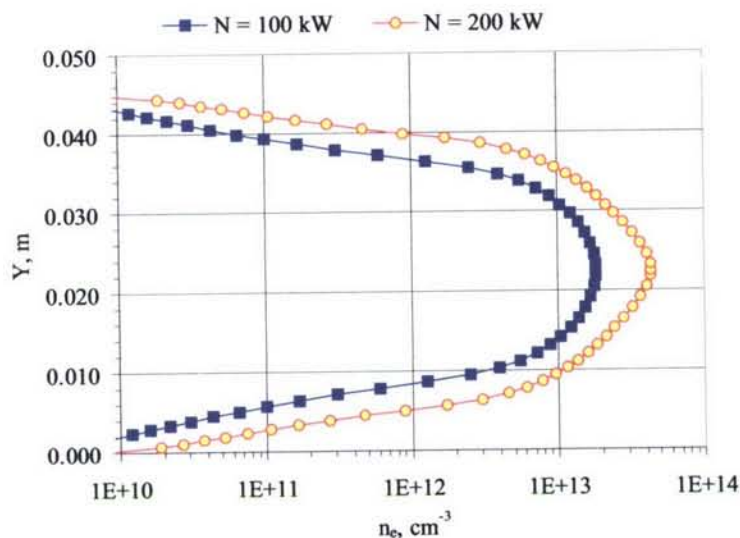


Fig.92d. Electron number density.

References

1. Zalogin G.N., Zemlyansky B.A., Knotko V.B. et al. High frequency plasmatron facility for investigation of aerophysical problems using high enthalpy gas flows. *Cosmonautics and Rocket Engineering*, 1994, № 2, pp.22-32. (In Russian)
2. Vasilievsky S.A., Kolesnikov A.F. Numerical simulation of equilibrium inductive plasma within the plasmatron cylindrical channel. *Fluid Dynamics*, 2000, №5, pp.164-173.
3. Vlasov V.I. Theoretical investigations of high-temperature gas flow in HF-plasmatron discharge and working chambers. *Cosmonautics and Rocket Engineering*, 2001, № 23, pp.18-26. (In Russian)
4. Abele D.V., Degres G. Numerical of high-pressure air inductive plasmas under thermal and chemical non-equilibrium. AIAA Paper, 2000, 2000-2416.
5. Yos J.M. Transport Properties of Nitrogen, Hydrogen, Oxygen and Air to 30000K. Rep. RAD-TM-63-7, AVCO Corp., 1963.
6. Landau L.D., Lifshitz E.M. Theoretical Physics. Electrodynamics of condensed matters. M.: Nauka, 1982.
7. Van Doormaal J.P., Raithby G.D. 1984 Enhancement of the SIMPLE Method for Predicting Incompressible Fluid Flows. *Numerical. Heat Transfer*, V.5, №2. pp.147-163.

4. EXPERIMENTAL MODEL DEFINITION

At the first stage of this experimental series as a model of an external MHD generator the flat plate with electrodes on its surface (see Fig.93) is used. The model is

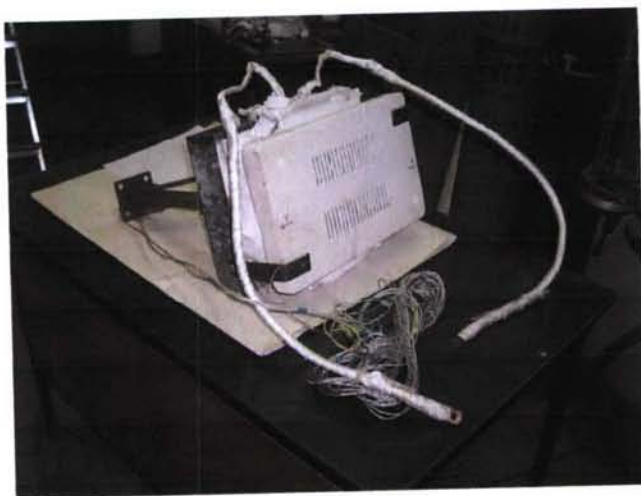


Figure 93. The general view of the external MHD generator model.

a plate of size 250 x 400 mm with 38 electrodes on wind surface and an electromagnet system on under wind side. The model made of an insulating thermal protection material. The electromagnet system consist of two spool. At letting through the electromagnet system electric current of ~ 5 KA the value of magnet induction can be up to ~ 0.5 Tesla. The electric current arises in result of a condenser battery discharge.

In Fig.94 the model of the external MHD generator is showed in the test section at the time of the preliminary test. The model was installed at small angle of attack and streamlined by plasma flow exhausting through a subsonic flat nozzle of exit size 50 x 270 mm.



Figure 94. The model in the working chamber at the time of the preliminary test.

Before test the component of magnet induction B_z along axes Z, X and the components of magnet induction B_x and B_y along axes Z, X , accordingly, were measured. The measurements of the magnet induction components realized by using of the magnet induction device III 1-8.

As the welding generator ПОО-300 of direct current up to 300 A and the impulse electric accumulate supply ГОО-301 were used. The electric accumulate supply ГОО-301 consist of 1800 μF condenser battery with maximum voltage $\sim 3\text{ kV}$ and impulse current up to $\sim 6000\text{ A}$.

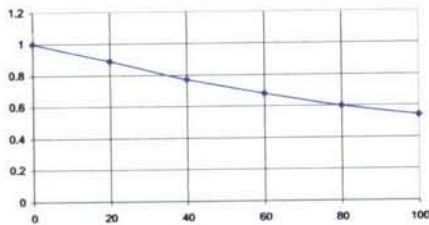


Figure 95. B_z dependence on Z .

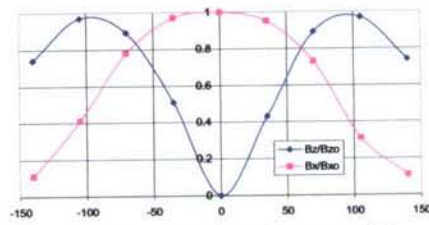


Figure 96. B_z and B_x dependences on X .

The magnet induction measurements at direct current of about 300A through the solenoid are showed in Fig. 95 and Fig.96. The magnet induction dependence on X was measured on plane $Z=0$.

From the figures you can see, that value of B_z reduces at Z and X coordinates increasing. The value of B_x has a minimum at axis Z , and near the solenoid peripheral pass through a maximum, which appearance can be explained by a geometry of the solenoid magnet lines. To calculate the values of B_z and B_x at another current value I through the solenoid it is necessary use next formulas:

$$B_z = B_{z0} I / I_0, \quad B_x = B_{x0} I / I_0, \quad \text{where } B_{z0} = 116\text{ H}, \quad B_{x0} = 70\text{ H} \quad \text{at } I_0 = 300\text{ A}.$$

We can mark that magnet induction component B_y dependence on axis Y practically agrees with magnet induction component B_x dependence on axis X with accuracy up to 10 %.

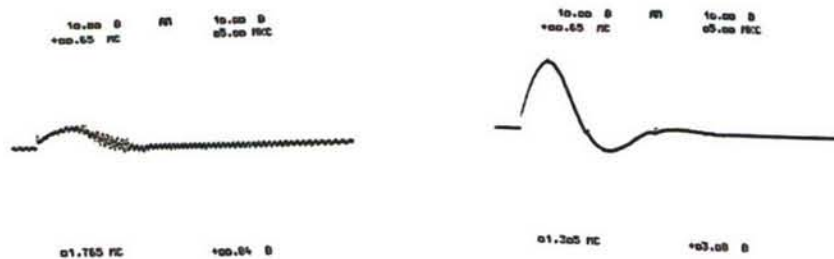


Figure 97 Solenoid current oscillogram with plasma flow (left) and without (right).

At the tests with impulse electric power supply the current through the solenoid was measured by using shunt and electron oscillograph C9-8. The current oscillograms with and without plasma flow are presented in Fig.97. It is seen that both curves are quickly decreased sinusoids.

The right and left numbers at the foot of the both oscillograms correspond with maximum shunt voltage and quarter of the time period from what it is necessary to subtract preset time 0.65 ms. The shunt coefficient was equal 2 A/mV. It lets to calculate maximum solenoid current value in test without plasma flow as $I_{max}=6160A$, characteristic frequency $f = 225$ Hz, appropriate magnet induction component $B_z = 2380H$ and $B_x=1440 H$, and for the test with plasma $I_{max}=1680A$, $f=380Hz$ $B_z=650H$, $B_x=390H$. For so frequencies skin-layer does not bring in mistakes of the measurements, because depth of impulse magnet field penetration is a lot of time less than its thickness.

The large difference solenoid currents in the test with and without plasma can explain by electric discharge from high voltage solenoid terminal to grounded working camera and devices, connected with it electrically. In result of one a part of current does not pass through shunt, and we can see circuit through ground.

The preliminary test allowed finding out the external magnetic system has lacked that will be eliminated at next steps.

The preliminary tests have shown that the facility and main equipment are ready for systematic experiments.

5. COMPLEX DIAGNOSTICS OF PLASMA FLOW IN HIGH FREQUENCY PLASMATRON

High temperature diagnostics

In order to perform any researches in HF-plasmatron it is required detailed diagnostics of plasma flow parameters. Moreover these data are used to verify computational procedures and codes.

Gas flow in the discharge chamber and in the gas stream of the HF-plasmatron is accompanies by a number of physical and chemical processes (dissociation, ionization, chemical reactions, excitation of molecule inner degrees of freedom, energy interchange between particles of different kinds), which proceed at low pressures in non-equilibrium mode. At pressures $p > 20-25$ mbar the state of gas in subsonic flow is close to thermodynamics equilibrium. In this case the diagnostics of the flow comes to determination of the following parameters: stagnation enthalpy H_0 , pressure p , velocity V and heat transfer coefficients for probes, which are used in diagnostics. Other parameters – temperature of the gas, density, composition, including concentration of electrons – are predicted by calculations using equation of state and laws of chemical masses and by special spectroscopic measurements.

In principle the stagnation enthalpy could be predicted using measured temperature of the gas (for example, by spectral technique). In air or nitrogen such approach features considerable error because of large energy intensity of nitrogen dissociation and as result sharp dependence of gas enthalpy via temperature. So the value H_0 could not be determined with adequate accuracy. Temperature variation in 5% (300°C at temperature level 6000°C) in the range of spectral measurement errors results in error of 15-20% in enthalpy H_0 .



Figure 98. Transducer for pressure measurement

The diagnostics techniques for high temperature gas flows are often based on measurements not of unknown parameters, but some values depending on them. The required parameters of the flow are predicted by calculations using rather complicated gas dynamics and physical and chemical models of non-equilibrium gas. This approach in its turn is an additional source of errors in determination of unknown parameters, these errors to be caused first by perturbation of gas stream during insertion of probes, sometimes rather large sizes (compared with stream diameter) and secondly by imperfection of computational modeling of flow and heat transfer in subsonic high temperature non-equilibrium gas stream.

The method to determine plasma flow parameters at the flow axis is based on measurement of static pressure p in the working chamber of plasmatron, heat flux to high catalytic material and pressure difference between total and static pressures Δp . Static pressure is measured rather reliably by means of the standard measuring instruments using pressure transducers of IKD type. One of such transducers is presented in Fig.98. Feed opening is located on the wall of facility working chamber.

Table 1

Designation	Range of Measurements	Errors of measurements	
		absolute, mbar	relative, %
IKD6TD-30	1.3-13.3	1.2	3
IKD6TD-50	1.3-66.5	2	3
IKD6TD-100	1.3-133	1.5	1.5

Heat flow rate, which depends on catalycity of transducer surface, is calculated using following formula

$$q_w(K_w) = \alpha/c_p [H_0 - i_w(K_w)] \tag{1}$$

Here α/c_p – heat transfer coefficient, weakly depended on gas composition in boundary layer. For hemispheric probes of small sizes (less than stream diameter) the velocity gradient in stagnation point of hemisphere is known from exact solution of such problem and it equals $3/2 V/R$. Here V – flow velocity, R – radius of sphere. The experiments were carried out using hemispherical probe 24 mm in radius. In stagnation



Figure 99. Calorimetric probe

point of this probe there is a copper calorimetric sensor to measure heat flux in regular mode (see Fig.99).

While using a probe shaped as cylindrical butt-end, the additional unknown parameter, heat transfer coefficient, arises owing to complicated flow around such models with restricted subsonic stream. This parameter could be determined both experimentally and by numerical solution of flow problem using Navier-Stokes equations.

Pressure differential of the total p_0' and static pressure p is related with velocity by the formula



Fig 100. Pitot' tube

$$\Delta p = p_0' - p = 1/2 \gamma_0 \rho V^2 \quad (2)$$

where $\gamma_0 = 1 \dots 1.3$ – correcting factor, depending on Reynolds number Re_∞ at $Re_\infty \leq 100$, which characterizes deviation from Bernoulli law at low Reynolds number Re . According to [16] the dependence of γ on Re is described by formula

$$\gamma = 1 + \frac{7.25}{Re + 0.455\sqrt{Re}}$$

The value of p_0' is measured using impact tube (Fig.100).

Measurements of above mentioned values make it possible to determine all unknown parameters of plasma flow, required for processing experiments of any types. While measuring stagnation enthalpy of gas it should bear in mind the following. This

technique for enthalpy determination comes to measurements of heat flux $q = \alpha/c_p (H_0 - h_w)$, $H_0 = h_0 + V^2/2$ at known parameters α/c_p and h_w . This method provides adequate results in dense gases, but there are two reasons, which require special substantiation for application of this method to rarefied non-equilibrium flow.

The enthalpy of dissociated gas equals $h = c_p T + h_d$, where h_d – enthalpy of atom formation (due to dissociation nitrogen and oxygen).

For equilibrium external flow the value $h_d = h_d(p, T)$ is determined by calculation. But the value h_w for frozen or non-equilibrium boundary layer depends on surface catalycity of the probe. So in chemically frozen boundary layer

$$h_w = C_p T_w + \frac{h_d}{(1 + Le^{-2/3} Z)}, Z = \frac{K_w \rho_w}{\alpha / C_p} \quad (3)$$

In the temperature range $T_0 = (5 \dots 10) \cdot 10^3$ K ratio $h_d/H_0 \sim 0.4 \dots 0.7$ (in the air flow), so the possible uncertainty in value of h_w generally speaking could give a considerable error in determination of H_0 . Only excluding the influence of h_d on heat flux i.e. at $Z \gg 1$ it could be possible to avoid this error.

From above considerations it is clear that the main problem, which governs the accuracy of plasma flow parameter determination, is a selection of values K_w for reference materials. The same problems arouse for American researchers during diagnostics of supersonic high enthalpy flow while studying catalytic properties of thermal protection materials for vehicle Space Shuttle [17]. As the rule the catalycity of materials, used as reference materials features large dispersion. It is because there are both various techniques to prediction this value, degree of purity and technological features of manufacturing, and presence of different contaminations in gas. In this study all calorimetric sensors are made of copper.

For copper it is chosen the value $K_w = 25$ m/s. This value was determined earlier in air flow in the HF-plasmatron [18]. The close values $\gamma = 0.17$ ($K_w = 28$ m/s at $T_w = 300$ K) and $\gamma = 0.15 \pm 20\%$ ($K_w = 25$ m/s) were determined also in nitrogen [19] and in air [20].

The Fay-Riddell's formula gives a good approximation for calculation heat flux at the stagnation point of hemisphere in subsonic flow.

$$\frac{\alpha}{C_p} = 0.71 \left(\frac{\rho_\delta \mu_\delta}{\rho_w \mu_w} \right)^{1/3} (\rho_w \mu_w \beta)^{1/2} Pr^{2/3} \quad (4)$$

where $\beta = 1.5 V/R$ – velocity gradient at the outer edge of the boundary layer.

The second problem, which should be discussed, is application of the formula (4) at relatively low Reynolds numbers $Re = 5 \dots 50$, realized at experiment conditions. The results, known for hypersonic velocities give a considerable deviation (up 40%) of the value $St \cdot Re^{1/2}$ from the constant, corresponding to asymptotically thin boundary layer at high Reynolds numbers, for which the formula (4) proven.

In the given range of Re numbers the thickness of temperature boundary layer is of same order as bluntness sizes and it could expect a considerable deviation of heat flux law from that for thin boundary layer. But experiments, in which Re number varies with variation of sphere radiuses, show that in subsonic flow ($M \sim 0.2$) and at low temperature factor $T_w/T_0 \sim 0.05$ at least in the range of $Re \sim 5 \dots 50$ in influence of Reynolds number on heat transfer coefficient is not high.

As air viscosity equals $\mu_\delta/\mu_w = (T_\delta/T_w)^{0.7}$, the coefficient $(\rho_\delta\mu_\delta/\rho_w\mu_w) \sim (T_\delta/T_w)^{0.1}$ does not introduce a noticeable contribution to the error in heat transfer coefficient determination. If writing α/c_p as

$$\frac{\alpha}{c_p} \sim (\rho_w\mu_w V)^{1/2} \sim (\rho_w\mu_w)^{1/2} \left(\frac{2\Delta p}{\gamma\rho_\delta} \right)^{1/4} \sim (\rho_w\mu_w)^{1/2} \rho_\delta^{-1/4} \left(\frac{\Delta p}{\gamma} \right)^{1/4}$$

it could be concluded that error in determination of γ and Δp about 30...40% comes only to insignificant (7...10%) error in heat transfer coefficient and so in calculated enthalpy H_0 .

In order to measure heat flux to copper probes the copper calorimetric sensors were used equipped with chromel-alumel or chromel-copel thermocouples. The sensors operate in regular mode.

The calorimetric probe consists of a hemisphere of 24 mm in radius. The copper calorimeter is located at the stagnation point of the hemisphere. The calorimeter is made of copper of high purity, 3 mm in diameter and 3.5 mm in height. The chromel-alumel thermocouple (wire diameter equals 0.2 mm) is calked into the calorimeter. The thermocouple measures the temperature of the calorimeter T_w . The probe is inserted into working flow for $\tau=1.5-2$ s. During this time the temperature of the calorimeter grows in 50 – 80°C.

In order to measure high heat fluxes (up to 5 MW/m²) it is used a calorimetric probe of water -flowing type. In Fig.101 such calorimetric probe is presented before and during experiment.



Fig. 101. Calorimetric probe for measurement of high heat fluxes before and during experiment

The measurement of heat flux by calorimetric sensors is based on the measurement of rate of temperature increment. The heat flux, which comes to sensor surface from boundary layer, is proportional in regular mode to the rate of temperature increment ($q_w \sim dT_w/d\tau$). Accuracy of such measurements equals $\pm 8\%$.

In order to predict plasma flow parameters using the set of measured values the iteration procedure was developed, which used a code for numerical computational of non-equilibrium boundary layer on the body with low -catalytic surface.

The main stages of this procedure are following:

1. The zero approach is given for H_0 . The value of gas velocity in the stream is determined using the measured value of Δp .
2. A series of computations of boundary layer on hemisphere $R = 24$ mm in radius is made for various H_0 until calculated and measured values of heat flux becomes equal.

Then the value of velocity is precised according to p. 1. Convergence becomes after 3-4 iterations .

The values of heat flux and parameter distribution near probes and models in subsonic flow if HF-plasmatron are calculated using numerical solution of equations for boundary layer.

These equations for chemically non-equilibrium laminar multi-component boundary layer for planar ($v=0$) or axisymmetric ($v=1$) bodies take the form:

$$\begin{aligned}
 \frac{\rho U}{H_y} \frac{\partial U}{\partial x} + \rho V \frac{\partial U}{\partial y} &= -\frac{1}{H_y} \frac{\partial P}{\partial x} + \frac{1}{r^v H_y^2} \frac{\partial}{\partial y} \left(r^v H_y^2 \mu \left[\frac{\partial U}{\partial y} - \frac{KU}{H_y} \right] \right) \\
 \frac{\partial(\rho U r^v)}{\partial x} + \frac{\partial(\rho V r^v H_y)}{\partial y} &= 0 \\
 \frac{\rho U}{H_y} \frac{\partial \mathcal{C}_k}{\partial x} + \rho V \frac{\partial \mathcal{C}_k}{\partial y} &= -\frac{1}{r^v H_y} \frac{\partial}{\partial y} (J_k H_y r^v) + W_k, k=1,2,\dots,N \\
 \frac{\rho U}{H_y} \frac{\partial \bar{\alpha}}{\partial x} + \rho V \frac{\partial \bar{\alpha}}{\partial y} &= \frac{1}{r^v H_y} \frac{\partial}{\partial y} \left(r^v H_y \lambda \frac{\partial T}{\partial y} \right) + \frac{U}{H_y} \frac{\partial P}{\partial x} + \mu \left(H_y \frac{\partial}{\partial y} \left(\frac{U}{H_y} \right) \right)^2 \\
 &\quad - \frac{1}{H_y r^v} \frac{\partial}{\partial y} \sum_{k=1}^N i_k J_k \\
 P &= \frac{\rho}{M} RT, i = \sum_k C_k i_k, J_k = -\rho D_k \frac{\partial \mathcal{C}_k}{\partial y}
 \end{aligned} \tag{5}$$

where U, V – velocity components along x – axis (along the body) and y – axis (normal to the body surface), C_k – species mass concentrations, W_k – chemical source term, i_k – enthalpies of species, μ, λ, D_k – transport coefficients, J_k – diffusion flow of k – component, $H_y = 1 + Ky$ – metric coefficient, K – surface curvature, M – mixture molecular mass, R – gas constant, r – distance from the body axis. Reactions of nitrogen and oxygen dissociation, exchange reactions with nitrogen oxide and reactions of NO^+ are taken into account during solution this set of equations.

Transport coefficients for the gas mixture are evaluated on the basis of wellknown relationships of molecular kinetics.

At the stagnation point of a blunted body these equations reduce to a system of ordinary difference equations and just these equations are solved for specification of required parameters.

At the body surface the velocity components are assumed to be equal to zero (no slip and no blowing). The wall temperature are assumed to be known $T_w = T_w(x)$ or derived from equation of heat balance. The wall is supposed to be catalytic with respect to recombination of O and N atoms, so the boundary condition for concentrations is the following.

$$J_A = K_w \rho \mathcal{C}_A = \frac{2\gamma_A}{2 - \gamma_A} \rho \mathcal{C}_A \sqrt{\frac{RT_w}{2\pi M_A}}$$

where $A = \text{O, N}$; γ_A – recombination probability.

The following parameters of free stream should be known to solve the problem:

- jet stagnation enthalpy H_0
- pressure p
- velocity gradient $(dU/dx)_0$ (or jet velocity U and equivalent model radius R_{eff})

- mass species concentrations c_k .

The equations, together with the appropriate boundary conditions, are integrated by an implicit weighted finite-difference scheme.

The experiments are carried out for subsonic mode of the plasmatron with nozzle outlet of 180 mm.

In Fig.102. the general view of the plasmatron during the experiment is presented.



Fig. 102. The general view of the plasmatron during the experiment

Total number of experiments equals 18, three experiments per each flow regime. The experiments are carried out according to the following procedure.

The probes for measurements of heat flux and pressure difference are mounted into the working chamber using insertion mechanisms.

The doors of the working chamber are shut down. The air is pumped out from the facility by a vacuum pump until the pressure becomes about 1 mbar.

The HF-generator is turned on in accordance with technological instructions: first of all the water pumps are turned on for water cooling of inductor, generator tubes, diffuser and heat exchanger of the facility, after that the voltage is supplied to the electric circuits.

After heating generator tubes the initiation of discharge in the discharge channel is carried out feeding high frequency voltage to the inductor.

After HF-discharge has arisen, the operator set regulation parameters, required for providing a prescribed regime. Another operator set a proper debit flow rate of plasma forming gas - air or nitrogen. The monitoring for pressure in the working chamber is realized with pressure transducers.

After reaching the required regime of the plasmatron the probe for heat flux measurement is inserted into the stream for 1sec, then the probe is withdrawn and the probe for measurement of pressure difference is inserted into the stream for 120sec. When measurements are completed, the electric supply to the HF-generator is turned off.

The calculated values of required parameters – H_0 , T , V , ρ , C_N , n_e – are presented in Tables 2 and 3. Oxygen molecules are dissociated for all regimes of plasmatron and mass concentration of oxygen atoms equals $C_0 = 0.23$.

As follows from presented results the heat fluxes increase linearly with increasing of energy supply. Mean square dispersion of such linear approximation is less than 5%.

Table 2

$p=25$ mbar

N, kW	ΔP , Pa	q_{sph} , kW/m ²	H, MJ/kg	V_{jet} , m/s	C_N	ρ , kg/m ³	T_{jet} , K	n_e , cm ⁻³
88	18.4	828	21.7	174	0.31	1.02E-03	5610	8.3E+12
128	36.7	1228	26.5	262	0.44	9.04E-04	5860	1.1E+13
171	56.7	1421	28.0	335	0.47	8.70E-04	5940	1.3E+13

Table 3

$p=50$ mbar								
N, kW	ΔP , Pa	q_{sph} , kW/m ²	H, MJ/kg	V_{jet} , m/s	C_N	ρ , kg/m ³	T_{jet} , K	n_e , cm ⁻³
97	14	993.6	23.1	111	0.34	1.90E-03	5860	2.0E+13
139	23.5	1311	26.5	152	0.43	1.75E-03	6050	2.5E+13
227	34	1628	31.0	191	0.54	1.57E-03	6310	3.5E+13
	32.5	1739						

Error in determination of main parameters of plasma flow is directly related with inaccuracy of heat flux measurements $\sim 10\%$, as well as with inaccuracy in catalycity of copper.

Decrease in copper catalycity down $K_w = 10$ m/s comes to significantly high error $\sim 15\%$ in determination of H_0 . Increase in copper catalycity affects less on the values of predicted parameters than catalycity decrease.

MHD method of plasma velocity measurement

In order to perfect the applied method a number of independent measurements of plasma parameters are scheduled. In particularly the velocity of plasma flow is proposed to measure by magnetohydrodynamic method (MHD). This method allows determining the directional velocities of electrons and ions. In view of plasma quasi-neutrality the velocities of electrons and ions equal one another.

The MHD method of plasma velocity measurement is the following. Two parallel wire, which are called probes, are placed along the flow of ionized gas. Electric potential drop arises between these probes in the presence of magnetic field, which is oriented perpendicularly to the plane of probes. This potential drop is proportional to the velocity of plasma flow. See [21] for more details of this method. According to Ohm law this electric potential drop equals

$$\mathbf{j} = \sigma(\mathbf{E} + \mathbf{V} \times \mathbf{B}) + \rho_e \mathbf{V} \tag{6}$$

where \mathbf{j} and \mathbf{E} – current in probe circuit and electric field intensity between the probes, σ – plasma electric conductivity, \mathbf{V} – directional velocity of charged particles in plasma, \mathbf{B} – magnetic induction, $\rho_e = e(n_i - n_e)$ – density of electric charges in plasma, n_i and n_e – densities of ions and electrons.

In equation (6) it is possible to neglect of the term $\rho_e \mathbf{V}$ due to quasi-neutrality of plasma ($n_e \approx n_i$) and of term \mathbf{j} , because the probes are connected to device with high internal resistance, some orders higher than resistance of plasma between probes, which could be considered as isolated probes in plasma, so the current between probes is a negligible quantity. Thus from (6) follows

$$\mathbf{E} = -(\mathbf{V} \times \mathbf{B}) \quad (7)$$

The relation (6) could be written in absolute units

$$U = VBL \quad (8)$$

where L – distance between the probes, $U = EL$ – tension between the probes due to the MHD effect. Other components of vector production (6) equal zero, because the measurement are made in the location where the magnetic field \mathbf{B} has only one component, which is normal to plasma velocity \mathbf{V} .

The measurement instrument, which is connected to the probes, could record signal, which differs from presented in equation (8) because of non-equipotentiality of plasma and non-uniformity of concentration and temperature distribution. So the instrument readings should corrected as following

$$U = U_B - U_0 \quad (9)$$

where U_B and U_0 voltages at the probes measured by instrument correspondingly at the presence of the magnetic field and at the absence of the magnetic field \mathbf{B} for the same plasma flow, U – voltage between the probes, required for determination of the plasma velocity according to formula (8). The value of correction U_0 in (9) could be expected to be low due to small distance between the probes (~ 10 mm).

The evaluation of U in the formula (8) is made for following parameters: $V=500$ s, $B=4 \cdot 10^{-3}$ T, $L=10^{-3}$ m, gives $U=16$ mV.

Measurement of electron temperature and concentration in plasma by double probe method

The method of double probe was first proposed in [22,23]. This method is used as following: two practically identical small electrodes are inserted into plasma, then the measurements are carried out in order to study the dependence of current in probe circuit via tension between electrodes, this tension to be supplied from external source. Below the consideration is made for cylindrical probes.

The double probe is an isolated system, so total current to this probe from plasma equals zero. The current to each electrode equals the difference between electron current and ion current. While varying the tension between electrodes the potential of each electrode with regard to plasma is set in such manner, that the currents to the electrodes from plasma will equal one another. Irrespective of the tension, supplied to the electrodes, they always are under the negative potential with regard to plasma. The potential of the positive electrode, i.e the electrode with more higher potential relatively to another (negative) electrode, insignificantly exceeds the potential of isolated probe. This is because the current from plasma to the double probe is formed by the ion current of the negative electrode. This current is compensated

generally by the electron current to the positive electrode, which increases exponentially with potential increasing. So the potential of the electrode, which collects electrons, could not greatly differ from floating potential of isolated probe and exceeds it a little. If the potential difference is high enough, then this value practically equals the potential of negative electrode. The value of potential for isolated probe could be estimated using the formula [24]

$$U_{is} = 1.15 \frac{T_e}{11600} \lg(0.5 \frac{M_i}{m_e}) \quad (10)$$

where U_{is} – absolute value of isolated probe potential with regard to plasma in volts, T_e – electron temperature in kelvins, M_i and m_e – masses of ion and electron.

The formula for calculation of the electron temperature T_e was derived in [25]:

$$T_e = \frac{11600}{(dI/dU)_{I=0}} \left(\frac{I_{i1} I_{i2}}{I_{i1} + I_{i2}} \right)_{I=0} \quad (11)$$

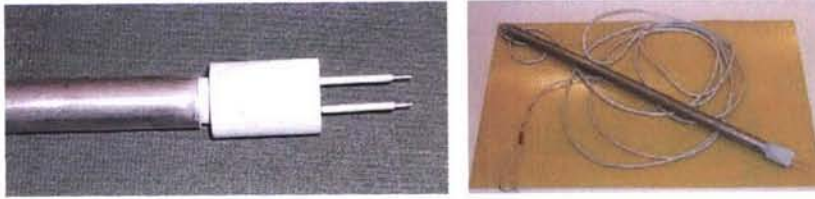


Fig. 103. The double probe

Here the tension U is measured in volts, and currents I_{j1}, I_{j2} – saturation currents to the electrodes 1 and 2 – are measured in arbitrary units. The values in (11) are taken from probe characteristic at $U = \Delta U$ or at $I = 0$. In practice in non-equipotential plasma it is more convenient to use the condition $I = 0$.

The concentration of electrons, n_e , is determined according to Bohm formula for cylindrical probe

$$I = 0.4en_e \sqrt{2kT_e / M_i} S_c$$

where I – ion saturation current to the negative electrode, e – charge of electron, k – Boltzmann constant, $S_c = 2\pi R_c L + \pi R_c^2$ – total collecting surface of the electrode, L – length of the electrode, R_c – radius of the near-electrode layer, which collects ions. As a first approximation for the negative charged electrode it could be assumed $R_c = R_0$, where R_0 – radius of the probe. For more precise calculations the radius R_c is chosen as higher value between two values: $(R_0 + D)$, where D – Debye radius, and layer value according to the "three second" law [24].

The plasma velocity V is taken into account during probe measurements at $V \geq (3kT_i/M_i)^{1/2}$, where T_i – ion temperature. If the probe is located inside the boundary layer, where plasma flow velocity is much less than free stream velocity, it is possible to neglect this effect.

In Fig.103 there are presented the photos of the double probe, prepared for measurement of concentration and temperature of electrons in plasma flow.

Electron density n_e and electron temperature T_e in subsonic plasma, which flows out from the cylindrical channel of High Frequency Plasmatron (HFP), are determined by probe technique. The probes are located in center of plasma flow at the distance of 70mm from outlet opening of the channel. The double probe consists of two electrodes, made of tungsten-rhenium alloy. The initial radius of electrodes is $R_0 = 0.25$ mm, and their length equals $L = 5$ mm. Before and after every test the diameters and lengths are measured because of electrodes erosion in plasma flow as well as ceramics tube erosion, used for insulating of electrodes. The distance between the electrodes equals 8 mm. The general view of the double probe is presented in Fig.104.

The scheme of runs and measurements is given in Fig.106. In the runs there are

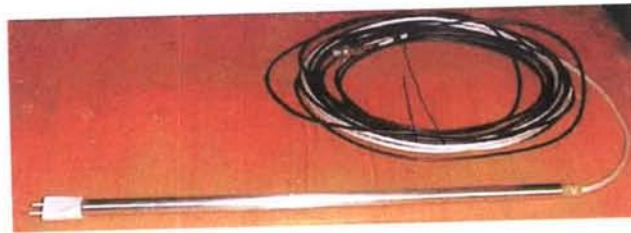


Fig. 104. Double probe for electron density and electron temperature measurements.

used sawtooth-voltage generator G6-34, memory digital oscilloscope S9-8, which are fed from power supply network through isolating transformer. This transformer is used to avoid electric currents between measuring circuit and ground. The current and voltage on the probe are recorded by the oscilloscope S9-8, the current signal being taken from high-precision measuring resistor $R = 20\Omega$. The noise bridging owing to the HFP is made using capacitors $C_I = 0,1$ mF and $C_U = 0,01$ mF in the circuits of current and voltage.

The photo of the probe in plasma flow during the run is presented in Fig.105.

In these runs the air is used as the working gas. The four regimes of the HFP



Figure . 105. The probe in plasma flow

are studied according to Table 4. Here p , T , V are pressure, temperature and velocity of plasma flow accordingly at the HFP outlet, W is the power of oscillator for given run.

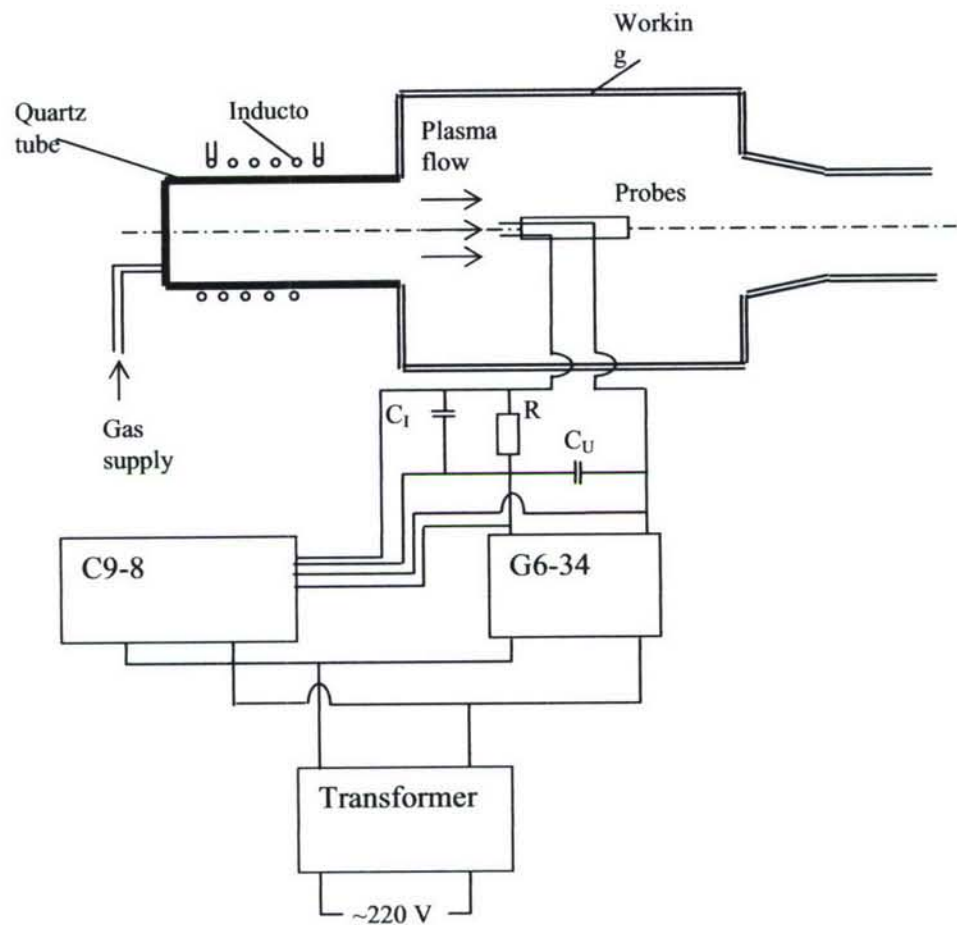


Fig. 106. Scheme of runs and measurements.

Table 4

Regime number	W , kW	p , N/m ²	T , K	V , m/s
1	100	1000	5500	500
2	200	1000	6000	700
3	100	3000	5500	200
4	200	3000	6000	300

Table 5

Regime number	principal ion	M_i	σ_{in} , m ²	λ_{in} , mm
1	O ⁺	16	$33.4 \cdot 10^{-20}$	0.23
2	O ⁺	16	$32.7 \cdot 10^{-20}$	0.25
3	NO ⁺	30	$16.0 \cdot 10^{-20}$	0.16
4	O ⁺	16	$32.1 \cdot 10^{-20}$	0.086

Some kinds of ions and neutral components are formed in the HFP due to dissociation and ionization processes. The neutral components and ions are assumed to be in thermodynamic equilibrium as regard to their temperature. In every regime there is a principal ion component, which gives the main contribution in electron formation as compared with other ion components. In Table 5 there are given the principal ions and their molecular weight M_i , section s in and free length σ_{in} , averaged according to collisions with neutrals O, N, N_2 , which concentrations in plasma flow are higher, then concentrations for other neutrals. The values for cross-sections are taken from [26-29].

The free length λ_{in} is calculated as $\lambda_{in}=1/(n\sigma_{in})$, the total density n of particles

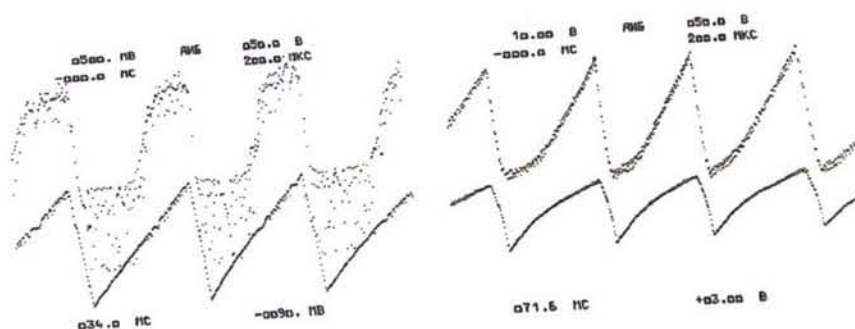


Figure 107. Probe characteristics for regimes 1 (a) and 4 (b)

is determined from relation $p = nkT$, where Boltzmann constant is $k = 1,38 \cdot 10^{-23}$ J/K.

The collisions between ions are neglected because the plasma is assumed to be weakly ionized.

According to Table 3 the free length of ion is less than probe radius $\lambda_{in} \leq R_0$ for all regimes. This situation is intermediate between low density plasma ($\lambda_{in} \ll R_0$) and high density plasma ($\lambda_{in} \gg R_0$). Therefore the experimental data handling is performed using the formulae as for low density so for high density weakly-ionized plasma. In order to predict the value n_e and T_e the voltage-current characteristics of the probe are recorded using measuring scheme (see Fig.106) at the frequency range 15 - 20 Hz. The typical characteristics are given in Fig.107 for regimes 1 and 4.

The upper curve corresponds to the probe current, the lower curve - to the sawtooth voltage, supplied by the generator G6-34 to the probe, the upper part corresponding to the positive voltage, and the lower part corresponding to the negative part. The characteristics look like characteristics for single probe, but not for double probe. This fact is due to the generator operation. The generator alters the potential of its output electrode relative to its second electrode, which is connected to the generator case, so it is under constant potential. The probe electrodes are connected to the generator electrodes and reproduce their potentials.

The ion current for regime 1 is very unstable, so the data are handled using least-squares method. In regime 4 it can be seen the incomplete electron branch of characteristic for single probe because of limited current of generator (~150 mA). The ion branches of characteristics are used to predict n_e and T_e . Only for regime 1 the temperature T_e is determined using electron branch of characteristic.

The electron temperature for low density plasma and for high density plasma is predicted from the probe characteristics using the same formulae [24]

$$T_e = \frac{e}{k \cdot \operatorname{tg} \alpha} \text{ or } T_e = \frac{11600}{\operatorname{tg} \alpha} \quad (12)$$

$$\operatorname{tg} \alpha = \Delta \ln(dI / dU) / \Delta U \quad (13)$$

i.e. the electron temperature is calculated using slope of the curve $\ln(dI/dU)$, where I and U are measured in arbitrary units, in dependence on voltage U , measured in volts. Here $e=1.6 \cdot 10^{-19}$ K is the electron charge.

The electron concentration in low density plasma is determined using Bohm's formula for cylindrical probe:

$$I_i = 0,4en_e \sqrt{2kT_e / m_i} S \quad (14)$$

Here I_i – ion saturation current, $m_i = 1,66 \cdot 10^{-27} M_i$ – ion mass, where M_i is taken from Table 2, $S = 2\pi R_0 L + \pi R_0^2$ – total surface of the probe.

The electron concentration in high density weakly-ionized plasma is determined using relation [23] for cylindrical probe

$$n_e T_e = \frac{I_i p \sigma_{in}}{0,24\pi(2L + R_0)ek} \left(\frac{m_i}{2kT} \right)^{1/2} \ln \frac{L}{R_0} \quad (15)$$

where p and T are taken from Table 2, and section σ_{in} – from Table 3. It should be noted that formula (4) is applied for high density weakly -ionized plasma.

As result of handling experimental probe characteristics for regimes 1 - 4 the concentrations of electron are calculated at $\lambda_{in} \gg R_0$ and $\lambda_{in} \ll R_0$ and they are given in Table 6.

Table 6

Regime number	T_e , K	n_e , cm^{-3} at $\lambda_{in} \gg R_0$	n_e , cm^{-3} при $\lambda_{in} \ll R_0$	$n_{e, \text{average}}$, cm^{-3}
1	32000	$1,0 \cdot 10^{12}$	$2,2 \cdot 10^{12}$	$1,6 \cdot 10^{12}$
2	40000	$1,8 \cdot 10^{13}$	$3,0 \cdot 10^{13}$	$2,4 \cdot 10^{13}$
3	36000	$6,7 \cdot 10^{12}$	$1,7 \cdot 10^{13}$	$1,2 \cdot 10^{13}$
4	29000	$2,8 \cdot 10^{13}$	$1,6 \cdot 10^{14}$	$9,4 \cdot 10^{13}$

It can be seen from Tables 6 and 4 that while pressure and power consumption increase the electron density increases independently on technique of handling. The difference is the greater the higher pressure of plasma. In the last column of Table 6 there is given the electron density n_e averaged through two considered values.

Spectral Diagnostics

For diagnostics of a plasma air jet two systems of spectral measurements of relative and absolute intensity of radiation of high-temperature air are used in the region of a spectrum from 230 up to 1100 nm. The scheme of experiment is given in Fig.108. The first system, representing at lower part of Fig.108, includes a series of spectrometers of high resolution with fiber optics, the positioning system with fixed on

it the optical lens at an optical fiber aperture, the stepwise motor and, computer with the software, on which input the signal from a spectrometer output is supplied.

Depending on a problem a spectrometer is used with the necessary resolution, spectral range of sensitivity in a total wavelength range of 210 up to 1100 nm and time of registration. Time of registration of a spectrum may be done from 3 ms up to 60 s.

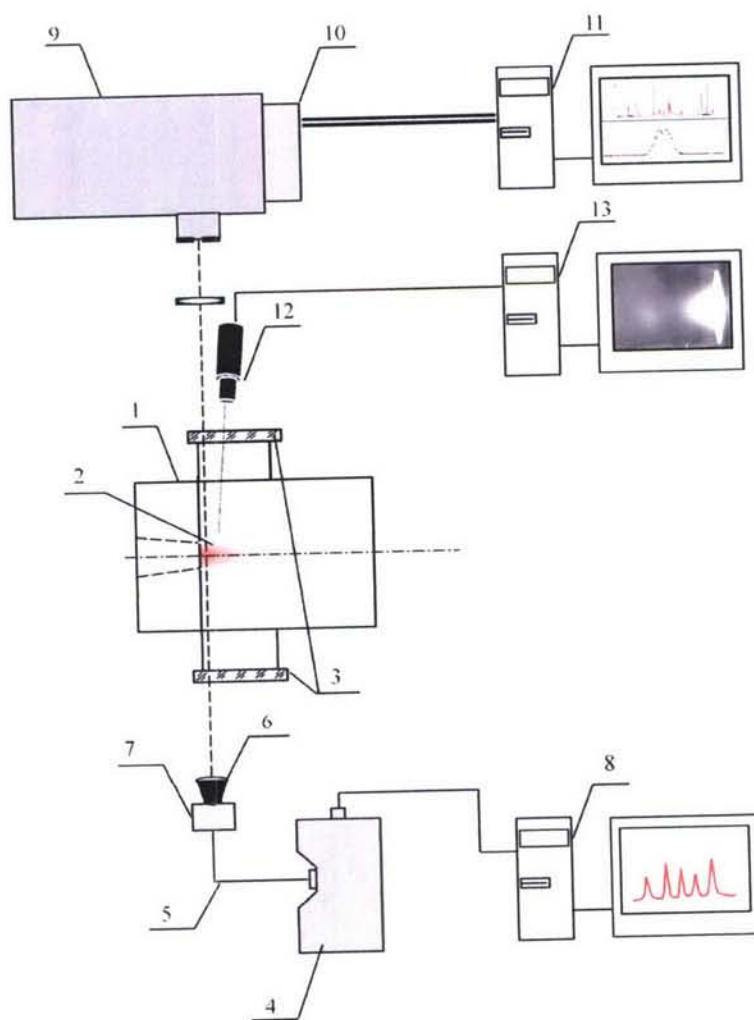


Fig.108. Optical measurement scheme

1 – Chamber, 2 – Plasma air jet, 3 – Quartz window, 4 – Fiber optic spectrometer with linear CCD array, 5 – Optical fiber 0.6mm, 6 – Collimating lens, $f=100$ mm or 10 mm, 7 – Positioning system with stepwise motor, 8 – PC, 9 – Spectrograph DFS 452, 10 – Multichannel spectra registration MORS-2, 11 – PC with the interface card, 12 – Frame capture system, 13 – PC

The angular resolution of the used lenses is equal $6 \cdot 10^{-3} \dots 6 \cdot 10^{-2}$ and its linear resolution - up to 1 mm.

The positioning system with the stepwise motor and fixed on it lens of given fiber provide scanning a flow in the chosen section. The minimal step of scanning -5 microns. The system for spectral measurements (Fig.9) consists of a diffraction spectrograph DFS-452 (5) and a multichannel optical spectrum analyzer MORS-2. The analyzer incorporates two photometer heads with photodiode CCD arrays (TDS1250A by Toshiba) (6). The heads are connected by a cable with the interface card plugged into PC. Each photodiode array (PDA) comprises the 12-digital-to analog converter

In the spectrograph, the diffraction gratings of 600 and 1200 grooves per mm are used, which provide reciprocal linear dispersion of 1.6 and 0.8 nm/mm, respectively.

Both PDA are fastened to a plate that has the same size and shape as a spectrograph cassette and takes the place of the cassette. Each PDA contains about 3700 photosensitive elements 8 μ m in length and 200 μ m in height. The spectral region of the sensitivity is 190-1000 nm. The spectrum recording time changes in a discrete way and may be varied from 20 to 1000 ms. One of the PDAs is used to record a spectrum, while the other PDA allows measuring the intensity distribution across the plasma jet at a given wavelength.

Video Monitoring System

The system for input of images VS_CTT-249/S/E-2001 comprises a digital camera VS-CTT-249 (3), a controller of input/output of images VS-2001 inserted into PCI bar of PC (8) and possesses the following parameters:

number of working elements	742.580
size of the sensitivity region	6.4 \times 4.8 mm
frame repetition frequency	50 Hz
frame exposure time	2.7 μ s-20s
digital-to-analog converter	10 bits
volume of the working memory	16 Mb
of the input/output controller	
spectral sensitivity of VS-CTT-249	350-850 nm

All camera parameters (exposure, option of the matrix working region) are set by the controlling program and may be changed during the recording process.

Spectra interpretation and plasma diagnostics methods

As an example in Figs.109, 110 the spectra of a plasma air jet of U-13 facility at a range from 350 up to 1040 nm, obtained by means of the first system, are given. Mode of plasma generator operation: power $W = 100$ kW, pressure - 0.6 atm. The results of an identification of a spectra and recommendations for their use for diagnostics of plasma consist in the following:

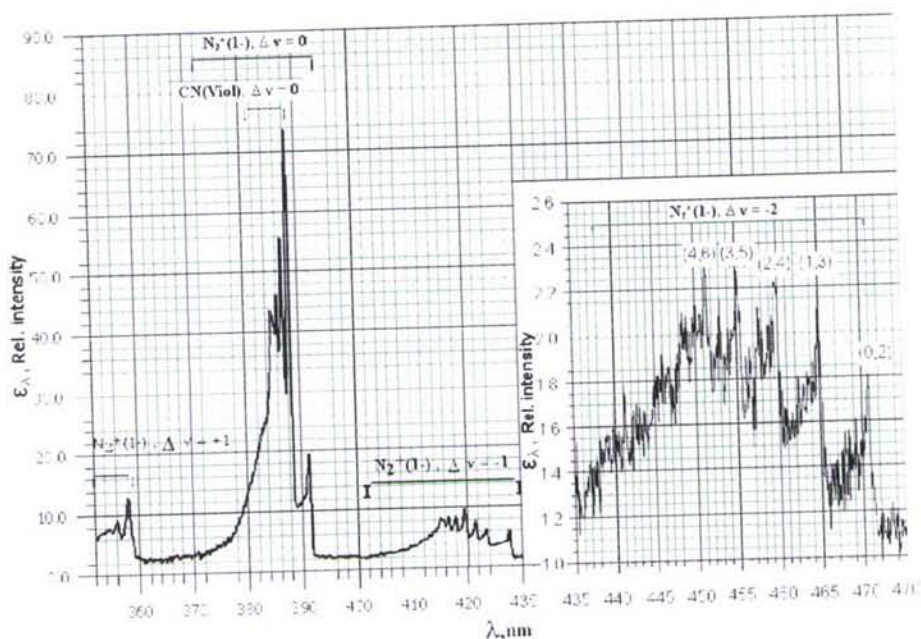


Fig.109. Plasma jet spectral radiation in the near UV- and the visible ranges. Exposure time for the left spectrum is 30 ms, spectral resolution 4 \AA , for right spectrum is 3 ms and 0.4 \AA accordingly

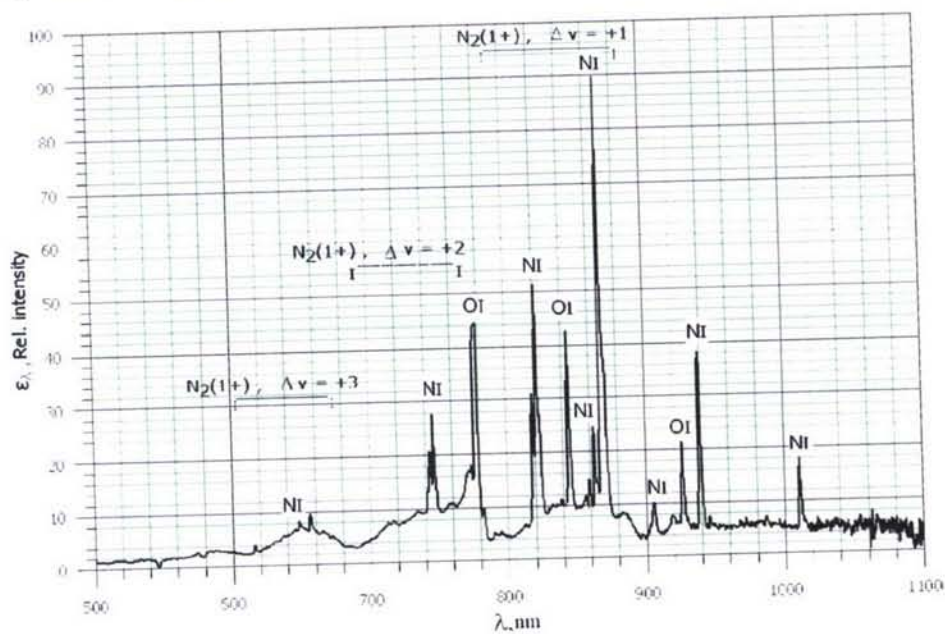


Fig.110. The same for visible and near IR range. Spectral resolution 4 \AA

In the spectrum the intensive electronic, vibrational and rotational structure of the bands of first negative system of the ion $\text{N}_2^+(\text{B}^2\Sigma_u^+ - \text{X}^2\Sigma_g^+)$ (region of the spectrum

from 340 up to 475 nm) and first positive system of the molecule N_2 ($B^3\Pi_g - A^3\Sigma_u$) (region of the spectrum from 500 up to 900 nm) is observed as belonging to hightemperature air.

In a spectrum intensive lines of oxygen and nitrogen atoms (region of a spectrum from 700 up to 1100 nm) with high energy of excitation ~ 10 -14 eV also are observed.

In electronic vibrational and rotational spectra N_2^+ and N_2 the bands with high energy upper vibrational level $v \geq 4$ are observed, that it is possible to use for accurate definition of the appropriate vibrational temperatures. In the N_2^+ (1-) bands the unresolved rotational structure of vibrational bands is observed (for an example in Fig.110 the ro-vibrational structure of a series of bands with $\Delta v = v' - v'' = -2$ is shown as registered by the equipment having the spectral resolution 0,04 nm).

Along with a spectrum of radiation of air plasma components in the bands there are observed admixture molecular bands of ultra-violet OH system ($A^2\Sigma^+ - X^2\Pi$) ($\lambda\lambda = 300 - 350$ nm), NH band ($A^3\Pi - X^3\Sigma$) ($\lambda\lambda = 335$ -340 nm), CN UV-bands CN ($B^2\Sigma^+ - X^2\Sigma^+$) ($\lambda\lambda = 388.3$ nm and 418.1 nm) etc. The well resolved rotational OH spectrum of a band (0,0) will be used for determining of rotational temperature. The spectra of easy ionized impurities are not revealed.

The air plasma emission spectra taken in the 230-1000 nm region are abundant in vibronic bands belonging to different diatomic molecules and molecular ions (N_2 , OH, CN, N_2^+ , NO, some others). Besides, in the red end near IR-region (700-1050 nm), a number of relatively strong NI and OI lines are observed. Together, this allows the assessment of basic plasma parameters using the well-developed methods of quantitative spectroscopy.

1. The electron temperature, T_e , can reliably be derived from the NI (OI) line intensity ratios using the Boltzmann exponent method, because in the spectrum there exist the lines corresponding to the transitions between the atomic levels spaced by the energy gaps of more than 2 eV, whereas the expected T_e -values are estimated to approach 0.5 eV. Those lines are as follows: NI ($\lambda = 746.9, 821.6, 824.2, 868.6, 904.6, 938.7$ and 872.9 nm) and OI ().

2. The electron number density, n_e , may in principle be determined by the Stark half-widths of the Lorentz components extracted from the Voigt profiles of the recorded NI (OI) lines. The used measuring technique does allow the line profiles to be taken with the required spectral resolution. However an appreciable Doppler and apparatus broadening, typical of the present conditions, offer great difficulties for this procedure to be practically realized. Much more realistic approach seems to consist in determining nevalues from the Boltzmann-Saha distribution of atoms over the higher energy levels when its being extended to the continuous spectrum.

3. The rotational temperature, T_r , will have been determined through the line-byline numerical simulation of the rotational structure of (0-0), (0-1), and (1-2) bands of the N_2^+ First Negative System (electronic transition $B^2\Sigma_u^+ - X^2\Sigma_g^+$) to best fit the measured and calculated spectra. The band heads are 391.4, 427.8, and 423.6 nm, respectively. If necessary, allowance will be made for the N_2^+ $B^2\Sigma_u^+ - X^2\Sigma_g^+$ (1-1) band and for the principal sequence $\Delta v = 0$ of the CN "violet" system superimposed on the vibronic bands above-mentioned.

4. The vibrational temperature, T_v , will be derived by two methods. The first one is a global fit of the spectral regions of the sequence $\Delta v = -1$ of the N_2^+ 1- system allowing for the superimposed sequence $D = -1$ of the CN "violet" system. The second method consists in determining the temperature of population of low-lying vibrational levels of N_2 and N_2^+ using the integrated intensities of vibronic bands forming the sequence $\Delta v = -1$ of the N_2 Second Positive System (transition $C^3\Pi_u \rightarrow B^3\Pi_g$) and the sequence $\Delta v = -2$ of the N_2^+ First Negative System.

5. The translation temperature, T_m , of heavy components of the investigated air plasma is assessed assuming $T_m = T_r$. The obtained values will be compared to those derived from the Doppler half-widths of the IR-lines of NI and OI.

6. The populations of vibrational levels, N_v , may be derived starting from the sum S of the integrated intensities of the rotational lines falling into the narrow spectral region in the vicinity of the band head. Because the characteristic rotational temperatures are sufficiently high, this sum is practically independent of T_r -values and $S = C \cdot N_v / T_r$, where C depends only on molecular constants and the Honl-London factors. Thus given T_r , one immediately arrives at the sought quantity of N_v . There can also be drawn some inferences about the populations of the irradiating electronic terms of the diatomic components.

The preliminary analysis of the ro-vibrational spectrum N_2^+ has shown, that the vibrational and rotational temperatures are close on value and equal $\sim 6400 \pm 200K$.

6. SPECTROSCOPY OF THE AIR PLASMA ENVIRONMENT AT THE MODEL SURFACE

. Measurement system

For diagnostics of the plasma environment at a surface of model the system of spectral measurements of relative and absolute intensity of radiation of high-temperature air is used in the spectrum region from 230 up to 1100 nm. The experimental system and its general view are given in Fig.111 and 112, accordingly.

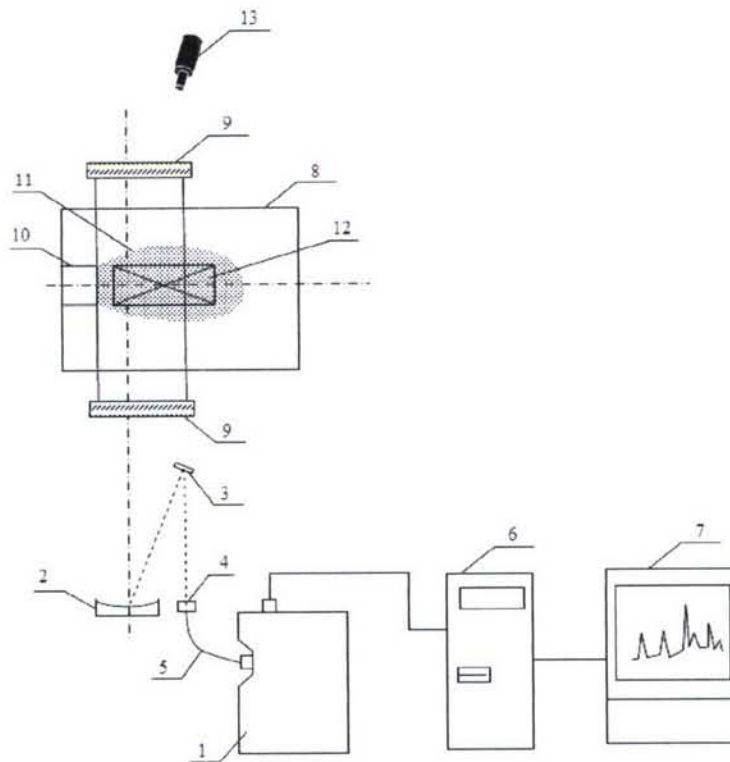


Figure 111. 1 - spectrometer with fiber optics and the detector - CCD-RULER, 2 - spherical mirror with focus $f = 1300$ mm, 3 - rotary mirror, 4 - position ruler with step-by-step engine, 5 - quartz fibre diameter of 0.6 mm, 6 - personal computer, 7 - monitor, 8 - chamber, 9 - quartz windows, 10 - flat nozzle, 11 - plasma jet, 12 - model, 13 - registration system of plasma images.

The measurement system includes a two-channel spectrometer with fiber optics (1), a spherical mirror ($f = 1300$ mm) (2), a rotary mirror (3), a position ruler with the step-bystep engine (4) and the optical fiber fixed on it with diameter of 0.6 mm (5) and a computer with the software (6) on which input the signal from an output of a spectrometer moves. The spherical mirror is on a double focal length from an axial line of model and projects the image of plasma with scale 1:1 at the plane of the end face of the optical fiber. Thus the line-of-sight passes parallel to the model plane and is perpendicular its axes on distance of 1 mm from model.

The position ruler with the step-by-step engine and the optical fiber fixed on it provides scanning a stream in the chosen section. The spatial resolution at scanning makes size $0,6 \pm 0,2$ mm.



Figure 112. The model in the plasma flow

Identification of spectra and its use for plasma diagnostics

Plasma diagnostics was carried out near to a surface of an external MHDG model. As the MHDG model the flat plate with electrodes on its surface and having the sizes 250 ± 400 mm was used. The model was made of a dielectric and heat protective

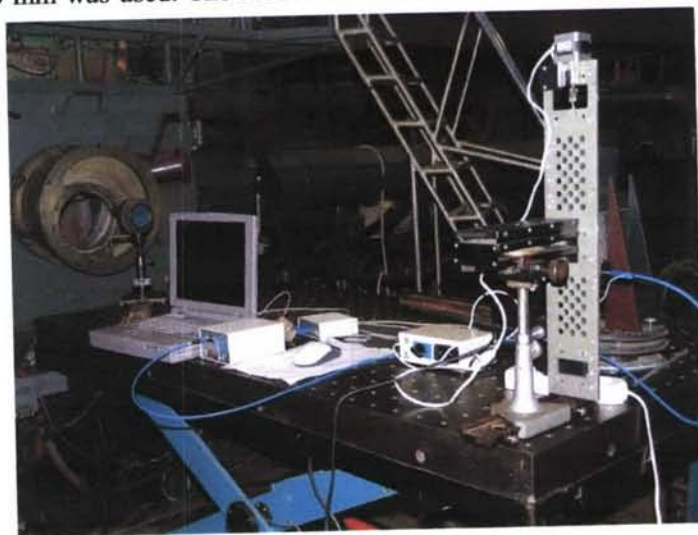


Figure 113. A general view of measurement system.

material and was placed under a angle of attack $\sim 5^\circ$ in a plasma flow expiring from plasmotron through flat nozzle. In Fig.113 the photo of this model during experiment is presented.

Upstream edge of model and working section, in which the shooting of the spectrum was recorded, are located in 70 and 200 mm from the nozzle edge, accordingly.

As examples in Fig.114 and 115 the spectra of a plasma air jet near a model wall at the distance 0.6 mm from its surface are given. The spectra are taken at a plasma generator regime: the power $W=100$ kW and pressure $p=0.05$ atm.

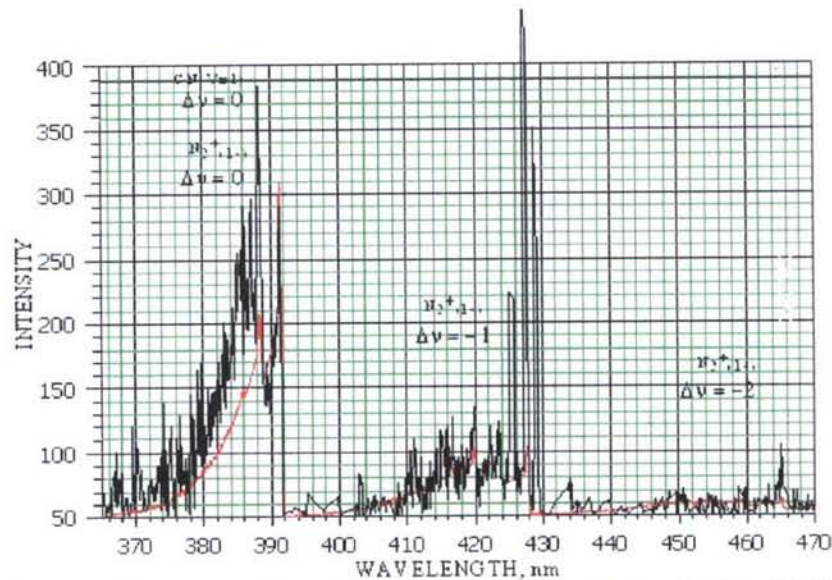


Figure 114. Experiment (black), and calculation (red) spectra. $T_v=T_r=T_{tr}=6400K$

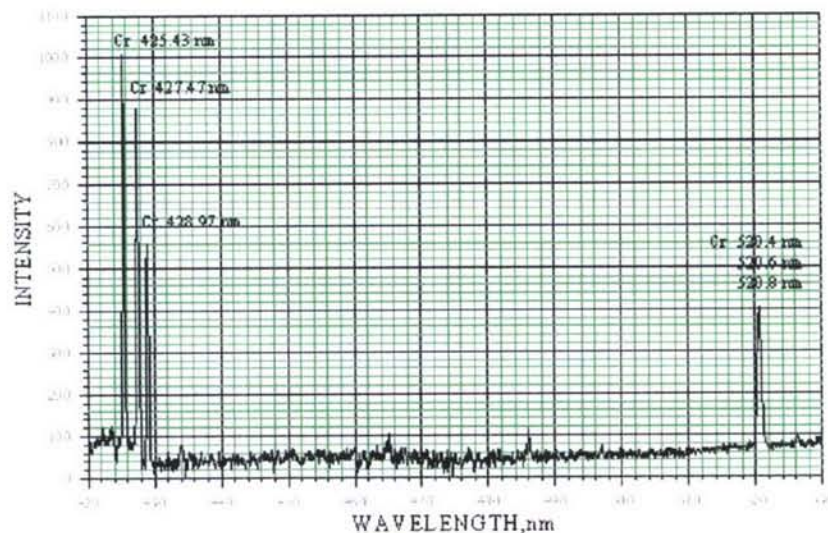


Figure 115.

In the spectrum the intensive electronic - vibrational-rotational band structures of an ion of nitrogen $N_2^+(B_2\Sigma_u^+ - X_2\Sigma_g^+)$ (bands in the region of a spectrum from 340 up to 475 nm with $\Delta v=v'-v''=0, -1, -2$) are observed which are used for diagnostics of plasma.

In the spectrum along with radiation of air plasma also admixture molecular bands of violet system CN ($B_2\Sigma^+ - X_2\Sigma^+$) ($\lambda\lambda$ 388,3 nm and 418,1 nm), and also intensive chromium lines $\lambda\lambda$ 425,43; 427,47; 428,97 nm (multiplet lines $3d^5(6s)4s - 3d^5(6s)4p$) and $\lambda\lambda$ 520,8; 520,6; 520,4 nm (multiplet lines $5d^5(6s)4s - 3d^5(6s)4p$) are observed.

Table 7

No.	λ , nm	$A_{ki}(10^{+8} s^{-1})$	g_k	E_k, cm^{-1}
1	425,43	0,315	9	23498,84
2	427,47	0,307	7	23386,35
3	428,97	0,316	5	23305,01
4	520,45	0,509	3	26801,93
5	520,60	0,514	5	26796,28
6	520,84	0,506	7	26787,50

Chromium lines also were used for diagnostics of plasma. It was preliminary established that these lines are not reabsorbed and radiation in these lines can be considered as well as in molecular model of bands N_2^+ in optically thin approach.

As a whole the registered spectra have allowed to define the following parameters of near-wall plasma:

1) Rotational temperature T_r is determined by numerical modelling of rotational structure (0-0), (0-1), (1-2) of first negative systems N_2^+ when T_r is determined from a condition of the best agreement of the measured and modelled spectra. The wavelengths at sharp edgings of bands are 391.4; 427.8 and 423.6 nm.

2) Vibrational temperature T_v is determined by full modeling of the bands with $\Delta v=0, -1, -2$ in view of their overlapping.

3) The electronic temperature T_e is determined from intensity of spectral lines of chromium atoms. As under conditions of our experiments a population of the top levels is in equilibrium with electronic gas the electronic temperature T_e was determined on relative intensity of multiplet lines under the formula:

$$T_e = 1.4388(E_1 - E_2) \ln \left(\frac{A_1 g_1}{\lambda_1} I_2 \middle/ \frac{A_2 g_2}{\lambda_2} I_1 \right) \quad (16)$$

In the formula: 1, 2 - numbers of lines, A - Einstein factor, g - statistical weight of the top level, E - energy of the top level, I - intensity of a line. The spectroscopic data for chromium lines are given in Table 7.

Results of the spectral diagnostics

The on-line recording of the jet spectra having been performed with not high resolution (the apparatus width $\sim 0.4\text{nm}$), the overlapped lines CrI 520.54, 520.60, and 520.84nm were not spectrally resolved. The triplet mentioned has however been resolved using a special program developed in [30] (Fig.116). The populations of the

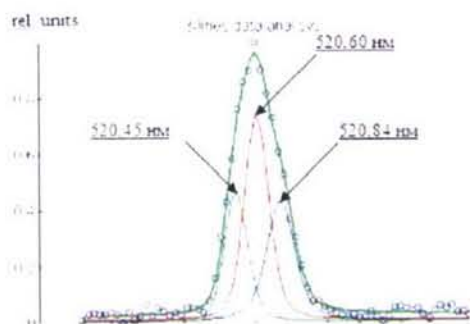


Figure 116. Analysis of the populations of the irradiating states of CrI for determining the electron temperature T_e .

upper levels corresponding to the lines mentioned are given in Table 7 and obtained on the assumption that there exists a quasi-Boltzmann distribution over these levels at the electron temperature T_e (see Fig.117 b,c). The electron temperature thus derived is $T_e = 6200 \pm 1000\text{K}$ of the populations of the irradiating states of CrI for determining the

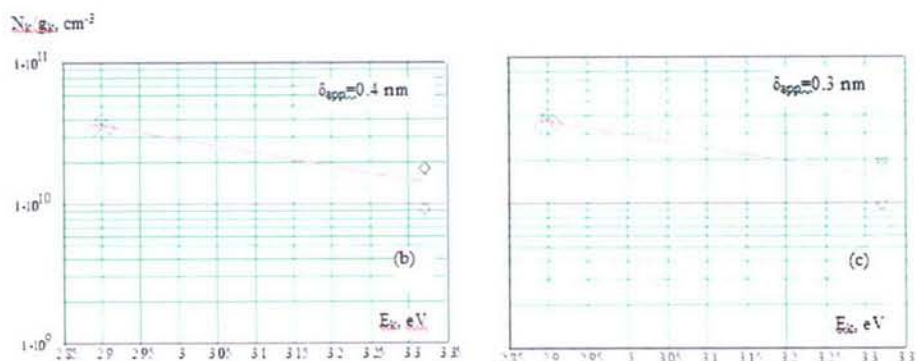


Figure 117 Correlation of experimental and calculated population distribution over two spectral levels.

electron temperature T_e .

In order to determine T_e – values more precisely, the apparatus with a spectral resolution being not worse than 0.1nm should be employed. Besides, additional CrI levels with energy $E_{\text{upp}} = 3.85\text{eV}$ are to be involved to include lines 435.18 and 434.4nm in consideration.

Simulation of the (0-0) band of N_2^+ 1- system in the 388.4-391.4nm region, assuming the rovibronic lines to be shaped by Gauss with the half-width of 0.3-0.4nm typical of the given experiment, has shown that the rotational temperature cannot be

determined satisfactorily from the measured spectrum. Comparison of the measured and simulated summary $N_2^+ + CN$ spectrum in the 384-388.5nm region (Fig.118) allows, however, a fairly realistic estimate for both rotational, T_r , and vibrational, T_v , temperatures. As a result one arrives at $T_r \approx T_v = 6500 \pm 1000K$.

The use of the experimental technique with a higher spectral resolution (0.03-

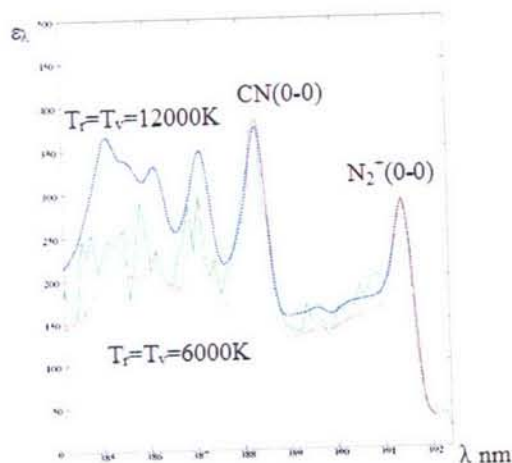


Figure 118 Simulation of the summary spectrum formed by the band (0-0) of N_2^+ 1- system and by the "violet" bands (0-0), (1-1), and (2-2) of CN for determining rotational, T_r , and vibrational, T_v , temperatures

0.05nm) would permit assessment of the rotational temperature T_r by matching the measured and simulated spectra of the N_2^+ 1- system in the not overlapped 388.4-391.1nm region with an accuracy better than 10%.

By this means the results of the given spectral measurements are firmly indicative of that the analysis of the thermodynamic state of the plasma flow investigated requires the spectral resolution of the recording apparatus to be increased by an order of magnitude.

7. NUMERICAL SIMULATIONS OF MHD INTERACTION IN THE TEST SECTION OF HF PLASMATRON

Problem setup

Predictions to the MHD flow in the test section of HF plasmatron were made with the IVT RAN code Plasmaero. The computational domain is clear from Fig.119. The inclined surface, which follows the nozzle exit, simulates the test plate with the electrode system. Electrodes represent the metallic strips directed to the direction

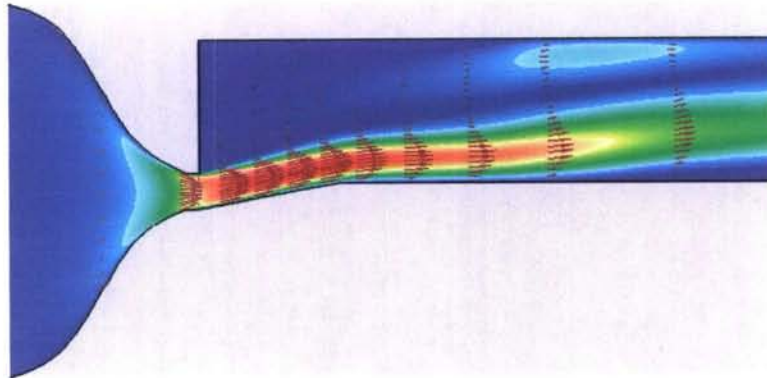


Fig.119. Mach number distribution and velocity field, no MHD.

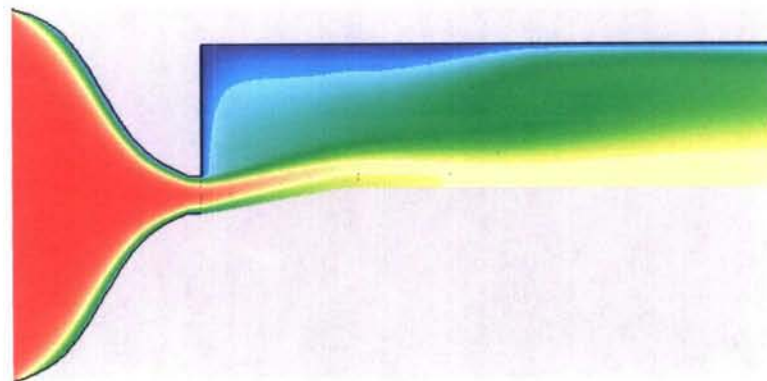


Fig.120. Temperature distribution, no MHD.

normal to the plane of figure. Therefore, the Faraday current is supposed to flow in this direction. It is assumed that the nozzle surface is grounded, and the test section is isolated from the ground. The test plate is also assumed to be electrical insulator.

The computational domain was constructed as follows. The test section geometry is almost same as experimental one. The length of the test plate and angle of attack correspond to the adopted experimental values. The nozzle exit height also corresponds to the real size and equals to 0.05 m. The shape of the nozzle of length of 0.25 m was designed to provide the flow conditions at the nozzle exit close to the experimental ones. The domain of the length of nearly 1 m is a portion of the whole

domain taking part in calculations. The outlet boundary of the domain locates 1 m right of that shown in Fig.119.

The gasdynamic conditions in the test section were computed based on the following considerations. First, the nozzle shape was designed to obtain the static pressure in the test section of the level of 2000 Pa and flow Mach number at the nozzle exit of order of 0.25. Second, the total enthalpy at the nozzle inlet was taken to be 40 MJ/kg. Calculation of equilibrium air composition at pressure 2000 Pa corresponding to specified total enthalpy gives the temperature as high as 6500 K. Then, the following nozzle inlet conditions were specified as the input data for the flow computations. The inlet temperature was taken 6500 K, the inlet velocity was taken 65 m/s, and pressure was extrapolated from the interior. To provide more realistic flow within the test section the outlet cross-section of the domain (right boundary in Fig.119) was moved far from the test section. At this boundary the static pressure 2000 Pa was specified. The wall conditions were specified as follows. The domain boundaries, except the test plate, the wall downstream the test plate, the nozzle inlet and outlet station, were considered as the constant temperature walls, with the temperature 600 K. The test plate and the downstream wall were assumed to be adiabatic.

In general, the finite rate air chemistry could effect on the flow. However, calculations of the reacting MHD flows in large domains are very expensive. Therefore, simplified approach was used in the current study. Namely, the thermodynamic flow data estimated from the at-point calculations of chemical composition of air were fixed in the two-dimensional flow computations. In MHD flow calculations the specific heat ratio was specified as 1.3 and molecular weight of the air was taken as 20. Finally, the electrical properties such as mean electron collision frequency and electron concentration were calculated on the base of approximations of gas temperature build from the equilibrium composition calculations.

The magnetic field in the domain was calculated as follows. Real magnetic system consisting of five thick coils has been considered. Internal diameter of the innermost coil is 0.2 m and the thickness of the coil is 0.01 m. The diameter of each next coil increases on 0.02 m. The geometry and position of the magnetic system is schematically shown in figures below as black-colored rectangle just under the test plate. Such magnetic system generates three-dimensional magnetic field similar to that given by the ideal magnetic dipole. For the flow predictions the magnetic field configuration obtained in the central plane of the test plate is taken as two-dimensional field.

Results

At this stage we shall consider the steady-state magnetic field, and steady-state MHD flows are of primary interest. First, the no-MHD solution is considered as initial guess for the low-value magnetic field. The obtained solution is taken as initial one for higher-value magnetic field and so on. Fig. 119 represents the Mach number distribution and velocity field for the no-MHD case. The Mach number value at the nozzle exit is 0.51 and velocity has the value 870 m/s. The temperature field is shown in Fig.120.

At the nozzle inlet the value 6500 K was specified, and at the nozzle exit the temperature has the value of 6100 K in the central part of the jet coming on the test plate. One feature of the flow in the test section is the presence of large re-circulation

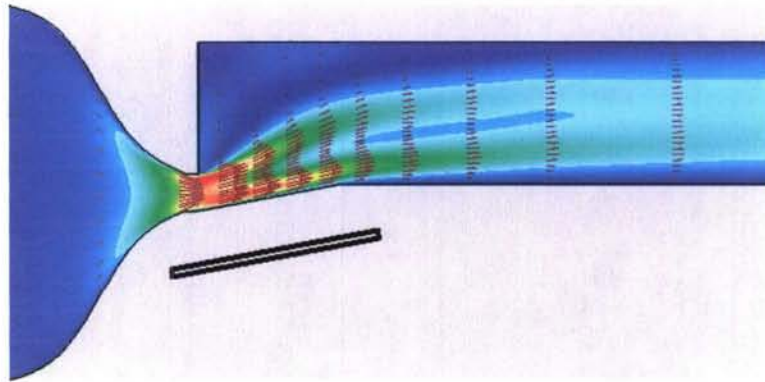


Fig.121. Mach number distribution and velocity vectors, $B = 0.2$ Tesla.

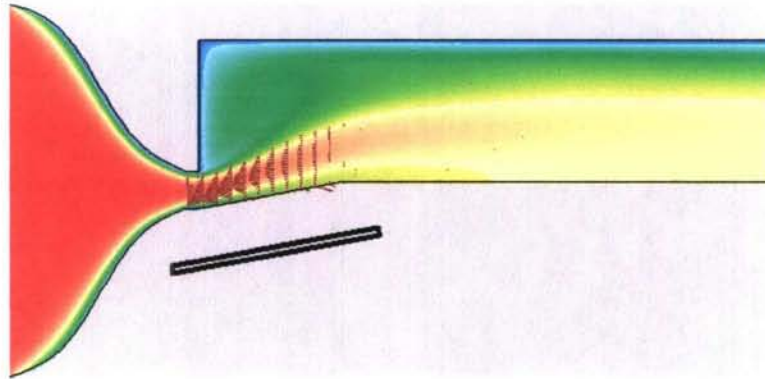


Fig.122. Temperature distribution and electromagnetic force vectors, $B = 0.2$ Tesla.

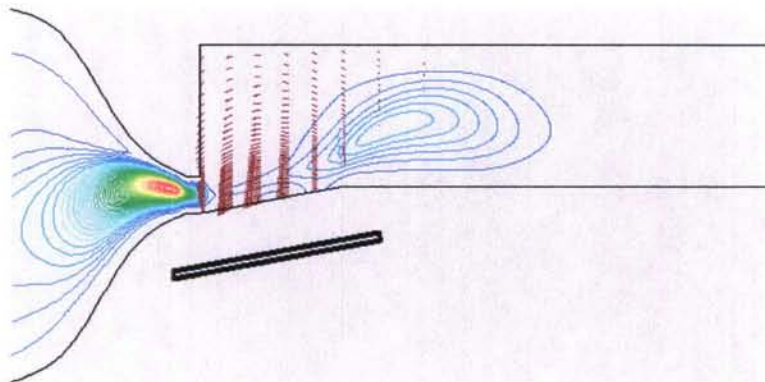


Fig.123. Current streamlines and electric field vectors, $B = 0.2$ Tesla.

zone in upper part of the test section. Second feature is the presence of rather thick boundary layer on the test plate, which potentially may be an obstacle for the electric current flow.

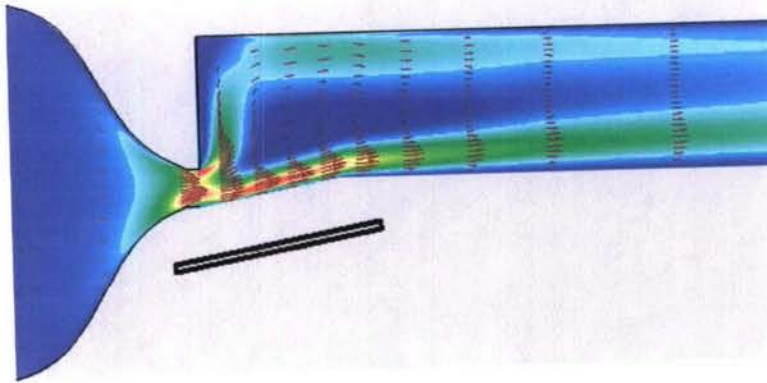


Fig.124. Mach number distribution and velocity vectors, $B = 0.4$ Tesla.

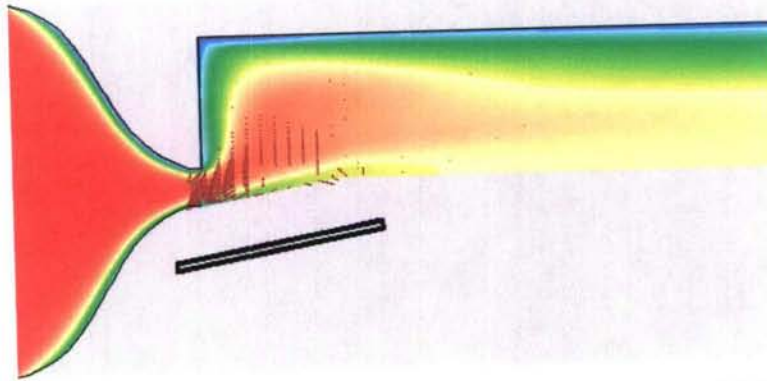


Fig.125. Temperature distribution and electromagnetic force vectors, $B = 0.4$ Tesla.

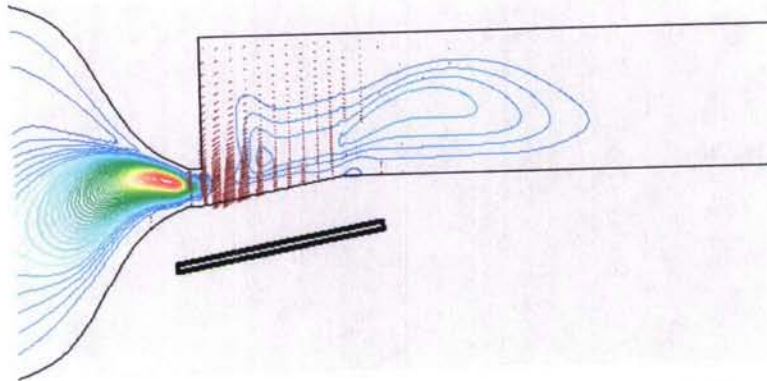


Fig.126. Current streamlines and electric field vectors, $B = 0.4$ Tesla.

Fig.121 through Fig.123 show the flow fields obtained for the lowest considered magnetic field of 0.2 Tesla. Fig.121 represents the Mach number distribution and velocity field. In Fig. 122 the temperature is shown along with the electromagnetic force $[\mathbf{J} \times \mathbf{B}]$ distribution. Fig.123 demonstrates the distribution of the electric potential (colored contours) and electric field strength (vectors).

It is well seen that due to MHD interaction the flow expands outward the test plate. In general the flow decelerates as the force acts against the flow, velocity at the nozzle exit diminishes to 770 m/s. The lower part of the jet above the test plate works

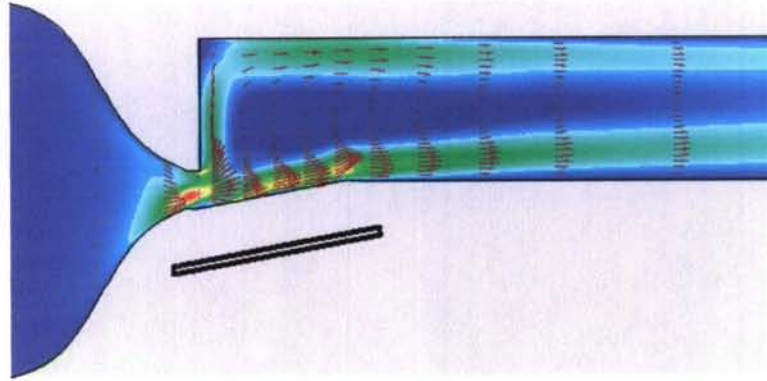


Fig.127. Mach number distribution and velocity vectors, $B = 0.6$ Tesla.

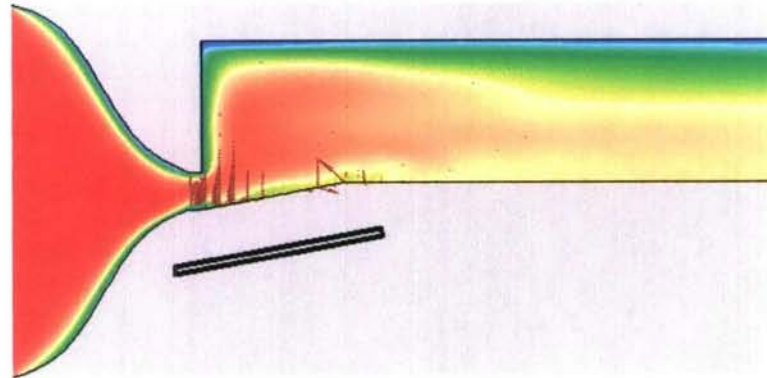


Fig.128. Temperature distribution and electromagnetic force vectors, $B = 0.6$ Tesla.

as the MHD generator, while the upper part represents the MHD break (energy consumes and flow decelerates). Non-uniformities of electrodynamic characteristics take place over the edges of magnetic system, where the magnetic field strongly varies as well as the conductivity diminishes due to drop of temperature along the flow. The current (in the plane of figure) shown in Fig.123 has typical structure for such configurations and boundary conditions structure: two loops of Hall current usually take place left and right of the magnetic system. The electric field shown in Fig.123 by vectors has also typical configuration: it is directed against the flow since the total Hall current is close to zero.

Next set of figures corresponds to the characteristic magnetic field at the surface 0.4 Tesla. Fig.124 represents the Mach number and velocity fields; Fig.125 represents the temperature distribution and electromagnetic force vectors; Fig. 126 demonstrates the electric current streamlines and electric field strength vectors for this case.

While the structure of electrodynamic characteristics is in principal the same as is for the lower magnetic field case, there are remarkable changes in flow structure. Namely, original jet splits on two jets: high-velocity jet flows along the plate as the jet

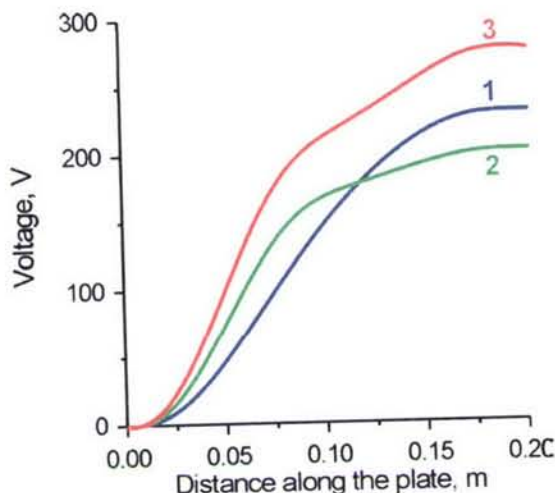


Fig.129. Distribution of voltage along the test plate: 1- $B=0.2$ Tesla, 2- $B=0.4$ Tesla, 3- $B=0.6$ Tesla.

before, and another one goes up. The high temperature zone occupies almost entire volume of the test section. The region of the most intensive interaction moves toward the nozzle. In both these cases the steady states have been achieved. The characteristic time period for the steady state to establish is of order of 5-20 ms.

At higher values of magnetic field induction the steady-state solutions were not achieved. Fig.127 demonstrates quite non-uniform Mach number distribution and velocity vectors for the case of magnetic field value 0.6 Tesla. This is one of the flow realizations corresponding to the time moment 10 ms after the magnetic field was increased from 0.4 to 0.6 Tesla. New features of the flow appear, namely the flow accelerates in the nearwall regions, and the flow separation takes place at the trailing edge of the plate. The temperature distribution and electromagnetic force corresponding to the same moment are shown in Fig. 128. At even higher magnetic fields the non-uniformity of the flow increases, separation zone near the trailing edge rises too. Also full stagnation of the flow may occur at the nozzle exit over short time intervals.

For three cases of constant magnetic field Fig. 129 represents the distribution of electric potential along the test plate. Still monotonous distribution of the potential takes place for the considered cases. However, another situation may take place. As example the MHD flow was considered assuming that lower-temperature, slower flow comes out the plasmatron into the nozzle. Namely, the temperature 6000 K and the velocity 45 m/s are specified at the nozzle inlet. The Mach number value at the test section inlet is 0.25 (maximum). For these conditions the calculations have also been done for several values of magnetic field induction. As magnetic field increases the potential distribution becomes more and more non-uniform. This is accompanied with generation of large re-circulation zone over the test plate. Such flow structures may lead to a current constriction and arcing in real flows.

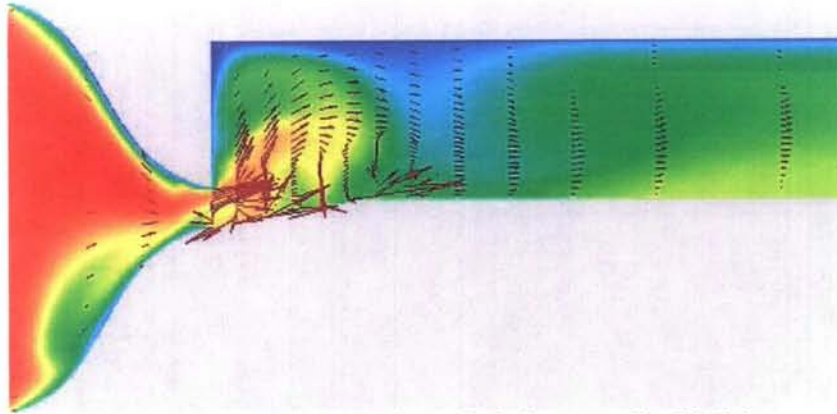


Fig.130. Temperature distribution and velocity vectors, $B = 1.2$ Tesla.

For lower inlet temperature Fig.130 demonstrates what may happen at high magnetic field. In the case considered the flow stagnates at the nozzle exit during initial period after the magnetic field switches on. Fig.130 shows a flow pattern at time moment 3 ms.

8. SUBSONIC HFP WT EXPERIMENTS WITH MODIFIED MODEL

Model definition

The model concept is based on a dual purposes idea to provide:

- (1) Experimental data for numerical code validation developed for

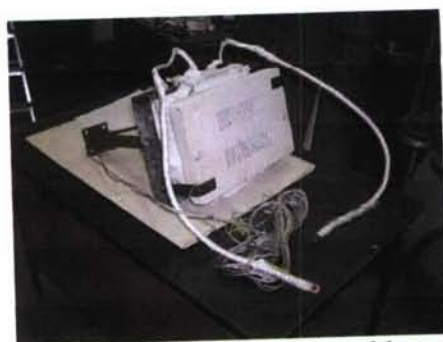


Figure 131. The general view of the external MHD generator model.



Figure 132. Magnetic System 2 of the two-coil type.

- (2) To study MHD interaction and MHD energy conversion at the configuration proposed for on-board applications.
- As a model of an external MHD generator the flat plate with electrodes on its surface (see Fig. 131) is used. The model is a plate of size 250 x 400 mm with 38 (19 pairs) electrodes flash mounted into the flow faced surface and the electromagnet system

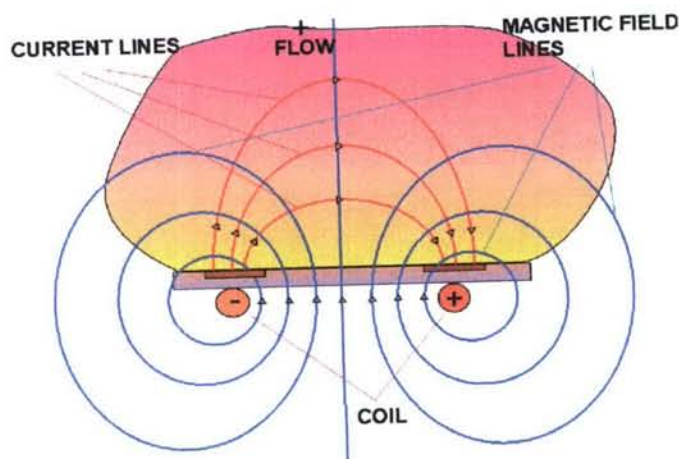


Figure 133 Schematic diagram of the cross-flow section of the experimental arrangement

attached to the back model surface. The model made of an insulating thermal protection material.

The electromagnet system of pulse type consists of two coils of 23 turns each (Fig.132). The on-design electrical current supplied by a battery is about 1.5 kA that results in center point magnetic induction as high as ~ 0.5 T.

It seems that such a configuration could allow solving both tasks mentioned above. In

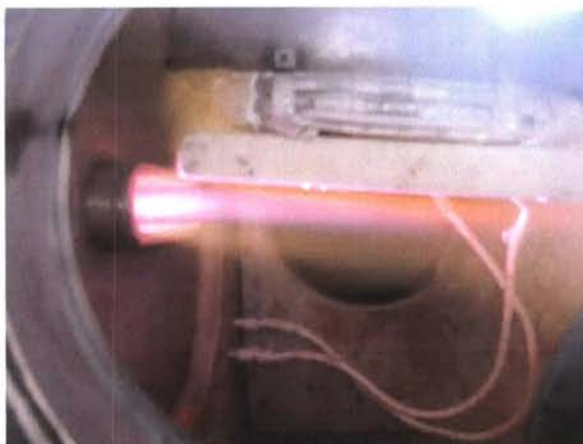


Figure 134. The model in the working chamber at the time of the preliminary test.

Fig. 133 the schematic diagram of the experimental arrangement in a cross-flow section is qualitatively shown. In this figure the flow direction is normal to the cross



Figure 135. Main components of the modified model.

section; the magnetic field is closed to the dipole type; the electrical current lines are normal to the magnetic field lines. It leads to the obvious solution to locate the electrodes just above of the coil leads. In reality the current distribution is much more complicated due to, first of all, the strong Hall effect. The latter results in very significant longitudinal electric field $E_{Hall} \sim \omega\tau UB$, where $\omega\tau$ is so called Hall parameter much larger 1 under experimental conditions. The effective MHD interaction under strong Hall effective conditions is possible if the Hall field E_{Hall} is kept closed to the ideal value defined above. To meet this requirement the electrodes are segmented in flow direction (19 pairs), and are loaded independently.

In Fig.135 the model of the external MHD generator is shown outside the test section at the time of the preliminary test. The model is installed at small angle of attack and streamlined by plasma flow exhausting through a subsonic flat nozzle of exit size 50 x 270 mm.

After preliminary tests the strong influence of the 'cold' boundary layers formed at the



Figure 136. The modified model assembled.

metallic nozzle walls was established. To decrease the negative effect of the cold boundary layers blocking the electrical current to the surface electrode, the model was shifted towards the nozzle edge and oriented under angle of attack of 10° .



Figure 137. The modified model without thermo protective material in the HFP WT test section.

Unfortunately, the model design, and especially the magnet located above the thick plate didn't allow placing the working plate surface into the most heated core flow. For this reason the cold boundary layer effects was still principal limitation mechanism from the point of view of electrical power extraction. It will be discussed below in more details. Under such conditions the model was kept in the flow as long as possible (typically 15-20 seconds) in order to increase the surface temperature to the maximal available value ($\sim 1000^\circ\text{C}$).

The electromagnet system used is a short duration operation device. The magnet is fed by a battery. The magnetic induction depends of the battery voltage. At the initial battery voltage equal to 3 kV the value of the magnetic induction is about 0.4 Tesla at the plate flow faced surface.

For the magnet system power supply the standard power unit of the solid-state

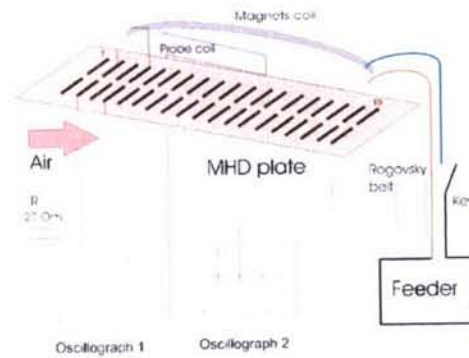


Figure 138. The measurement scheme in experiments on MHD interaction

laser system ГОС-300 is used. It consists of the condensers store (20 pieces of 100 mF each), high-voltage rectifier and inductive loading. The measurement of the pulse current through the magnet lead is provided with the Rogovsky' belt calibrated with a shunt in separated measurements.



Figure 139. Video frames in the moment of strong electromagnetic field interaction with a plasma flow.

The experimental results

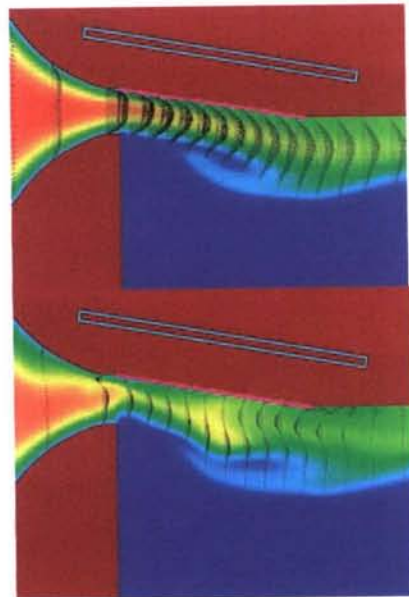


Figure 140. Temperature (filled) and flow velocity (vectors) distributions for no magnetic field case (upper frame), and at approximately maximal magnetic field (lower frame)

obtained in several series of runs are described in detailed in our 2nd year Annual report.

The main positive result of these series is the clear demonstration of the strong MHD interaction by means of low speed (TV standard) flow visualization (see Fig.139 where four subsequent frames of flow above the model are presented) qualitatively confirmed with 2D numerical simulation illustrated in Fig.140.

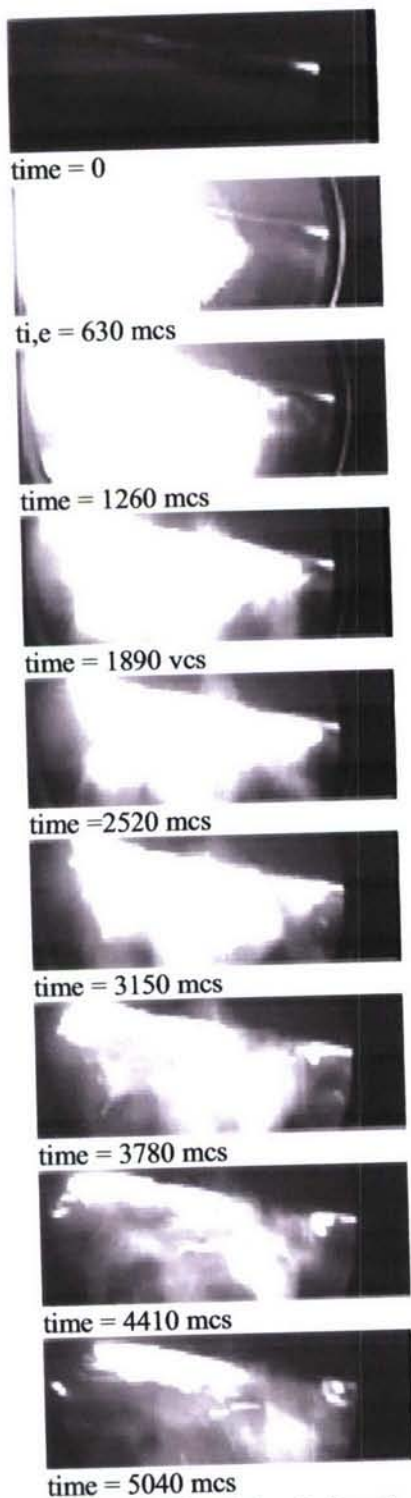


Fig.141. Filtered visualization of MHD interaction at the model

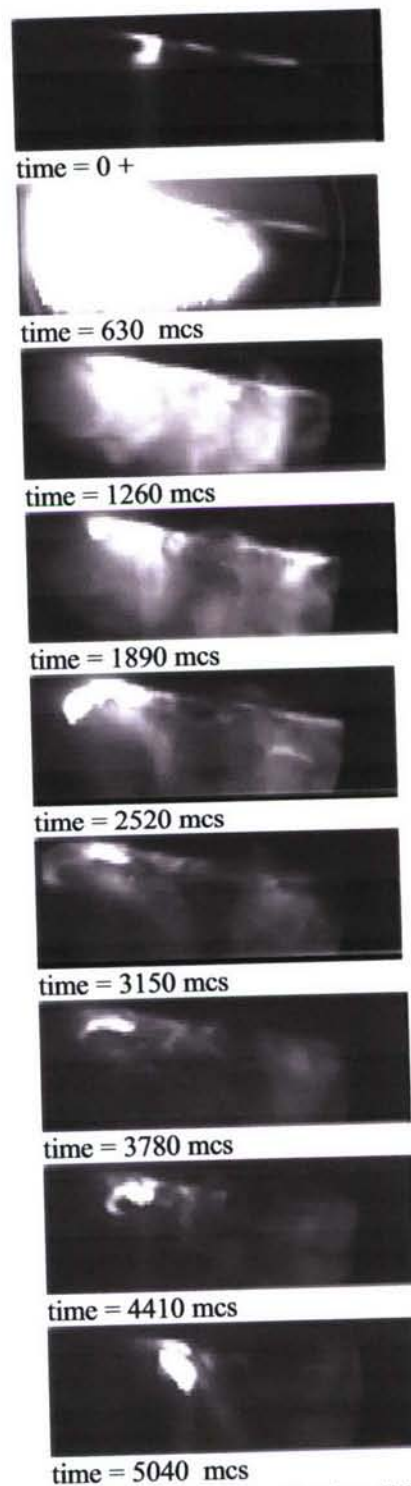


Fig.142 Filtered visualization of MHD interaction at the model. Reduced exposure time

At the same time the cold boundary layer was still dominating effect resulting

in only very low potential response on magnetic field pulse.

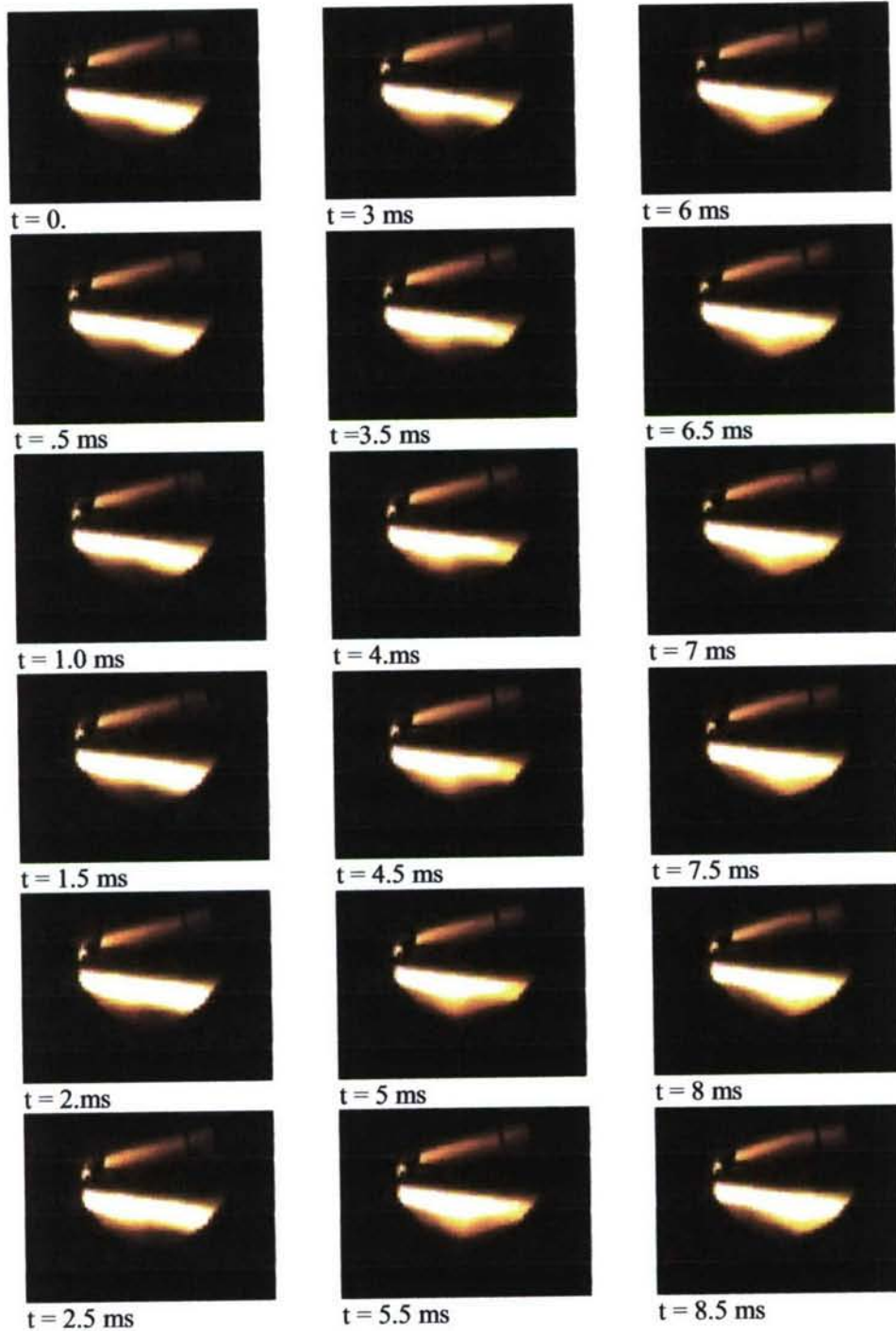


Fig.143. Visualization of the MHD interaction at the model. Magnetic filed pulse is represented by time period (0, 2ms).

For this reason the new modified model has been designed, fabricated and tested.

The main idea of new modification is to provide the model location inside the flow core. The model consists of two plastic plates, plastic frame and magnetic system coil (see Fig.135). The flow faced surface is protected by a high temperature material. Electrodes (13 pairs) are made of copper. Leading edge is protected by the copper cup (not shown in Fig.136). The total thickness of the model is about 20 mm.

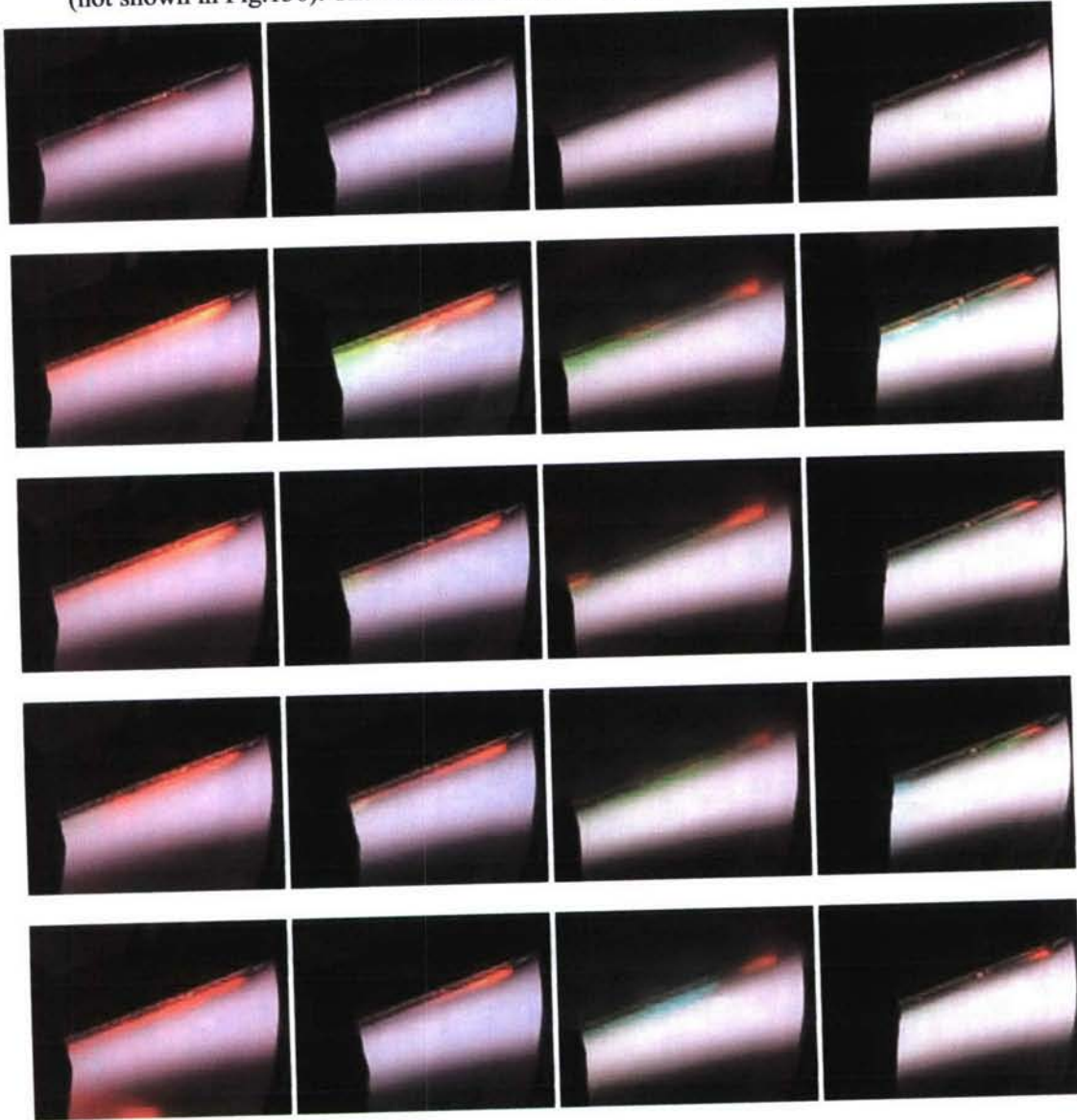


Fig.144. Model photographs in a plasma flow taken by a video camera SONY NP-F330 without a magnetic field (first line) and with a magnetic field in runs: a - 2216, b - 2217, c- 2218, d- 2219.

It should be noted that the simplified variant of the model (without thermo protective material) was also used in the preliminary test series. This model is shown in Fig.137 when installed in the HFP WT test section.

Experiments

The main goal of two series of experiments with the modified model was to improve the time resolution of flow visualization using fast speed cameras. Two different digital cameras were used both with approximately 2000fps. The first one can provide color pictures with relatively low space resolution in visible spectral band. The second – black-and-white- with better space resolution. In the case of B&W camera the spectral filtering was applied. The filter has provided a rather narrow band around 777nm wave length corresponding to the oxygen atomic line. (This filter was successfully tested in our earlier experiments on MHD interaction in hypersonic airflow (see also the next Chapter).

The electrical potential and magnet current measurements were carried out with the same technique as in previous experiments. Unfortunately, in the recent experiments the electromagnetic noise created by the ignition system used to start up the magnet was too high, and no useful data on the electrode potential were obtained.

Operational mode of the facility used in all recent series was characterized by lower power input and consequently by lower pressure: 0.100 atm and 100 kW as compared to 0.200 atm and 200kW typical of previous tests. The working surface of the model was installed at $AoA = 5^\circ$, and the leading edge was located approximately near the flow centerline.

In Fig.143 consequent frames of high-speed visualization in visible band are presented. The first four-five frames correspond to the magnetic field pulse. It is surprisingly that first of all the magnetic field pulse could create only very low changes of bright area configuration, and the second, significantly stronger changes occurred after magnetic field canceled again. It is in the strong controversy with non-armed eyes observation and low-speed visualization.

In order to resolve this confusing result the visualization with another black-and-white digital camera was used. Furthermore, the filtering, which was successfully used earlier has been applied also.

The visualization of two realizations is presented in Fig.141 and Fig.142. The exposure time in the case of Fig.142 was reduced twice in compared with the case of Fig.141.

Four first frames cover the magnetic filed pulse. It is clearly seen that during the pulse MHD interaction results in the dramatic change the luminosity and in the strong flow filed modification. The flow separation has been created. The complicated flow field structure relaxes relatively slow (relaxation period is 10-20 times longer than characteristics gasdynamics time defined as the ratio of the model length and characteristics flow velocity. The relaxation process is characterized by formation several strong large-scale vortexes burn at the upstream and downstream model edges. Luminosity of the flow is gradually decreasing during the relaxation, and for this reason the later stages are better resolved with larger exposure time.

It is important that two realizations illustrated in Fig.141 and Fig.142 are quite similar that confirms the well reproducible feature of the MHD interaction at this facility.

The main result of this preliminary series with modified model is that the fact of the strong MHD interaction earlier observed only once due to poor time resolution has been confirmed on the regular base.

Unfortunately the potential measurements were failed due to strong influence of electromagnetic noise found in the new measurement scheme.

The next step planned for October will be devoted to MHD interaction study with three synchronized diagnostics: visualization by high-speed camera, accurate potential recording, and the first attempt to measure static pressure response during the magnetic field pulse. As an example in a Fig. 144 the photos obtained with usage of the video camera SONY NP- F330 in runs 2216 - 2219 at pressure in a working section 30, 50, 100 and 150 mbar, accordingly, and a plasmatron power of 200 kw in the moment and after supply of an impulse current on an exciting coil are adduced. The maximum rating of a magnetic field induction in these experiments did not surpass 0.4 T.

Let's pay attention, that brighter flash is observed at smaller pressure (first column).

Due to the best visibility achievable with the help of this video camera, on the obtained snapshots zones of a heightened luminosity (plasmoids) clearly are visible, which one arises near the plate surface as a result of a pulse magnetic field. the higher brightness is observed at smaller pressure in a plasmatron test section that, possible, could be explained by higher conductivity of an oncoming plasma flow in this case.

It is very important to mark, that the time of current coming through the MHD generator coil exciting a variable magnetic field (and initiating plasmoids) makes value ~ 2 msec, and the plasmoids life time, as follows from a Fig. 144, more than 160 msec.

Induced electrode voltage were measured with a digital oscilloscope. The

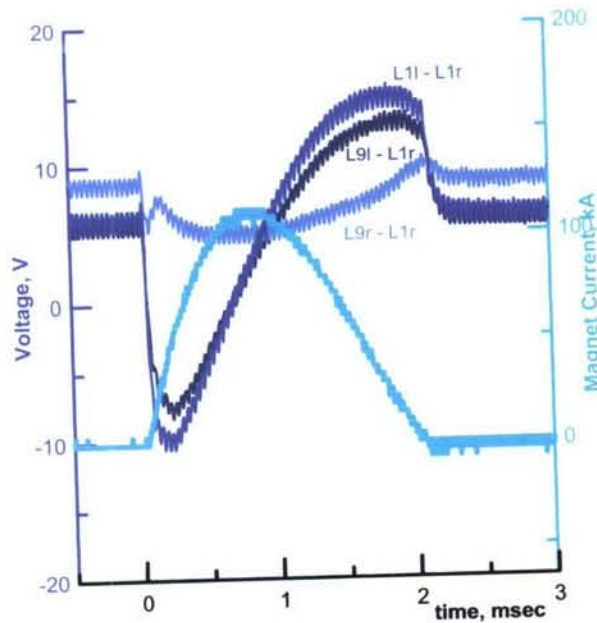


Fig 145. Electrode voltage drops and magnet current.

results obtained in this series are qualitatively very similar to the previous observations: the main contribution to the measured voltage is provided by the time variation of magnetic flux rather than by "steady-state" flow in the transverse magnetic field nature, i.e. $V \sim \partial B / \partial t \cdot L \cdot d \gg u B d$. As a typical example of the voltage drop recording the experimental results of the 2216 run are plotted in Fig.4. The curve L1l-L1r represents the Faraday (transversal) voltage measured at the 1st electrode pair, the

curve L9r-L1r presents the Hall (longitudinal) voltage between the 1st and 9th right electrodes. The light blue curve presents the magnet current.

For diagnostics of a plasma air jet two systems of spectral measurements of

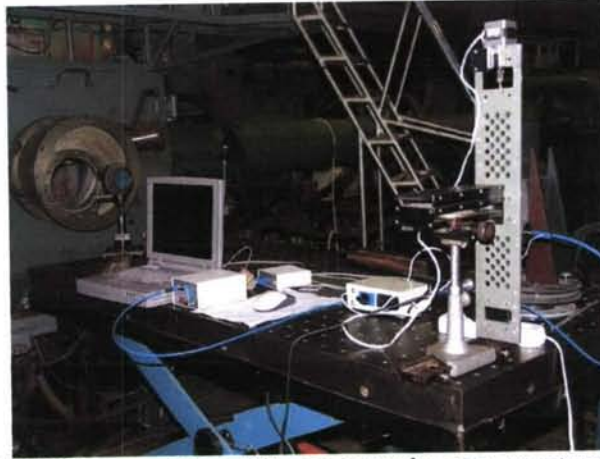


Fig.146. The general view of the spectroscopic measurements system .

relative and absolute intensity of radiation of high-temperature air are used in the region of a spectrum from 230 up to 1100 nm. The scheme of experiment is given in a Fig.146. The first system, representing at lower part of fig.1, includes a two-channel

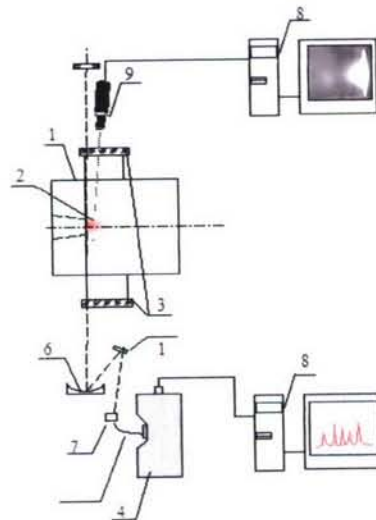


Fig.147. Optical measurement scheme

1 - Chamber, 2 - Plasma air jet, 3 - Quartz window, 4 - Fiber optic spectrometer with linear CCD array, 5 - Optical fiber 0.6mm, 6 - Spherical mirror, focal distance 450 mm, 7 - Positioning system with stepwise motor, 8 - PC, 9 - Frame capture system, 10 - Mirror

spectrometer with fiber optics (1), a spherical mirror ($f = 450$ mm) (6), a rotary mirror (10), a position ruler with the step-by-step engine (7) and the optical fiber fixed on it with diameter of 0,6 mm (5) and a computer with the software (8) on which input the signal from an output of a spectrometer moves. The spherical mirror is on a double focal length from an axial line of model and projects the image of plasma with scale

1:1 and small demagnification on a plane of an end face of an optical fiber. Thus the line-of-sight passes parallel to the model plane and is perpendicular its axes on distance of 0-5 mm from the model.

The position ruler with the step-by-step engine and the optical fiber fixed on it

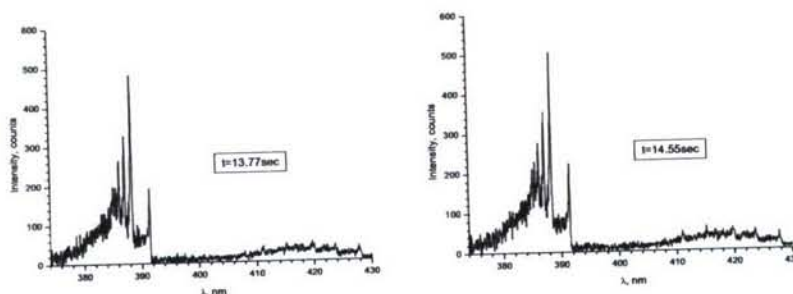


Fig.148. The air plasma radiation spectra obtained at different time moments in the range 370- 430 nm ..

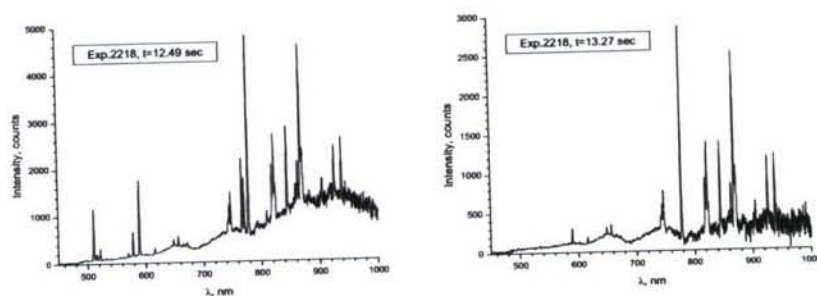


Fig.149. The air plasma radiation spectra obtained at different time moments in the range 450- 1000 nm.

provides scanning a stream in the chosen section. The spatial resolution at scanning makes size $0,6 \pm 0,2$ mm. Depending on a problem a spectrometer is used with the necessary resolution, spectral range of sensitivity in a total wavelength range of 230 up to 1100 nm and time of registration. Time of registration of a spectrum may be done from 3 ms up to 60 s. The angular resolution of the used lenses is equal $6 \cdot 10^{-3} - 6 \cdot 10^{-2}$ and it linear resolution - up to 1 mm.

The positioning system with the stepwise motor and fixed on it lens of given fiber provide scanning a flow in the chosen section. The minimal step of scanning -5 microns,

The second system for spectral measurements (upper part at Fig.147) consists of a digital video-camcorder (9) equipped with a set of interference filters. The camcorder allowed visualization of the plasma-model interaction in the spectral regions corresponding to molecular bands and emission lines of interest.

In Fig.146 is represented the general appearance of the spectral recording system shown in the lower part of Fig.147.

The plasma spectral diagnostics was aimed at determination of electron temperature in the layer attached to the model surface. The temperature was

determined from analysis of rovibrational spectra of electron bands of N_2^+ , CN , N_2 . In addition emission lines of oxygen O and impurity line of copper Cu were used. As an example, spectra obtained in experiments № 2220 ($p = 30$ mbar, $N = 200$ kW) and № 2218 ($p = 100$ mbar, $N = 200$ kW) are demonstrated in Fig. 148. The spectra were obtained at different time moments during scanning of the plasma layer in the spectral region 370–450 nm. Similar spectra in the region 450 – 1000 nm are given in Fig. 149.

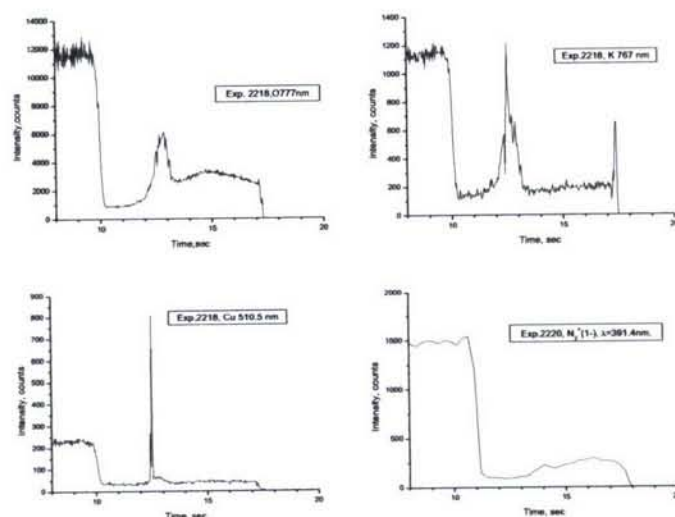


Fig.150. Time dependence of the radiation intensity of the air plasma in the lines of oxygen, ionic nitrogen molecular bands and impurity lines

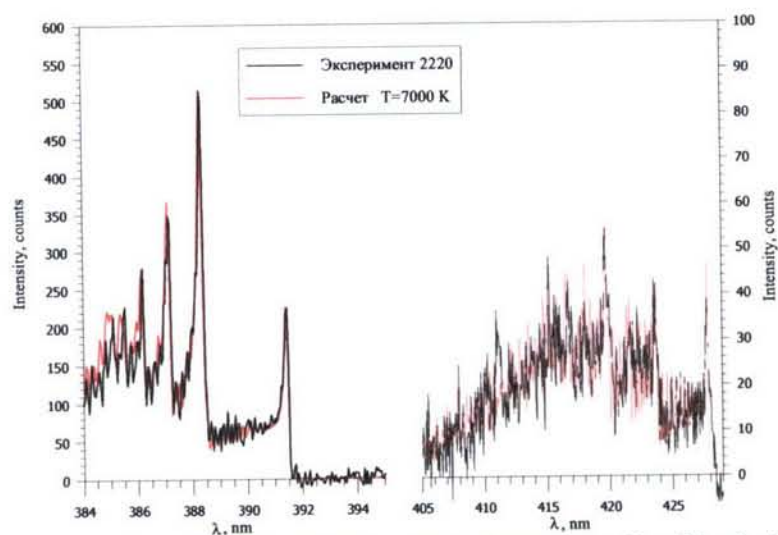


Fig.151. Comparison of experimental and modeled radiation intensities of the air plasma in the $N_2^+(1-)$ and $CN(v)$ molecular bands.

Rovibrational structure of the 1st negative nitrogen system $N_2^+(B^2\Sigma_u^+ - X^2\Sigma_g)$ characteristic to the hot air and molecular bands of the violet $CN(B^2\Sigma^- - X^2\Sigma^+)$ system are observed in the spectral region of 375 – 450 nm in Fig. 149. Molecular bands of $N_2(B^3\Pi_g - A^3\Sigma_u)$ 1st positive system are well seen in the region $\lambda\lambda$ 550 – 775 nm in

Fig.149. Also in this figure emission lines of oxygen O nitrogen N are observed in the region $\lambda\lambda$ 750 – 1000 nm along with some impurity lines of K , Na and Cu .

Typical examples of the time dependent intensities of the atomic emission line O (λ 777 nm), impurity lines K (λ 766 nm), Na (λ 589 nm) and molecular band edge of N_2^+ (I^-) (λ 391.4 nm) are presented in Fig.150.

Preliminary analysis of the intensity of molecular spectra $N_2^+(I^-)$, $N_2(I^+)$,

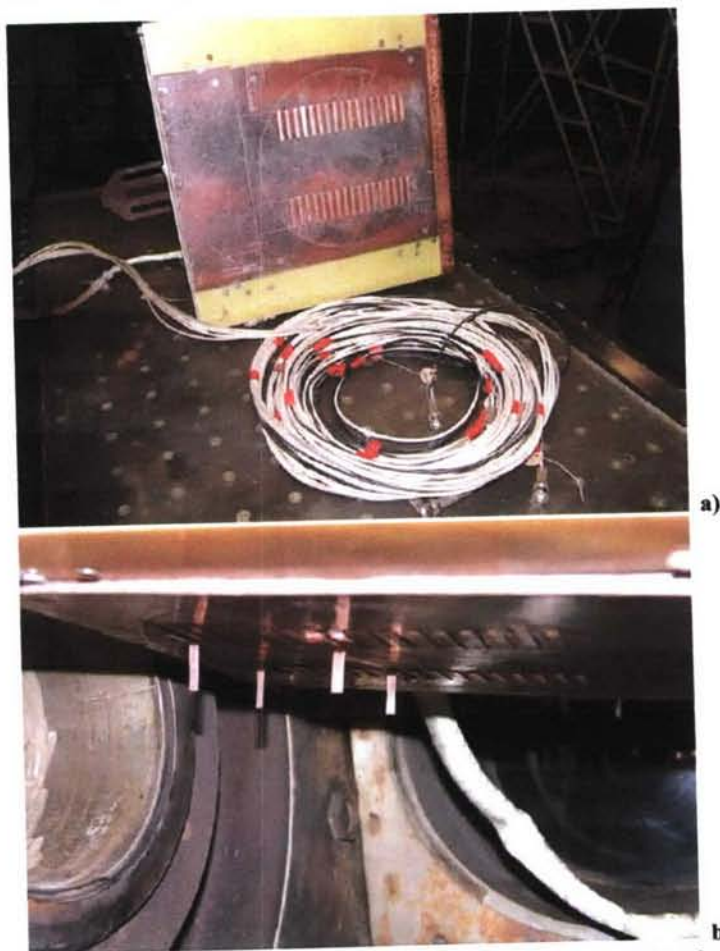


Figure 152. Model used at HFP WT after modification. a) equipped with flush mounted electrodes only; b) with additional pin electrodes installed at the 1st and the 10th electrode pairs in the test section

$CN(V)$ and emission lines $O(\lambda\lambda$ 777; 844; 926 nm) $Cu(510.5; 321.3; 522.0; 570.0; 579.2$ nm) resulted in the following:

1. Time dependence of the radiation intensities shows presence of an interval of about 160 ms right after magnetic field turning on where intensity of atomic lines O , N , Cu , K , Na increases. This is illustrated in Fig.151. Determination of the plasma temperature in experiment 2218 ($P=0.1$ atm, $W=200$ kW) based on comparison of the intensities of the oxygen emission line pares 777/926; 844/926 and pares of lines Cu 510.3/515.3; 521.3/578.2; 521.3/570.0 resulted in the interconsistent value of $T=8200\pm150$ K. Over the intensity maximum, the temperature derived from the oxygen line intensity ratios

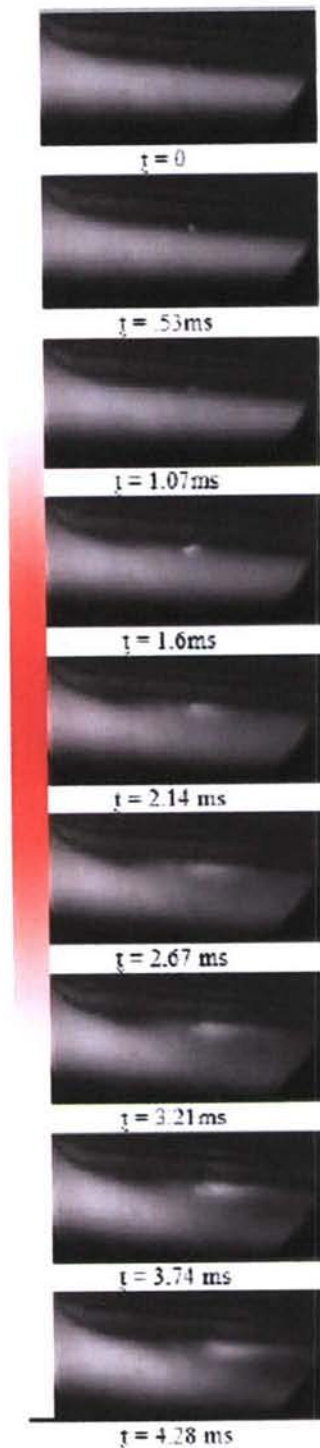


Figure 153. Visualization of the MHD interaction during the magnetic field pulse. Magnetic field strength is marked by the colored strip at the left side.

falls down to 6900 ± 150 K. Emission lines of Cu were not observed at that time.

2. Plasma temperature derived from analysis of the rovibrational structure of the electron band

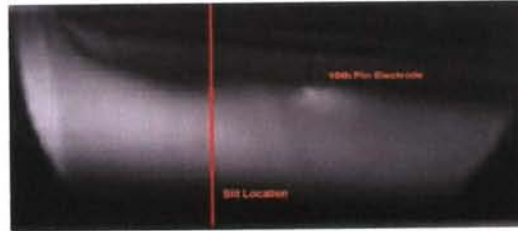


Figure 154. "Slit" location.

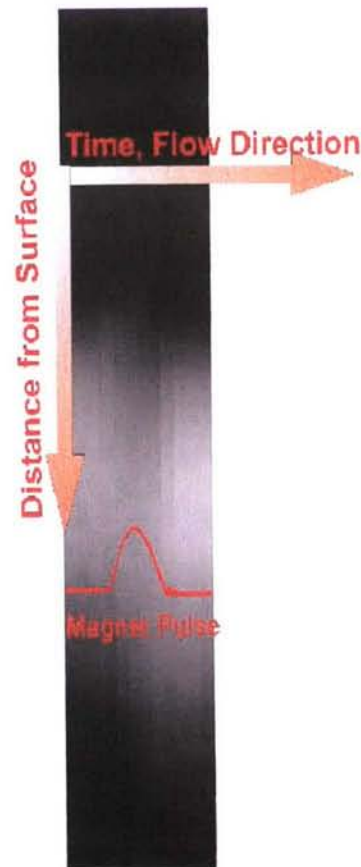


Figure 155. Streak images of the flow in cross-section as indicated in Fig.150.

$N_2^+(I-)$ also consists similar value $T \approx 7000$ K. Fig. 151 demonstrates comparison of the modeled and measured intensity distribution in

the spectra of $N_2^+(I-)$ и $CN(V)$ in experiment 2220 ($p=0.03$ atm and $N=200$ kW). Best coincidence of the modeled and measured spectra is observed at 7000K.

Experimental Study of the Pin Electrodes

In our previous report we have concluded that experimental results obtained both at HFP WT and HV MHD WT are affected dramatically by the poor electrical contact of the flush mounted electrodes with the electrically conducting flow core. To check this idea the recent experimental series at both facilities were devoted to

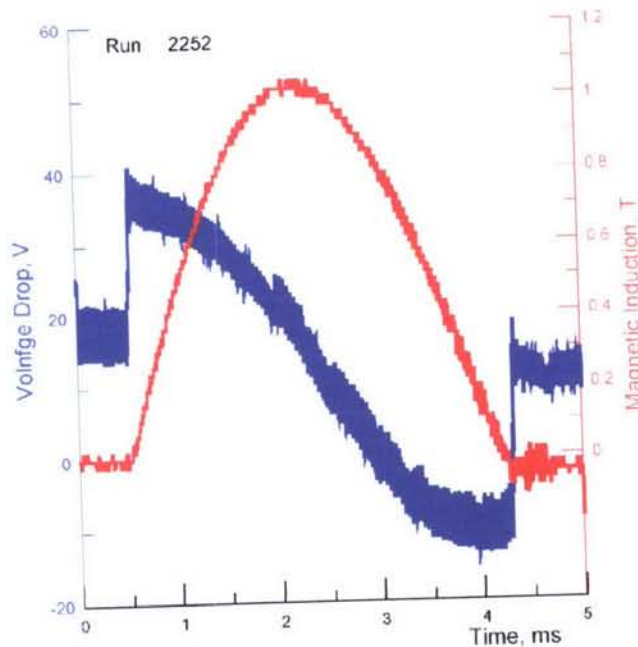


Figure 156. Voltage at the first electrode pair and magnetic induction during the magnet current pulse.

specifically designed models. The modifications made are rather simple, but the results have confirmed the proposed explanation. The first 'breakthrough' result was reached at HV MHD WT that will describe in the next section. The similar modification implemented at the model used at HFP Facility has provided also significant improvement of the experimental data quality.

The modification is illustrated in Fig.152 for HFP WT model, and practically similar design was used for the Model 6 tested at HV MHD WT.

The typical results of the recent series with 'pinned' electrodes are presented in Fig.152 through Fig.155. During the magnetic field pulse the main flow has been significantly shifted from the wall that is resulted from the deceleration effect within the interaction zone.

The streak images presented in Fig.155 demonstrate very good synchronization of the flow shift away of wall during the magnetic field pulse. It should be noted that these and also practically all previous observations shown that the after-pulse flow remains disturbed for rather long time interval much longer than the pulse duration. It

is mostly probable due to subsonic operation mode of the HFP facility for which the strong gasdynamic disturbances propagate both downstream and upstream. The latter could result in significant accumulation of the energy in the low-speed plasma source that discharges afterward rather slowly. Another mechanism of delayed response is probably due well visible damages of some hardware components (such as electrodes) provided by pulse impact. As an example of such a pulse consequence one can see in Fig.153 the pin electrode firing initiated by the magnet pulse.

Qualitatively the recent results correspond well to the previously reported observations. The pin electrodes seem do not change significantly the amplitude of the interaction effect but rather improve the reliability of potential measurements that is probably due to the much better contact the pin electrode with the 'hot' well electrically conducting flow core. This expected result confirms our previously made conclusions that one of the critical experimental conditions is the electrode problem, which is very well known from the experience of MHD power conversion studies.

The potential record of the run illustrated above with visualization results is presented in Fig.156.

As it is compared with the previously obtained records the amplitude of voltage signal at the first electrode pair has exceeded the level of 20 Volts. The main feature of the time dependent behavior of this signal is now much more pronounced and clearly seen – the electrode voltage is practically proportional to the time derivation of the Rogovsky's belt signal also plotted in Fig.156. This means that the electrode voltage is induced by $\partial B/\partial t$ rather than by $\mathbf{u} \times \mathbf{B}$.

It seems that in spite of very strong pronounced non-equilibrium nature of the flow in HFP facility the influence of the 'cold' wall on electrode transport to the electrodes is still dominating. Thus, after the many problems already solved (in particularly in our study) the electrode problem has become now the most critical issue for the practical implementation of the external MHD system for hypersonic flights. However, referring to the on-ground MHD energy conversion experience we could expected that such a problem will be successfully resolved.

UV Spectra of the HFP gas flow

Spectral investigation of air plasma at MHD interaction in the working part of the high-frequency plasmatron were accomplished at input power 200 kW and pressures of 50 and 100 mbar. The plasma was studied near a model representing a flat plate $0.25 \times 0.25 \text{ m}^2$ with dynamic cooper blunt edge 0.045 m diameter, tilted at 10° angle. Pulsed magnetic field of $\sim 3 \text{ ms}$ duration and $\sim 1 \text{ T}$ intensity was generated by a coil located inside the plate. Subsonic plasma flow originated in the plasmatron infrastructure initiated by heating from a high-frequency generator having 440 kHz frequency. The observable flow diameter was 0.18 m.

Spectral study of plasma near the model included simultaneous registration of plasma spectrum in the wide band region 240-1100 nm, the plasma UV-image and emission intensity time history at the central wavelength of an interference filter $\lambda = 254 \text{ nm}$, FWHM=23 nm. Figure 1 illustrates the experimental scheme.

Below is a list of the instruments including their designations.

Intensified UV-imager (11), operating wavelength region 240-330 nm, for plasma imagery in the UV-region of spectrum.

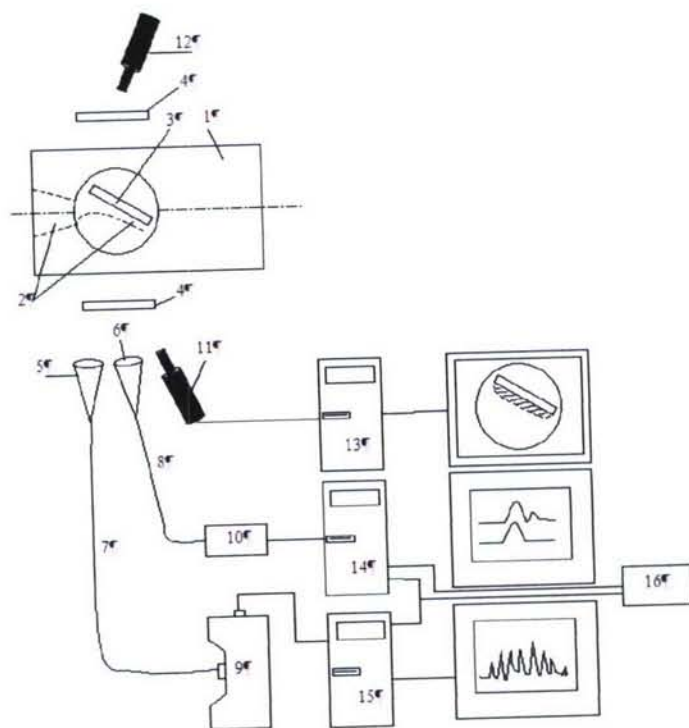


Figure 157. Optical experimental scheme

1. Experimental chamber; 2. Plasma at MHD interaction; 3. Model; 4. Silica windows; 5, 6. Lens $f = 100 \text{ mm}$, $\varnothing 20 \text{ mm}$; 7, 8. Optical fibers $\varnothing 0,6 \text{ mm}$; 9. SD2000, S2000 spectrometers; 10. Photomultiplier R636; 11. UV - imager; 12. SONY NP-F330; 13, 14, 15. PC; 16. Rogovski belt.

Spectrometer (9) SD2000, wavelength region 330-1100 nm and S2000, wavelength region 230-380 nm, for measurements of the plasma spectra synchronized with the Rogovski inductive loop within time interval $\Delta t = 4.8$ ms in the UV-region of

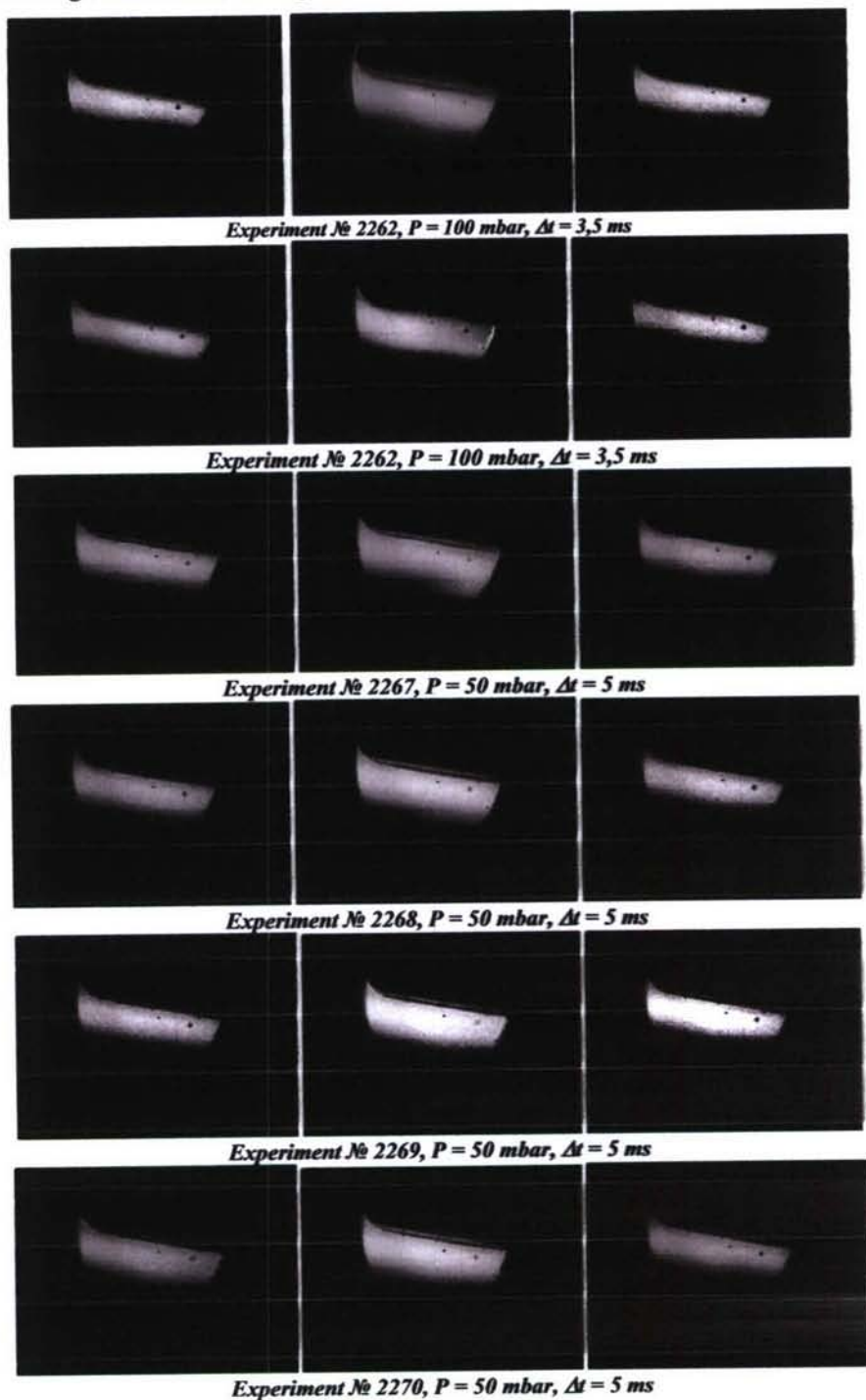


Figure 158. Snapshots of the model in the plasma flow obtained by UV-images before magnetic field pulse (1st column), during the magnetic field pulse (2nd column) and after the magnetic field pulse (3rd column).

spectrum.

Photomultiplier R636-10 (10) with Ga-As photocathode, operating wavelength region 200-800 nm, for measurements of the plasma emission intensity at 254 nm time

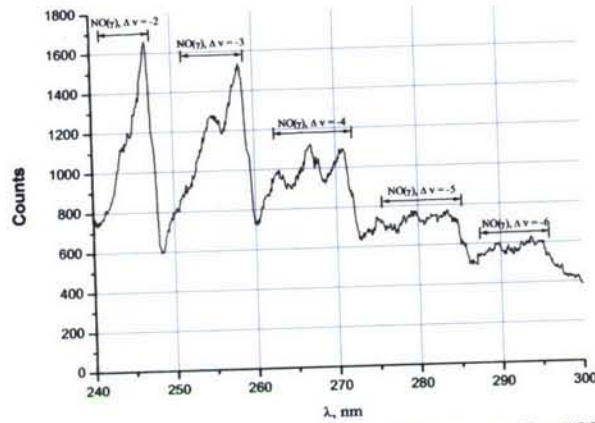


Fig159. Experimental emission spectrum of air plasma, $P = 100$ mbar

dependence synchronously with the Rogovski inductive loop.

SONY NP-F330 (12) camcorder for the plasma flow visualization.

Rogovski inductive loop (16) triggering the spectrometer and photomultiplier.

The loop current is monitored through oscilloscope.

The Rogovski inductive loop (16) generates a 5 V signal, which triggers PM (10) and SD2000 spectrometer (9). The single spectrometer spectrum exposure time was set at $\Delta t = 4.8$ ms that corresponds to the magnetic field pulse duration. The UV-imager (11) frame rate was 25 fps, while the single frame exposure was $\Delta t = 5$ ms. The data were stored in the PC (13, 14, 15). Camcorder (11) operates with 25 fps rate. Figure 158 shows UV-images of the model inside the plasma before the magnetic field

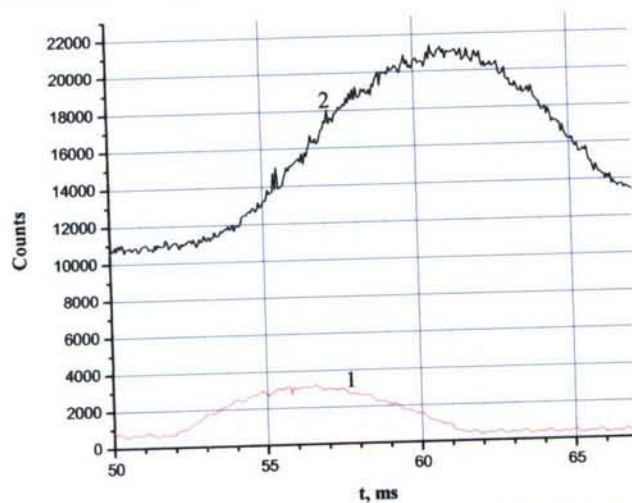


Fig. 160. Oscillogram: 1. Rogovski belt voltage; 2. PM voltage.

switched on, at the time the magnetic field was on and after the field. Because the plasma emission study was made in the UV spectral region, apparent enhancement of

the plasma emission intensity and increase of the plasma layer width is obviously seen in the snapshots.

Figure 159 illustrates plasma radiation spectrum in the UV wavelength region

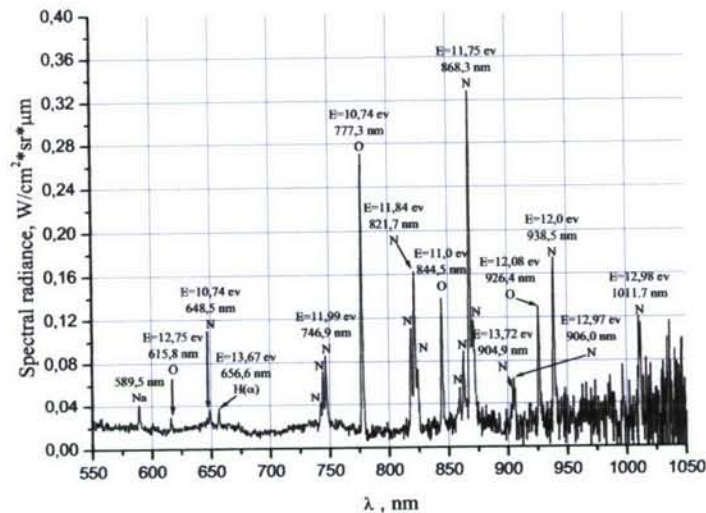


Fig. 161. Experimental emission spectrum of the air plasma, exposition $\Delta t = 4.8$ msec, $P = 50$ mbar, $W = 200$ Kw

taken from the UV-imager operating field of view. The spectrum shows that NO(γ) air plasma bands provide maximal contribution to the plasma emission intensity.

Oscilloscope traces of the Rogovski loop voltage together with PM signal time history are shown in Figure 160. The figure shows that PM signal reaches maximum at the descent part of the Rogovski loop voltage curve.

Plasma spectral diagnostics included the plasma temperature measurements in the layer near the model. Radiation spectra taken with exposure time $\Delta t = 4.8$ ms starting from Rogovski loop triggering pulse are shown in Figures 161 and 162. As it may be seen from figure 4 the moment when the spectra were taken corresponds to the time of the current input into the electromagnetic coil. The spectral intensity of the nozzle radiation was calibrated through standard tungsten lamp SI-8-200, so figures 5 and 6 shows the data for two pressures 50 and 100 mbar in terms of absolute values. Analysis of the spectra in figures 5 and 6 that at the moment of the magnetic field application ~ 4.8 ms a high temperature air glow was observed with no impurities contamination (for instance Cu, K). Well developed system of oxygen and nitrogen lines that have high excitation energies ~ 10 -13 eV. Pairs of lines having upper level excitation energy difference of ≈ 1 eV were selected for determination of electron temperature that ensured good accuracy of the measurements.

Results of the air plasma temperature measurements for operating pressures $P = 50$ and 100 mbar are given in table 1. The temperature was determined from ratio of oxygen and nitrogen pairs of lines. The following conclusions may be done basing on the table data:

1. The temperatures derived from the oxygen lines ratio are well corresponded
2. Temperatures of the air plasma measured at $p=50$ mbar are somewhat higher (~ 500 K) than those measured at $p=100$ mbar
3. The temperature value reaches a considerable value $\approx 10000 - 11000$ K at the moment when the magnetic field is applied.

Note that before the magnetic field is applied, temperature value is about $T \cong 6900$ K.

It should be also noted that temperature determined along the exposure time of $\Delta t = 30$ ms at the moment of magnetic field application is $T=8200$ K.

Thus, the following conclusions can be done:

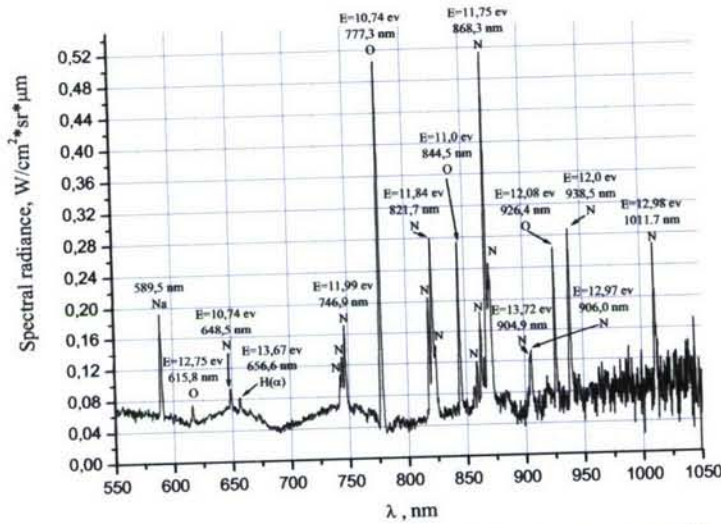


Fig. 162. Experimental emission spectrum of the air plasma, exposition $\Delta t = 4.8$ ms, $P = 100$ mbar, $U = 200$ kV

- 1. Synchronization of the spectra acquisition time with the moment of magnetic field application allowed substantially improve the air plasma temperature measurements and raise the measurement accuracy to 10000-11000 K (at $\Delta t = 4.8$ ms) compared with former 8200 (at $\Delta t = 30$ ms).
- 2. Spectral analysis of the plasma radiation has shown that MHD effect increases the plasma temperature and plasma layer width in a pure air plasma. The effect is not related to easily ionized plasma impurities (K, Cu etc), being inherent to the air plasma conductivity.
- 3. A time lag between magnetic field front and air plasma heating is observed. Maximum of the air temperature was found after the Rogovski inductive loop current and magnetic field went through their maximums.
- 4. The method of plasma glow pattern visualization in the UV-region of spectrum was found to be very promising, because it considerably reduces interference with impurities radiation (K, Cu and others)

Table 1

λ (nm)	Component	ΔE , (eV)	T , (K)	
			$P = 50$ mbar	$P = 100$ mbar
615,8/777,3	O	2,01	10730	10320
615,8/844,5	O	1,75	10120	9360
926,4/777,3	O	1,34	11040	11100
868,3/848,5	N	1,01	11420	10610
648,5/938,5	N	1,26	9970	9520
			$T_m = 10660 \pm 400$	$T_m = 10220 \pm 900$

IV. TASK 2. MHD ENHANCEMENT OF MIXING AND COMBUSTION

1. INTRODUCTION

Among the variety of methods intended to intensify the mixing and combustion in the non-premixed high speed flows the MHD-assisted mixing looks attractive since both the capability of electro-magnetic force to cause to the fluid motion and a hot temperature of the current-conducting formations could be utilized. In the earlier work [1] the numerical tests were carried out, which demonstrated a principal feasibility to apply the MHD method for the combustion intensification.

At the same time, first experimental test runs started in IVTAN have shown that the interaction of the plasma formations with the gas flow is much more complicated then it was thought. The real discharge properties are of great importance and can hardly be reproduced in simple thermally-equilibrium models. Another heavy problem is that a real discharge appears essentially three-dimensional and strongly non-uniform in space and time, thus it is quite questionable to apply 3D numerical simulations for studying the discharge/flow interaction.

The task of the paper is to develop the Lagrangian model, which, from one side, is qualitatively correct and, from the other, gives the means to study real discharges in the gas flows and in electric and magnetic fields. The model developed could be referred to as a macro-balance one. It takes into account the features of the plasmas to be dealt with: non-equilibrium dissociation and ionization processes, spatial non-uniformity, the magnetic field influence, cooling etc. An attempt is made to introduce into the model the capability to account for such features of the discharges as bending, expansion, local breaks and re-connections.

It is clear that such macro-balance model cannot capture all the features specific for real discharges. Therefore, some important characteristics should be "tuned" from experimental observations or, which seems easier, from numerical simulations. The latter are assumed to be used for verification tasks, for study of some specific details of the discharges. For these purposes the 2D numerical model was developed, which seems to capture the main phenomena of the arc discharges, such as non-equilibrium processes in molecular gases inherent to the initial and probably consequent discharge stages, collision energy transfer, including the inelastic collisions, the heat and diffusion transfer. 2D model was tested for the conditions of experiments which are currently in progress. Since detailed comparison of numerical and experimental data is still difficult, numerical results on the evolution of the arc discharge are mainly presented in the paper. The test numerical runs of the application model in the original form without "tunings" were carried out. The results are compared with those obtained with 2D arc model. The perspectives of the application model and future developments are discussed.

2. ARC MODEL FORMULATION

Formation of the arc is quite complicated process. The first stage is the streamer discharge, on which, the channel (or channels) of poorly ionized strongly non-uniform plasma is formed. One of the specific features of the streamer stage is high electric field near the streamer head, while the electric field in the channel beyond the head is

essentially lower than a breakdown field value. This channel can be considered as the initial stage for the arc formation.

We shall treat the channel as the region of cold heavy gas with probably excited internal vibrational and electronic states and partially ionized. The channel connects two electrodes, so the electric field exists within it. Such a post-streamer stage is considered as the initial stage of arc formation. The transition of channel to the arc, quasi-equilibrium hot formation, is thought to be described by the set equations expressing continuity, momentum and energy conservation for the medium as a whole. A medium is assumed to consist of neutral particles, atoms and molecules, positive ions and electrons.

We assume that after a streamer – stage passed electrons represent already maxwellian gas with the temperature T_e ; all heavy particles have one translational temperature T ; diatomic molecules like N_2 or O_2 can be vibrationally excited and the mean vibrational energy of molecule can be determined by some vibrational temperature T_{vk} for each k -th sort of molecules.

In addition to general conservation laws, the equations are added describing the transport of electron energy, transport of vibrational energy, the electrical conditions in the channel. Specific is the question on chemical kinetics in such a medium. In general, more sophisticated models are needed to calculate a chemical composition. However, we assume that at near-arc stage the reduced kinetics mechanism could help to estimate the chemical composition. The mechanism includes the electron impact reactions and reactions with participation of molecules. We just assumed that the electron impact reactions are governed by electron temperature, rather than a gas one. At this stage we want to assess the energetic characteristics of the arc column first of all. Therefore, no special consideration of kinetics of vibrationally excited gas is made at this stage. The main mechanisms determining the arc evolution are assumed to be as follows: electron-atoms collisions, electron-molecules collisions (which depend on both electron and vibrational temperature), dissociation and ionization by electron impact, vibrational-translational relaxation. Energy of any species can be transported due to convective and diffusive fluxes.

With these assumptions, the following set of equations was solved:

$$\frac{\partial \rho}{\partial t} + \nabla(\rho \mathbf{U}) = 0 \quad (1)$$

$$\frac{\partial \rho \mathbf{U}}{\partial t} + \nabla(\rho \mathbf{U} \cdot \mathbf{U}) + \nabla \tilde{\tau} = -\nabla P \quad (2)$$

$$\frac{\partial \rho e_0}{\partial t} + \nabla((\rho e_0 + P)\mathbf{U}) + \nabla \mathbf{q} + \nabla(\mathbf{U} \cdot \tilde{\tau}) = j^2 / \sigma \quad (3)$$

$$\frac{\partial \rho e_e}{\partial t} + \nabla(\rho e_e \cdot \mathbf{U}) + P_e \nabla \mathbf{U} + \nabla \mathbf{q}_e = j^2 / \sigma - Q_{ev} - Q_{eT} - Q_i \quad (4)$$

$$\frac{\partial \rho e_v^k}{\partial t} + \nabla(\rho e_v^k \cdot \mathbf{U}) + \nabla \mathbf{q}_v^k = Q_{ev}^k - Q_{vT}^k \quad (5)$$

$$\frac{\partial \rho_i}{\partial t} + \nabla(\rho_i \cdot \mathbf{U}) + \nabla \mathbf{J}_i = \dot{w}_i \quad (6)$$

Here, ρ is the gas density, \mathbf{U} is the velocity, e_0 is specific total energy, e_e is electron energy, e_v is the mean vibrational energy for each of the diatomic molecules. If total number of species is N_s , then $N_s = N_1 + N_v + N_1^+ + N_2^+ + 1$, where N_1 is the number of monatomic species, N_v is the number of diatomic species, N_1^+ is the number of monatomic ions and N_2^+ is the number of diatomic ions.

ρ_i is the density of i -th species, and $c_i = \rho_i / \rho$ is the mass fraction of it.

$P_e = n_e k T_e$ is the electron pressure, n_e is the electron number density, $n_e = \rho_e / m_e$, m_e is the electron mass, k is the Boltzman constant and T_e is the electron temperature.

The pressure P is the sum of partial pressures

$$P = \sum_{i=1}^{N_s} P_i = \sum n_i \cdot k T_i = \rho R [(1 - x_e) T + x_e \cdot T_e] \quad (7)$$

Here, x_e is the mole fraction of electron gas, $x_e = c_e \cdot M / M_e$, M_e is the molecular weight of electron gas and M is the molecular weight of mixture,

$$M = \left(\sum c_i / M_i \right)^{-1}$$

R is the mixture gas constant, $R = R^0 / M$, R^0 is the universal gas constant.

Energies are determined as follows

$$e_e = \frac{3}{2} n_e k T_e = \frac{3}{2} c_e R_e T_e \quad (8)$$

where $R_e = R^0 / M_e$ is the electron gas constant

$$e_v = c_v \frac{R_v \theta_v}{\exp(\theta_v / T_v) - 1} + \frac{5}{2} c_v R_v T \quad (9)$$

c_v is the mass fraction of v -th sort of molecules, $R_v = R^0 / M_v$ is the gas constant of v -th species, θ_v is the characteristic vibrational temperature of v -th species and T_v is v -th species vibrational temperature

$$e_0 = \sum_{i=1}^{N_1} e_i^0 + \sum_{v=1}^{N_v} e_v + \sum_{i=1}^{N_1^+} e_i^1 + \sum_{i=1}^{N_2^+} e_i^2 + e_e \quad (10)$$

e_i^0 and e_i^1 represent the, specific energy of monoatomic species, atoms and ions:

$$e_i^{(0,1)} = \frac{3}{2} c_i R_i \cdot T + h_i^f \quad (11)$$

$$e_i^2 = \frac{5}{2} c_i R_i \cdot T + h_i^f \quad (12)$$

h_i^f in (11) and (12) are the formation enthalpies of atoms and ions.
The fluxes in (1-6) represent the fluxes due to viscosity, heat conductance and mass diffusion:

$\bar{\tau}$ is the viscous stress tensor, $\mathbf{q}_e = -\lambda_e \nabla T_e$ is the electron heat flux, $\mathbf{q}_v = -\rho D_v \nabla (c_v e_v)$ is the flux of vibrational energy, $\mathbf{q}_0 = -\lambda \nabla T + \sum h_i J_i$ is the gas heat flux,

$$\mathbf{q} = \mathbf{q}_0 + \sum \mathbf{q}_v + \mathbf{q}_e \quad (13)$$

The mass diffusion fluxes \mathbf{J}_i are defined as

$$\mathbf{J}_i = -\rho D_i \nabla c_i \quad (14)$$

The transport properties μ , λ , λ_e , D_i , D_v are estimated on the approach reported in [1, 2]. The general idea is to correct collision integrals so that transport coefficients, μ and λ , are obtained close to that obtained when next-order Sonine-polynomial decompositions are applied. In calculating collision integrals each type of them is approximated by functions of temperature and, in general, composition and pressure. These were taken from the works [3, 4].

The source terms were calculated as follows:

$$e_{eT} = 3kn_e(T_e - T) \sum \frac{m_e}{m_i} v_{ei} \quad (15)$$

where summation is performed over all sort of species, and v_{ei} is the frequency of elastic collisions estimated as $v_{ei} = n_0 v_e Q_{ei}$ for neutral particles and

$$v_{ei} = 6\pi \left(\frac{e^2}{12\pi\epsilon_0 k T_e} \right)^2 \ln \Lambda \quad (16)$$

for ee - and ei -collisions.

Here n_0 is the total number density, n_e is electron number density, v_e is electron thermal velocity, ϵ_0 is the permittivity of the free space. Coulomb logarithm Λ was calculated as

$$\Lambda = 12\pi \left(\frac{\epsilon_0 k}{e^2} \right)^{3/2} \cdot \left(\frac{T_e^3}{n_e} \right)^{1/2}$$

The electron-vibrational transfer was modeled as in [5]:

$$Q_{ev} = An_e n_v \omega_e P_{1,0} \left\{ \frac{f(T_e)}{[1-f(T_e)]^2} - \frac{f(T_v)}{[1-f(T_v)]^2} \right\}$$

$$f(T) = \exp\{-1.44\omega_e/T_e\}, \quad \omega_e = 2358.57 \text{ cm}^{-1},$$

$$P_{1,0} = 0.45 \cdot \exp\{-10^4/T_e\}$$

Vibrational-translational relaxation was estimated from Landau-Teller expression:

$$Q_{vT} = \frac{e_v(T_v) - e_v(T)}{\tau_{vT}} \quad (17)$$

where $e_v(T)$ is the equilibrium vibrational energy and τ_{vT} is the relaxation time.

Electrical conductivity is evaluated as

$$\sigma = \frac{e^2 n_e}{m_e v_e}, \quad v_e = \sum n_i v_e Q_{ei} \quad (18)$$

Divergence-operator in (1)-(6) is $\nabla = \frac{\partial}{\partial x} + \frac{1}{r^\xi} \frac{\partial}{\partial r} r^\xi$, $\xi=1$ for axi-symmetric problems.

$j = \sigma E$ is the electric current density and E is the electric field.

At this stage the simplest (in the sense of composition) mixture is considered containing N_2 , N , N_2^+ , N^+ , e .

1D axi-symmetrical arcing is considered to qualitatively capture the main features of the discharge in attempt to formulate the arc model suitable for experimental data analysis.

In experiments on MHD assisted mixing and combustion started in IVTAN the arc discharge is created between two electrodes with the electrode gap of the length of 3.5cm. To breakdown the gaseous gap the high-voltage pulse is first applied until 0.01J (this is the energy accumulated by the source) is inputted into discharge. Then 5kV/100ohm power source holds the discharge during 50μs. To simulate the experimental setup the non-uniformities of the arc properties along the gap are neglected and the arc properties are assumed to change only in radial direction. Therefore, in governing equations (1)-(6) all terms containing $\partial/\partial x$ are omitted, where x is the direction along the gap. The initial stage is specified as follows. In the cold gas (nitrogen) a thin channel of diameter of some 0.1mm is established. It is assumed that

non-zero electron concentration takes place within the channel, and that electrons have a temperature of order of 1ev. Initial values in between 10^{-4} to 10^{-2} for electron mole fraction were tried. Electric field is then determined as

$$E_x = V_x / L \quad (19)$$

where L is the electrode gap length and arc voltage is expressed as

$$V_x = I \cdot R_a, \quad R_a = L \int_0^\infty \sigma r \, dr \quad (20)$$

I is the total current and $I = \int_0^\infty j r \, dr$, R_a is the arc resistance.

From the other hand, the circuit equation gives $V_x = \varepsilon(t) - I \cdot R_0$, where $\varepsilon(t)$ is the source ε and R_0 is the resistance of the power source.

For the breakdown stage

$$\varepsilon(t) = \varepsilon_0 \sin(\pi \cdot t / t_0), \quad \varepsilon_0 = 50 \text{ kV}, \quad t_0 = 1 \mu\text{s}, \quad R_0 = 0 \quad (21.1)$$

For the next stage

$$\varepsilon = 50 \text{ kV}, \quad R_0 = 100 \text{ ohm}. \quad (21.2)$$

The first stage terminates when the total energy released by power source $\int I \cdot V_x \, dt$ achieves the value 0.01J.

The profiles in Figs.163 to 166 demonstrate the main characteristics of the discharge. In Fig.163 temporary evolutions of the temperatures at the arc axis are shown. It is well seen that at the initial stage the power is inputted into the vibrational excitation of diatomic nitrogen molecules rather than ionization or heating of gas.

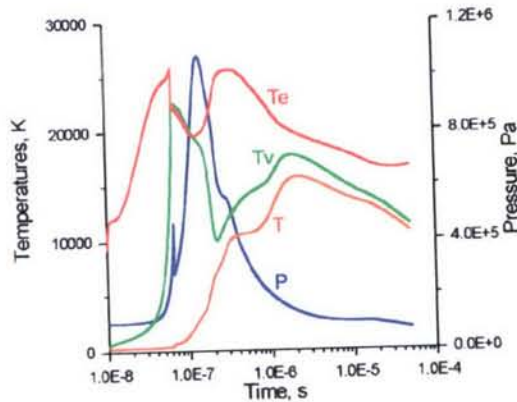


Fig.163. Electron temperature (red), vibrational temperature (green), gas temperature (brown) and pressure (blue) at the discharge axis versus time.

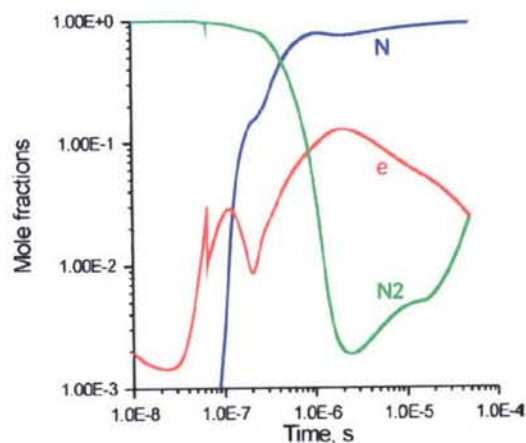


Fig.164. N_2 (green), N (blue) and electron (red) mole fractions versus time.

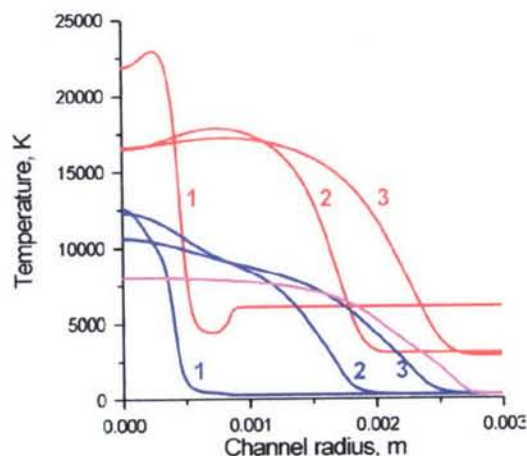


Fig.165. Electron temperatures (red) and gas temperatures (blue) at different time moments: 1 – $t=1\mu\text{s}$, 2 – $t=25\mu\text{s}$, 3 – $t=50\mu\text{s}$. Magenta-colored curve shows the electron temperature distribution at $t=70\mu\text{s}$.

The current flows only due to initial electrons, which concentration slightly drops. Nevertheless initial breakdown power pulse appears to be sufficient to maintain the discharge on later stage. The heating of gas occurs due to two processes: vibrational-translational relaxation and elastic collisions of electrons with atomic nitrogen. The second process becomes dominating in more and more extent as molecules dissociate.

Note that while evolution of discharge the pressure enhances because of high electron temperature and dissociation process. This leads to the formation of the shock wave, which leaves the channel and plays no significant role in further discharge evolution. Nevertheless, the pressure within the channel seems to play some role. Start of rapid gas heating (grow of translational temperature) correlates well with both pick pressure and rapid drop of vibrational temperature. The latter is due to diminishing of vibrational-translational relaxation time with growing pressure. Within the time period of nearly $2\mu\text{s}$ the dissociation completes and ionization becomes maximum

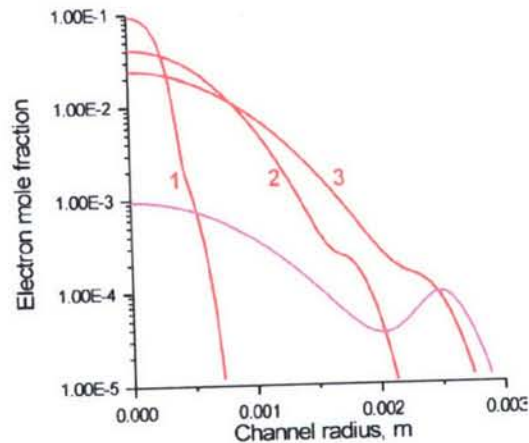


Fig.166. Electron mole fraction distributions along the channel radius at different time moments: 1 – 1 μ s, 2 – 25 μ s, 3 – 50 μ s. Magenta-colored curve shows electron mole fraction at $t=70 \mu$ s.

(see Fig.164). Further evolution of the arc column can be characterized with the following features. The column width extends, but the extension rate slows down with time. Despite the resistance of the arc column diminishes because of growing cross-section of the column, the electrical power decreases as the electrical circuit is functioning in the operation mode close to short-coming one. Decrease in inputted power leads to decreasing of temperatures (vibrational temperature is very close to the translational one at most of second stage period).

This is illustrated by Figs.165 and 166. In Fig.165 electron and gas temperatures are shown at different time moments: 1 μ s, 25 μ s, 50 μ s. The power supply terminates at $t=50 \mu$ s. Also shown is the electron temperature distribution at $t=70 \mu$ s, that is when the arc simply decays. In Fig.166 the radial distributions of electron concentration are presented for the same time instances. The edge of the column is seen well. The size of the arc column becomes a bit less than 3mm at the end of the power supply. The visible size of course should be less.

Remarks

First, even though the initial strongly non-equilibrium stage of the arc discharge evolution is simulated not quantitatively well (there were several strong assumptions made in problem formulation), it is hoped that the later stage of discharge is described right. And the model may become a base for developing the Lagrangian model, which is intended to be used in much more complicated conditions.

Second, it is assumed that the model will be used for fitting the parameters of Lagrangian problem and testing it.

3. LAGRANGIAN MODEL

The main assumptions used in constructing the Lagrangian Model are as follows.

- 1) For a first time let's adopt that the mass within the channel is nearly constant.

- 2) The mass-averaged characteristics of the arc column are considered: therefore we shall operate with some effective, averaged quantities. These are specified to be constant within the column. Actually, some shape functions may be used to fit the averaged values to calculated ones obtained in numerical simulations to the simplified situations.
- 3) The fluxes through the column surface are described using simplified approach based on the effective layer hypothesis.
- 4) While moving under action of electromagnetic force (which was omitted in the above model), it is assumed that acceleration term includes not only the mass of the column itself, but also some effective mass of the undisturbed flow, which is influenced by the arc column.

Integrating the Eqs (1) to (6) over a column volume and taking into account assumptions made above, one could obtain:

$$\frac{d}{dt} \int \rho dV = M = \text{const} \quad (22)$$

$$M^* \frac{d\mathbf{U}}{dt} = [\mathbf{J} \times \mathbf{B}] \cdot V \quad (23)$$

$$M \frac{de_0}{dt} + q \Delta S = S_{e_0} \cdot V \quad (24)$$

$$M \frac{de_e}{dt} + q_e \Delta S = S_{e_e} \cdot V \quad (25)$$

$$M \frac{de_v^k}{dt} + q_v^k \Delta S = S_{e_v} \cdot V \quad (26)$$

$$M \frac{de_i}{dt} + J_i \Delta S = \dot{\omega}_i \cdot V \quad (27)$$

The set of equations (22)-(27) should be extended with kinematic equation representing the motion of the column:

$$\frac{d\mathbf{r}}{dt} = \mathbf{U}, \quad (28)$$

where \mathbf{r} is the position-vector of the column mass-center and \mathbf{U} is the velocity-vector.

Here, e_0 , e_e , e_v^k have the sense of the mass-averaged values of energies from Eqs. (1)-(6). S_{e_0} , S_{e_e} and S_{e_v} are the volume-averaged right-hand-side terms from Eqs. (3)-(5), respectively. q , q_e , q_v^k and J_i have the sense of surface-averaged normal fluxes at the edge of the column. M is the column mass, which is considered to be constant. Therefore,

$$M = M_0 = \rho_0 V_0, \quad (29)$$

Where, V_0 is the initial column volume. This value is considered as empirical quantity. Suppose that equations of state (relationships for e 's and P) and expressions for source-terms are same as in Eqs. (8)-(10) and (7). Equations (19)-(21) for electrical characteristics hold and in the Lagrangian Model.

The fluxes are specified as follows. For example,

$$q_e = -\lambda_e^* \frac{\Delta T_e}{\delta_e^*} \quad (30)$$

where λ_e^* is the effective coefficient of electron heat conductivity. ΔT_e is the electron temperature drop between the core and, for example room temperature. Finally, we shall estimate the effective "heat-conductance layer" as

$$\delta_e^* \approx \min\{(2\kappa_e \cdot t)^{1/2}, R_a\} \quad (31)$$

where $\kappa_e \sim \frac{1}{3} v_e l_e$ is the electron diffusivity, v_e is the thermal velocity of electrons, l_e is the free-path length, and R_a is the column radius. It can be estimated from mass conservation relation (29): since $\rho = \rho(P, T, T_e)$ we have $M = \rho \cdot L \cdot \pi R_a^2 = \rho_0 V_0$.

Analogous estimations can be made for other fluxes.

Relations (22)-(28) along with electrical part of the model (19)-(21) are written not for a whole column (along the axis), but for a some small part of it. All the column is assumed to consist of several parts of such columns (sub-columns). The length L from (19) implies the length of the sub-column and, V_x from (19) implies the voltage drop. The total voltage drop between the electrodes is a sum of all partial voltage drops. The reason for introducing such a partition of the arc column resulted from experimental observations of arc in the flow and in the external magnetic field. It was well detected that the different parts of the arc are under different flow conditions. The arc column cross-section varies along the axis, it can be bend-shaped, to break down and re-connect. We shall try to simulate these effects with Lagrangian Model. The breakdown – re-connection model being under development assumes that the strong electric field may arise between two points of strongly bended column, which are close enough. The electric field between these points within the column is of coarse, smaller. Therefore, the electrical breakdown may occur between these points of the column, which redirects the current to another channel and "switches off" the previous one.

The Lagrangian Model has been tested for no magnetic field conditions, that is, simple arc between electrodes was considered. Such an arc was numerically simulated in the previous section. Some characteristics are presented in Figs. 167a and 167b. In Fig. 167a the gas temperature from 1D model (curve T_1) and the gas temperature from Lagrangian model (curve T_0) are shown. Also, electron temperatures from 1D (curve T_{e1}) and Lagrangian model (curve T_{e0}) are presented. It is seen that there are essential differences between two models, inspite, the fact that absolute values of temperatures

are rather close. The curves qualitatively differ from each other in the dynamics of evolution.

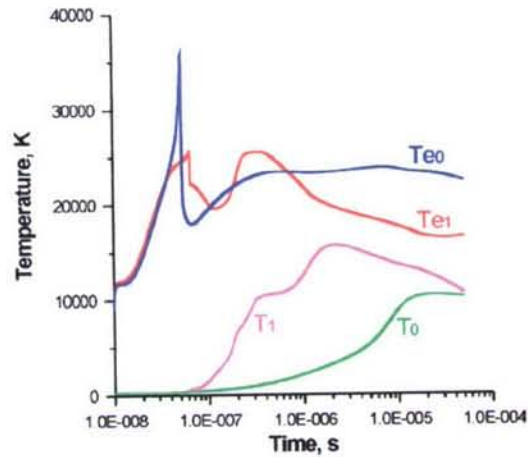


Fig.167a. Comparison of the temperatures for 1D model (curves T_1 and T_{e1}) and application model (curves T_0 and T_{e0}).

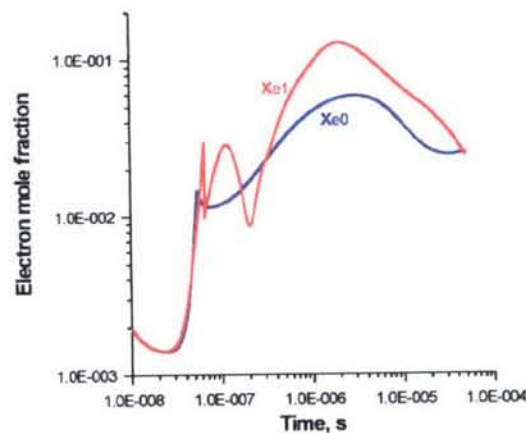


Fig.167b. Comparison of electron concentrations for 1D model (curve x_{e1}) and application model (curve x_{e0}).

It is supposed that gasdynamic expansion is important even for such small time periods. In 1D model the pressure changes significantly, which leads to the formation of the shock wave. The latter leaves the column, but it may expand in rarefaction zone behind the shock. In application model the pressure is considered to be constant. Only heating from source power and heat conductance can influence on the column size. The electron concentrations presented in Fig.167b reflect the same differences in the dynamics of evolution. Although, the differences in the absolute values are not thought to be critical.

The different dynamics demonstrated by two models reflects also in the column size. In 1D model the final size of the column determined from the temperature and electron concentrations (see Figs.164 and 165) is about 3mm. The column radius obtained in application model is as less as four times. Initial mass of the column

locates within the region of the radius close to that obtained in application model. These three size scales are shown in Fig.168. The curve R_1 shows the change of real arc column size (the region where 99% of total current flows) versus time. Curve $R_1(M_0)$ relates to the region, in which initial mass of column locates. The curve R_0 represents the arc column radius obtained in application model. The plot shows that initial mass expands nearly in the same manner in both models. This indicates that the actual arc gains additional mass from outer cold gas. The only mechanism for it is the diffusion of hot electrons (even ambipolar) from the core to outer region of the column. This was not assumed in application model to be an important effect and the model should be corrected.

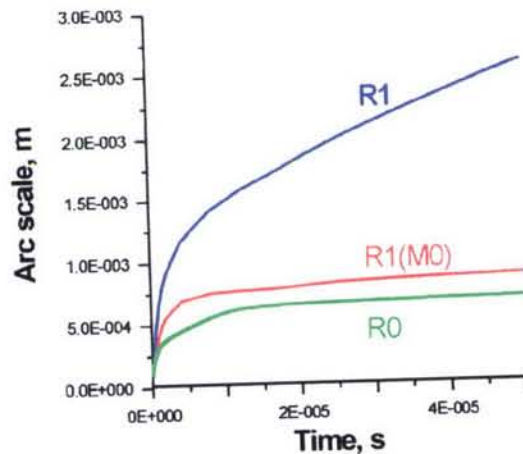


Fig.168. Size of arc column in 1D model (curve R_1), size of initial mass region in 1D model (curve $R_1(M_0)$) and size of arc column in application model (curve R_0).

Conclusions

In developing the approach of applying the MHD-method to intensify mixing and combustion in non-premixed flows the problem of adequate description of the discharge properties was encountered. In the paper the Lagrangian model was developed as the means to study the MHD interaction of the electrical discharges in high speed flows. It takes into account the specific features of the discharges in the molecular gases: non-equilibrium dissociation and ionization, electron-vibrational transfer, vibrational-translational relaxation. Such model is believed to be capable of assessing the characteristics of the discharges of very complicated geometry in the flows and in the magnetic field.

For purposes of verification and analysis, the 2D/1D arc model was developed, which takes into account the same most important effects as the application model does. The arc discharge between two electrodes was numerical simulated for the conditions of experimental pilot facility designed in IVTAN. Comparison of the result obtained with 2D model and application model revealed that there are still misunderstandings in the concept of the application model. Nevertheless, after necessary corrections such a model may be a useful tool in studying the MHD interaction of arc discharge in magnetic field with non-premixed flows.

4. PARAMETRIC STUDY OF MHD MIXING EFFECTS

The previous study has concerned the feasibility of the electric arc to initiate and maintain the combustion via the motion across the fuel/oxidizer interface due to electromagnetic field. It was numerically shown that such a discharge both initiates combustion process in the mixing layer due to high temperature of the arc and increases the mixing/combustion volume due to arc motion and enhanced diffusion of species in the volume. The combustion was detected to be self-sustained during rather long time even the current and/or magnetic field is switched off.

In those computations rather simple models of the medium were used.

First, the chemical kinetics mechanism used is considered to be appropriate to the combustion under thermal equilibrium. In addition, the kinetics under temperatures higher than 3000K can differ from that considered before. Therefore sophisticated kinetic scheme should be tested which includes interactions with the charged particles, first of all, electrons. The neutral-neutral interactions should be revised for temperatures higher than 3000K.

Second, the transport properties of the multi-component mixture should be revised due to availability of electric field and charged particles. First of all the conductivity of plasma should be computed more accurately. The electron-neutral and electron-ion collisions are of importance. In general these interactions depend upon electron concentration and electron temperature, the latter being different from heavy particles temperature. Other transport properties such that viscosity, heat conductivity and diffusion coefficients can significantly be affected by the charged particles interactions. Moreover, the approach to mass-diffusion used up to now should be re-evaluated. This approximate approach is based on the Fick's law and effective diffusion coefficients. The approach is known to be stable while time-integration, but may be inadequate in plasmas with the deep property gradients. In this case the Stefan-Maxwell equations solution may become necessary.

Third, the radiation emission from the discharge region was estimated with the approximate model. It was assumed that total radiation losses from optically thin plasma can be calculated by simple law taking into account the local absorption coefficient. Special study is still needed to understand whether the radiation losses are important from the viewpoint of energy balance. If so, they should be evaluated with more sophisticated model.

This Report is primarily intended to analyze the plasma models used before and to select the models more suitable for the discharges under consideration. Three items will be analyzed below: chemical kinetics, transport properties and radiation losses.

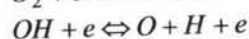
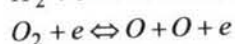
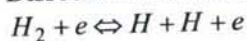
Chemical kinetics

Let's first recall the kinetic scheme used in previous calculations. The scheme is given in Table 1. It takes into account all main stages of the combustion process: excitation, ignition and heat release stage. The mixture is assumed to be in local thermal

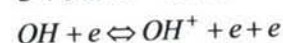
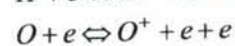
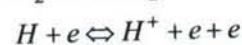
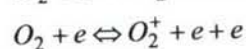
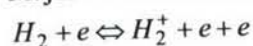
equilibrium. Under plasma conditions, the electron-impact reactions may play the significant role.

The following interactions are planned to be included in the scheme.

1) Dissociation reactions

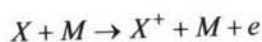


2) Major ionization reactions



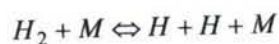
This set of reactions is thought to be important on any stage of the combustion process. The data on these reactions are now being sought in the literature. The role of direct dissociation/ionization of water is now investigated. Interactions of electrons with several intermediate species like HO_2 , H_2O_2 will probably be neglected since their lifetime is rather small as well as their concentrations.

Ionization of main species due to neutral-neutral collisions of type of



where X denotes H_2 , O_2 , O , H , OH , and M denotes any of the species will probably be not considered since such reactions occur under high temperatures (probably higher than 1eV). At the same time electron-impact reactions may take place due to high electron temperatures, which, in turn, may take place in high electric-field-strength discharge. Therefore, the set of dissociation/ionization reactions formulated above should depend on the electron temperature.

Another aspect of the scheme being developed arises from consideration of higher-temperature range. Within the arc, the temperatures higher than 3000K may occur. Hence, the dissociation reactions of type of



which were included in the previous scheme may occur with the reaction rates different from those considered before. The preliminary list of reactions which are assumed to be included in the kinetic scheme is given in Table 2.

Transport properties

In the previous work the transfer of species, viscous momentum and heat was modeled by the well-known multi-component diffusion model formulated. Commonly used simplification of multi-component diffusion applied the effective diffusion coefficients and Fick's law to estimate species mass-flux was implemented in the code. All transport coefficients were estimated with using so called collision-integrals of viscous and diffusion types. In turn, the collision-integrals are obtained by integration of collision cross-sections over the energy space. The values of collision-integrals, $\Omega^{(e,s)}$, were taken as approximations of temperature functions. These approximations used the Lennard-Jones interaction potential to obtain the deflection angle of the collided particles as function of impact parameter and relation energy, then the relevant cross section, and, finally, the collision integrals. The Lennard-Jones interaction potential model is known to work well for temperatures below nearly 1000K. At higher temperatures another models should be used for interaction potential. In addition, the interaction of charged particles should take into account the screened Coulomb potential.

Another aspect of the problem is related to using the Fick's law for mass-flux expression. It is easy to implement into the code, but the accuracy of the approach remains under question. More relevant, although time-consuming, is the solution of Stefan-Maxwell relation-ships for mass-diffusion fluxes. The set of Stefan-Maxwell equations can be expressed as

$$\nabla x_i = \frac{M}{\rho} \sum_{j \neq i} \left(\frac{x_j J_j}{M_j D_{ij}} - \frac{x_i J_i}{M_i D_{ij}} \right), \quad i=1, N-1 \quad (32)$$

$$\sum J_j = 0$$

where J_i is the mass-flux of species i due to diffusion (only concentration diffusion is taken into account), x_i is the mole fraction of species i , M_i is the molecular weight of i -th species and D_{ij} are the binary diffusion coefficient. System (32) should be resolved for J_i . This requires matrix inverting, $\mathbf{J} = \tilde{\mathbf{D}}^{-1}(\nabla \mathbf{x})$, which is extremely costly. Therefore, iterations are usually applied to obtain J_i . Nevertheless, this procedure still remains expensive compared with simplified models. Probably one of the best from the viewpoint of cost-accuracy consideration is the Yos model. The model gives diffusion flux of species i as

$$J_i = -\rho \frac{M_i}{M} \left(\frac{1-c_i}{1-x_i} \right) D_{im} \nabla x_i \quad (33)$$

$$D_{im} = \frac{1-x_i}{\sum_{j \neq i} x_j / D_{ij}}$$

Here D_{im} is the effective diffusion coefficient, c_i is the mass-fraction of species i .

In the case of Stefan-Maxwell relationships the driving force can take electric force into account directly. In Yos model it is neglected. Regardless of the diffusion model, the binary diffusion coefficients have to be calculated. Their calculation requires the

knowledge of collision integrals. Two approaches are planned to try for collision-integral calculations.

First, collision-integral for neutral-neutral collisions $\Omega_{ij}^{(1,1)}$ is approximated as function of temperature: $\Omega_{ij}^{(1,1)} = (a_{ij} + b_{ij} \ln T)^2$, where parameters a_{ij} and b_{ij} can be found from known values of $\Omega_{ij}^{(1,1)}$ ($T_1=300K$) and $\Omega_{ij}^{(1,1)}$ ($T_2=20000K$) and assuming that Lennard-Jones interaction potential is valid at low temperatures,

$$\varphi_{ij} = 4\epsilon_{ij} \left[\left(\frac{\sigma_{ij}}{r} \right)^{12} - \left(\frac{\sigma_{ij}}{r} \right)^6 \right].$$

At high temperatures Born-Mayers potential $\varphi_{ij}(r) = A_{ij} \exp(-\alpha_{ij} \cdot r)$ is used. Ion-neutral collision-integrals can be calculated using empirical correlations:

$$\Omega_{A^{\pm},N}^{(1,1)} = f(T) \cdot \Omega_{A,N}^{(1,1)}$$

$$f(T) = 1 + \left(\frac{1150}{T + 600} \right)^2$$

Collision-integral of electron with any neutral particle is assumed to have constant value of 4\AA^2 .

Interactions of charged particles are described with using screened Coulomb potential:

$$\varphi(r) = \frac{1}{4\pi\epsilon_0} \frac{e_i e_j}{r} \exp(-r/r_\Delta),$$

where $r_D^2 = \frac{\epsilon_0 k T}{n_e e^2}$ is the Debye length.

The following approximations are assumed:

$$\Omega_{++}^{(1,1)} = 0.523 r_L^2 \ln(1 + 0.6\Lambda) [\text{\AA}^2],$$

$$\Omega_{+-}^{(1,1)} = 0.405 r_L^2 \ln(1 + 2\Lambda) [\text{\AA}^2],$$

if $1 \leq \Lambda \leq 100$

and

$$\Omega_{++}^{(1,1)} = \Omega_{+-}^{(1,1)} = 0.5 r_L^2 (\ln \Lambda - 0.305),$$

if $\Lambda > 100$.

Here

$$r_L^2(T) = \left(\frac{e^2 z_1 z_2}{4\pi\epsilon_0 k T} \right)^2 [\text{\AA}^2],$$

$$\Lambda(T, n_e) = \frac{r_D}{r_L} = A \frac{T^{3/2}}{n_e^{1/2}}.$$

To calculate viscosity and heat conductivity we plan to use approximations of type of Wilke-Vasil'eva:

$$\mu = \sum_{i=1}^N c_i \frac{Sc_i}{d_i}$$

$$\lambda = \sum_{i=1}^N \frac{c_i}{M_i} \left[c_{pi} + 2.5R^0 (1.5Sc_i - 1) \frac{1}{d_i} \right]$$

where

$$d_i = \sum_j \frac{c_j}{M_i D_{ij}}$$

The Schmidt number $Sc_i(T) = \frac{5\Omega_{ii}^{(1.1)}}{6\Omega_{ii}^{(2.2)}}$. It is assumed that $\Omega_{ii}^{(2.2)} = 1.1 \cdot \Omega_{ii}^{(1.1)}$ for all components.

In second approach the collision-integrals values can be take in closed form as functions of temperature [41]. In this work the collision-integrals were calculated for many equilibrium air species interaction including the charged particles interactions.

In the future it is assumed to implement both transport coefficients models to take into account charged particles interactions.

More details are presented in our previous publications.

Radiation from plasma

In the calculations made earlier the simplest radiation model was used. The model used the concept of "gray-body" with effective absorption coefficient. Such concept just estimates the level of radiation power, probably upper limit of it. Currently, we don't know how accurate these estimations are. Detailed analysis of radiation emission is extremely complex problem, and it is hardly possible to do by our selves. Nevertheless, work is now carried out to find acceptable level of radiative losses description.

Table 1. List of reactions for H_2 - O_2 combustion

- 1) $H_2 + O_2 \Leftrightarrow OH + OH$
- 2) $OH + H_2 \Leftrightarrow H_2O + H$
- 3) $H + O_2 \Leftrightarrow OH + O$
- 4) $O + H_2 \Leftrightarrow OH + H$
- 5) $O + H_2O \Leftrightarrow OH + OH$
- 6) $H + H + M \Leftrightarrow H_2 + M$

- 7) $H + O_2 + M \rightleftharpoons HO_2 + M$
- 8) $OH + H + M \rightleftharpoons H_2O + M$
- 9) $HO_2 + H_2 \rightleftharpoons H_2O_2 + H$
- 10) $HO_2 + HO_2 \rightleftharpoons H_2O_2 + O_2$
- 11) $H + HO_2 \rightleftharpoons OH + OH$
- 12) $H + HO_2 \rightleftharpoons H_2O + O$
- 13) $H + HO_2 \rightleftharpoons H_2 + O_2$
- 14) $O + HO_2 \rightleftharpoons OH + O_2$
- 15) $OH + HO_2 \rightleftharpoons H_2O + O_2$
- 16) $OH + OH + M \rightleftharpoons H_2O_2 + M$
- 17) $HO_2 + H_2 \rightleftharpoons H_2O + OH$
- 18) $HO_2 + H_2O \rightleftharpoons H_2O_2 + OH$
- 19) $H + H_2O_2 \rightleftharpoons H_2O_2 + OH$
- 20) $OH + M \rightleftharpoons O + H + M$
- 21) $O + O + M \rightleftharpoons O_2 + M$

Table 2. Suggested list of reactions for H_2 - O_2 combustion with ionization

- 1) $H_2 + e \rightleftharpoons H + H + e$
- 2) $O_2 + e \rightleftharpoons O + O + e$
- 3) $OH + e \rightleftharpoons O + H + e$
- 4) $H + e \rightleftharpoons H^+ + e + e$
- 5) $O + e \rightleftharpoons O^+ + e + e$
- 6) $OH + e \rightleftharpoons OH^+ + e + e$
- 7) $H_2 + e \rightleftharpoons H_2^+ + e + e$
- 8) $O_2 + e \rightleftharpoons O_2^+ + e + e$
- 9) $H_2 + O_2 \rightleftharpoons OH + OH$
- 10) $OH + H_2 \rightleftharpoons H_2O + H$
- 11) $H + O_2 \rightleftharpoons OH + O$
- 12) $O + H_2 \rightleftharpoons OH + H$
- 13) $O + H_2O \rightleftharpoons OH + OH$
- 14) $H + H + M \rightleftharpoons H_2 + M$
- 15) $H + O_2 + M \rightleftharpoons HO_2 + M$
- 16) $OH + H + M \rightleftharpoons H_2O + M$

- 17) $HO_2 + H_2 \Leftrightarrow H_2O_2 + H$
- 18) $HO_2 + HO_2 \Leftrightarrow H_2O_2 + O_2$
- 19) $H + HO_2 \Leftrightarrow OH + OH$
- 20) $H + HO_2 \Leftrightarrow H_2O + O$
- 21) $H + HO_2 \Leftrightarrow H_2 + O_2$
- 22) $O + HO_2 \Leftrightarrow OH + O_2$
- 23) $OH + HO_2 \Leftrightarrow H_2O + O_2$
- 24) $OH + OH + M \Leftrightarrow H_2O_2 + M$
- 25) $HO_2 + H_2 \Leftrightarrow H_2O + OH$
- 26) $HO_2 + H_2O \Leftrightarrow H_2O_2 + OH$
- 27) $H + H_2O_2 \Leftrightarrow H_2O_2 + OH$
- 28) $OH + M \Leftrightarrow O + H + M$
- 29) $O + O + M \Leftrightarrow O_2 + M$

Arc-Driven Mixing and Combustion

To highlight the main effects we consider a simplified problem. Assume that the rectangular parallelepiped is filled with separated air and hydrogen.

It was found that the region of disturbance of the original contact boundary is essentially higher compared to original arc diameter. The characteristic size of combustion zone is comparable with the size of the domain. The combustion zone is well detected by the water mass fraction distributions. The water mass fraction reaches the value of ~ 0.21 (maximum) at the final stage. The maximum temperature varies from $\sim 5000K$ at 5mcs to $3900K$ at the final moment. The comparison shows that mixing process is mainly due to arc motion.

The situation becomes quite different when arc is ignited in the air. In this case no essential mixing zone enhancement is observed, while temperature becomes as high as $\sim 7200K$. The mixing zone surrounds the arc, which is as narrow as original one. In this case, the maximum water concentration reaches the value of 0.1. It is clear that total water production is significantly higher in the first case. Even if one compares the flow patterns at the same time moments (35mcs), the more developed combustion zone in the first case is evident.

Post-Discharge Reacting Volume Evolution

In order to understand what is an *ignition* capability of such an MHD driving mechanism the next step study has been undertaken to observe the evolution of the reacting volume after the current and/or magnetic field switches off. The problem configuration is basically the same as it was used in the previous Section. The two problems were considered.

The first one was the similar to the previous case when the arc initiates in hydrogen and enters into the air due to electromagnetic force. In 25 microseconds after the arc

generation the magnetic field is switched off, while the electric current remains. In the second case in 25 microseconds after the arc generation both electric current and magnetic field are switched off.

It was found that there are significant discrepancies in details of different cases considered. However this large difference doesn't play any role, since combustion initiates at rather moderate temperatures. One can say that in no current case the temperature is maintained only due to combustion. The total production of water, which is considered as the combustion efficiency, is approximately equal for both no-interaction cases.. Maximum production is observed for the reference case from the previous study because of more developed interface surface due to arc motion.

Numerical prediction of arc-driven mixing and combustion under experimental conditions

The simplified problem has been considered, in which hydrogen (fuel) and air (oxidizer) were originally separated. Mixing and combustion were stimulated by the electric arc moved by the applied magnetic field across the fuel-oxidizer interface. It was numerically shown that the motion of the arc increases the contact surface while the high temperature within arc provides ignition and combustion around the interface. It was found that combustion occurs during rather long time after switching off the electric current.

Results discussions are presented in paper [6].

The formulations considered above were used as the first-stage predictions to parameters of the small-scale facility being designed. In a future coupled experimental work and numerical analysis is hoped to give more knowledge about the topics of interest.

Experimental facility preliminary design

At this stage a preliminary analysis of the possible approaches is undertaken.

The main components are as following:

1. High pressure vessels for working gas storage;
2. The nozzles for formation of two co-flow streams of the gas to be mixed;
3. Electrodes system to provide pulse electrical discharge in the flow;
4. Pulse magnetic system to create magnetic field in proper direction in the mixing volume;
5. Power supply systems of electrical discharge and the magnetic system;
6. Diagnostics/visualization equipment;
7. Ventilation

Possibility acceptable in a case of utilization of the Schlieren technique could be a mixing experiment with two streams with different temperature (density).

The proposed scheme of the experiment consists of the several steps:

1. The initialization of the co-flow free jets in the test volume;

2. The initialization of the pulse discharge across the streams parallel to the interface between two gases;
3. The synchronized induced magnetic field should be oriented perpendicular to the main discharge current, and correspondingly parallel to the interface;
4. The visualization system should record the effect of the $\mathbf{j} \times \mathbf{B}$ pondermotive force acting in the vicinity of the interface.

At the next stage the ignition and combustion process affected by the pondermotive force and concentrated heat release due to Joule dissipation will be studied as well.

The experimental parameters are estimated with utilization of the results of the theoretical analysis and numerical simulation.

Typical value of the current should be around 10-100 Amps, and the magnetic induction is about .5 – 1.T. These parameters provide the current channel displacement in several millimetres resulting in penetration of heated portion of one component to another co-flow stream during the observation time. The latter is defined by the velocity of the flow and the size of observed area.

Conclusions

The new concept of MHD driven Advanced mixing of gaseous fuel-oxidant system in a high-speed combustor is formulated.

- The background of such a concept consists of the earlier developed model of kinematics mixing in vortex turbulent flows.
- The vortex nature of the Lorentz body force resulting from perpendicular vectors of electrical current and externally applied magnetic field provides the flow vorticity intensification.
- The enhancement of the mixing under such conditions is characterized by an exponential growth of the contact surface square in a turbulent flow.
- The second mechanism – molecular diffusion is responsible for the creating the flammable mixture in a physically small volume.
- These two mixing mechanisms are combined to formulate the concept of reacting volume – the volume where the combustion is only possible.
- Besides of the qualitative physical model the proper numerical model has been developed to study the process on the microscopic scale.
- This model includes the treatment of chemical reacting flows on the base of full Navier-Stokes approach, chemical kinetics model, and MHD effects model.
- Preliminary results confirm the basic physical ideas. The combustion in co-flow streams can be effectively initiated and controlled by the manipulation of the electrical parameters: strength of external magnetic field and electrical discharge current.
- The dramatic growth of the reacting volume and, hence, the combustion performance in the presence of MHD interaction was clearly demonstrated.

5. NUMERICAL SIMULATION OF COMBUSTION IN COUNTER-FLOW STREAMS

In the current study the attempt is made to simulate the combustion of injected propane to the airflow in the setup close to those made experimentally in [7]. Two operation modes are studied:

- 1) External supersonic airflow at Mach number 2;
- 2) External subsonic airflow at Mach number 0.09.

Several propane flow rates were specified in the supersonic operation mode, namely a) 0.2 g/s, b) 0.4 g/s, c) 0.6 g/s. Average of them was tested in the subsonic operation mode. The two-dimensional Navier-Stokes equations coupled with equations for

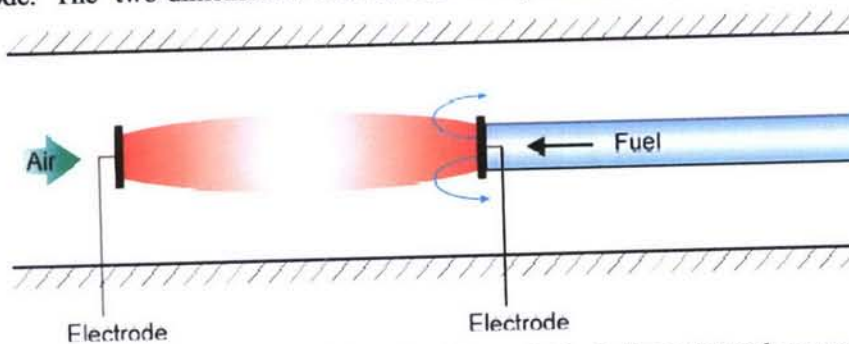


Fig.169. Schematic of computational domain to study the discharge-induced propane combustion.

species densities were numerically solved to find all the flow fields. The one-equation brutto-kinetics mechanism [8] was applied to simulate the change-of-rate of propane conversion. The effect of pulse-repetitive electrical discharge was simulated by specifying the average energy power rate in the region between two electrodes. The magnitude of the power rate was estimated from the experimental data [7]. It corresponds to the average electric current of 1A and the average electrode voltage of order of 300 Volts. From these the amplitude of the energy power rate was estimated to

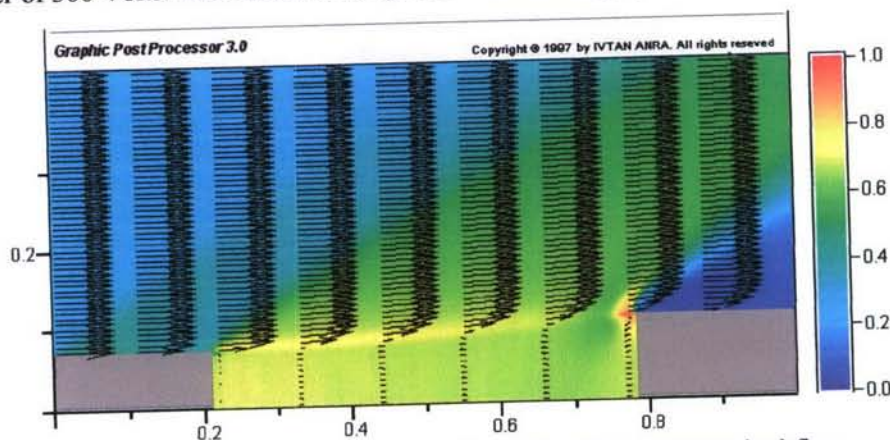


Fig.170. Original pressure and velocity distributions for the supersonic airflow.

be $4 \cdot 10^9 \text{ W/m}^3$. All important flow characteristics were obtained and efficiency of combustion was estimated for two different operation modes.

Combustion of propane was simulated in the geometry shown in Fig.165. Distance between electrodes is 8.0 mm, left electrode diameter is 2 mm, and right electrode diameter is 3.0 mm. Parameters of the airflow were as follows.

- 1) Pressure is 13800 Pa, Velocity is 510 m/s,
Temperature is 162 K, Mach number is 2 (supersonic operation mode).
- 2) Pressure is 10^5 Pa, Velocity is 30 m/s,
Temperature is 300 K, Mach number is 0.09 (subsonic operation mode).

Results. Supersonic flow.

Original flow field for the supersonic airflow and propane injection without combustion is presented in Fig.170 by pressure and velocity distributions. It should be noted that almost all space between electrodes is occupied by propane, which flows

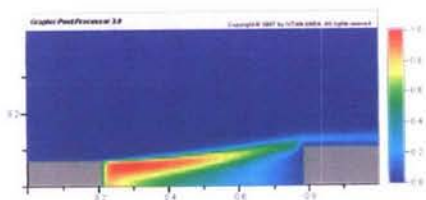


Figure 171. Temperature distribution for supersonic airflow and propane flow rate 0.2 g/s.

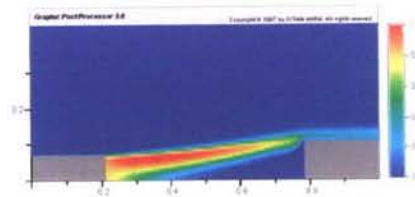


Figure 174. Water distribution for supersonic airflow and propane flow rate 0.2 g/s.

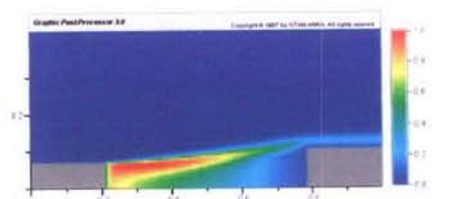


Figure 172. Temperature distribution for supersonic airflow and propane flow rate 0.4 g/s.

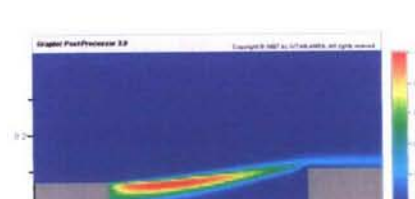


Figure 175. Water distribution for supersonic airflow and propane flow rate 0.4 g/s.

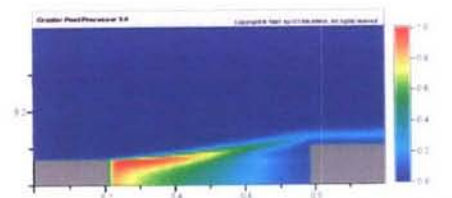


Figure 173. Temperature distribution for supersonic airflow and propane flow rate 0.6 g/s.

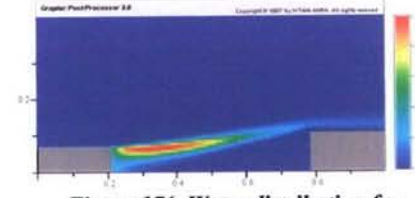


Figure 176. Water distribution for supersonic airflow and propane flow rate 0.6 g/s.

mostly against the airflow. Fig.171 through Fig.173 presents the temperature fields obtained for three values of propane flow rate: 0.2 g/s, 0.4 g/s, and 0.6 g/s, consequently. Maximum temperature value is 3650K for 0.2 g/s, 2830K for 0.4 g/s and 2440K for 0.6 g/s. Fig.174 through Fig.176 show the fields of water corresponding to the same cases of Fig.171-173. It is seen that for this configuration the higher fuel flow rates lead to the worse combustion efficiency. This is also confirmed by distributions of temperature and fuel concentrations in the mid-plane between electrodes shown in Fig.177. Curves F1 through F3 represent the propane mole fractions for cases (a) through (c), respectively. Curves T1 through T3 represent temperature distributions for the same cases. Curve mapped as T0 corresponds to the initial no-combustion flow field. Rather high values of temperature are due to applying brutto-kinetics mechanism, which can be used just for qualitative estimations. More accurate reduced kinetics mechanism is expected to give more realistic values. Fig.178 represents the water and temperature distributions at the outlet cross-section of the computational domain. Curves W1 through W2 correspond to cases (a) through (c), respectively. Temperature distributions are mapped as in Fig.177. The same tendency is well seen: the higher fuel flow rate, the worse efficiency of combustion.

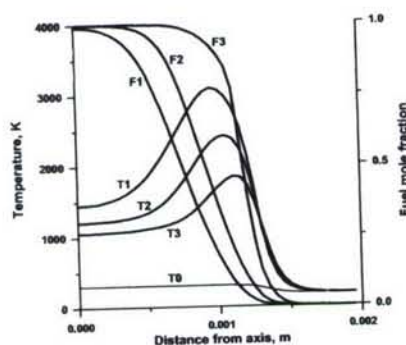


Figure 177. Temperature and fuel distribution at mid-cross-section for supersonic airflow.

Curves T0 through T3 designate temperature, curves F1 through F3 designate fuel concentration.

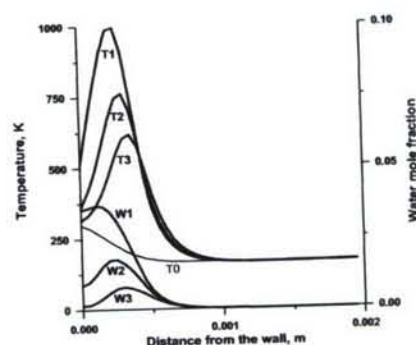


Figure 178. Temperature and fuel distribution at outlet cross-section for supersonic airflow.

Curves T0 through T3 designate temperature, curves F1 through F3 designate fuel concentration

Results. Subsonic airflow.

The problem formulation is almost same as was for the supersonic airflow. After the original flow field was calculated the discharge is switched on and the propane is injected in absolutely same manner. The total flow rate of propane was specified as 0.2 g/s (this corresponds to the Case of Fig.171 in supersonic operation mode), i.e. constant velocity 35 m/s was set at the injection cross-section. Mention that for subsonic airflow the average inlet velocity was set to 30 m/s, static pressure equals to 10^5 Pa, and temperature equals to 300 K. At the inlet the total pressure and stagnation temperature are specified as boundary conditions. Original flow field (no discharge, no propane injection) is shown in Fig.179, where the pressure and velocity field is presented.

The evolution of the mixing and combustion is shown in Fig.180 through Fig.187 and Fig.180 through Fig.207. In Fig.180 through Fig.193 the temperature distributions at several time moments are shown. In Fig.194 through Fig.207 the fuel mole fractions are shown for the same time moments. It is seen that combustion of propane distinguishes qualitatively for two different operation modes, supersonic and subsonic.

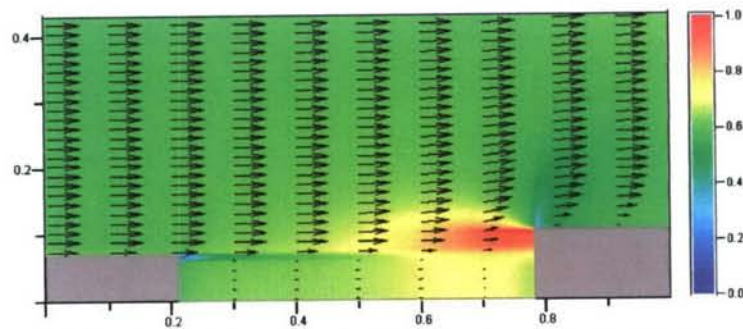


Fig.179. Original pressure and velocity field for subsonic airflow.

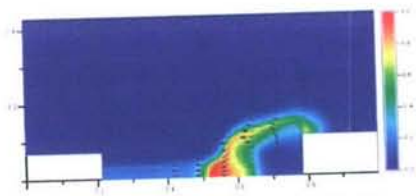


Fig. 180. Temperature and velocity distributions, time = 0.075 ms

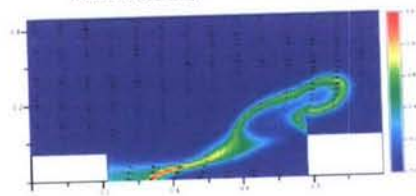


Fig. 181. . The same as Fig.19. $t=0.15\text{ms}$

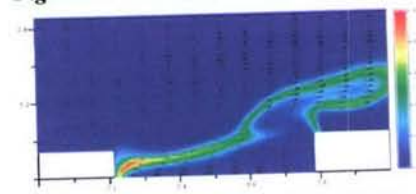


Fig. 182. The same as Fig.19. $t=0.185\text{ms}$

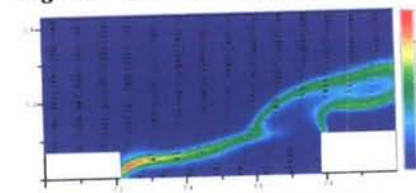


Fig. 183. The same as Fig.19. $t=0.2\text{ms}$

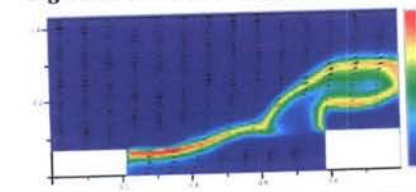


Fig. 184. The same as Fig.19. $t=0.25\text{ms}$

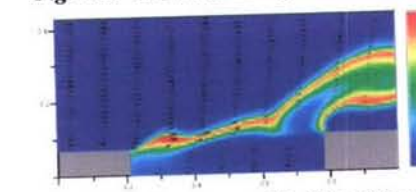


Fig. 185. The same as Fig.19. $t=0.3\text{ms}$

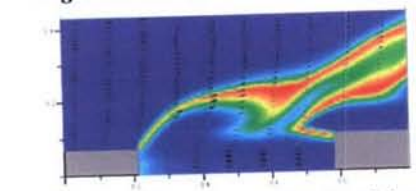


Fig. 186. The same as Fig.19. $t=0.5\text{ms}$

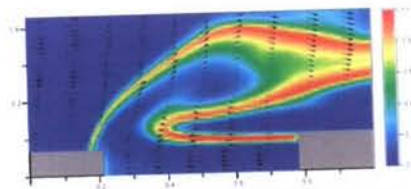


Fig. 187. The same as Fig.19. $t=0.75\text{ms}$

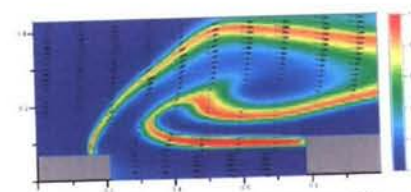


Fig. 188. The same as Fig.19. $t=1.0\text{ ms.}$

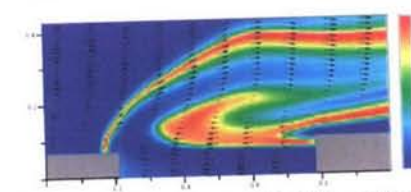


Fig. 189. The same as Fig.19. $t=1.5\text{ ms}$

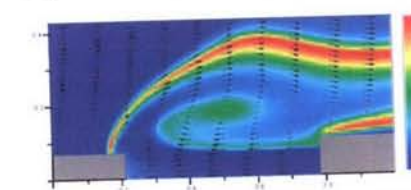


Fig. 190. The same as Fig.19. $t=2.0\text{ ms}$

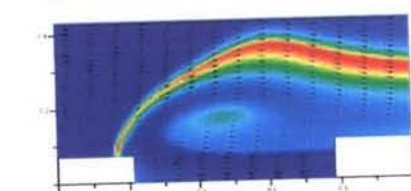


Fig. 191. The same as Fig.19. $t=2.5\text{ms}$

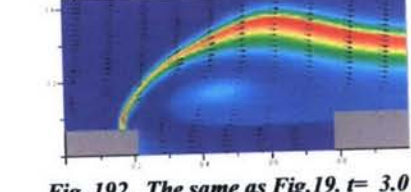


Fig. 192. The same as Fig.19. $t=3.0\text{ ms.}$

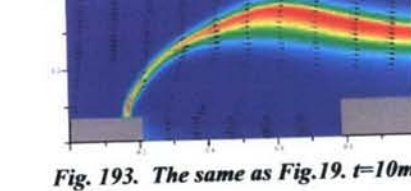
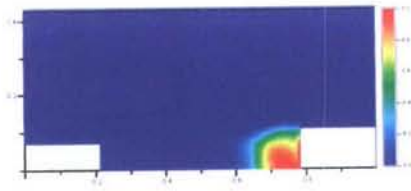
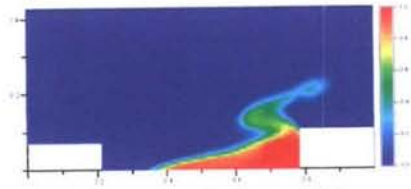
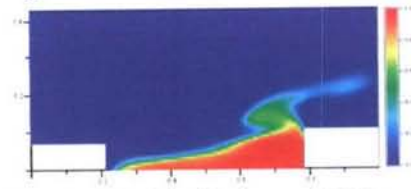
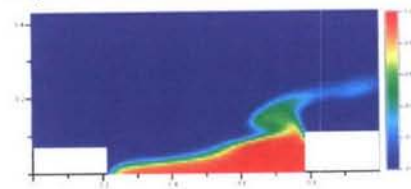
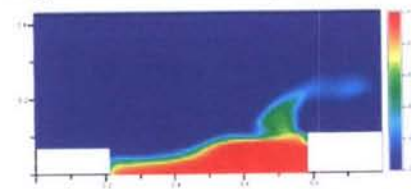
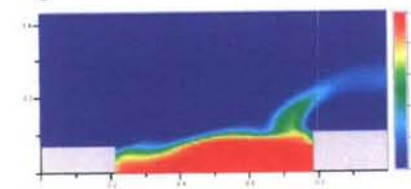
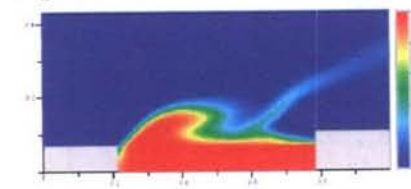
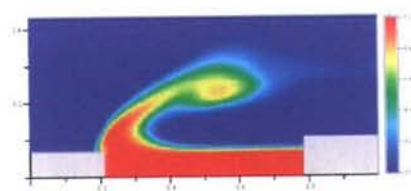
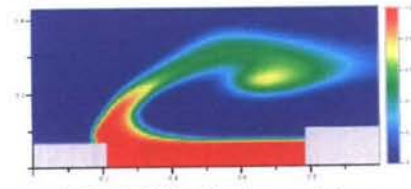
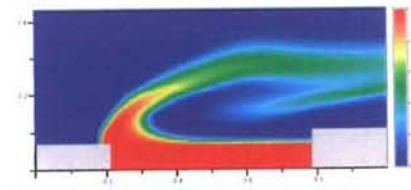
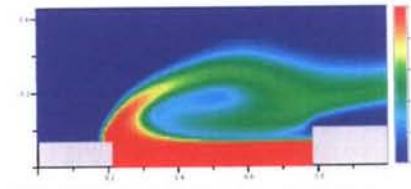
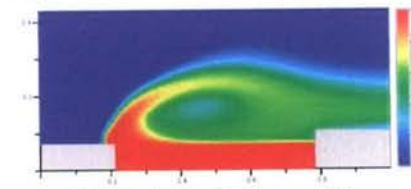
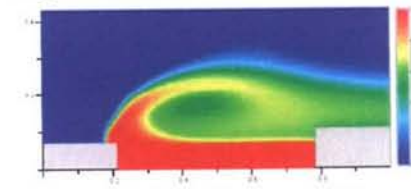
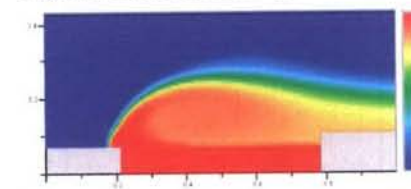


Fig. 193. The same as Fig.19. $t=10\text{ms.}$

Fig. 194. Fuel distribution, $t = 0.075\text{ms}$.Fig. 195. Fuel distribution, $t = 0.15\text{ms}$ Fig. 196. Fuel distribution, $t = 0.185\text{ms}$ Fig. 197. Fuel distribution, $t = 0.2\text{ms}$ Fig. 198. Fuel distribution, $t = 0.25\text{ms}$.Fig. 199. Fuel distribution, $t = 0.3\text{ms}$.Fig. 200. Fuel distribution, $t = 0.5\text{ms}$ Fig. 201. Fuel distribution, $t = 0.75\text{ms}$ Fig. 202. Fuel distribution, $t = 1.0\text{ms}$ Fig. 203. Fuel distribution, $t = 1.5\text{ms}$.Fig. 204. Fuel distribution, $t = 2.0\text{ms}$.Fig. 205. Fuel distribution, $t = 2.5\text{ms}$ Fig. 206. Fuel distribution, $t = 3.0\text{ms}$ Fig. 207. Fuel distribution, $t = 10.0\text{ms}$

In the first case the region of combustion is restricted by the bulk cavity between two electrodes, in which the re-circulation zone originally appears and which is filled in with propane. The combustion occurs in a thin mixing flow, which doesn't allow the fuel to enter deeply to the main airflow. Another flow structure takes place in the low-speed flow case. After ignition the fuel penetrates into the airflow deep enough. It takes several milliseconds for the flow to be a quasi-steady. The characteristic radial size of the final combustion zone is of order of 5 mm. Both two features, very small visible characteristic size of the combustion zone in supersonic flow and large visible size of it in low-speed flow, qualitatively correspond to the experimental photos of the discharge made in [7].

At steady state the temperature in the combustion layer is of order of 2500 K, while during several hundreds of microseconds after ignition it can be as high as 2900 K.

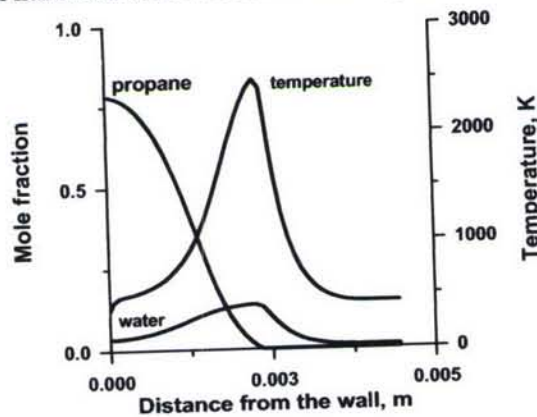


Fig.208. Propane and water mole fractions and temperature distributions at the outlet cross-section, subsonic flow.

Some outlet distributions are shown in Fig.208. It is seen that intensive combustion takes place in the region far enough from the discharge zone. This is also qualitatively corresponds with the experimental observations. In the subsonic flow case the role of far field boundary conditions becomes very important. Calculations carried out with the wall boundary conditions at the upper boundary showed that the spatial structure of the discharge changes, though it correlates better with the experimental image. Reproduction of the experimental design in the numerical simulations takes, however, more time because larger computational domain should be considered.

6 NO EFFECT ON THE IGNITION OF HYDROGEN AND HYDROCARBONS IN NON-PREMIXED LAYERS OF COLD FUEL AND HOT AIR

On study of plasma-assisted combustion it is widely used several kind of electrical discharges. One of them is arc discharge. The arc discharge was employed under investigation of the ignition and combustion in the counter-flow jets of oxidant (air) and cold fuel (gaseous propane) in the work [1]. The products of reactions initiated by arc discharge differently influence ignition of non-premixed layers of fuel and oxidant. One-dimensional simulation of mixing and combustion showed that the ignition time in each point of combustion zone is determined by the multi-component diffusion [2]. Radicals (O atoms) in hot air zone resulting from discharge play a part of source of high-enthalpy component and bring to the growth of temperature due to recombination and other chemical reactions, and O atom weakly affects the induction time [2]. This is the principle distinction from the preliminary premixed fuel and oxidant where the presence of radicals reduces the induction time appreciably. Other important component produced in discharge zone is nitrogen oxide. Its concentration may amount to some percents. Experiments carried out in H_2 -air mixture [3] and in the counter-flow jets [4] showed nitrogen oxide may promote hydrogen and hydrocarbons combustion under rather low temperatures of 770-1300 K in some range of pressure, temperatures and NO concentrations.

In given paper to determine the nitrogen oxide influence area on ignition time and temperature the axi-symmetric problem of the radial development of electrical arc channel in air was carried out. The radial dependences of temperature and NO concentration in several time instants were obtained. The goal of modeling was to find the main processes, which affect the ignition rate and temperature ignition limit. The one-dimensional simulation of NO effect on induction time in the system of cold hydrogen ($T_0=300$ K) and sufficiently hot air ($T_0=790-1100$ K) holding the different NO percentage (10^{-3} -3%) was performed. The comparison with results in preliminary mixed fuel and air, and with experiment in the counter-flow jets was done. The chemical kinetics mechanism of hydrocarbons (CH_4 , C_2H_6 , C_3H_8) oxidation and combustion was assembled to describe the influence of NO on these processes. The dominated reactions for every stage, induction time in dependence on temperature, CH_4 and NO content in CH_4 -air mixture are presented.

Simulation of electrical arc discharge

The computational model used in simulating the evolution of electric discharge is basically described in [5]. In the current paper options related to the non-equilibrium plasma are omitted and it is assumed that both heavy particles and electrons have the same temperature at any location of the plasma bulk. The discharge is supposed to occur in the gap between two flat electrodes. The length of the gap is taken to be 1 cm. External electric circuit is assumed to provide 1 Ampere DC current in the gap. It is also guessed that electric field strength has only one component aligned with the electrode-to-electrode direction. Neglecting near-electrode phenomena one can consider all plasma properties unchangeable in the electric current flow direction. Finally, axi-symmetric discharge is considered. All these assumptions allow formulating the one-dimensional axi-symmetric problem to calculation of plasma properties in the gap.

The numerical model is based on a solution to Navier-Stokes equations coupled with the mass conservation equations for every species. The source terms in the species conservation equations are evaluated from 7 species chemical kinetics model. Transport properties of multi-component fluid are estimated on the base of temperature approximations to collision integrals of viscous and diffusion type. Details are referred to [6, 7]. Thermodynamic properties of species are determined by specifying the formation enthalpies and polynomial dependencies of constant-pressure heat capacities on temperature. Ideal gas equation-of-state is assumed to hold for every species, and Dalton's law is used to determine the gas pressure. Relationship between electric field strength and total current is resulted from Ohm's law. To complete total plasma resistance is to be calculated.

Initial and boundary conditions are specified as follows. As initial state the plasma column is specified, in which Gaussian distribution of temperature and electrons along radius is given. Typically, 0.5 mm was used as the half-width of Gaussian; at-axis temperature was taken between 5500-7000 K; at-axis electron mole fraction was tried between $10^{-6} - 10^{-5}$. The electrons were balanced with NO^+ . Initial

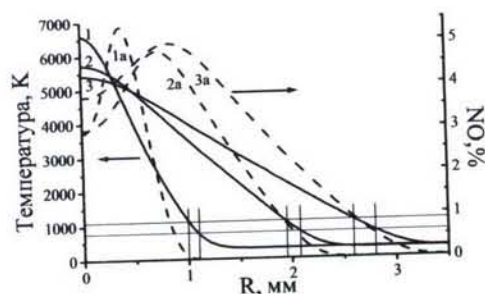


Fig.209. Radial evolution of arc channel in air. Dependences are given for different instants of time:

1,1a - 40 μs , 2,2a - 500 μs , 3,3a - 800 μs .

Thin lines mark the ranges where sensitization of ignition is possible: $T=770-1200\text{ K}$, radial distribution of density is calculated at pressure $P_0 = 10^5\text{ Pa}$, and temperature distribution described above. Symmetry conditions are set at the symmetry axis, i.e.

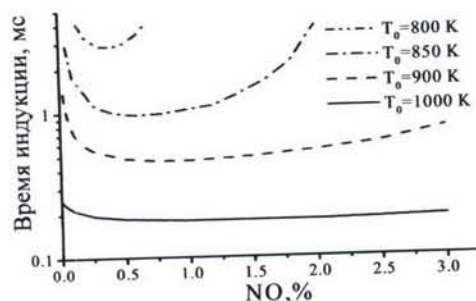


Fig.210 Induction time in dependence on initial NO content in hot air at the boundary of fuel and oxidant layers for several temperatures of hot zone. (H_2 layer is at $T_0=300\text{ K}$).

zero radial derivatives for all variables except radial velocity are specified at the axis, and zero radial velocity is set at $R = 0$. At the outer boundary distant from the

symmetry axis on 4 cm, zero derivatives are specified along with fixed static pressure value, $P_0 = 10^5$ Pa.

In Fig.209 the temperature and NO radial distributions in the vicinity of arc channel is presented. The thin horizontal and vertical lines mark the range of low temperature $T=770-1200$ K where nitrogen oxide may accelerate the oxidation process of hydrogen. According to Fig.210 these temperatures are corresponded $[NO]=0.05-1\%$. The NO concentration is "frozen" when airflow drifts NO from discharge zone and may achieve the amount more then 1 percent. In general the formation near discharge of some NO distribution is determined by velocity of airflow, pressure and fuel flow rate. Non-uniform NO distribution in airflow may bring to cellular structure of ignition and non-uniform character of initial stage of combustion.

Discussion of results

The calculations showed non-monotone ignition character at the boundary of two layers in dependence on NO concentration as well as in stoichiometric H_2 -air mixture. The NO influence already begins with a small concentration, for example, 10 ppm for mixture. The induction time was defined in the maximum of H atom

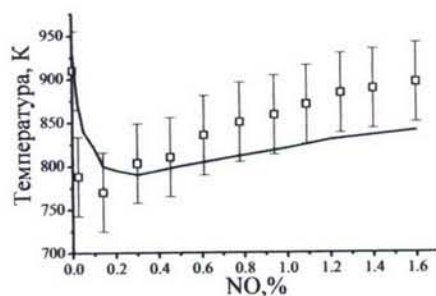


Fig.211. Ignition temperature in dependence on NO concentration in air at the boundary of two layers (H_2 layer is at $T_0=300$ K). The lines are modeling, symbols are experiment [4].

concentration; this moment corresponds to the temperature of 1600 K at the boundary of layers. Fig.211 illustrates the dependence of induction time on NO percentage for H_2 and air layers at initial air temperature of 800-1000 K. The minimum induction time τ_{in} at $P=10^5$ Pa and $T_0=900$ K of air is observed at 0.5-1% NO and equal to $\approx 460\mu s$, whereas in the stoichiometric mixture $\tau_{in}=225\mu s$. Nitrogen oxide virtually does not influence ignition of hydrogen at $T_0 \geq 1100$ K for non-premixed gases and stoichiometric mixture. These results are in agreement with experimental dependences [3,4]. In the

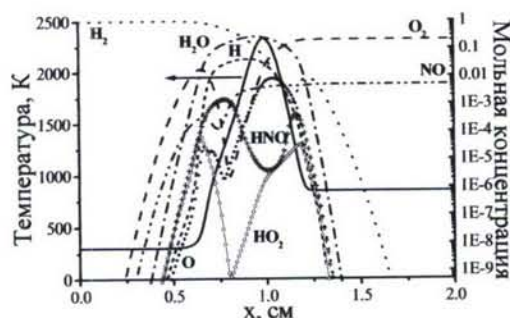


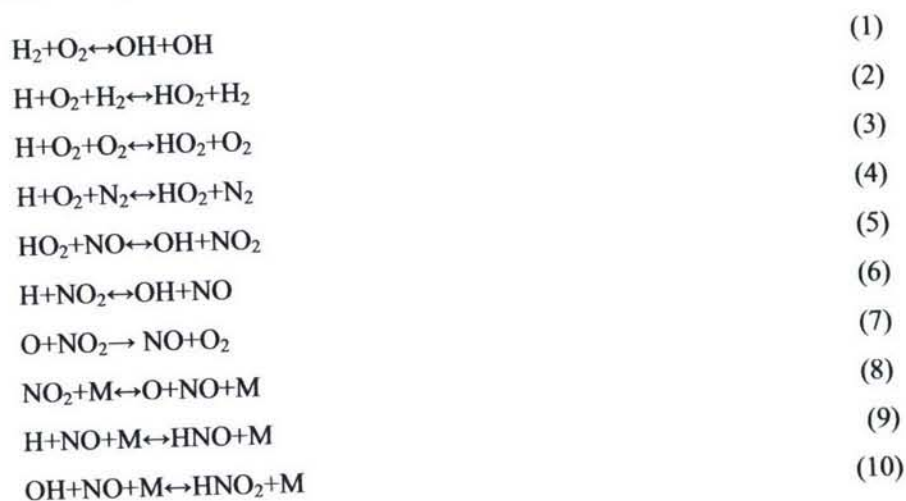
Fig.212 Temperature and concentrations of components within 1.2 ms in ignition kernel. H_2 layer is at $T_0=300$ K, air layer is at $T_0=850$ K, $[NO]_0=0.5\%$.

absence of NO at $T_0 < 930$ K and in the presence of 2.1% NO at $T_0 = 850$ K the ignition at the boundary of two layers did not occur at the time less 4.2 ms (residence time of ignition kernel in the reaction volume). It is noted τ_{in} rapidly increases near $T_0 = 900$ K without NO, and for stoichiometric mixture $\tau_{in} \sim 6$ ms at $T_0 = 910$ K as in experiment [8] as in our calculations.

In Fig.212 the dependence of temperature ignition limit as a function of NO concentration in air is shown. Corresponding to these temperature values the ignition time at the boundary is found in the range of 3-4.2 ms. The results of experiments in counter-flow jets [4] at strain rate $k_{exp} = 300 \text{ s}^{-1}$ are indicated by symbols. The distance between two nozzles was equal to 2 cm. These values are limited the residence time of ignition kernel in the reaction zone. In given work the calculation domain was limited by 2 cm and the boundary between cold and hot layers was located in the middle of domain. The direct comparison is possible only taking into consideration a tangential component of flow velocity, for example, in two-dimensional simulation, because of counterflow improves the mixing, and as a consequence, accelerates the ignition. However, in experiment [9] the ignition temperature at $P_0 = 10^5$ Pa virtually was insensitive to strain rate in the fairly wide range. In Fig.3 one can see if a counterflow is available the temperature ignition limit decreases from 910 K without NO to 770 K with 0.14% NO, but in calculations it decreases from 930 K to 790 K at 0.3% NO.

During induction time a mixing zone of fuel and oxidant amounts to some millimeters, its width is determined by diffusion and thermal conductivity. The distribution of most components at ignition instant and combustion has a non-monotone behavior with some extremism (see Fig.208). The size of combustion zone may define with respect to H_2O profile line; it is about 1 cm. The behavior of NO_2 is close to HO_2 profile line.

In the combustion process with NO the chemical kinetics scheme and role of individual components are changed, for example, HO_2 . This radical facilitates branching instead of termination of chain (reactions (5), (6)). The main reactions, which result in sensitization of ignition or prohibit the branching of chain under certain conditions of temperature and concentrations, are following:



Reactions (1)-(5) essentially influence the initial combustion process and induction time. At high initial NO concentration the disappearance of O and H atoms in interacting with nitrogen oxide becomes appreciable and the combustion process

does not develop (reactions (8)-(10)). The kinetic scheme included 15 components and 77 elementary reactions. The constants rates have been taken mainly from [10]. This kinetic scheme has been tested (without NO) on experiments [3,8,11] and results of comparison were very good.

The modeling showed the maximum temperature shift was observed at $[\text{NO}]_0=0.3\%$ and equal to 140 K (without NO $T_0=930$ K) for non-premixed layers of H_2 and air, and 175 K (without NO $T_0=915$ K) for stoichiometric H_2 -air mixture. The ignition occurred at time ~ 4 ms.

Thus, NO effect on ignition and combustion takes place in comparatively narrow range of temperatures and sufficiently wide range of NO concentrations. Induction time at the boundary of fuel and oxidant with different temperatures (H_2 and air) is greater than induction time for stoichiometric H_2 -air mixture by a factor of two and more under considered conditions. The ignition temperature is shifted to lower values, at more than 100 K. In hydrocarbon-air mixtures NO affects only the conversion stage of combustion process shortening it up to the order of magnitude.

References

- [1] A.I. Klimov, V.A. Bityurin et al. - In Proc. of The 4nd Workshop on Magneto-plasma-aerodynamics in Aerospace Applications, 9-11 April, Moscow, Russia. 192 (2002).
- [2] V.A. Bityurin, A.N. Bocharov, E.A. Filimonova and A.I. Klimov - In Proc. of The 15 Inter. Conf. on Gas Discharges and their Applications, 5-10 Sept., Toulouse, France. 973 (2004).
- [3] M. Slack and A. Grillo - Investigation of Hydrogen-Air Ignition Sensitized by Nitric Oxide and by Nitrogen Dioxide, NASA Report CR-2896. 38 P. (1977).
- [4] Y. Tan, C.G. Fotache and C.K. Law - Combustion and Flame. **119**, 346 (1999).
- [5] A. Bocharov, S. Leonov, I. Klement'eva, V. Bityurin - In Proc. of 41st Aerospace Sciences Meeting and Exhibit, Reno, NV, AIAA Paper 2003-5878 (2003).
- [6] A.I. Zubkov, G.A. Tirskiy, V.A. Levin, V.I. Sakharov - Motion of bodies in Earth's and Planet's Atmospheres with Supersonic and Hypersonic Velocities under Conditions of Chemical Conversions, Heat Transfer and Radiation. Rep. No.4507, Institute of Mechanics of Moscow State University (1998).
- [7] A.V. Andriatis, S.A. Zhukotov, I.A. Sokolova - J. Mathematical Modeling. **4**, No 1(1992).
- [8] A.D. Snader, J.Z. Robertson et al.- Shock tube studies of flue-air ignition characteristics. Tech. Report AFAPL-TR-65-9, 1965.
- [9] C.G. Fotache, T.G. Kreutz, D.L. Zhu and C.K. Law - Combust. Sci. and Tech. **109**, 373 (1995).
- [10] D.L. Baulch et al J. Phys. Chem. Ref. Data . **21**,411 (1992)
- [11] G.I. Schott, J.L. Kinsey - J. Chem. Phys. **29**, 1177 (1958)

7. INTERACTION OF CONSTRICTED DISCHARGE WITH A COLD FLOW IN EXTERNAL MAGNETIC FIELD

In this Section the numerical simulations of evolution of the constricted discharge in the flow and in external magnetic field are presented. The numerical experiment setup is taken to be close to the planned physical experiments. The layout of computational experiment is shown in Fig. 213. The concept of such a formulation is as follows: mainstream flows from left to right. The counter-flow jet is injected through the pipe toward the mainstream flow. The discharge is assumed to initiate between wire electrode attached to the pipe and another electrode looking as the surface of cylinder. The external magnetic field should interact with the discharge

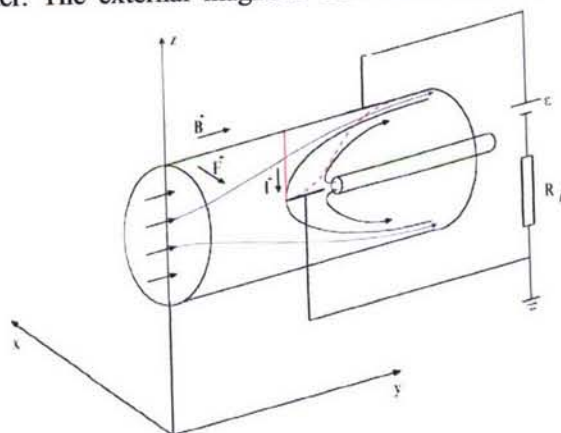


Fig.213. Schematic of the computational setup.

current and to provide a pondermotive force in the direction perpendicular both to the flow direction and electric current flow. The motion of the constricted discharge should intersect the contact surface between two flows thus providing additional vorticity and mixing in fluid. The goal of the current simulations is to study the evolution of the

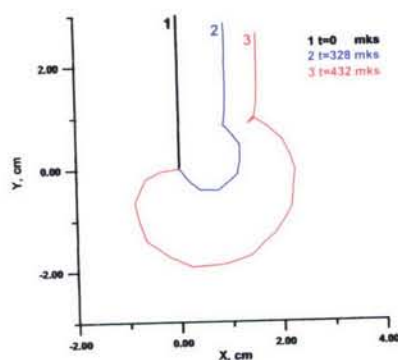


Fig.214. Position of the discharge column at different time moments. View from the mainstream flow, nominal discharge current $I = 1$ Amp.

constricted discharge in such complex flow and in the presence of the external magnetic field.

The thermodynamics of the discharge plasma has been presented in the previous Reports and in several AIAA Conferences. Here the dynamics of the discharge is mostly stressed. Since the column of the discharge may deform the newly developed adaptive model takes into account these deformations and automatically

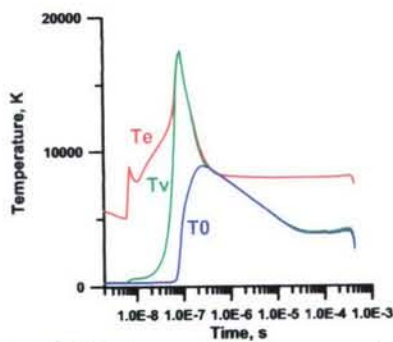


Fig.215. Column-averaged temperatures vs. time, $I = 1$ Amp.

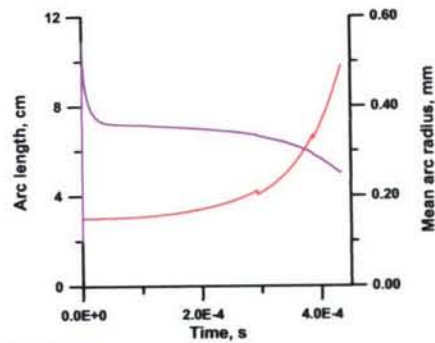


Fig.216. Column-averaged radius (blue) and column length (red) vs. time, $I = 1$ Amp.

changes a computational partition of the discharge. Special treatment has also been

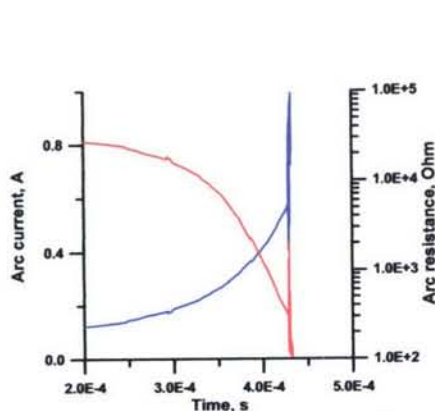


Fig.217. Column-resistance (blue) and current (red) vs. time, $I = 1$ Amp.

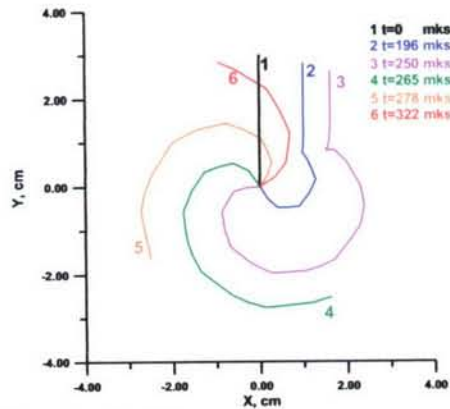


Fig.218. Position of the discharge column at different time moments. View from the mainstream flow, nominal discharge current $I = 5$ Amp.

developed to meet the impact of any part of the column with the electrodes. Below some numerical results are presented demonstrating the evolution of the constricted discharge in the counter flow and in the external magnetic field, Figs.213 through 222.

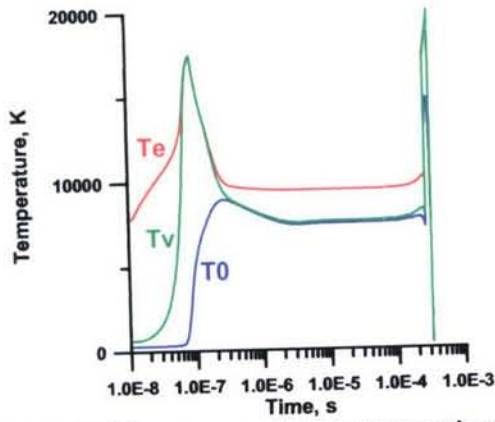


Fig.219. Column-averaged temperatures vs. time, $I = 5$ Amp.

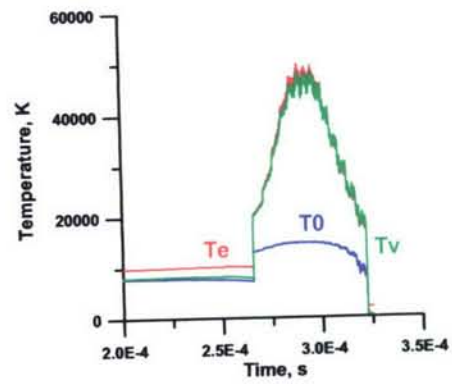


Fig.220. Column-averaged temperatures near the column breakdown vs. time, $I = 5$ Amp.

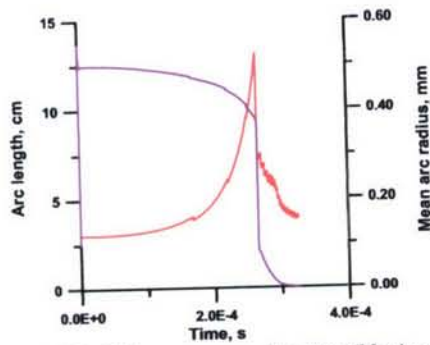


Fig.221. Column-averaged radius (blue) and column length (red) vs. time, $I=5$ Amp.

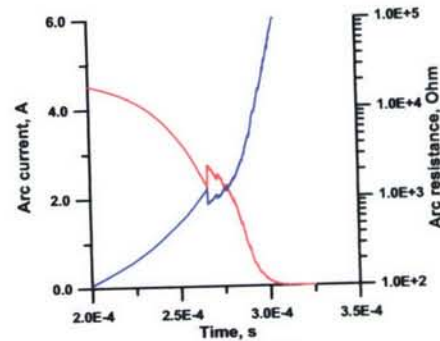


Fig.222. Column-resistance (blue) and current (red) vs. time, $I = 5$ Amp.

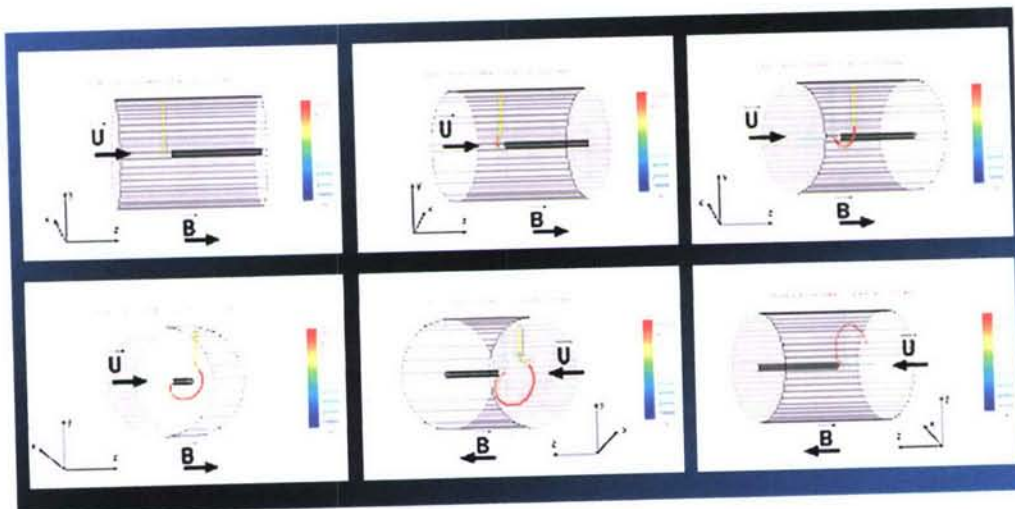


Fig.223. Visualization of the computational constricted discharge, $I = 5$ Amp, $B = 0.1$ Tesla. Pictures are from left to right and from up to down.

Concluding remarks

A new model of the constricted discharge has been developed to meet an experimental environment in studies on MHD/Plasma assisted mixing and combustion. The earlier developed discharge plasma model was incorporated into the current one and is applied to every small element of the discharge column.

It was established that characteristics of the discharge are mostly dependent on the extension of the column due to interaction of the column with the flow and magnetic field.

The residence time of the constricted discharge has been estimated. Under considered conditions it takes hundreds of microseconds for discharge to breakdown.

The electric current break is due to strong deformation of the portions of the discharge column nearest to the central wire electrode.

Common features of the constricted discharge have been found:

A discharge is shaped like a spiral, which position and deformations of its elements are determined by the flow and electromagnetic force.

The discharge tends to locate on the contact surface of two flows and to break it. This is considered as the main effect in intensifying vorticity and mixing in flow by MHD interaction.

The intermediate results of this study are presented and discussed at several national and international forums: von Karman Lecture Series (Oct 2003), 42nd AIAA Aerospace Sciences Meeting and Exhibit (Reno, NV, January 2004), Symposium on Advanced Energy Technology (Sapporo, Japan, March 2004), several papers are submitted to Schole-Seminar on Magneto-Plasma-aerodynamics for aerospace applications (April 20-21 2004, IVTAN, Moscow).

References.

1. V.A.Bityurin, V.A.Zeigarnik, A.L.Kuranov, On a Perspective of MHD Technology in Aerospace Applications, AIAA-Paper 96-2355, New Orleans, 1996
2. V.A.Bityurin, A.N.Bocharov, J.Lineberry, MHD Aerospace Applications, Invited Lecture, Intern Conf, on MHD Electrical Power Generation and High Temp. Technologies, Beijing, PDC, October 12-15, 1999.
3. J.T.Lineberry, V.A.Bityurin, A.N.Bocharov, D.S.Baranov, A.B.Vatazhin, V.I.Kopchenov, O.B.Gouskov, V.I.Alferov, A.S.Boushmin, Cylinder with Current in Hypersonic Flow, In: The 3rd Workshop on Magento-Plasma-Aerodynamics in Aerospace Applications, Moscow, April 24-26, 2001, pp15-25
4. V.A.Bityurin, D.S.Baranov, et al Experimental Study of MHD Interaction in a Hypersonic Flow with Cylindrical Body, , In: The 4th Workshop on Magento-Plasma-Aerodynamics in Aerospace Applications, Moscow, April 9-11, 2001, pp144-151
5. J. Lineberry, V.A.Bityurin, A.N.Bocharov, Analytical Study of MHD Flow Interaction Around a Right Circular Cylinder in Transverse Hypersonic Flow // 14th International Conference on MHD Power Generation and High Temperature Technologies, AIAA-2002-2112, Maui, Hawaii, May 20-23 2002.
6. V.A.Bityurin, V.G.Potebnya, A.L.Tseskis, On Evolution of A Current-Carrying Plasma Clot in Media with A Random Velocity Field, // Letter to JTP), 1996, V.22, No.2, pp.80-83
7. V.A.Bityurin, V.G.Potebnya, A.L.Tseskis, On Energy Transfer in Gas-Plasma Flows with Current-Carrying Clusters, Magnetohydrodynamics, 1997, V.33, No.3, pp.297-305
8. J.M.Ottino, The kinematics of mixing: stretching, chaos, and transport, Cambridge University Press, 1997. 364 pp
9. V.A.Bityurin, A.I.Klimov, S.B.Leonov, V.G.Potebnya. On interaction of Longitudinal Pulse Discharge with Bow Shock// In Prospectives of MHD and Plasma Technologies in aerospace Applications, Moscow, IVTAN, March 24-25, 1999, pp 114-119
10. V.A.Bityurin, A.N.Bocharov, Advanced MHD Mixing of Reacting Streams, 39th AIAA Aerospace Sciences Meeting & Exhibit, 8-11 January 2001/Reno, NV, AIAA Paper 2001-0793
11. A.N.Bocharov, S.B.Leonov, D.S.Baranov, I.B.Klement'eva, V.A.Bityurin. On MHD Enhanced Mixing and Combustion in Co-Flow Streams // The 4rd Workshop on Magneto- and Plasma - Aerodynamics for Aerospace Application, IVTAN, Moscow, 9-11 April, 2002
12. A.N. Bocharov, V.A. Bityurin, I.B. Klement'eva, S.B.Leonov, Experimental and Theoretical Study of MHD Assisted Mixing and Ignition in Co- Flow Streams // 14th International Conference on MHD Power Generation and High Temperature Technologies, Maui, Hawaii, May 20-23 2002.
13. A.N. Bocharov, V.A. Bityurin, I.B. Klement'eva, S.B.Leonov, A Study of MHD Assisted Mixing and Combustion // 41st AIAA Aerospace Sciences Meeting and Exhibit, Reno, Nevada, 6-9 Jan 2003.
14. Klimov A. I., Bityurin V., Kuznetsov A., Vystavkin N., Tolkunov B. External and Internal PAC in Airflow // In: 42nd AIAA Aerospace Sciences Meeting and Exhibit, Reno, Nevada, 4-7 January, 2004.
15. A.N. Bocharov, V.A. Bityurin, E.A.Filimonova, A.I.Klimov Numerical Study

- of Plasma Assisted Mixing and Combustion in Non-Premixed Flows// In: 42nd AIAA Aerospace Sciences Meeting and Exhibit, Reno, Nevada, 4-7 January, 2004.
16. Chue S.H. Progress in Aerospace Science, 1975, vol. 16, N 2, p. 147-223.
 17. Scott C.D. Catalytic Recombination of Nitrogen and Oxygen on High
 18. Temperature Reusable Surface Insulation.– AIAA Paper, 1980, No. 80-1477, 9 p.
 19. Zalogin G.N., Itin P.G., Knotko V.B. et oth. Diagnostics of Non-equilibrium
 20. Plasma and Catalycity Prediction in HF-Plasmatron// Plasmachemistry-89, v.2,
 21. M.: INKhS RAN, 1989, p.245-271. (In Russian).
 22. Nguyen-Xuan F., Makkard O., Cavadias S. at al. Catalycity Measurements on Metallic and SiC Material Surfaces, in a Pulsed Plasma Reactor // Second European Symposium on Aerothermodynamics for Space Vehicles. Noordwijk. 1994.
 23. Zhestkov B.E., Knivel A.Ya. Experimental Study of Heterogeneous Recombination //Proc. TsAGI. 1981. Issue 2111, p.215-227. (In Russian).
 24. Levin A.L., Khmelinin B.A. Measurement of Jet Velocity in the Plasmatron by MHD Method. Teplofizika Vysokikh Temperatur, v.9, No.2, p.413 – 419, 1971. (In Russian).
 25. Biberman L.M., Panin B. Measurement of Parameters in Electrodeless High Frequency Discharge Using Two Probes. Journal of Theoretical Physics, v.21, issue 1, pp.12-17, 1951.
 26. Johnson E., Malter L. Floating Double Probe Method for Measurements in Gas Diagnostics. Phys. Rev., v.80, pp.58-68, 1950.
 27. Kozlov O.V. Electrical Probe in Plasma. M., Atomizdat, p.292, 1969. (In Russian).
 28. Rusanov V.D. Modern Methods of Plasma Study. M., Gosatomizdat, p.183, 1962. (In Russian)
 29. Gordeev O.A., Kalinin A.P., Komov A.L. et all. Interaction potentials, elastic sections, collision integrals for air components at temperature up 20000 K// Review of thermal and physical properties of substances. IVTAN, no. 5(55), 1985.
 30. Gerasimov G.Ya., Kalinin A.P., Lyusternik V.E. et all. Collision integrals, potentials for atom-molecule and ion-molecule interaction of air components up 20000 K// Review of thermal and physical properties of substances. IVTAN, no.5(67), 1987.
 31. Stallcop J.R., Patridge H., Levin E. Analytical fit for the determination of the transportproperties of air // J. of Thermophysics and Heat Transfer. 1996. V. 10. No.4. P. 697-699
 32. Phelps A.V. et al Compilation of the electron cross section // <http://jila.colorado.edu/collision-data>, JILA, University of Colorado, 1997.
 33. V.Chinnov et al. Instr.Exper.Techn. 44, 32, 2001
 34. Zalogin G.N., Zemlyansky B.A., Knotko V.B. et al. High frequency plasmatron facility for investigation of aerophysical problems using high enthalpy gas flows. Cosmonautics and Rocket Engineering, 1994, № 2, pp.22-32. (In Russian)
 35. Vasilievsky S.A., Kolesnikov A.F. Numerical simulation of equilibrium inductive plasma within the plasmatron cylindrical channel. Fluid Dynamics, 2000, №5, pp.164-173.
 36. Vlasov V.I. Theoretical investigations of high-temperature gas flow in HF-

- plasmatron discharge and working chambers. *Cosmonautics and Rocket Engineering*, 2001, № 23, pp.18-26. (In Russian)
37. Abele D.V., Degres G. Numerical of high-pressure air inductive plasmas under thermal and chemical non-equilibrium. *AIAA Paper*, 2000, 2000-2416.
 38. Yos J.M. Transport Properties of Nitrogen, Hydrogen, Oxygen and Air to 30000K. Rep. RAD-TM-63-7, AVCO Corp., 1963.
 39. Landau L.D., Lifshitz E.M. *Theoretical Physics. Electrodynamics of condensed matters*. M.: Nauka, 1982.
 40. Van Doormaal J.P., Raithby G.D. 1984 Enhancement of the SIMPLE Method for Predicting Incompressible Fluid Flows. *Numerical. Heat Transfer*, V.5, №2. pp.147-163.

8. 2D ANALYSIS

Introduction

In previous Sections the 3D Application model has been developed and preliminary results on the MHD-assisted mixing have been presented obtained with this model. Comparisons with the first experimental results have shown that many features of the discharge evolving in the magnetic field are captured well with the Application model. The conclusion has been drawn that the model can be applied to study MHD-assisted mixing and combustion in flows of non-premixed fuels and oxidizers.

However, some uncertainties still remain concerning the behavior of the discharge in flow and magnetic field. In particular, the key postulate of the Application model is the conserving mass hypothesis. Second, experimental photos of the discharge generated in the hollow-electrode/thin-wire-electrode reveal that discharge looks as diffusive and quite smeared near the wire-electrode. This circumstance may be important for understanding how re-connections occur, and how large is the role of diffusive processes. Third motivation of the current efforts is an attempt to see how the MHD-intensified mixing effects on the combustion process.

In the current Suction the attempts are undertaken to make clear the important details said above, which may allow us to improve the Application model and to make it more suitable for future studies. Three problems are considered. The first Subsection is intended to test the hypothesis of conserving mass – key point of the model allowing to enclose the mathematical formulation of the model. This hypothesis is checked through test but typical two-dimensional problem. To get more details about re-connections, about the role of diffusive processes for the experimental conditions currently considering the two-dimensional problem (the second Subsection) is formulated and the results of numerical simulations are presented. The last Subsection is devoted to problem formulated and solved recently which is probably the first-time attempt to observe the effect of intensified mixing on the combustion of hydrogen in air.

Validation of conserving mass. hypothesis

This problem is intended to simulate the motion of the discharge along the hollow electrode, if the experimental setup being considered is implied. Assuming that cylindrical surface of electrode may be treated as the plane one we consider the following problem. The column of discharge is directed in the direction perpendicular to the plane, in which the motion of the column occurs, see Fig.224. In Fig.224 the uniform magnetic field as high as 1 Tesla is directed along the X-axis; the electric current flows in the direction normal to the plane considered. The total electric current of 1 Amp is specified. The electromagnetic force, $\mathbf{J} \times \mathbf{B}$ causes the motion of the column in positive Y-direction. The periodicity conditions imposed on the lower and upper boundaries are to simulate the closed (cylindrical) surface of the electrode. The discharge under consideration may be thought as that which is observed experimentally, but the cylindrical geometry changes to Cartesian one. We assume that at any point of the domain the air plasma is in local thermodynamic equilibrium. The aim of this numerical experiment is to check the total mass of arc column while periodical motion of it due to magnetic field and current. In calculations the discharge mass is defined as the mass of gas through which the electric current flows, that is current-weighted mass of gas.

Main results are shown in Fig.221. Blue curve on the graph represents the temporary evolution of the current-weighted mass of the arc column. It is seen that the total mass remains almost constant during two periods of arc motion except for initial

stage, when the original temperature field (gaussian with maximum temperature value of 6000K) comes into equilibrium with the electric characteristics. Period means that the arc column passed through, for example, the lower boundary of the domain. Due to

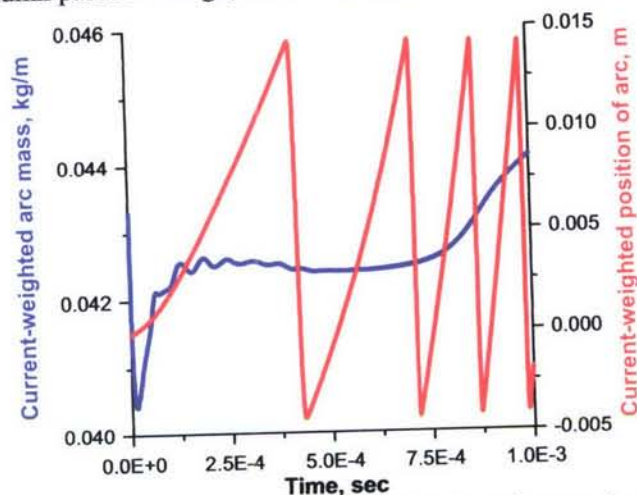


Fig.224. The current-weighted mass of the discharge column vs. time, blue curve; the current-weighted column position vs. time, red curve.

periodical conditions on lower and upper boundaries some heat remains along the column pass because the dissipative speed is rather low while the speed of column due to magnetic force is high. First of all this exhibits in the presence of column wake, which becomes more and more longer (see Fig.225). Every next time the arc passes through more and more heated and rarefied regions, since it runs up the wake of the previous column. Also this means that a volume of conductive part of the entire domain grows, which is the reason of increasing the value of current-weighted mass of the arc column. The red curve in Fig.221 shows the position of the column, which is defined as current-weighted Y -coordinate,

$$Y_j = \int j_z(x,y) \cdot y \cdot d\Omega / \int j_z(x,y) \cdot d\Omega,$$

where integration is performed overall the entire domain volume, Ω . Note, that the current-weighted mass is specified in the same manner with replacing y by density ρ

$$M_j = \int j_z(x,y) \cdot \rho(x,y) \cdot d\Omega / \int j_z(x,y) \cdot d\Omega.$$

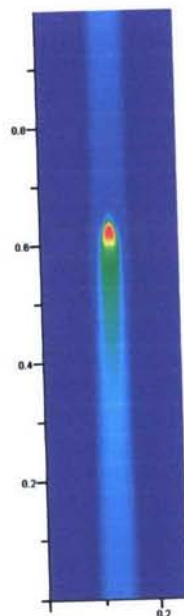


Fig.225. Temperature field at 2 ms after initiating the discharge (13 periods).

The red curve shows that the column accelerates from one period to another

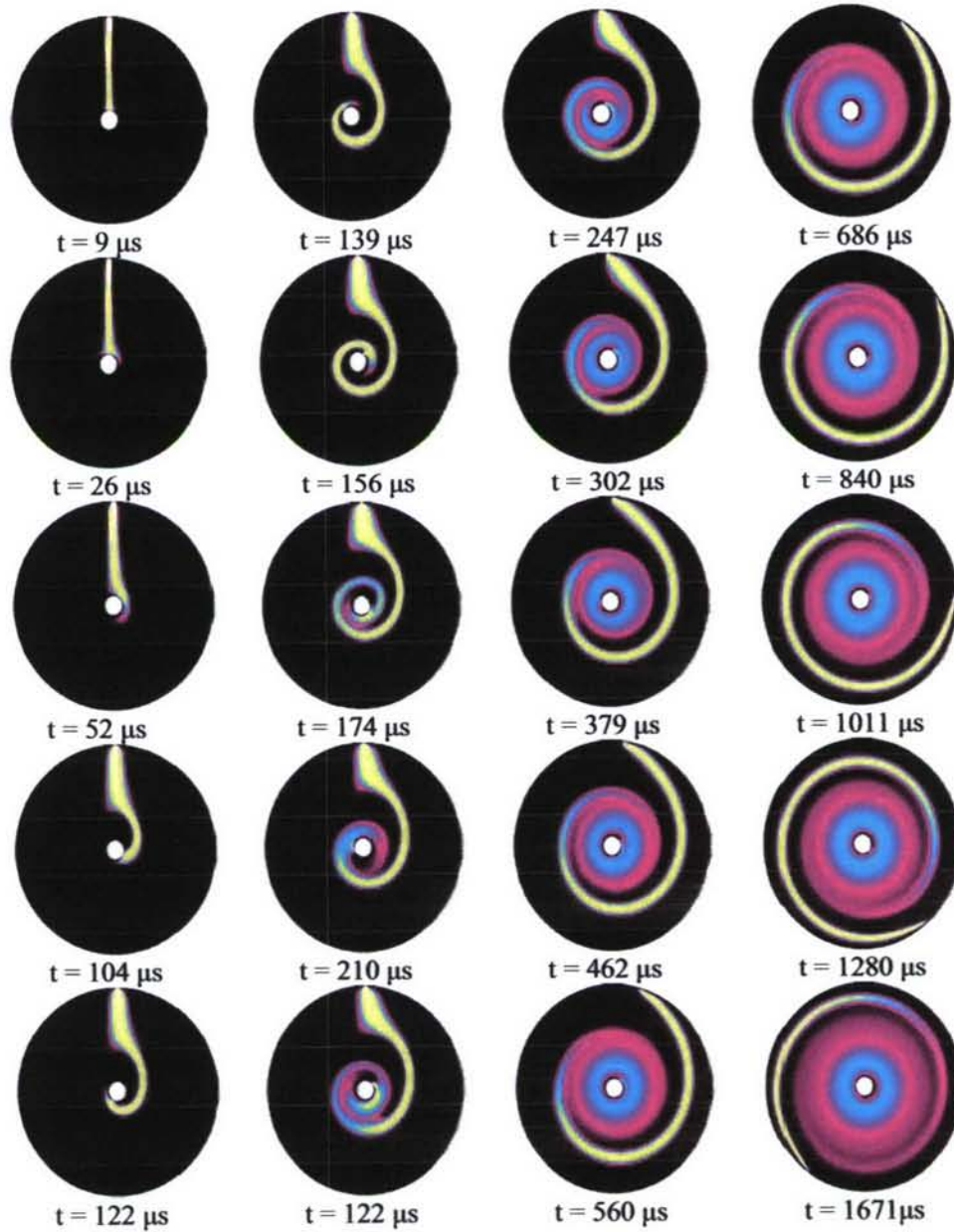


Fig.226. Time evolution of the electron mole fraction.

since the remained heat after every column pass accumulates. In real experiment the motion of the arc is essentially three-dimensional, and cooling is most probably higher than in the case under consideration. Therefore, we forecast that real case is closer to the evolution of the arc during initial two or three periods, when the hot wake is small and doesn't influence the arc motion. At these times the concept of conserving column

mass seems to be valid and can be used in the Application model to adequately

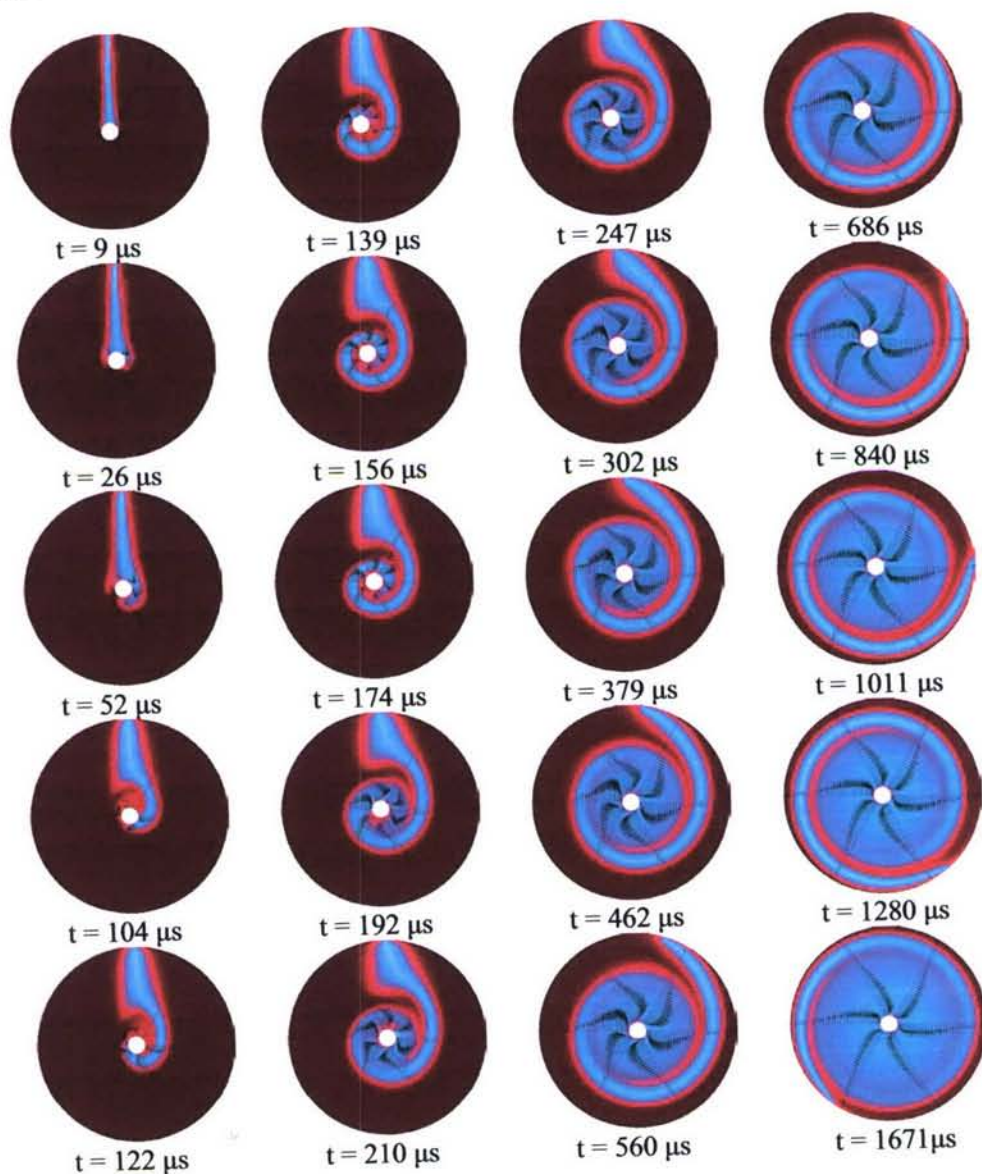


Fig.227. Time evolution of the temperature and velocity.

describe the evolution of the discharge in realistic, three-dimensional environment.

2D simulation of discharge between wire and hollow electrodes

The second problem is intended to reveal some features of the discharge in magnetic field, which are still captured not well in the Application model, but seem to exhibit in the experiments. This concerns details of re-connection effects, flow pattern near both wire and hollow electrode. The problem to be solved is formulated as follows. The electric discharge is initiated in the domain between thin wire electrode of diameter of 2 mm and external hollow electrode of diameter of 20 mm. Here we consider the

'plane' problem by assuming that flow field is uniform in the direction along cylindrical electrodes, Z-direction. The discharge is assumed to occur in air, and LTE plasma takes place. The magnetic field acts in Z-direction. The evolution of the discharge can be seen from Fig.228 and Fig.229. In Fig.228 the electron concentration (mole fraction) is shown, in Fig.4 the temperature and velocity-vectors are presented. The key feature of the discharge is the motion in the direction of electromagnetic field. At the initial stages the column tends to move right (see graphs). Since both edges of the column attach to electrode surface, the curvature of the column arises near the electrode. As consequence, the electric current changes the direction. In turn, the force changes the direction too. This process further develops thus changing the shape of column. Interestingly that the column takes a shape of spiral, the inner- most part being rotate fast around the internal wire electrode. The different speed of rotation of the column near the wire and hollow electrodes may be explained as follows. The electromagnetic force induces the pressure drop, which is almost same near both electrodes. But the pressure gradients differ in magnitude according to inverse radius. Therefore, local forces near the central part of the domain are much higher then

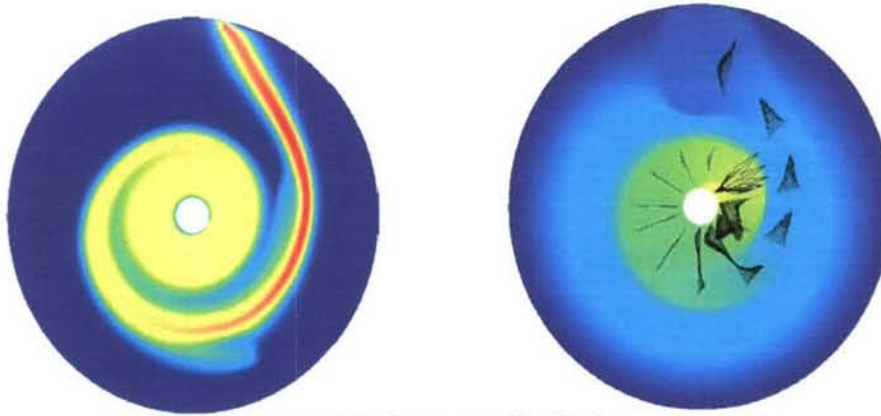


Fig.228. Temperature distribution.

Fig.229. Potential and electric current density distribution.

anywhere else. This leads to highest local acceleration of the column, and, hence, to highest speed of flow. For the observation time, the column makes nearly 26 turns around the inner electrode, while only one turn is made around the hollow one. Qualitatively the same features are observed in experimental runs. One of the important features is that in a thin boundary layer near the wire electrode the speed of the diffusive processes, first of all due to thermal conductance, is high enough. As we think, this results in permanent shifting of the column along the electrode surface. On size scale of order of column diameter, the no-slip condition may be disturbed. This observation should be taken into account in the Application model, in which zero-velocity condition often leads to the calculation halt.

As seen from both figures, the column expands in radial direction. This is because the current flows in azimuthal direction, therefore the force acts in radial one. After first few turns around the inner electrode the originally separated column parts become quite close to each other, i.e. some kind of re-connection takes place. Very soon the discharge looks as the single 'diffusive spot' around the wire electrode. This is a typical pattern observed in the experiments. In this diffusive spot the electric current of small density flows in general in radial direction while concentrating at the wire electrode surface and in the outer-most part of the column. The most important observation found from these numerical experiments is that the motion of originally

thin column of plasma makes global effect on a fluid in the whole domain. The cold non-conductive outer gas is also involved into motion, and this is the primary effect of the concept of MHD-assisted mixing.

2D simulation of discharge-assisted mixing and combustion.

To see how the MHD-mixing discussed in the previous section effects on a combustion the following problem has been considered. The same domain is originally filled with air (upper part of the domain) and hydrogen (lower part). The discharge is initiated in the same manner as before. The difference in two formulations is that Problem 2.3 takes into account finite-rate chemistry of hydrogen-air combustion and multi-component diffusion, while the Problem 2.2 deals with equilibrium-air discharge.

Typical flow fields are shown in Fig.228 – 229, which correspond to the time instant $t = 0.4$ ms. The character of the discharge evolution is principally same as in the previous problem. Fig.230 shows how the fuel (colored with magenta) is involved into oxidizer (blue) and contra versa. The hydrogen disappears near the wire electrode due to combustion process. The water mole fraction field shown in Fig.231 reveals that

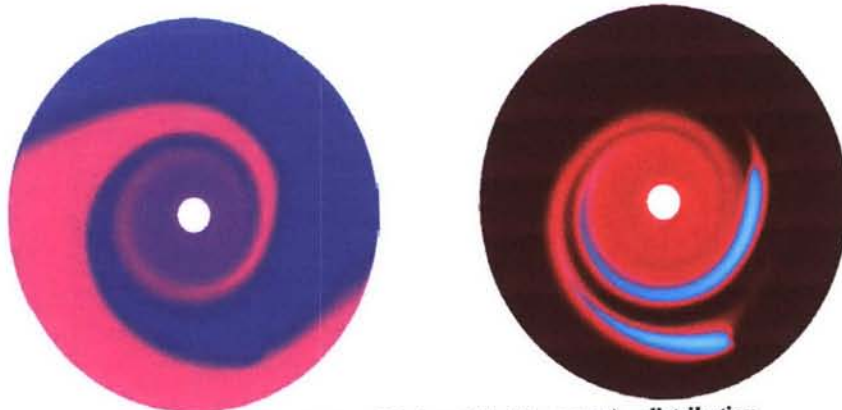


Fig.230. The oxidizer (blue) and fuel (magenta) distribution
Fig.231. Water mole fraction distribution

combustion takes place only at the contact surface. The latter increases while the fluid rotates due to MHD interaction. Also seen is the non-uniform, layer-like water concentration distribution. The temperature field is given in Fig.229. While being very similar to the distributions obtained in the previous Section, it reveals some increase in thickness of the column in regions where the water concentration reaches the maximum values. This extra heating is due to combustion. Finally, electric distributions are shown in Fig.228. The potential field has, in general, radial structure except for the place where the column attaches to the inner electrode. The electric current comes from the attachment spot and flows in both clock-wise and counter-clock-wise directions. It concentrates again in the outer-most part of the column.

9. EXPERIEMENTS

Axisymmetrical configuration

The new axisymmetrical arrangement of the experiment has been defined. This decision was provoked by the fact of the diagnostics and flow visualization problems



Figure 232. Typical visualization of the combustion in co-flow axisymmetric streams [7]

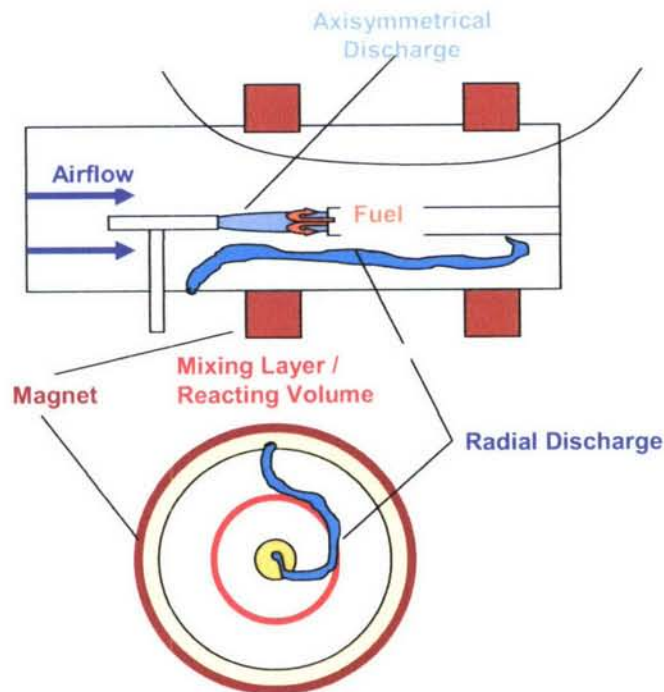


Figure 233. Schematic of axisymmetric configuration of co-flow streams experiment

found in the previous configuration used. Instead of plane co-stream flows the axisymmetrical configuration is now considered. The numerical simulation has demonstrated many advantages for such a case. From the other hand the visualization obtained in the experiments with axisymmetric counter flow injection (Fig.205) has

qualitatively confirmed the scenario of the ignition and combustion derived for such a case from numerical analysis. The modified schematic of the next step experiments is presented in Fig.233.

The schematic of the fuel injector with an DC/RF electrode is shown in

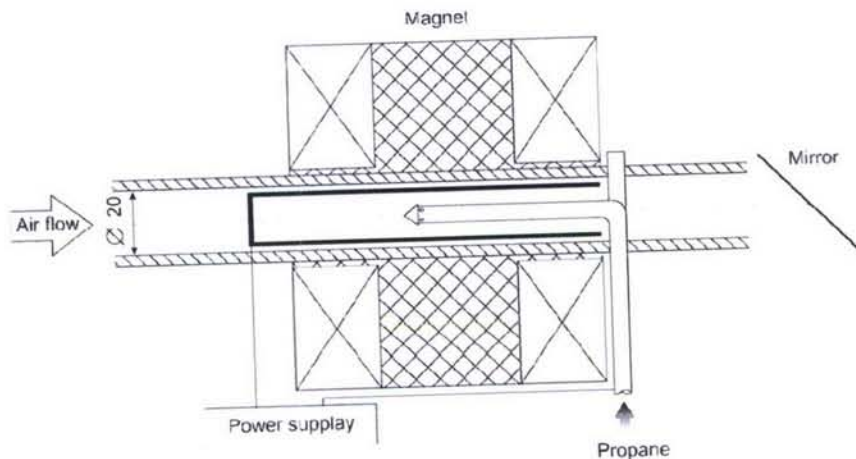


Figure 234. The schematic of the mixing zone .

The discharge will be initiated between the tip electrode axially located in the fuel injector tube and internal surface of the main flow train cylinder. The pulse magnetic field (~ 5 msec duration) will be created by a double coil powered by a battery. Two observation directions are planned: a side view through the cylinder wall and axial back view through a mirror installed at 45° to the main flow directions. The electrical



Figure 235. A general view of the experimental setup.

discharge current is to be 1-5 Amps, The magnetic induction at the discharge location is about 1T.

The test section will be installed at the existing facility shown in Fig.235. In Fig. 236 the magnet is shown.

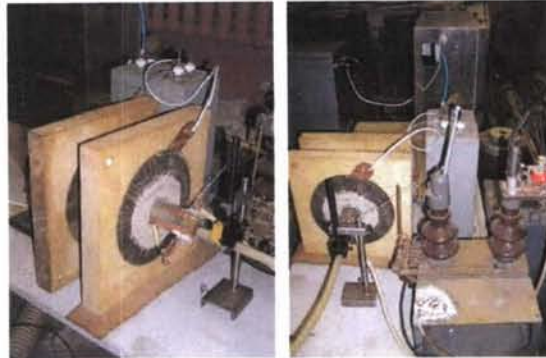


Figure 236. Front and back view of the magnet

Experimental Setup

Experimental facility designed to study MHD assisted mixing and combustion is shown in Fig.237. The base element of the facility is the pressure chamber in form of steel cylinder of 0.95 m length and 0.8 m diameter. There are four diagnostic windows of 20–42 cm diameter on the side face of the pressure chamber. Vacuum pump allowing to reach in pressure chamber the pressure value of 10^3 Pa is used for air exhausting.

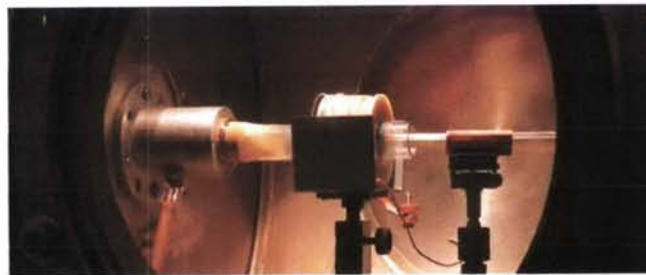


Fig. 237. The test section of the experimental setup.

Aerodynamic channel includes such elements as the flow-measuring washer, the electromechanical valve, the steel duct of 44 cm length and 34 mm diameter and the quartz glass pipe the same parameters. Fuel injecting is performed towards the main air stream through the injector system which is represented by the 4mm diameter ceramic tube mounted on the aerodynamic channel axis (Fig.238).

The electrical discharge is initiated between the annular electrode building-in quartz glass pipe and the wire electrode fixed on the ceramic tube axis.

The annular electrode width is 1 cm, the wire electrode diameter is 1.2 mm. Brass and tungsten are used as electrode materials.

Longitudinal magnetic field is generated in the system by the Helmholtz coil made of 2.2 mm diameter copper wire and positioned coaxially with the quartz glass pipe. Coil power supply comes true from the storage battery.

Stabilized power supply with 5 kV voltage and 1 A current in maximum is used for direct current discharge igniting.

There is the possibility to vary electrode and coil polarities in experiments.

The synchronization scheme gives proper sequence and time spacing between discharge switching on-off, valve opening, registration devices triggering and magnetic field switching on-off.

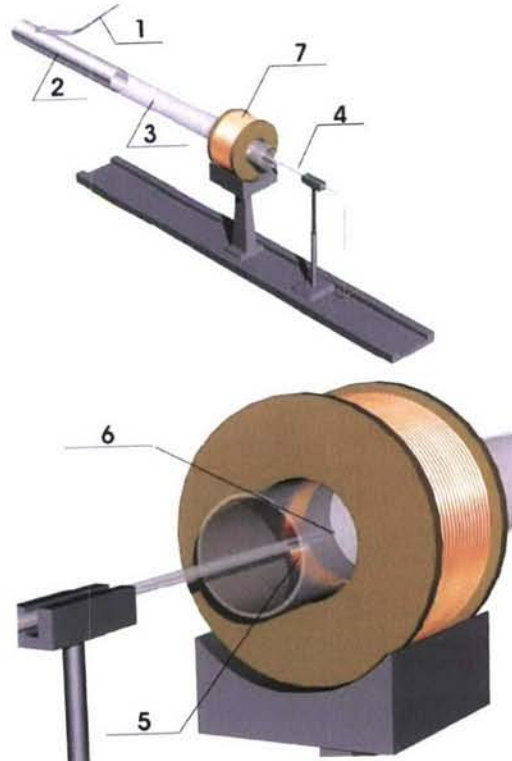


Fig. 238. The scheme of the facility.

1 - the electromechanical valve, 2 - the steel duct, 3 - the quartz glass pipe, 4 - the injector system, 5 - the annular electrode, 6 - the wire electrode, 7 - the Helmgoltz coil.

The high speed digital video camera Citius Imaging C10 with following parameters is used for discharge visualization: maximum matrix resolution is 652×496, pixel size is 10 mkm², maximum speed is 10000 fps, exposure time is from 6 mks and synchronization accuracy is about 1 mks, that allows to resolve the discharge evolution in flow and in external magnetic field.

Measuring signals are registered by the four-channel digital memory oscilloscopes Tektronix TDS 2414 and ASK 3107.

Scheme of operation

The scheme of the experiment is shown in Fig.239. The main stream (air) 7 comes into the test section from left to right. The fuel (propane) 8 is injected through the

injector system 5 from the right to the left. The discharge 3 is created between the annular 1 and wire 2 electrodes. The discharge current aligns with the external magnetic field 6 and as the result the electromotive body force causes the electrical discharge movement and deformation across the air-propane contact surface providing conditions for better mixing.

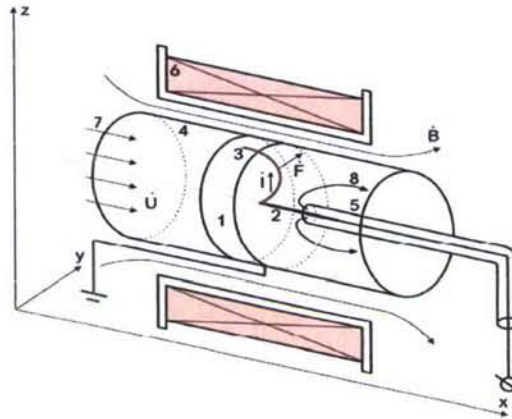


Fig. 239. Schematic of the experiment on MHD-assisted mixing and combustion.

Experimental Runs

Several operation modes were tested in this experimental study.

1. The electrical discharge in external magnetic field for non-flow conditions.
2. The electrical discharge in magnetic field with airflow.

Typical experimental conditions in the test section were as follows:

The magnetic field value was varied from 0.01 to 0.2 T.

Static pressure changed from 15 kPa to 25 kPa.

Air flow velocities were 10 m/s, 40 m/s, 80 m/s.

Previously calibrated measuring washers were used for the flow velocities

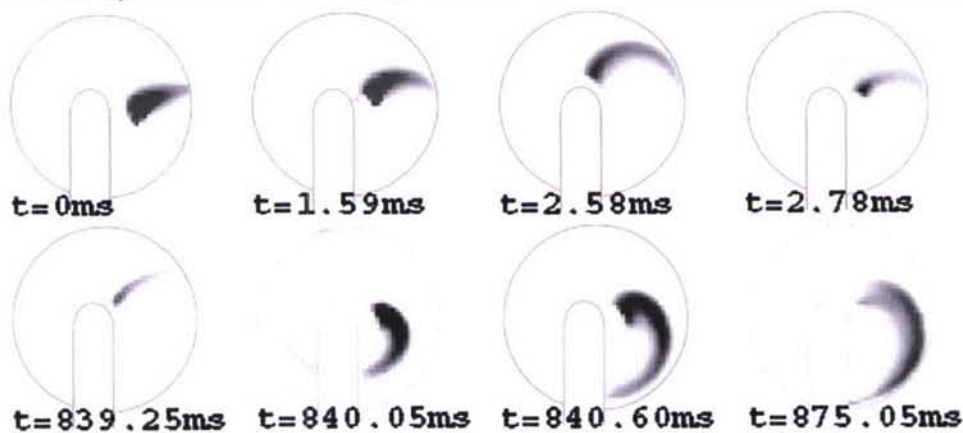


Fig. 240. The discharge evolution in 0.2 T magnetic field for non-flow conditions.
 $P=20 \text{ kPa}$, $I=0.9 \text{ A}$, $U=600 \text{ V}$.

establishment. Washers calibration was performed by three methods: through the leakage flow rate determination, through the flow rate determination with the flowmeter, through the flow velocities determination by means of Pitot tube. Aerodynamic channel length provided stabilized velocities profiles in the test section.

The discharge of 1 A current was typically registered.

Experimental Results

The experimental results are represented below.

Photos in Fig.240 demonstrate the discharge evolution in 0.2T magnetic field for non-flow conditions.

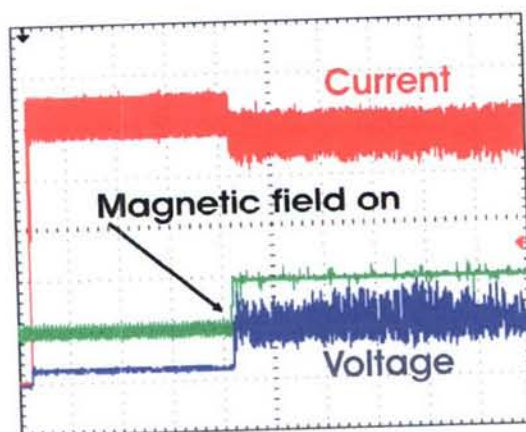


Fig.241. The discharge electrical characteristics in 0.2 T magnetic field for non-flow conditions.

Static pressure in the test section was 20 kPa. The discharge current and the voltage at magnetic field switched on time moments were 0.9 A and 600 V correspondingly.

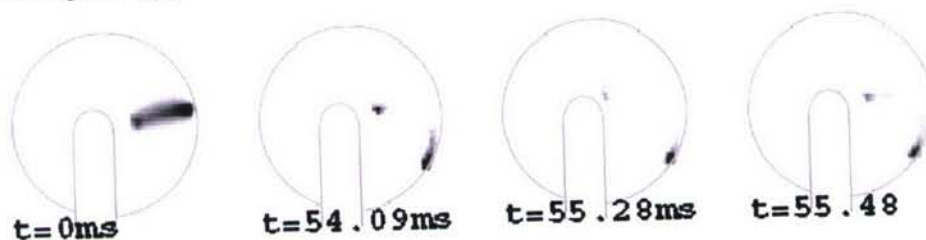
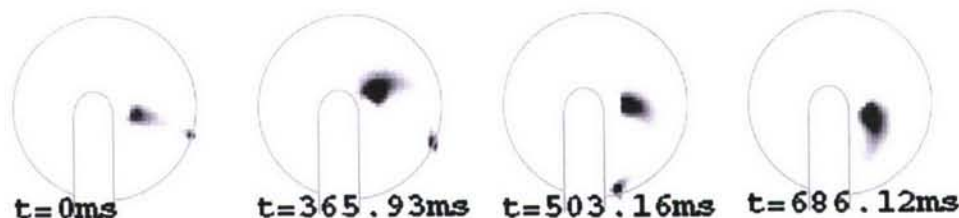


Fig. 242. The discharge evolution in 0.03 T magnetic field for non-flow conditions.
 $P=20 \text{ kPa}$, $I=0.9 \text{ A}$, $U=400 \text{ V}$.

Here and then the shooting exposure time is 0.023 mks, the shooting speed is 5 kHz, the matrix resolution is 60×52 . Circumferences in the photos represent the annular electrode, whereas the injecting tube with the wire electrode is imitated as the vertical pivot with the blunted edge. The discharge in the photos is depicted in quartz glass pipe cross-section plain. Its current direction is from the wire electrode to the annular one. The magnetic field is applied beyond the figure plain, so the electromotive body force acts in anticlockwise direction. The photos at zero time moments stand for

the non-magnetic field discharge existing; while others are correspond to the discharge evolution in the external magnetic field.

It is clearly seen from the photos the spiral shape and the rotation of the discharge caused by its current interaction with the transversal external magnetic field and by the re-connection effects. The important detail of the observed discharge is the higher curvature and the rotational speed of the arc channel near the central electrode.



*Fig.243. The discharge evolution in 0.01 T magnetic field for non-flow conditions.
P=20 kPa, I=0.9 A, U=200V.*

The corresponding oscillograms of the discharge characteristics are presented in Fig.241. One can notes that power input into the discharge channel increases when the magnetic field is switched on. It conforms to our earlier observations of the magnetic field effects on transverse discharge characteristics. The arc voltage fluctuations at the switched on magnetic field conditions reflect the re-connection effects.

The discharge in 0.03 T and 0.01 T magnetic fields without airflow is shown in Figs.242, 243. As distinct from previous case there is no intensive discharge rotation at the annual electrode here. Furthermore one can observe the cathode spot backward movement for the 0.01 T magnetic field case.

The discharge characteristics at magnetic field switched on time moments for these runs were 400 and 200 volts. The arc current and voltage traces are plotted in Fig.236.

Photos in Fig.245 represent the discharge evolution in 0.2 T magnetic field with airflow of 10 m/s velocity directed opposite the external magnetic field induction vector. Static pressure in the test section was 20 kPa. The discharge current and the voltage at magnetic field switched on time moments were 0.8 A and 1.2 kV

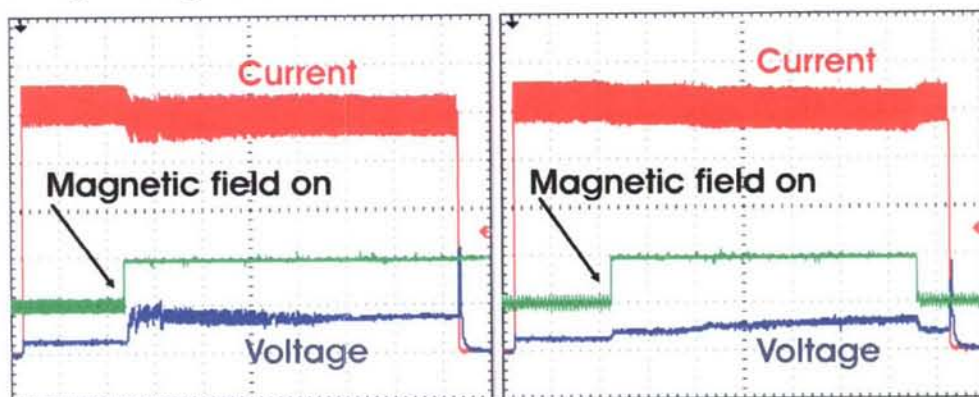


Fig. 244. The discharge electrical characteristics in 0.03 and 0.01 T magnetic field for non-flow conditions.

correspondingly.

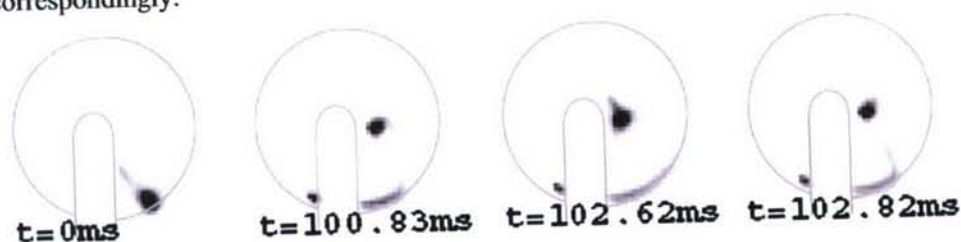


Fig. 245. The discharge evolution in 0.2 T magnetic field with

Here the flow effect becomes apparent in the significant discharge elongation resulted in the bright spots well pronounced at the both electrodes. Nevertheless, the discharge spiral feature with the annual electrode re-connection is still very well revealed.

The arc characteristics oscillograms are represented in Fig.246. It is seen that intensity of the discharge voltage fluctuations are much stronger defined even prior to the magnetic field switching on. The higher fluctuation level reveals the arc – cross flow interaction phenomenon.

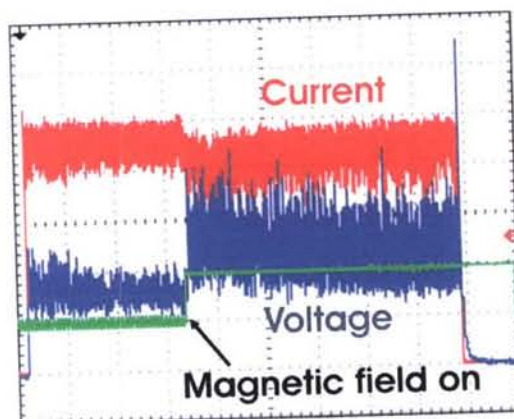
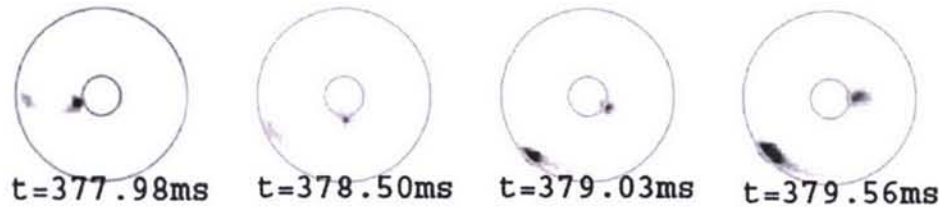


Fig. 246. The discharge electrical characteristics in 0.2 T magnetic field with airflow of 10 m/s velocity.

To resolve the discharge rotation frequency the brass central electrode of 10 mm diameter was installed instead of wire 1.2 mm diameter electrode.

The appropriate discharge evolution in 0.1 T magnetic field for non-flow condition is shown in Fig.247. The static pressure in the test section was 20 kPa. The discharge current and the voltage at magnetic field switched on time moments were 0.9 A and 500 V correspondingly.

The shooting exposure time is 0.011 mks, the shooting speed is 6 kHz, the matrix resolution is 52×48. The central circumferences on the images represent the 10 mm diameter electrode.



*Fig. 247. The discharge evolution in 0.1 T magnetic field for non-flow conditions.
P=20 kPa, I=0.9 A, U=500 V.*

Discharge Evolution in Gas Flow

To get more efficient discharge current – magnetic field interaction in gas flow it

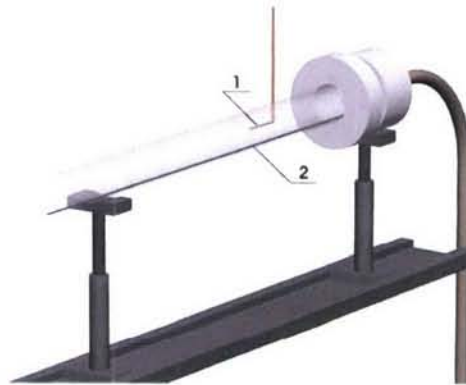


*Fig.248. The test section of the experimental setup.
1 – the wire central electrode, 2 – the tungsten rail electrode.*

was decided to use long tube electrode instead of ring annular one.

Preliminary investigations of the electrical discharge in gas flow have been carried out for the configuration of rail tungsten electrode (Fig.248).

In this experiment the electrical discharge is initiated between the wire central and rail electrodes.

Both electrodes diameter is 2.5 mm.

The electrical compressor is used for the appropriate gas flow organization. Flow velocities are determined with the flowmeter.

The discharge being attached by one of its ends to the central wire electrode slides by another end along with the rail electrode in gas flow.

Several operation modes were tested in this experimental study.

1. The electrical discharge in gas flow for the rail cathode configuration;
2. The electrical discharge in gas flow for the rail anode configuration.

Typical experimental conditions in the test section were as follows:

static pressure – 100 kPa;

gas flow velocity range – from 1.2 to 10.4 m/s at the entrance of the test section.

For the case of rail cathode configuration it was revealed the slow sliding of the cathode spot along with rail. The sliding time value before the discharge reconnection occurring is about 60 – 120 s for different flow velocity regimes. The discharge prolongation is about 10 cm and defined by the source capacity. Spot velocity is lower then flow velocity and probably determined by the heat mechanism.

In the case of rail anode configuration there is no significant discharge elongation down stream the flow but the anode spot velocity is rather high.

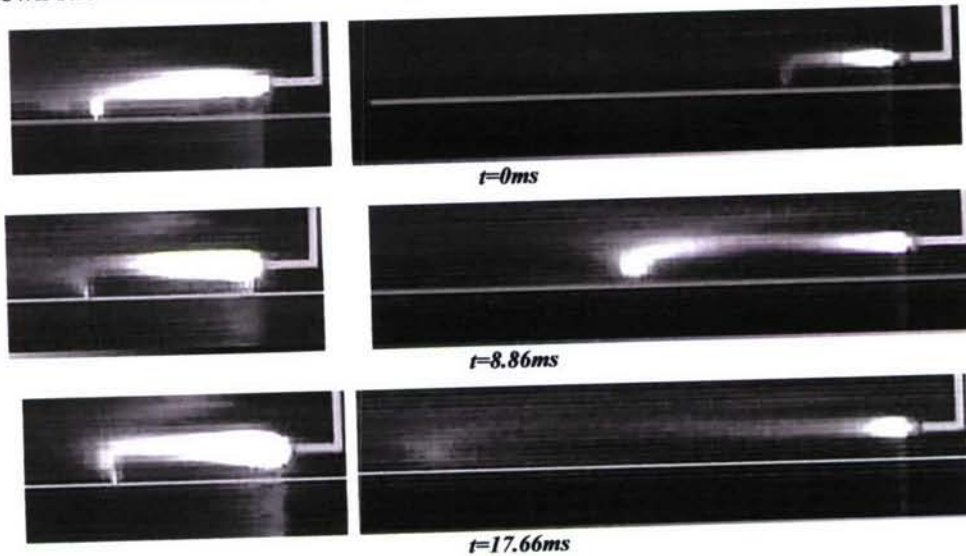


Fig.249. Discharge configuration for two cases.

Fig.249 represents the high speed camera photos of discharge evolution in rail cathode and rail anode configurations for the same time moments.

Corresponding oscillograms of the described above processes are presented below in Fig.250.

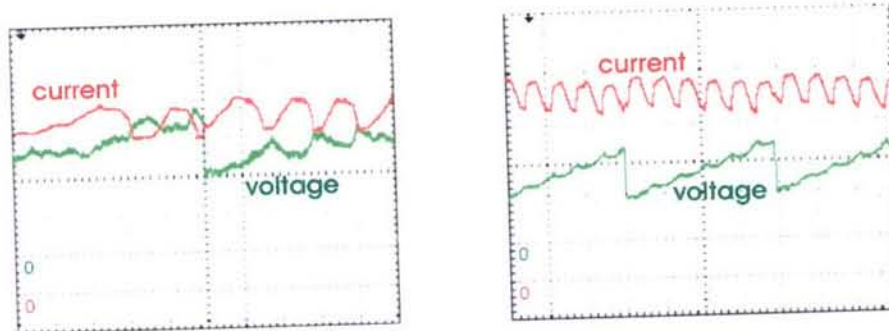


Fig. 250 Discharge evolution for the rail cathode and rail anode cases.
Flow velocity 1.2 m/s.

The discharge visualization is presented in Fig.251.

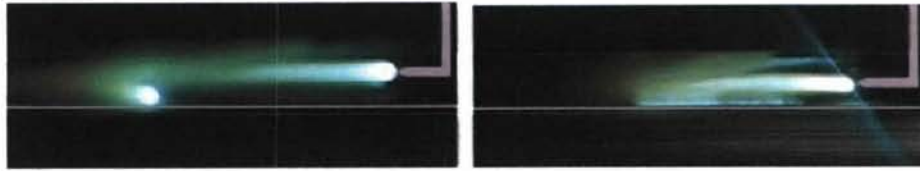
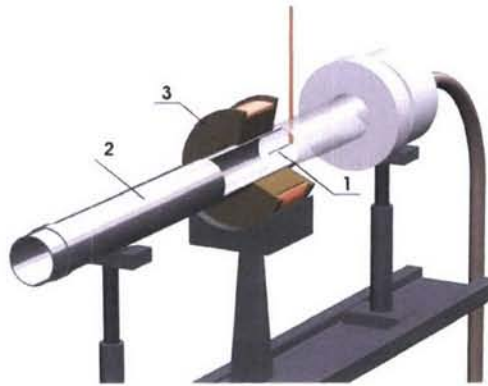


Fig. 251. Common speed camera photos of discharge evolution for the rail cathode and anode cases. Flow velocity 1.2 m/s.

Discharge Evolution in Gas Flow in External Magnetic Field

Experiments with the discharge in flow for rail electrode configuration prompted the proper way of new test section designing for the investigation of the electrical discharge interaction with gas flow in external magnetic field. (Fig.252).

The main element of the test section is the aerodynamic channel of 50 cm length



*Fig. 252. New experimental setup.
1 – the wire central electrode, 2 – the aluminum pipe electrode, 3 – the magnetic coil.*

and 34 mm diameter which consists of quartz glass tube and aluminum pipe – external electrode. Gas flow is organized by the compressor and flowmeter is used for velocity

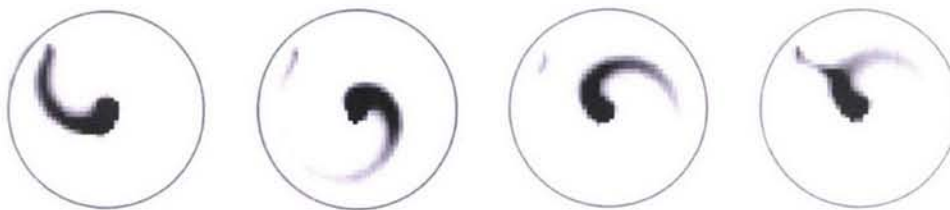


Fig. 253. Discharge evolution in gas flow of 0.2 m/s with external magnetic field of 0.1 T.

measurement. Longitudinal magnetic field of 0.1 T is created with the magnetic coil. The electrical discharge is initiated between the wire central and aluminum pipe electrodes.

In this configuration discharge has a possibility to slide in gas flow along with the external electrode that provides the perpendicular orientation of the discharge and aluminum pipe surface. As a result efficient discharge current – magnetic field interaction takes place.

High speed photos of the discharge – flow interaction in external magnetic field and characteristics oscillograms are presented below (Fig. 253– 255).

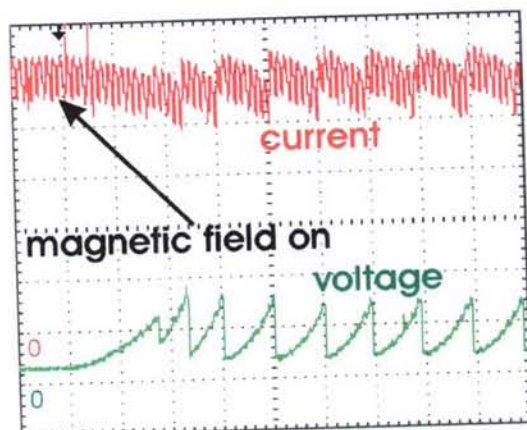


Fig. 254. The discharge electrical characteristics in 0.1 T magnetic field with airflow of 0.2 m/s velocity.

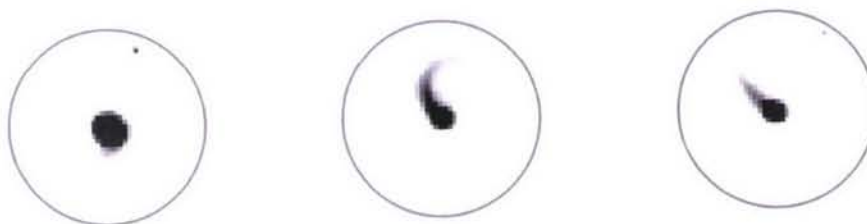


Fig. 255. Discharge evolution in gas flow of 1 m/s with external magnetic field of 0.1 T.

Discharge Evolution in Gas Flow of Counter Streams in External Magnetic Field

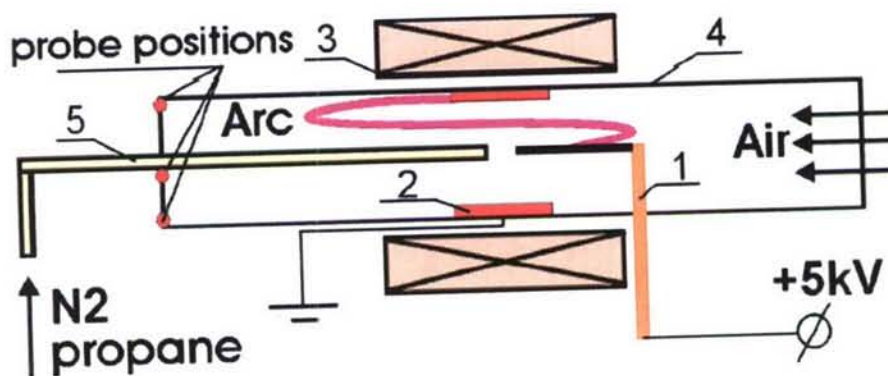


Figure 256. 1 – central tungsten electrode, 2 – annular electrode, 3 – magnetic coil, 4 – aerodynamic duct, 5 – fuel injecting system.

To model the situation of discharge evolution in gas flow of oxygen and injected fuel the following experimental setup has been created (Fig.252,253).

The aerodynamic duct is the glass tube with the length of 90mm and the diameter of 33mm. The fuel injection system is made of the 40mm length and 4mm diameter ceramic pipe. The electrical discharge is ignited between the central tungsten and annular copper electrodes. Magnetic field of the 0.1T value is created in the system.

The high speed digital video camera Citius Imaging C10 is used for discharge visualization.

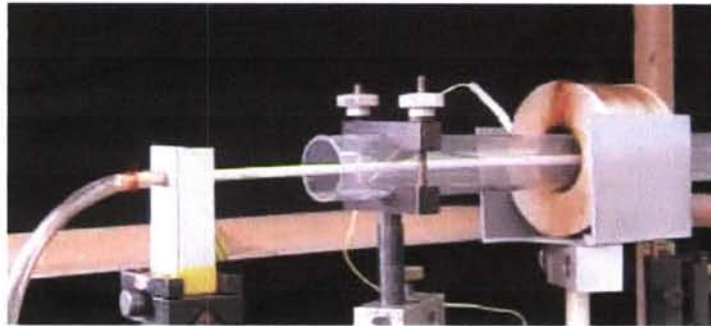


Figure 257. Photo of the test section setup.

Experimental conditions

Parameters of the experiments were as following:

Static pressure – 105 Pa,

Air flow velocity were varied from 1m/s to 3.5m/s,

Injected flow velocity were wide-ranging changed,

Magnetic field induction – 0.1T,

Discharge current and voltage – 0.8A and 1.5kV correspondingly,

Nitrogen was used as injected flow.

Results

Some images of the discharge evolution in combined flow and external

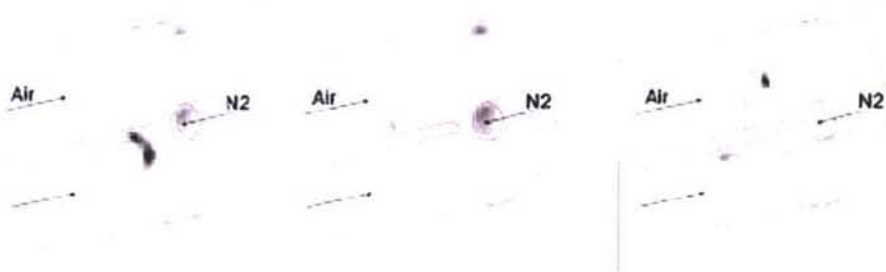


Figure.258. Discharge evolution in gas flow of counter streams in external magnetic field

magnetic field are presented below in Fig.254.

It is seen from the photos that discharge moves in opposite directions along with the both electrodes in flow of counter streams and rotates in external magnetic field. Discharge localizes near the contact surface of two jets and intersects it. All of that provides good conditions for mixing.

Combustion with the Discharge in Gas Flow of Counter Streams

To investigate the combustion completeness in such system some experiments on propane combustion with presents of the electrical discharge but without the magnetic field for a while were carried out.

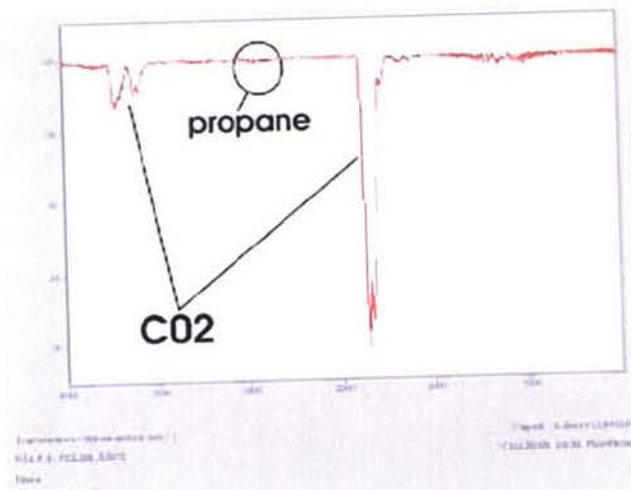


Figure.259. Spectrograms of combustion products for bottom probe position.

The experimental conditions were following:

Static pressure - 105 Pa,

Fuel - propane,

Air flow velocity - 2m/s,

Equivalence ratio - 8, 6 and 4.

To observe the combustion completeness some probes of the products were taken across the exhaust cross section of the combustor (the probe positions are shown in Fig.252).

Probe analysis was performed with the IR absorption spectrometer BUCK 500.

It was revealed that under the considered setup configuration and flow velocities there is no propane in combustion products. That means the full propane conversion takes place.

Typical spectrograms are shown in Fig.256.

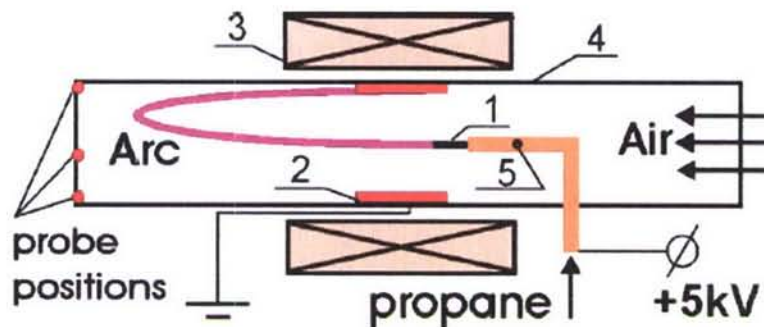


Figure.260. 1 – central tungsten electrode, 2 – annular electrode, 3 – magnetic coil, 4 – aerodynamic duct, 5 – fuel injecting system.

The negative aspect of the considered setup configuration is the intensive propane cracking and soot formation inside the injector pipe. That cracking is the result of the injector system heating by the discharge propagation downstream the flow.

To avoid that negative feature the new configuration has been proposed (Fig.260).

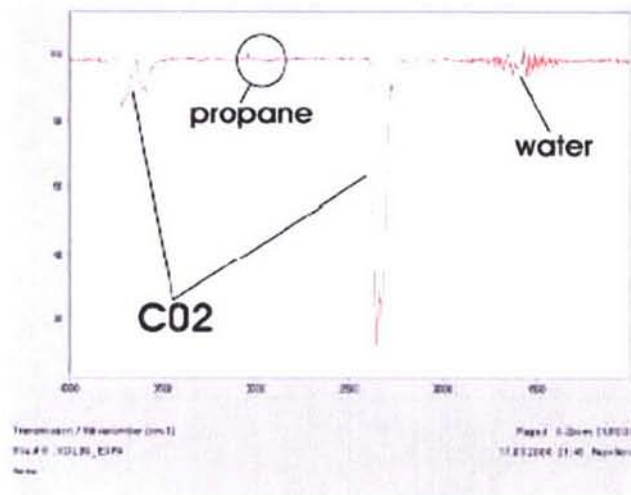


Figure. 261. Spectrograms of combustion products for bottom probe position.

Here the fuel injecting system is combined with the central electrode. Propane comes to the test section through the 1mm holes around the central electrode.

Combustion completeness investigation has been also performed in the configuration. Products probes were taken across the exhaust cross section of the combustor as it is shown in Fig.256

There was no soot formation any more.

Typical spectrograms are presented in Fig.261.

It is seen that under considered experimental conditions in such a setup configuration the full propane conversion takes place.

As for the external magnetic field switching on the flame front becomes more uniform along the combustor cross section and shortens along the combustor length. So the flame stabilization takes place.

But the field of our interest is a high speed combustion where non-full fuel conversion takes place because of the lack of intensive mixing. MHD mixing is considered to solve the problem.

Air flow velocities of the setups are limited by the break-down of the discharge which does not have the possibility to reignite in high speed flow in described configurations. So the new experimental setup is under design now to observe a high speed combustion.

CONCLUSIONS

Two variants of the modified plate model have been designed, fabricated and successfully tested at both experimental facilities: HFP WT and HV MHD WT.

New high-speed visualization technique applied has provided to resolve the strong MHD interaction at both facilities.

Numerical simulation has confirmed qualitatively the disturbed flow structure in a case of hypersonic tests. Numerical simulation of the MHD interaction at subsonic facilities is now in progress.

The breakthrough results have been obtained at both experimental facilities with the new type of electrodes – pin electrodes. It was confirmed experimentally that the very low induced current found in previous experimental studies was limited by the ‘cold’ boundary layers at the working surface of the models. Implementation of the pin electrodes allowed getting good electrical contact of the electrodes with well conducting core flow.

Improvement of the electrical contact load and measurement system resulted in the record level of the electrical power extraction from hypersonic airflow – more than 60W/electrode pair; and the well resolved voltage evolution during the magnetic field pulse at low speed HFP facility.

At both facilities visualization confirms the significant MHD interaction resulting in the clearly seen flow field modifications.

In frame of the work on Task II the combustion enhancement by the arc rotating in external magnetic field has been experimentally demonstrated.

The work planned for the last Quarter of the project includes the final experiments at all three experimental setup and analytical efforts to treat the experimental results and to develop the recommendation for future utilization of the obtained data.

The next steps of the experimental and theoretical studies are formulated.

References

1. Bocharov A., Bityurin V., Klement'eva I., Leonov S. Experimental and Theoretical Study of MHD Assisted Mixing and Ignition in Co- Flow Streams // Paper AIAA 2002- 2228, 40th AIAA Aerospace Sciences Meeting & Exhibit, 14-17 January 2002/ Reno, NV, P.8
2. Andriatis A.V., Zhlukto S.A., Sokolova I.A. Transport Coefficients for Chemical Nonequilibrium Components of Air Mixtures // J. Mathematical Modeling, v.4, No.1, 1992.
3. Zhubkov A.I., Tirskiy G.A., Levin V.A., Sakharov V.I. Motion of bodies in Earth's and Planet's Atmospheres with Supersonic and Hypersonic Velocities under Conditions of Chemical Conversions, heat Transfer and Radiation // Rep. No.4507 of Inst. Of Mechanics of Moscow State University, 1998.
4. Sokolova I.A., Tirskiy G.A. Calculations and Approximations to Collision Integrals for the Components of Mixtures Containing O, N, H, C, F, Na, S, Si // Rep. No.2857 of Inst. Of Mechanics of Moscow State University, 116p., 1993.
5. Gordeev O.A., Kalinin A.P., Komov A.L., etc. Interaction Potentials, elastic Cross-Sections, Collision Integrals of Air Components for Temperatures up to 20000K // Review on thermophysical properties of substances, Acad. of Sci. Of USSR, Inst. Of High Temp., 1985, No.5(55), 100pp
6. V.A.Bityurin, A.N.Bocharov, Advanced Assisted Mixing of reacting Streams, // Paper AIAA 2001- 0793, 39th AIAA Aerospace Sciences Meeting & Exhibit, 8-11 January 2001/ Reno, NV
7. Klimov A. I., Bityurin V, Kuznetsov A., Vystavkin N, Tolkunov B. External and Internal PAC in Airflow// In: 42nd AIAA Aerospace Sciences Meeting and Exhibit, Reno, Nevada, 4-7 January, 2004
8. A.N. Bocharov, V.A. Bityurin, E.A.Filimonova, A.I.Klimov Numerical Study of Plasma Assisted Mixing and Combustion in Non-Premixed Flows// In: 42nd AIAA Aerospace Sciences Meeting and Exhibit, Reno, Nevada, 4-7 January, 2004.

GENERAL CONCLUSIONS

1. MHD hypersonic airflow at the dynamics pressure of tenths atmosphere over the circular cylinder with the azimuthal magnetic field was studied with three different numerical models.
2. The 2-D Navier-Stokes/MHD coupled perfect gas based models both neglecting and including Hall effect demonstrate dramatic influence of MHD interaction on hypervelocity flow around cylinder:
 - The significant shock front displacement and dispersion;
 - The significant relaxation of pressure distribution around cylinder;
 - The significant reduction in temperature around cylinder;
 - The dramatic reduction in heat flux.
 - On the other hand a significant total drag penalty accompanies interaction due to $\mathbf{j} \times \mathbf{B}$ body force.
 - The potential practical application to hypersonic flights is predicted for such a configuration.
3. The real gas based model including finite rate chemical kinetics of (seeded) air has changed the evaluation of the originally considered approach:
 - The natural ionization degree is rather low resulting in the dominating role of the Hall effect that reduces the effective MHD interaction by orders of magnitude;
 - The actual MHD interaction parameter reveals no dependence of magnetic field magnitude since the Hall parameter square becomes much higher of 1;
 - Under low-pressure conditions the characteristic size of the MHD interaction area is to be 1m or larger and the required ionization degree is to be higher than 1%. The latter seems to be very problematic for real flight conditions even with external ionization because of energy consumption;
 - To block the negative influence of the Hall effect on the MHD interaction effectiveness new revolutionary conceptual configurations of MHD on-board systems are required.
4. The experimental study of MHD interaction at the circular cylinder in a cross-flow has revealed many problems associated with the on-ground experimental conditions:
 - a small model size results in:
 - dominating role of non-equilibrium processes;
 - low MHD interaction parameter;
 - strong influence of surface (electrode) effects.

- strong influence of the test section walls both electro-dynamically and gas dynamically (boundary condition problem);
5. From the other hand the cylinder experimental and analytical studies have provided the initial data base for further development in the MHD application field:
 - the basic idea of MHD interaction effects and their potential applications in high speed flight has been confirmed;
 - new effects have been found, for example, the rather strong in-wake interaction and dramatic increase of the total drag. These two allowed to extend the studies with different models – wedge, plate and others, and to formulate a novel concept “MHD parachute” for reentry trajectory optimization;
 6. With the wedge shaped model series the **first experimental** demonstration of MHD flow control has been obtained under hypersonic conditions corresponding to real flight. The numerical simulation has provided the effective tool of experimental data analysis and treatment.
 7. The experimental series with the flat plate model has demonstrated (**also at the first time**) the significant electrical power extraction from hypersonic airflow with the simplest surface MHD generator equipped with on-board magnetic system.
 8. In the experimental series with subsonic air (non-seeded) flow the MHD interaction has been also demonstrated. It was found that under subsonic conditions the main contribution to in-flow induced current has been provided by the time variation of magnetic field rather than by air motion. Similar effect has been found later under hypersonic conditions but its role is rather small.
 9. The subsonic and hypersonic results reveal reasonable well correlation with each other providing the extended experimental and analytical database for future works in this field. and in particular in the development of MHD control of reentry flights – the most impressive prospective of MHD aerospace applications.
 10. In frame of the Task II – MHD Control of Internal Flow the main efforts have been undertaken toward the enhancement of mixing, ignition and combustion control in high speed co-flow streams:
 - The concept of the vortex generation by non-potential body force resulting from constricted discharge in cross magnetic field has been formulated and confirmed;
 - The concept of the Reacting Volume as a measure of convective-diffusion mixing rate has been formulated and confirmed;
 - The multi level numerical model family has been developed and implemented into in-house PlasmaAero code family providing simulation of reacting media motion in external electrical and magnetic fields including electrical space separation effects;

- The series of laboratory scale experiments has been formulated and performed, gradually improving the MHD assisted mixing by fast moving arc across of main flow;
 - The seasonable good correlation has been found between experimental and simulation results;
 - Under experimental conditions available at this stage the MHD interaction has provided the flame stabilization and faster combustion (shortening flame) and the ignition of the rather lean mixture;
 - The physics of the arc driven flow has been clarified in many interesting and important aspects such as the arc velocity distribution along the radius of the circular duct;
 - The corresponding plasma-chemistry database of the typical hydrocarbon gaseous fuel in air is developed and used effectively in supporting of experiments and experimental datatreatment.
11. In-house PlasmaAero code family has been significantly upgraded during the project work to provide sophisticated description of the different aspects of magneto-plasma aerodynamics and related processes.
12. The intermediate results of this work are discussed regularly at the International and National forums such as WIG, AIAA Meetings, Moscow International Workshop on Magneto-Plasma Aerodynamics and others. More than 20 publications have been prepared under the Project work.

ACKNOWLEDGEMENT

The research team of the ISTC/EOARD Project 2196p thanks EOARD and AFOSR administrations for financial and moral support this emotional work, our special thanks to Waine Donaldson and Surya Surampudi of EOARD and Julian Tishkoff of AFOSR who provided us the effective friendly atmosphere during the work. We thank also our colleagues of IVTAN, TsAGI and TsNIImash for technical support and contribution.